

An Embryonic-inspired Approach to Engineer Functional Human Cardiac Tissue

Submitted in partial fulfillment of

the requirements for the degree of

Doctor of Philosophy

in

Biomedical Engineering

Quentin Jallerat

M.S., Biomedical Engineering, Columbia University
M.S., Engineering / Diplôme d'Ingénieur, École Centrale Paris

Carnegie Mellon University
Pittsburgh, PA

May, 2016

Élévation

Au-dessus des étangs, au-dessus des vallées,
Des montagnes, des bois, des nuages, des mers,
Par delà le soleil, par delà les éthers,
Par delà les confins des sphères étoilées,

Mon esprit, tu te meus avec agilité,
Et, comme un bon nageur qui se pâme dans l'onde,
Tu sillones gaiement l'immensité profonde
Avec une indicible et mâle volupté.

Envole-toi bien loin de ces miasmes morbides;
Va te purifier dans l'air supérieur,
Et bois, comme une pure et divine liqueur,
Le feu clair qui remplit les espaces limpides.

Derrière les ennuis et les vastes chagrins
Qui chargent de leur poids l'existence brumeuse,
Heureux celui qui peut d'une aile vigoureuse
S'élancer vers les champs lumineux et sereins;

Celui dont les penses, comme des alouettes,
Vers les cieux le matin prennent un libre essor,
— Qui plane sur la vie, et comprend sans effort
Le langage des fleurs et des choses muettes!

Charles Baudelaire, *Les Fleurs du Mal*

Dedication

To my parents, Eric Jallerat and Isabelle Baillet, who have been present and supportive at every single step. Their dedication to my brother's and my own well-being is truly overwhelming. My extended family, Gérard and Christine, has helped me grow to the person I am today.

To my wife, Dr². Jenny Yuan, who brings both balance and excitement to my life and has stuck with me through countless trips on the megabus red-eye. We made it!

To my many friends who got their PhDs long before me, you have made me believe that there would be an end. As much as I would like to claim that American PhDs are tougher than French PhDs, I know, Philippe, that you completely deserve your job in the secretive research division of a global corporate empire. Obviously if you come across an elixir to live a thousand years, I hope you will remember me (as soon as you are done testing it on yourself).

To Clarke, Bradbury, Asimov, and Dick, they have been a much bigger part of my education than my parents probably intended when I started picking up books from their shelves. I would not be on this path without science-fiction and good friends to talk about it. I am driven by a desire to witness the future come about and I will always wonder which seat provides the best view. Working at the cutting-edge of regenerative medicine has truly been inspiring.

Acknowledgements

To Prof. Feinberg, I am deeply grateful for the opportunity to join the group. From the time of my first visit, I have found his vision and ambition contagious. With his help, his continuous teaching, and unceasing push for science, I believe I have grown and accomplished much over the last five and a half years.

The thoughtful and generous advice of Profs. Campbell, Davidson, and LeDuc has been critical to shape my work and make sure I would not get lost in a 50 year grand plan to solve cardiac disease. Their collective expertise continuously informed my protocols and allowed me to achieve much despite my initial lack of knowledge in most aspects of my thesis.

My work would not have been possible without the incredible support from the department of Biomedical Engineering; Prof. Wang's dedication to academic excellence and collaborative research has created an exceptional environment; everybody in the department's administration (Kristin Kopf, Vanessa Calvin, Prof. Zapanta, and many others I should not name lest I reveal how long I have been here) has always been incredibly supportive and patient even when I blundered.

Starting this adventure in a group of 3 led me to work with many colleagues as our laboratory grew. From the old guard, Dr. John Szymanski and Dr. Rachelle Palchesko-Simko have been great sources of inspiration and motivation. Working with John, I discovered the exhilaration of "crushing" science late at night during our many many projects together. He inspired the idea of using gelatin as a sacrificial substrate, which I describe in chapter 3. From there, Rachelle and I took it to the next step and micropatterned collagen I hydrogels. Since then, she has pushed the limit of the technique well

past the point where I could follow. My “younger” colleagues and friends, Rebecca Duffy, Ivan Batalov, and TJ “Thomas” Hinton have been a pleasure to work with and have given my work a breadth I would not have dreamed of: from bioprinting an embryonic heart scaffold to differentiating human stem cells and creating contractile muscle, they have allowed me to follow in their tracks more often than they followed mine. I have fed on the motivation and optimism of my young colleagues, Emily Sevcik, Andrew Lee, and Sarah Abdollahi, during the dark times but I do hope that I will inspire them to find their pace and to keep believing. I thank Dr. Alkiviadis Tsamis for taking what John and I started to a whole new level. Over the years, many amazing undergraduate students have provided great help with my projects and I look forward to following their careers. Finally, I am deeply thankful to all in the group and beyond for giving a patient ear to my existential concerns, expressed in sometimes less than fluent English. I understand that getting my mumbling accent is a normal part of the learning curve for any new lab member.

Beyond our laboratory, I am grateful for the generous help provided by Mathilde Vermeer and Dr. Peter Van Der Meer to start our human embryonic stem cell culture, and by Dr. Wu at Stanford University for the induced pluripotent stem cells.

The scientific enterprise does not run only on dreams and coffee. I have been very lucky to receive significant funding first from the DOWD-ICES Fellowship, then from the Richard K. Mellon Foundation Presidential Fellowship for the Life Sciences. Prof. Feinberg was able to finance my research thanks to the NIH, the AHA, the NSF, and the HFSP and gave me repeated opportunities to present my work at international conferences.

Abstract

Each year, more than 130,000 Americans die from myocardial infarction, commonly known as a heart attack. There is currently no therapy to repair the injured myocardium, which does not regenerate by itself. Cardiac tissue engineering offers a possible path toward treatment: by engineering the cell environment with scaffolds, and physical and biochemical stimuli, researchers can grow cardiac muscle *in vitro*. Yet, reproducing the physiology of adult cardiac muscle remains an elusive goal. First, researchers use cardiomyocytes derived from human pluripotent stem cells, which are immature and embryonic-like. Second, it is only during embryonic development that we can learn how to turn poorly organized and immature cardiomyocytes into a fully integrated and functional cardiac tissue *in vivo*. The extracellular matrix plays a critical role during morphogenesis and is already used as a template for tissue engineering scaffolds. I hypothesize that the extracellular matrix of the embryonic myocardium contains cues that guide embryonic-like cells to grow and mature into strong cardiac muscle.

In this work, I studied the extracellular matrix in the chick embryonic heart to derive structural parameters from the fibronectin and laminin matrices. In parallel, I characterized a novel scaffold fabrication technique that enables the transfer of micrometer size patterns of proteins onto natural hydrogels. I found that high concentration COL1 hydrogels with micropatterned fibronectin lines maximized the alignment of chick cardiomyocytes. Finally, I used human embryonic stem cell-derived cardiomyocytes to create aligned cardiac sheets on this ideal substrate. Human cardiac sheets generated contractile stresses of 1-25 kPa under electrical stimulation, comparable to adult left ventricular

myocardium. Further, I built 3D multilayered cardiac constructs by stacking single cardiac sheets layer-by-layer. Our micropatterned hydrogels enabled, for the first time, the study of the contractile properties of multilayered constructs.

The techniques developed in this work attempt to bridge the gap between 2D microfabricated substrates and 3D engineered scaffolds and promote synergy between developmental biology and tissue engineering. Our work lays the foundation for engineering biomimetic scaffolds, modeled after the embryonic heart, to promote the maturation and growth of human cardiac tissue.

Table of Contents

LIST OF FIGURES AND ILLUSTRATIONS	XII
LIST OF TABLES	XIV
LIST OF ACRONYMS	XV
CHAPTER 1 INTRODUCTION	1
CHAPTER 2 BACKGROUND.....	7
2.1 THE MYOCARDIUM.....	7
2.1.1 Structure and function	7
2.1.2 Clinical need for cardiac repair.....	8
2.1.3 Morphogenesis of the myocardium	9
2.1.4 The extracellular matrix in adult and during development.....	11
2.2 THE CHICK MODEL	13
CHAPTER 3 CHARACTERIZATION OF THE EXTRACELLULAR MATRIX IN THE MYOCARDIUM DURING THE EMBRYONIC DEVELOPMENT.....	15
3.1 ABSTRACT	15
3.2 INTRODUCTION.....	15
3.3 MATERIALS & METHODS	18
3.3.1 Chick embryonic heart dissection.....	18
3.3.2 Fixing and immunostaining	19
3.3.3 Clearing samples by refractive index-matching	20

3.3.4 High resolution confocal microscopy	20
3.3.5 Characterization of the effect of clearing on nuclear morphology	21
3.3.6 Analysis of 3D image z-stacks of laminin and fibronectin.....	22
3.4 RESULTS & DISCUSSION.....	24
3.4.1 Refractive-index matching enables imaging the architecture of the whole heart.....	24
3.4.2 Clearing with BABB causes anisotropic deformation in the myocardium	26
3.4.3 The left ventricle myocardium is vascularized between day 5 and day 9 (stages HH 28 - 35)	29
3.4.4 Laminin and fibronectin, but not collagen type IV are found in the prevascular myocardium of the ventral left ventricle of 5 day-old chick embryos.	32
3.4.5 Fibronectin and laminin are colocalized in intercellular spaces in the avascular myocardium.....	34
3.4.6 Quantitative characterization of the fibronectin and laminin matrices.....	36
3.5 CONCLUSION.....	42

CHAPTER 4 DEVELOPMENT OF A TECHNIQUE TO ENCODE DIRECTIONAL ECM CUES ONTO A HYDROGEL TO GUIDE CHICK CARDIOMYOCYTE

ALIGNMENT.....	43
4.1 ABSTRACT	43
4.2 INTRODUCTION.....	43
4.3 MATERIALS & METHODS	47
4.3.1 Hydrogel casting.....	47

4.3.2 Transferring ECM patterns onto hydrogels	48
4.3.3 Chick primary cardiomyocyte isolation and culture.....	50
4.3.4 Fixing and immunostaining	51
4.3.5 Image acquisition and analysis.....	51
4.3.6 Experimental design and statistics	52
4.4 RESULTS & DISCUSSION.....	54
4.4.1 Patterning fibronectin lines on hydrogels with high fidelity.....	54
4.4.2 High concentration collagen I maximizes cardiomyocyte alignment with FN lines.....	56
4.4.3 Remodeling and competition of adhesive patterns cause loss of alignment	59
4.5 CONCLUSION.....	62
CHAPTER 5 CREATION OF ALIGNED HUMAN CARDIAC TISSUE.....	63
5.1 ABSTRACT	63
5.2 INTRODUCTION.....	63
5.3 MATERIALS & METHODS	65
5.3.1 Stem cell culture and differentiation.....	65
5.3.2 Stacking cardiac sheets	68
5.3.3 Muscular thin film assay.....	69
5.3.4 Immunohistochemistry and fluorescence microscopy	71
5.3.5 Orientational order parameter analysis	71
5.3.6 Characterization of collagen type I hydrogels.....	72
5.4 RESULTS & DISCUSSION.....	72

5.4.1 Growth and alignment of human cardiac sheets	72
5.4.2 Measuring contractile force generation with the muscular thin film assay.....	76
5.4.3 Stacking micropatterned hydrogels to create multilayered cardiac constructs with precise control of the 3D geometry of ECM cues.....	80
5.4.4 Multilayered constructs can be used in the muscular thin film assay.....	82
5.5 CONCLUSION.....	84
CHAPTER 6 SUMMARY AND FUTURE DIRECTIONS	85
6.1 SUMMARY.....	85
6.2 LIMITATIONS AND FUTURE DIRECTIONS.....	86
6.3 CONTRIBUTION TO THE FIELD.....	88
6.4 CONCLUSIONS	89
REFERENCES	90
APPENDIX A LIST OF PUBLICATIONS AND PRESENTATIONS	98
APPENDIX B MATLAB CODE	101
APPENDIX C PEER-REVIEWED ARTICLE 1.....	115
APPENDIX D PEER-REVIEWED ARTICLE 2.....	121
APPENDIX E BOOK CHAPTER	132

List of Figures and Illustrations

Figure 1.1. An embryonic-inspired approach to engineer functional human cardiac tissue.	6
Figure 2.1. Multiscale hierarchical structure of the myocardium.	8
Figure 2.2. Stages of cardiac morphogenesis.	9
Figure 2.3. Formation of the myocardium.	11
Figure 2.4. Composition of the cardiac ECM during development and in adult.	12
Figure 3.1. Dissection and imaging of the left ventricle of 5 day-old chick embryos.	18
Figure 3.2. Characterization of the ECM using Imaris and Matlab.	23
Figure 3.3. Imaging of a whole heart of a 5 day old chick embryos using refractive-index matching with BABB.	25
Figure 3.4. Effect of refractive-index matching on nuclear morphology.	28
Figure 3.5. Vascularization of the myocardium between day 5 and day 9 of development.	31
Figure 3.6. Spatial expression of laminin, FN, and collagen type IV in the left ventricle of 5 day – old chick embryos.	33
Figure 3.7. Colocalization of FN and Laminin in the myocardium in the left ventricle of 5 day old chick embryos.	35
Figure 3.8. Quantitative characterization of laminin and fibronectin volume distribution.	38
Figure 3.9. Characterization of ECM spacing in 3D.	39
Figure 3.10. Structural characterization of the fibronectin fibers.	40
Figure 4.1. Micropatterning ECM cues onto hydrogel scaffolds.	48

Figure 4.2. Calculation of the orientational order parameter.	52
Figure 4.3. Fidelity of Pattern Transfer.	55
Figure 4.4. Chick primary CMs align on micropatterned ECM scaffolds.	58
Figure 4.5. Remodeling of the fibronectin lines after culture.	60
Figure 5.1. Stem cell differentiation, purification, and conditioning.....	66
Figure 5.2. Alignment of human cardiomyocytes on collagen I hydrogels micropatterned with fibronectin lines.	74
Figure 5.3. Young’s modulus and thickness of collagen I hydrogels.	77
Figure 5.4. Contractile force generation by cardiac sheets under field stimulation.	79
Figure 5.5. Creation of multilayered cardiac constructs.	81
Figure 5.6. Stimulated contraction of two-layer cardiac constructs.	83

List of Tables

Table 2.1. Comparison of the timeline for the major phases of cardiac morphogenesis in mouse, human, and chick.....	10
Table 3.1. Distribution of the volume of ECM elements.....	37
Table 3.2. Design criteria for biomimetic ECM scaffolds based on the study of the embryonic myocardium.....	41
Table 4.1. Hydrogel composition used to build 3D functional cardiac tissue using established techniques.....	44
Table 4.2. Hydrogel composition tested to maximize cardiac alignment.	46
Table 4.3. Line width of fibronectin lines before and after transfer to different substrates	54
Table 4.4. Orientational order parameter (mean \pm standard deviation) of chick CMs on different substrates.....	57
Table 5.1. Young's modulus and thickness of collagen I hydrogels made on different days.....	76
Table 5.2. Twitch stress of cardiac MTF under stimulation (kPa).....	77

List of Acronyms

Word	Acronym
Extracellular matrix	ECM
Fibronectin	FN
Laminin	LAM
Collagen type IV	COL4
Collagen type I	COL1
Cardiomyocyte	CM
Pluripotent stem cell	PSC
Embryonic stem cell	ESC
Induced pluripotent stem cell	iPSC
Myocardial infarction	MI
Coronary heart disease	CHD
Muscular thin film	MTF
Poly(N-isopropylacrylamide)	PIPAAm
Polydimethylsiloxane	PDMS

Chapter 1 Introduction

Coronary heart disease (CHD) has been the leading cause of death in the US for several decades: according to the American Heart Association, each year an estimated $\approx 620,000$ Americans experience a new coronary attack (myocardial infarction or MI) ¹. MI has a dramatic and long-lasting effect on the quality of life of patients, and can eventually lead to heart failure. The combined direct and indirect costs of CHD were estimated to be \$204.4 billion in 2010.

MI occurs when a coronary artery is obstructed and the supply of oxygen and nutrients to the myocardium, the cardiac muscle powering the heart's pump, is interrupted. Cardiomyocytes (CMs) that compose the myocardium undergo apoptosis, dramatically reducing cardiac function. A single MI can wipe out more than 25% of ventricular CMs in a few hours ². There is virtually no regeneration of the myocardium in human adults³. After injury, the inflammatory response leads to further degradation of the myocardium's structure and, in the chronic phase, to the formation of a fibrous and non-contractile scar tissue. This forces a redistribution of the mechanical stresses within the rest of the myocardium and leads to the remodeling of the heart, typically marked by thinning of the heart wall and increasing diastolic volume. Eventually, the heart begins to fail and is unable to pump sufficient blood forward to supply other organs: this is heart failure. The prevalence of heart failure in the American population is expected to increase by 46% in 2030 compared to 2012 levels, affecting 8 million Americans.

Despite the urgent need for long-term treatment, the definitive option for patients in heart failure is still a heart transplant from a donor. However, the number of transplants available in any

given year has hovered around 2,500⁴ while the incidence of heart failure has steadily increased. Moreover, there are many with other conditions, exacerbated by cardiac dysfunction, who could benefit dramatically from a therapy to regenerate the myocardium.

A treatment that is actively being pursued in clinical trials is stem cell therapy. Adult mesenchymal stem cells in particular, can be injected into the myocardium or within the pericardium to mitigate the inflammatory response during the acute phase of MI and restore the pumping efficiency⁵. There are more than 30 refinements of this approach in Phase II or III of clinical trials showing promising results in minimizing damage to the heart and maintaining function⁶. However, the positive effects of stem cell therapy are limited to paracrine signaling that modulates the inflammation and has a cytoprotective effect on CMs. The microenvironment of the injured heart, with inflammation, poor vascularization, and fibrosis, is extremely hostile and does not provide the adequate regenerative cues for the injected cells. There is no significant integration and regeneration of the myocardium⁷. Currently, stem cell therapy can prevent the slow decline toward heart failure but cannot replace a heart transplant. To promote cardiac regeneration, it is essential to understand cardiac structure and physiology (see background in chapter 2).

Over the last two decades, cardiac tissue engineering has undergone a dramatic expansion within academic research. Researchers are aiming to grow cardiac muscle *in vitro* by designing the cell microenvironment to recapitulate native cardiac structure and function. Using scaffolds, chemical and physical stimuli, cells can be guided to assemble into a functional tissue. A thorough review of the challenges of cardiac physiology and how cardiac tissue engineering is addressing them has been published as part of the work for this dissertation (Appendix E)⁸. A description of the specific

techniques that inspired this work is given in introduction of chapter 4. Although there are numerous approaches, from casting artificial or natural hydrogels, using electrical or mechanical stimulation, the engineered muscle tissues remain far inferior to adult cardiac muscle in terms of contractile force generation, calcium handling, and conduction velocity. Despite significant progress, we are far from being able to produce cardiac patches to mend injured hearts and the technology has not yet crossed over toward clinical applications. In order to realize the potential of cardiac engineering, in the form of either a cardiac patch, or a platform for *in vitro* drug testing, we need to further refine the tools we use to control how cells interact and assemble into a coherent tissue.

A major breakthrough in cardiac tissue engineering is the development of pluripotent stem cell-derived CMs. For the last ten years, there has been constant refinement of techniques to guide the differentiation of human embryonic stem cells (hESCs), and more recently human induced pluripotent stem cells (hiPSCs) into CMs⁹. This allows the creation of human and even patient-specific cardiac constructs *in vitro*. However, pluripotent stem cell derived CMs (PSC-CMs) differ significantly from adult CMs and even from neonatal CMs, which have been extensively used with mouse and rat models¹⁰. PSC-CMs are immature, with poor cytoskeletal organization and calcium handling, and generate weak contractile forces. Their phenotype is closely related to early-stage embryonic CMs^{11,12}. Thus, a great deal of attention is currently focused on inducing embryonic-like CMs to mature to an adult state.

As there is no large scale regeneration of the myocardium in human adults, the only time to observe how the myocardium forms is during the embryonic development. The heart tube is the first organ to form in the early embryo, before looping and forming the four chambers of the mammalian

heart^{13,14}. At the beginning of this process, the myocardium is heavily trabeculated, and composed of a thin outer wall with many thin contractile cords crisscrossing the heart chamber. As the myocardium matures, the trabeculae fold back into the inner wall of the heart¹⁴. It thickens and gain its final structure: a stack of aligned CM sheets, layered with a shifting orientation that efficiently translate the axial shortening of CMs into an actual reduction of the cardiac volume during systole¹⁵. Since cardiac tissue engineers aim to use embryonic-like CMs to replicate a complex process that occurs exclusively in the embryo, any approach at creating cardiac muscle should be inspired by the study of cardiac morphogenesis during embryonic development.

So far, there has been little overlap between the fields of developmental biology and cardiac tissue engineering. Building on complex lineage tracking techniques, our understanding of the mechanisms driving cardiac morphogenesis has deepened, in particular with the identification of the cell populations, called heart fields, responsible for each part of the heart and the discovery of the leading signaling pathways^{13,16}. The study of cellular pathways during the early embryonic stages has already led to efficient differentiation protocols¹⁷. However, there has been no concerted effort to also derive design parameters for tissue engineering scaffolds from the study of embryonic development.

The extracellular matrix (ECM) is an ideal focus for further research as it is the template for current cardiac tissue engineering scaffolds and because of its critical role during development. Knocking out genes for the production of ECM proteins or for the integrins necessary to interact with the ECM are often embryonically lethal^{18,19}. The cardiac ECM in particular undergoes dramatic changes in composition and structure from the embryonic stage to the adult: for example, while the embryonic cardiac ECM is rich in fibronectin (FN), the adult ECM is dominated by laminin (LAM)

and collagen type I (COL1)²⁰⁻²². This raises the possibility that scaffolds derived from the adult ECM lack the necessary cues to drive immature cardiac cells to grow as a functional tissue.

I hypothesize that the ECM of the embryonic myocardium drives myocardium formation, and that scaffolds that mimic the structure and composition of the ECM can induce cardiac tissue growth *in vitro*.

Although the ECM has been successfully used to control the behavior of cardiac cells and tissues *in vitro*, there exists a significant gap in the capabilities of current ECM patterning techniques. In 2D, techniques grouped under the term soft lithography, such as microcontact printing, have enabled the patterning of ECM proteins to create adhesive patches on a flat substrate^{23,24}. By controlling the location and shape of the protein patches, researchers can guide the cell shape which impacts the formation of the contractile apparatus, and even leads to specific phenotype²⁵. Simple lines of FN on an elastomeric substrate induce the formation of a highly aligned cardiac sheet²⁶. In 3D, natural hydrogels can be cast to mimic the native environment. A landmark study by Ott *et al*, using a decellularized cardiac ECM seeded with cardiac cells, revealed the potential of the cardiac ECM to drive cardiac tissue organization and function²⁷. Since then, the decellularized cardiac ECM has been used either as a structural scaffold or as a homogenized hydrogel to promote cardiac function or to induce cardiac differentiation²⁸⁻³⁰. However, obtaining scaffolds from the embryonic ECM is not feasible. In order to provide an embryonic-like environment to embryonic-like cells, we need to build the scaffold from the ground up. This requires a control over the microscale structure and composition of the ECM that can only be achieved in 2D but not for 3D techniques.

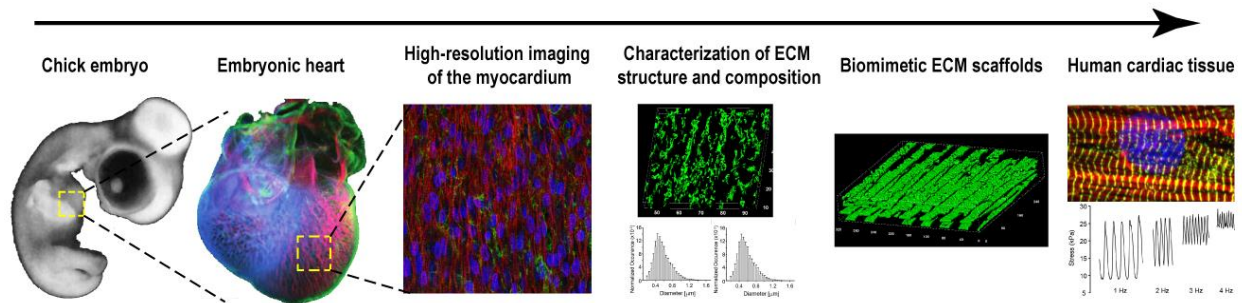


Figure 1.1. An embryonic-inspired approach to engineer functional human cardiac tissue.

In this dissertation, I develop a new embryonic-inspired approach to engineer functional human cardiac tissue (Figure 1.2). First, in chapter 3, I apply high resolution imaging techniques and adapt image analysis algorithms to characterize the structure and composition of the FN, LAM, and collagen type IV (COL4) matrices in the myocardium during the embryonic development of the chick. In chapter 4, Rachele Palchesko-Simko and I develop a new scaffold fabrication technique and micropattern FN lines onto natural hydrogels. I optimize the hydrogel composition to maximize the alignment of chick primary CMs along the FN lines. Then, in chapter 5, I demonstrate the implementation of our optimized patterning technique to create human cardiac sheets with hESC-CMs. I fabricate complex 3D multilayered constructs generating contractile forces comparable to human native myocardium.

This work lays the foundation for a systematic investigation, in a well-controlled *in vitro* environment, of the role that specific features of the embryonic ECM play in cardiac morphogenesis. This study proposes a more comprehensive approach to scaffold design, based on a thorough understanding of the driving mechanisms of tissue formation, leading to more efficient engineering of cardiac muscle.

Chapter 2 Background

2.1 The myocardium

2.1.1 Structure and function

The wall of the heart is constituted of three segments, the endocardium lining the inner surface, the myocardium, and the epicardium covering the outer surface. The myocardium is the actual muscle of the heart, composed of billions of CMs as well as fibroblasts, endothelial cells, and smooth muscle cells. It pumps blood over 2 to 3 billion cycles and is obviously critical for the proper function of all other organs. The pumping function relies on coordinated contractions across multiple scales (Figure 2.1). The smallest functional element is the actin–myosin motor, which consumes ATP when the head of the myosin heavy chain pulls on an actin filament. Intertwined actin and myosin rakes contained between two Z discs made of α -actinin constitute the sarcomere, the basic contractile unit of CMs. In adult cells, sarcomeres form myofibrils that span the width of the entire cell and connect to other cell cytoskeleton through dedicated connections in the cell membrane (intercalated discs)³¹. CMs are bundled into myofibers with very strong local alignment. These myofibers form near laminar sheets that wrap around the heart. A key feature of this hierarchical organization is the $\approx 90^\circ$ shift in CM orientation from the endocardium to the epicardium boundary¹⁵. This transforms the uniaxial shortening of individual cells into a twisting motion that effectively reduces the volume of the cardiac chambers, pumping blood out. Thus, myocardium function depends on the proper organization of contractile element from well-developed sarcomeres to highly aligned cardiac sheets.

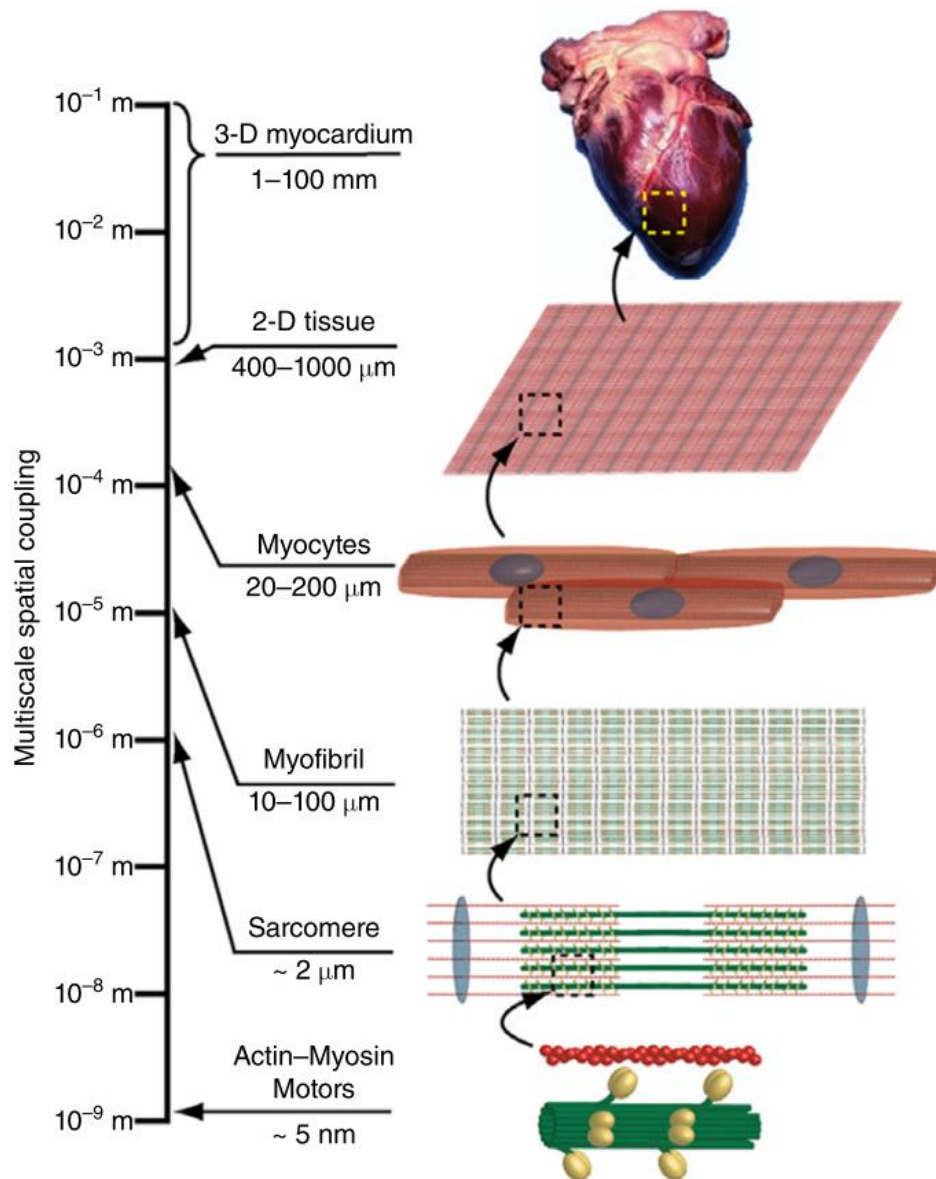


Figure 2.1. Multiscale hierarchical structure of the myocardium.
Adapted from Jallerat et al.⁸

2.1.2 Clinical need for cardiac repair

When the heart is injured, such as during MI, it does not heal properly and cardiac function is not recovered in human adult. The capacity to heal myocardium varies widely between species: zebrafish can regenerate up to 20% of lost myocardium, and even mice show significant cardiac regeneration shortly after birth². In humans, there is conclusive evidence of CM renewal: between 0.5

and 1.5 % of CMs are renewed every year in adults³. This indicates that we carry some of our CMs from birth to grave. Although the renewal rate increases after injury, it is still highly insufficient to recover the loss myocardium³². Other mechanisms proposed for endogenous cardiac repair are the recruitment of bone-marrow stem cells to the infarct site, or the proliferation and differentiation of resident cardiac stem cells. Significant controversy remains for both and their contribution to actual repair in the heart is not clear^{5,33}.

2.1.3 Morphogenesis of the myocardium

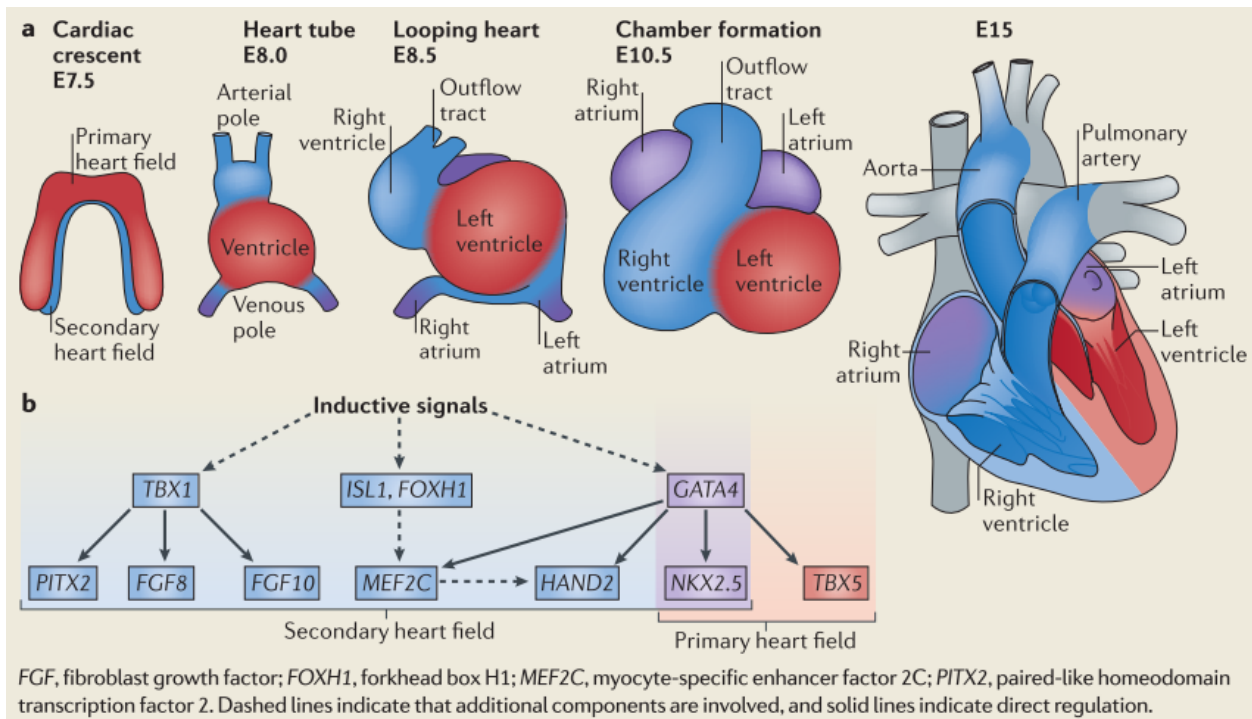


Figure 2.2. Stages of cardiac morphogenesis.

(a) Schematic of the main stages in the mouse model. (b) Diagram of signaling molecules involved in regulating each cell population. Adapted from Xin et. al.³⁴

The heart is the first organ to form during development. In the early embryo, mesodermal precardiac cells create the cardiac crescent, also known as the first heart field (Figure 2.2 and Table 2.1). Another population of cells called the second heart field underlies the cardiac crescent and gives

rise to many essential part of the four-chamber heart. The crescent migrates and both end fuse into the central heart tube, which then starts beating. Then, the tube loops to an S shape before settling to its final position. The last stages involves the separation of the different chambers (septation) followed by the development of the coronary vasculature and the formation of the valves.

Days of embryonic development	Cardiac crescent	Heart tube	Heart looping	Chamber septation	Fully formed myocardium
Mouse ³⁴	7.5	8	8.5	10.5	14.5
Human ³⁵	15	20	24	35	64
Chick ³⁶	1	1.5	2.5	5	8

Table 2.1. Comparison of the timeline for the major phases of cardiac morphogenesis in mouse, human, and chick.

After looping, the myocardium undergoes dramatic changes. It is originally composed of a thin compact layer (Figure 2.3). But CM proliferate rapidly to form trabeculae: thin cords of CM covered in endocardial cells that contribute to an overall increase in myocardial mass and pumping function, while enabling blood to flow throughout and supply CM before the formation of the dedicated coronary vasculature later in development (Figure 2.3 A). The myocardium progressively thickens by proliferation as well as by the folding of the trabeculae back onto the compact layer. The first capillaries become visible (Figure 2.3 B). Finally, in the fetus, all the trabeculae have folded onto the compact layer, which is very thick and composed of several layers of highly aligned CMs, with a full network of coronary vessels (Figure 2.3 C). In chick, the transformation of the compact myocardial layer from a loosely organized, thin, avascular tissue, to a strong vascularized muscle occurs between day 3.5 and 10 of development.

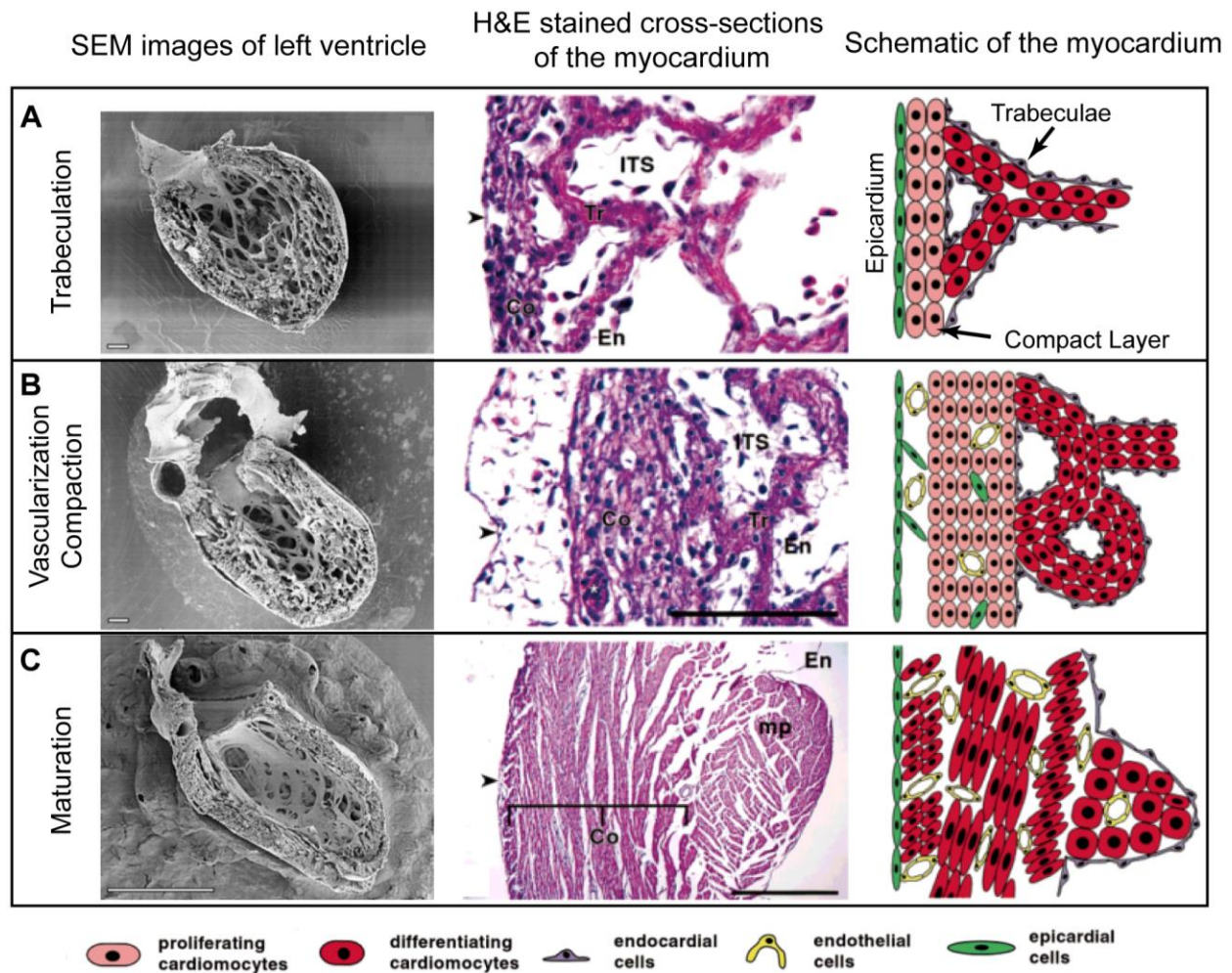


Figure 2.3. Formation of the myocardium.

(A) Trabeculation by CM proliferation at day 3.5 in the chick. (B) Vascularization of the compact layer and compaction of the trabeculae at day 6. (C) Fully formed myocardium in the fetus (day 10). SEM images are from the left ventricles of human embryos at matching stages (6 weeks, 12 weeks, fetus respectively) adapted from Sedmera et al.³⁷. H&E and schematics are from Sedmera et al.¹⁴

2.1.4 The extracellular matrix in adult and during development

The ECM is a complex network of proteins, proteoglycans, glycoproteins, and polysaccharides which constitutes the skeleton of every tissue. Structural components such as elastin, collagens type I and III maintain the mechanical integrity of the tissue, while basement membrane component such as perlecan, LAM, FN, and COL4 form dense mats around the cells and modulate signaling.

In the myocardium, which has a very high cellular density³⁸ with $\approx 10^8$ cells / cm³, a basement membrane surrounds each myofiber, and the interstitium between myofibers is rich in COL1³⁹. The composition of the ECM changes dramatically throughout development, preceding or associated with rapid transformation of the myocardium structure. The adult ECM is dominated by COL1, while the embryonic ECM's main component is FN (Figure 2.4). Modification or knock-outs of the expression of specific ECM components such as FN and LAM are often embryonically lethal⁴⁰.

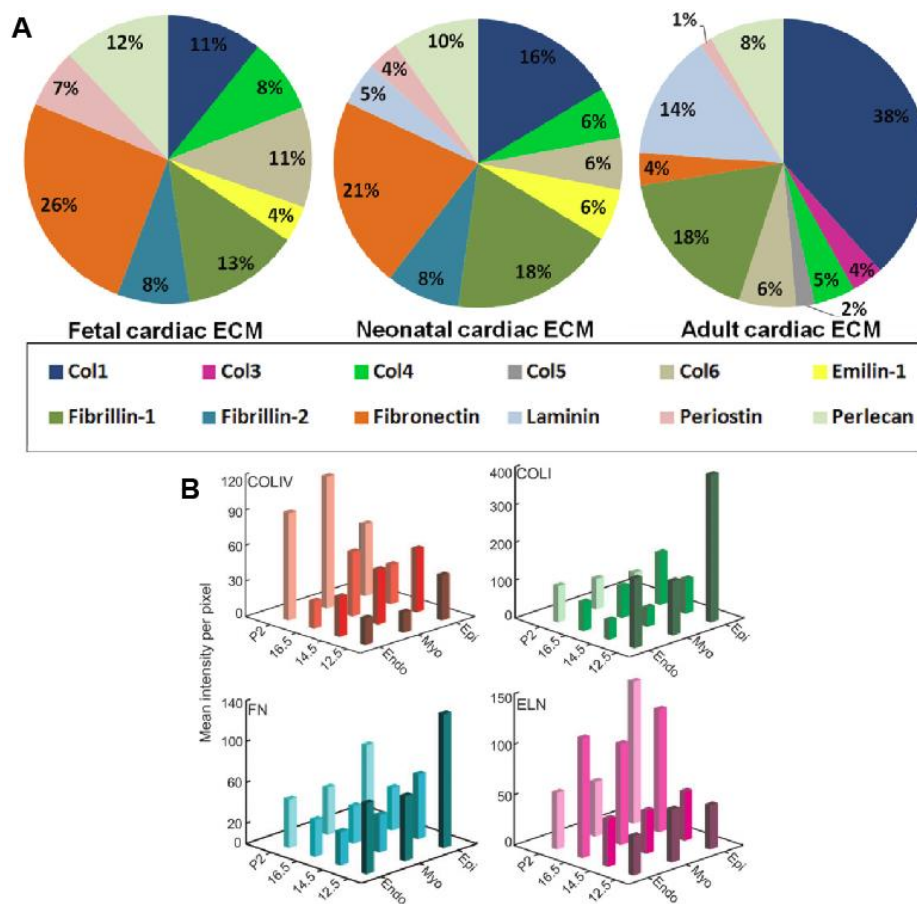


Figure 2.4. Composition of the cardiac ECM during development and in adult.
 (A) Relative weight of the ECM in the rat heart at different stages, measured using mass spectrometry and adapted from Williams et al.²⁰ (B) Relative composition of the ECM at different locations (Epicardium, Myocardium, Endocardium) at stages E12.5, 14.5, 16.5 and two day postnatal (P2) in mouse, measured as the intensity of immunohistochemistry signal adapted from Hanson et al.⁴¹

Cells interact with the ECM through membrane receptors called integrins. Integrins work as pairs of α and β subunits, which bind to specific sites on ECM proteins. CM ability to bind to different ECM component depends on their integrin expression. In particular, neonatal CM bind easily to all types of collagen and to FN and LAM while adult CM bind primarily to LAM and COL4⁴².

2.2 The chick model

I use the chick as a model in this dissertation. It follows the same developmental stages of cardiac morphogenesis as all vertebrates toward a four-chamber heart. It has been well studied since Hamilton and Hamburger published a thorough classification of all the stages of the chick embryo in 1951⁴³.

Several differences have been well documented¹⁴: the septum arise from compaction of trabeculae in the chick, while it is formed already compact in mammals; the asymmetry between left and right ventricles is much more pronounced in birds, where the compact layer of the myocardium in the left ventricle can be 5 times thicker than in the right ventricle, while mouse left and right ventricles exhibit similar thickness in the embryo; the pattern of trabeculation and the architecture of the valves are other points of difference. Some of these differences are related to the higher metabolic needs of birds to maintain flight muscles.

Beyond cardiac architecture, it is essential to compare the phenotypes of chick and human CMs. Chick CMs lack T-tubules, which are invagination of the cell membrane seen in mature mammalian CMs. They bring Ca^{2+} exchanges directly in proximity to the Z- line of the sarcomeres, to promote contraction kinetics⁴⁴. T-tubules effectively enable contraction of wide myofibril bundles,

allowing adult mammalian CMs to grow very wide to $\approx 20 \mu\text{m}$ while chick CMs have a fixed width of $\approx 6\text{-}7 \mu\text{m}$ ^{45,46}. Additionally, chick CMs do not develop M bands in mature sarcomeres⁴⁷. However, the ultrastructural differences between chick CMs and mammalian CMs are not visible during the embryonic development. This is why the chick remains one of the best model for high-throughput studies of cardiac morphogenesis.

Chapter 3 Characterization of the extracellular matrix in the myocardium during the embryonic development

3.1 Abstract

Cardiac tissue engineering utilizes scaffolds inspired by the native ECM to guide cardiac tissue growth *in vitro*. So far, the focus has been on the adult cardiac ECM despite the fact that embryonic ECM is a much likelier source of information to promote cardiac tissue formation. Little is known of the embryonic cardiac ECM beyond the relative expression of ECM components. There is a need to describe the embryonic ECM structure in detail so it can serve as a template for tissue engineering scaffolds. Here, I first used refractive-index matching to image the whole heart and build a 3D model of the trabeculated myocardium. I observed the development of the coronary vasculature between day 5 and day 9 of development and decided to focus on day 5 for our analysis. I imaged the compact layer of the myocardium at high resolution to determine the relative expression of collagen IV, FN, and LAM. Then, I characterized the FN and LAM matrices and extracted structural parameters (volume, spacing, fiber diameter, length, and orientation), which can be used to design biomimetic scaffolds.

3.2 Introduction

The native ECM provides mechanical support for every tissue; it mediates intercellular signaling via biochemical cues; and it is critical to homeostasis as well as to wound healing and morphogenesis. Thus, it represents the gold standard for tissue engineering scaffolds. In order to guide cells to proliferate, differentiate, and organize as tissues, researchers have developed a wide variety of

techniques using synthetic or natural material that can recapitulate most of the properties of the ECM⁴⁸, and in particular toward the generation of cardiac tissues *in vitro*⁸.

Among the most promising technology to have emerged in the last decade is the decellularization of living tissues to create acellular ECM scaffolds^{27,49–51}. Decellularized constructs keep most of the structures (vessel lumen, orientation, layers) of the heart. However, the composition of these scaffolds is not well known and varies significantly depending on the protocol used⁵². Nonetheless, decellularized biological scaffolds have shown great promise for regenerating some tissues such as skeletal muscle⁵³, skin⁵⁴, ligaments and tendons, with already many commercial products available for wound healing^{55,56}. Decellularized heart tissue has also been used as an injectable gel⁵⁷ or a vehicle for cell delivery³⁰ to improve cardiac function post-MI, and as a scaffold to promote differentiation *in vitro*²⁹.

The unique characteristics of the human heart pose significant limitations to the potential of decellularized scaffolds that have often been overlooked. First, there is virtually no regeneration of the myocardium in adults^{2,3}. The development of the myocardium during the embryonic development is driven by hyperplasia, while the postnatal cardiac growth relies almost exclusively on hypertrophy⁵⁸. Second, the myocardial ECM in the adult and in the embryo are dramatically different: the first is rich in LAM and COL1, while the second is dominated by FN²⁰. The unique composition of the embryonic cardiac ECM plays a critical role in the development of the myocardium^{21,22}. Thus, it is likely that any approach to engineer cardiac muscle, by replicating a process that only happens in the embryo, will need to follow the blueprint of the embryonic cardiac ECM.

A review by Ogle *et al.* highlights well the obstacles raised by our incomplete understanding of the spatial and temporal expression of ECM components during development and the need to better characterize the embryonic blueprint⁵⁹. A recent study started to fill the gaps, in particular by using immunohistochemistry (IHC) and RT-PCR to observe the expression pattern of COL1, COL4, elastin and FN in the developing heart⁴¹. While this is a great first step, the potential applications of this new knowledge to design scaffolds for cardiac engineering are limited: the use of slicing and standard IHC comes with the loss of the complete 3D architecture of the whole heart. Moreover, smart scaffold design must rely on a quantitative characterization of the ECM structure.

In this chapter, I focus on characterizing the embryonic ECM in the myocardium of the chick heart to extract structural parameters that can be used as design principles for the fabrication of ECM scaffolds. First, I looked at the whole-heart using refractive-index matching, providing a complete view of the architecture of the developing heart. Then, I characterized the deformation induced by refractive-index matching using the nuclei as a reference, and found that it was not suitable to obtain microscale information about the ECM. Using confocal microscopy, I imaged the outer layer of the myocardium in the left ventricle at different stages and identified the prevascular myocardium of 5 day old embryos (stages Hamburger-Hamilton⁴³ 28) as the ideal stage to study the myocardial ECM. I observed the expression of LAM, FN, and COL4 in the epicardium and the myocardium. Finally, I characterized the structure of the FN and LAM matrices in terms of volume, spacing, fiber diameter, fiber length, and fiber orientation relative to the myofibers.

Here I describe a straightforward approach to obtain structural information about the myocardial ECM at the micrometer level, in order to inform the design of better scaffolds for cardiac

tissue engineering. These results will enable a systematic investigation of the role embryonic ECM cues, in terms of structure and composition, have in guiding immature CMs to grow and organize as a tissue.

3.3 Materials & Methods

3.3.1 Chick embryonic heart dissection

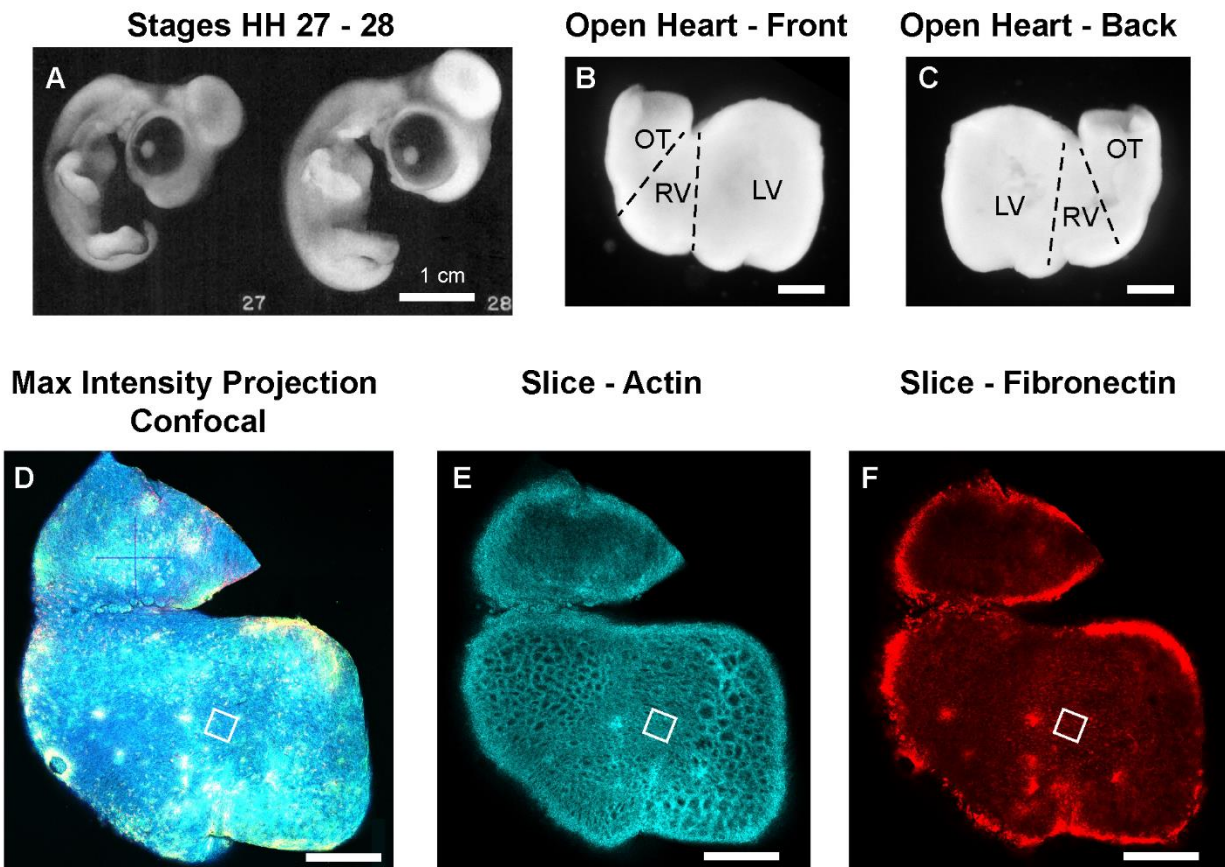


Figure 3.1. Dissection and imaging of the left ventricle of 5 day-old chick embryos. Day 5 embryos (stage HH 28) are selected and the hearts dissected. The atria are removed and the left ventricle opened from the back of the heart. By removing the rear of the right ventricle and making an incision at the apex of the left ventricle, the left ventricle can be flattened for easier imaging (B, C). After staining for nuclei (blue), actin (cyan), LAM (green), and FN (red), a + mark is bleached in the outflow track and a tiled z-stack is acquired (D). I can then keep track of the location of high resolution 3D z-stacks (white square) relative to the actin structure (E) and the ECM (F). Scale bars = 300 μ m.

White Leghorn eggs are incubated at 37° with 50% humidity. On the day of dissection, embryos are explanted and put in a saline solution (1x PBS with calcium and magnesium, buffered with 10mM HEPES). They are then compared to the reference stages from Hamburger and Hamilton⁴³ to select a population with homogenous developmental stage : stage HH 28 for day 5 (Figure 3.1 A), stage HH 31 for day 7, and stage HH 35 for day 9.

Whole hearts are carefully dissected, keeping most of the outflow track. For high resolution imaging, the atria, outflow track and right ventricle are removed. The left ventricles are then cut at the base in order to be flat for imaging (Figure 2.1 B&C). This makes a wide area available for high resolution imaging (Figure 2.1 D-F) as the strong curvature of the embryonic heart would otherwise quickly become an obstacle for objectives with short working distance.

3.3.2 Fixing and immunostaining

Whole hearts and isolated left ventricles are fixed for 15 min in 4% formaldehyde, then incubated for 2hrs at 37°C in PBS with 0.1% Triton X-100 and 5% goat serum for permeabilization and blocking. All incubations for staining are carried out overnight at 4°C in PBS with 5% goat serum or 10% bovine serum albumin. During the primary stain, either mouse anti-chicken FN (Sigma-Aldrich, #F6140), rabbit anti-COL4A3BP (Sigma-Aldrich, #AV52418), rabbit anti-laminin (Sigma-Aldrich, #L9393), or mouse anti-sarcomeric α -actinin (Sigma-Aldrich, #A7811) were used at a 1:100 dilution, in addition to 3/100 Alexa Fluor 633-conjugated phalloidin (ThermoFisher, #A22284) to stain F-actin. During the secondary incubation, goat anti-mouse antibodies conjugated to Alexa Fluor 546 (ThermoFisher, #A11030) and/or goat anti-rabbit antibodies conjugated to Alexa Fluor 488

(ThermoFisher, #A11008) are used at a 1:100 dilution. After each staining step, the samples are washed in PBS for three times 30 min. One drop of NucBlue (ThermoFisher, #R37606) per mL is added during the second washing step after secondary staining to mark the nuclei. Finally, the samples are fixed post-stain for 1hr in PBS with 4% formaldehyde. After three final rinses in PBS, the whole hearts are cleared and the flattened left ventricles are mounted directly in PBS.

3.3.3 Clearing samples by refractive index-matching

To clear whole hearts while preserving the actin staining, I follow a protocol by Kim *et al.*⁶⁰. Stained whole hearts are washed in solutions of increasing concentration of isopropanol to PBS (25%, 50%, 75%, 100%), then are left to fully dehydrate in fresh isopropanol for 30 min. Isopropanol is replaced by BABB (Murray's clear, a 1:2 solution of benzyl alcohol to benzyl benzoate), which has a refractive index of 1.54 matching cardiac tissue. After 1hr to equilibrate in BABB, the samples are near transparent and hard to see under the naked eye. Samples are then mounted with fresh BABB in a chamber made with a Fastwell (Electron Microscopy Sciences, # 70333-32) silicone ring between a microscope slide and a N1.5 glass coverslip.

3.3.4 High resolution confocal microscopy

Cleared whole-hearts are imaged using a Nikon AZ-C2 macrozoom confocal with a 5x objective (NA = 0.4). For dissected left ventricle, in BABB or PBS, an X mark is bleached in the outflow track by scanning orthogonal lines with the 488 laser at minimum scan speed with 20-30% laser power for about 15 seconds. A tiled z-stack is acquired with the same objective. Then 3D images are obtained using a high resolution 63x oil objective (NA =1.4) on a Zeiss LSM700 confocal

microscope. Samples mounted in PBS but imaged with an oil objective introduced a strong mismatch in refractive indices leading to spherical aberration and dilation of the z-axis⁶¹. I compensated for it by using the “refractive index correction” function of the Zen 2010 software: it compensates for the mismatch by using the ratio of the refractive indices of the medium of the sample ($n=1.33$ for PBS) and of the immersion medium of the objective ($n'=1.518$ for oil), $R = \frac{n}{n'} = 0.88$. This ensures that axial distances are accurately measured. I set the laser power and gain to increase through the depth of the myocardium to maintain ideal signal intensity in each slice of the final 3D image stack.

3.3.5 Characterization of the effect of clearing on nuclear morphology

I used a Leica SP5 multiphoton microscope with a 25x water immersion objective (NA = 0.95) and a Ti:Sapphire laser to obtain 3-D z-stacks of the nuclei (DAPI) with an excitation at 740nm and of the actin cytoskeleton (Alexa Fluor 633 phalloidin) at 810nm before and after clearing. The images were deconvolved with Autoquant X3 (Media Cybernetics) then analyzed with Imaris and Matlab. I first equalized the intensity of the signal across the depth of 3D image to compensate for signal attenuation. Then a preliminary segmentation of the nuclei was achieved based on local contrast using Imaris. However, the tissue was very dense, which makes it very difficult to separate individual nuclei for analysis. So I used the “Distance to Surface” Matlab Xtension with Imaris, to calculate a new channel where the intensity of the inner voxel of the nuclei is equal to the distance to the border of the segmented nuclei. This channel then provided a bright local maximum at the center of each nuclei, which allowed the “Surface” tool in Imaris to split each adjoining nuclei with a region growing algorithm. The segmented “surfaces” created for each nuclei were manually inspected and aberrant

objects deleted from the analysis (e.g. when poor segmentation was not able to separate a group of nuclei). After selecting the nuclei that were oriented along the main direction of alignment (Y-axis) in the myocardium, I extracted the dimensions of the bounding box that Imaris fit to each nucleus: the bounding box is the smallest rectangular cuboid in which the nucleus can fit; its longest dimension was named C and the two others A and B. I calculated the aspect ratio AR as $AR = \frac{C}{(A+B)/2}$. AR is thus always superior to 1. In the population of nuclei I selected, it is a measure of the elongation of the nuclei along the main direction of alignment.

3.3.6 Analysis of 3D image z-stacks of laminin and fibronectin

3-D images from all samples are deconvolved with Autoquant X3. First, I crop an area of the myocardium, just below the basement membrane of the epicardium (Figure 3.2). For both LAM and FN, I use the “surface” tool in Imaris 8.2 to segment the signal using the following parameters: local contrast threshold = 9, sphere diameter = 1 μm , smoothing = 0.1 μm . I filtered out elements that were smaller than 1 μm^3 and sorted the “surfaces” according to their volume.

A critical parameter for the design of scaffolds is porosity, or spacing. To measure spacing of the FN and LAM “surfaces” created by Imaris, I used the “Distance to Surface” Matlab Xtension to create new channels where the pixels outside of the “surfaces” have values equal to the minimal distance to the ECM “surface”. The “Distance to” channels were further processed using the “surface” tool (local contrast threshold = 2, no smoothing, sphere diameter = 0.1 μm) to segment and mask the local maxima of the signal. The resulting channel “Local Maxima of Distance to ECM” shows a network of sheets that pass exactly between ECM “surfaces”: each voxel of this channel is equidistant to the

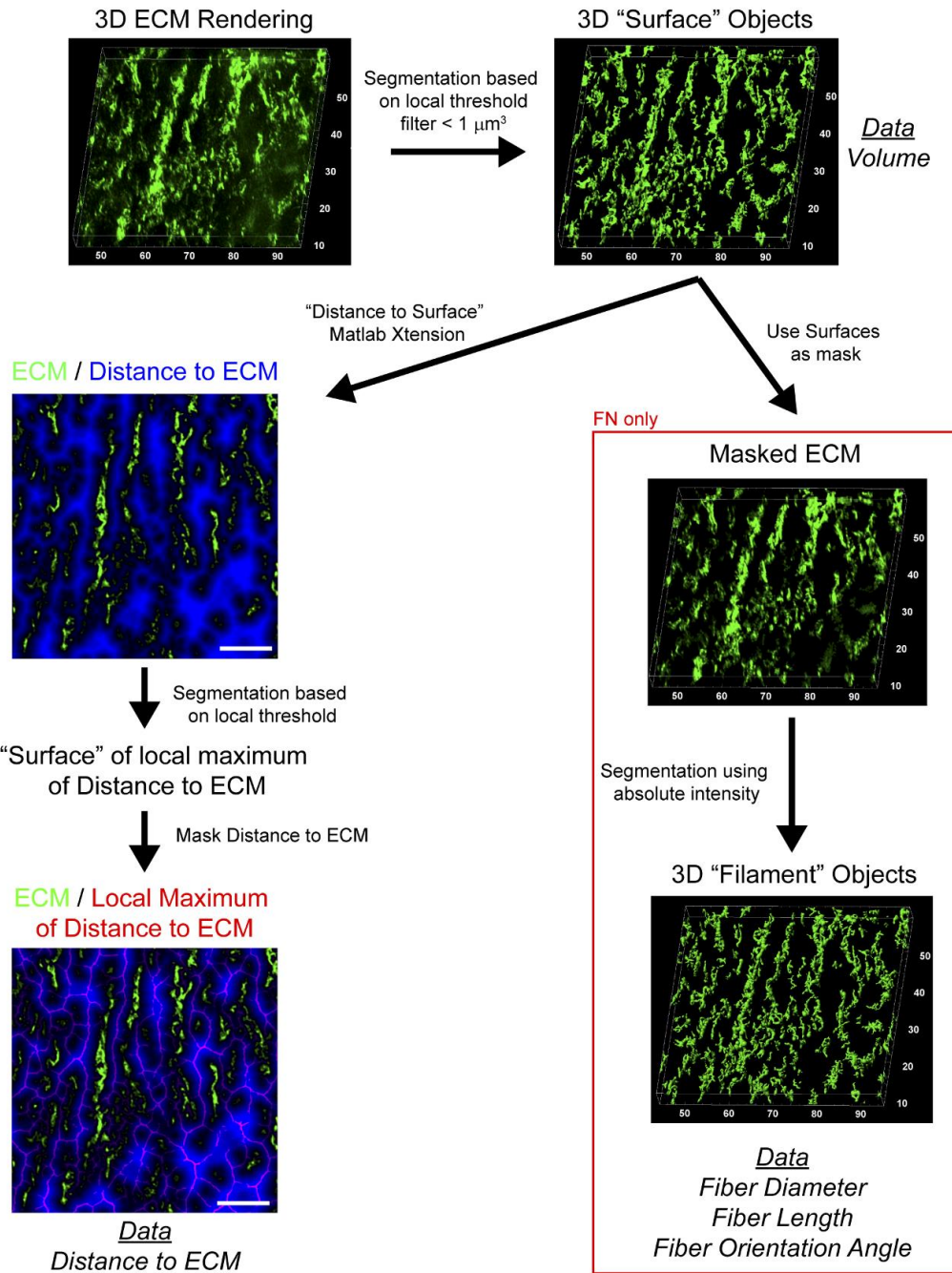


Figure 3.2. Characterization of the ECM using Imaris and Matlab.

3D images of the ECM are deconvolved then segmented using the "surface" tool in Imaris following a local contrast threshold algorithm. Left column: for LAM and FN, the "Distance to Surface" Xtension creates a new channel with voxel values equal to the distance to the closest ECM surface. Using the "surface" tool one more time, the local maxima of the "distance to ECM" channel are identified and can be used to characterize the spacing of the ECM in 3D. Right column: FN "surfaces" are used to mask the FN signal. Then the "Filament" tool of Imaris is used to segment the FN fibers and measure their diameter, length, and orientation angle.

closest ECM “surfaces” and the intensity is equal to the shortest distance to these surfaces. If the shortest path is drawn between two adjacent ECM “surfaces”, it will intersect the “local maxima of distance to ECM” orthogonally and in its middle. The intensity of the “local maxima of distance to ECM” at the point of intersection will be exactly half of the length of the shortest path between ECM “surfaces”. The channel representing the “Local Maxima of Distance to ECM” were then analyzed with ImageJ to produce histograms with set bins for each 3D z-stack.

For FN only, the “surfaces” were used to mask the original FN signal and create a channel without background. I then used the “Filament Tracker” tool to segment the FN signal into fibers with the following parameters: absolute intensity threshold, no preprocessing, and branch length to trunk radius ratio = 2. I removed loops that were shorter than 1 μm (those are often artifacts of the algorithm filling up larger volume of the signal with a “ball” of fibers). This analysis resulted in the fiber diameter and fiber length. Finally, fibers longer than 1 μm were filtered and their orientation angles relative to the X axis used to create a histogram for each sample.

3.4 Results & Discussion

3.4.1 Refractive-index matching enables imaging the architecture of the whole heart

Imaging the entire heart is essential to understand its final structure and how it develops. In the embryo, the process of cardiogenesis has been well described with scanning electron microscopy^{14,37,62}, in particular regarding the formation, then retraction and compaction of the trabeculae. Trabeculae play a major role in the distribution of mechanical stresses in the developing heart⁶³. They become like fenestrated sheets by stage HH27, then slowly resorb into the outer layer of

the myocardium as the coronary vasculature develops³⁶. Thus, imaging the entire embryonic heart can provide critical information on the 3D architecture of the trabeculated myocardium, which is the only instance of avascular cardiac myogenesis *in vivo* and a template for engineered cardiac tissues.

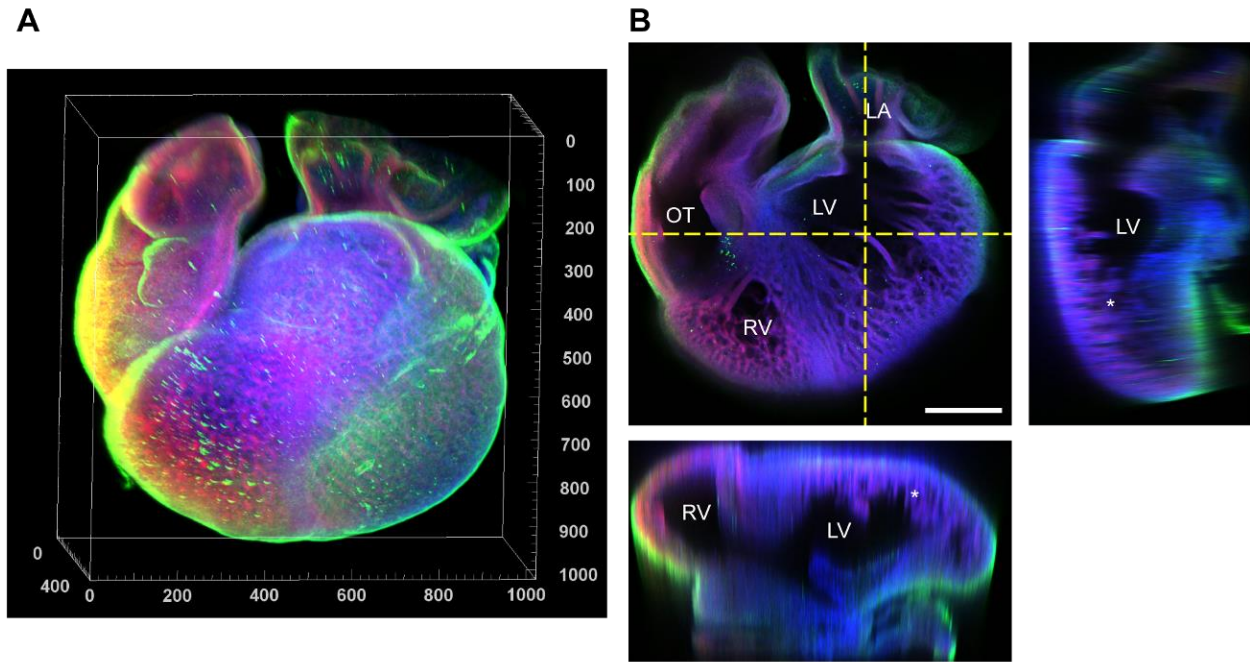


Figure 3.3. Imaging of a whole heart of a 5 day old chick embryos using refractive-index matching with BABB.

(A) 3D rendering of the heart stained for nuclei (blue), F-actin (red), and FN (green). Scale is in μm . (B) A single slice and two cross-sections of the heart in the planes marked by yellow dotted lines show the different chambers and the trabeculation of the myocardium at this stage (marked by *). Scale bar is 200 μm . RV = Right Ventricle, LV = Left Ventricle, OT = Outflow Track, LA = Left Atrium.

After clearing, whole hearts mounted in BABB were near transparent and provided good immunofluorescent signal from the actin cytoskeleton and the nuclei throughout the samples. The lumen of the cardiac chambers as well as the complex trabeculation are visible in 3D renderings and cross-sections of a z-stack acquired using a low magnification laser-scanning confocal microscope (Figure 3.3). The detailed images of the heart were segmented to create a 3D model that could be bioprinted in alginate at a 20:1 scale using FRESH⁶⁴. Although beyond the scope of this dissertation,

using FRESH bioprinting to build a rough but very first scaffold of a trabeculated heart shows great potential toward recapitulating the main features of cardiac morphogenesis *in vitro* (see Appendix D).

Unlike nuclei and actin stains, antibody staining was uneven through the samples. The FN signal was strong in the epicardium but dim in the endocardium. As the endocardium is known to feature a rich basement membrane containing FN⁴¹, the lack of FN signal throughout the trabeculae in our experiments is likely due to the limits of antibody penetration during staining⁶⁵. Antibodies diffuse poorly through thick tissues. This problem can be solved by partially opening the heart to allow staining to proceed from the inside and outside in parallel. However, this leads to a disruption of the morphology of the heart, which is exacerbated by dehydration and clearing. As clearing with BABB makes the heart brittle as well as transparent, any morphological deformation (flattening or folding) of the sample cannot be rectified once the heart is cleared. Thus, whole-heart imaging using refractive index matching provides critical information regarding the 3D architecture of the developing heart but cannot be used to extract quantitative information about the ECM in the trabeculae and the endocardium.

3.4.2 Clearing with BABB causes anisotropic deformation in the myocardium

I then focused on the ECM in the outer wall of the myocardium, where antibody penetration and signal strength is strong. Since clearing with BABB (and the preceding washes in isopropanol) causes dehydration, there is significant shrinkage of the sample. This is one of the well documented issues with high-refractive index organic solvents used for microscopy^{65,66}. In order to provide accurate

structural information about the ECM, the deformation caused by clearing needs to be quantified and adjusted for.

Using dark field microscopy, I observed that the hearts shrank by $\approx 30\%$ in each dimension (data not shown). I use the nuclei as a reference to understand and accurately measure the BABB-induced morphological deformation of the samples. The nuclei are easily stained and imaged before or after clearing using multiphoton microscopy. Nucleus shape has often been studied in relation to gene expression⁶⁷ and even to cardiac tissue function⁶⁸ and can be modeled as an ellipsoid. I characterized the nuclei volume and aspect ratio by looking at the myocardium before (Figure 3.4 A) and after clearing (Figure 3.4 B). I used Imaris image analysis algorithms to segment the nuclei in both conditions (Figure 3.4 C, D). The nuclei volume was $281 \pm 103 \mu\text{m}^3$ before clearing vs. $81 \pm 36 \mu\text{m}^3$ after (Figure 3.4 E), a $\approx 71\%$ decrease. Further, I selected the subset of the segmented nuclei that were aligned with the main direction of the myocardium. Their aspect ratio was $1.4 \pm 0.2 \mu\text{m}$ and $1.6 \pm 0.3 \mu\text{m}$, before and after clearing respectively (Figure 3.4). In BABB, the nuclei are thinner and more elongated in the main direction of alignment of the myocardium, showing that shrinkage is anisotropic. In this densely cellular tissue, I consider that the deformation of the nuclei is representative of the deformation of the local myocardium in response to dehydration and mounting in BABB. So I estimate that the total sample volume decreases also by $\approx 70\%$ after clearing, and, since a set amount of ECM is now contained in 30% of the native volume, the ECM is then (1:30%) ≈ 3.3 times denser in the cleared sample than in the native tissue. Adjusting for such a large

deformation while attempting to accurately measure submicrometer features in the ECM is unrealistic, pushing us to consider alternative approaches.

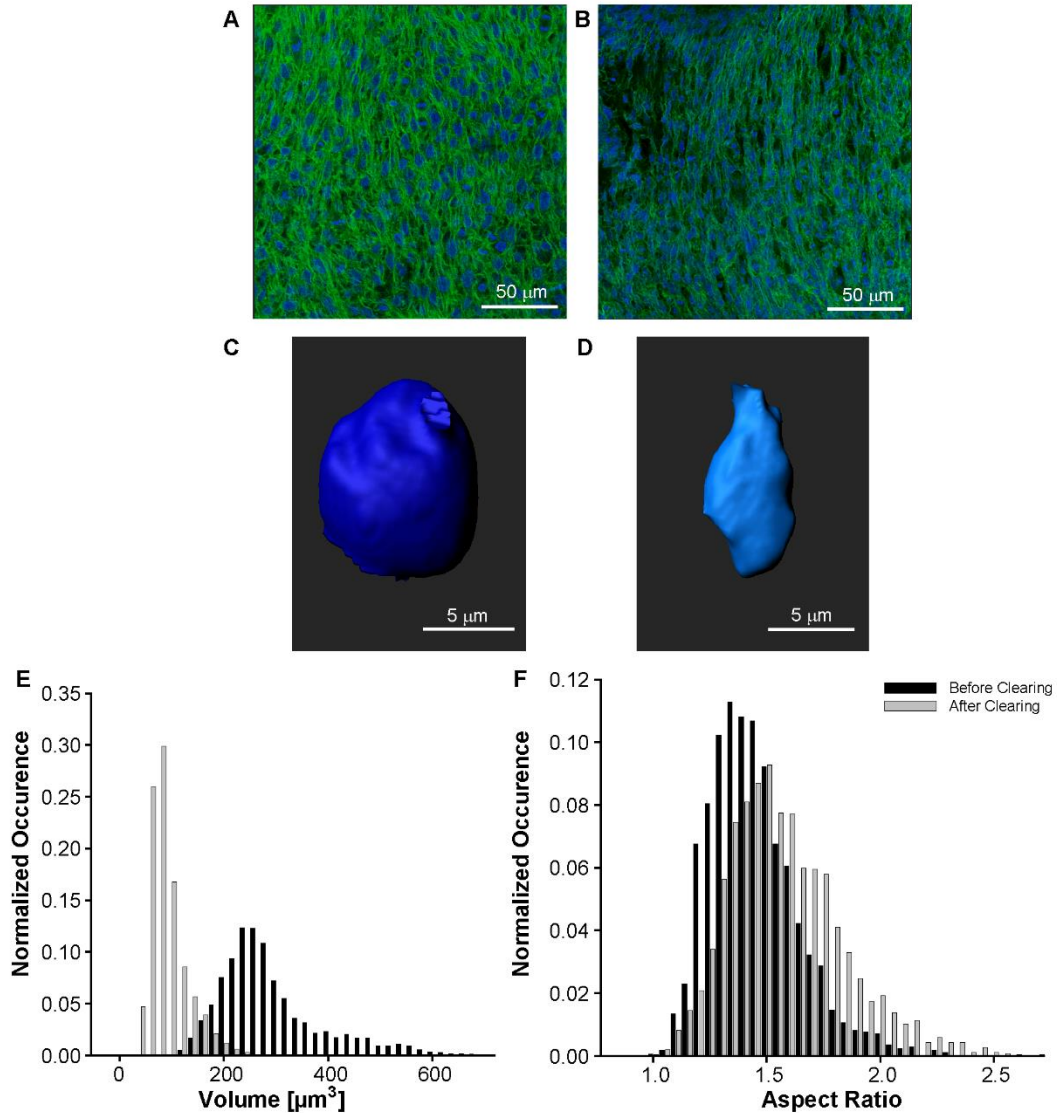


Figure 3.4. Effect of refractive-index matching on nuclear morphology.

The left ventricles of 7 day old chick embryos were imaged before clearing while mounted in PBS (A), and after clearing mounted in BABB (B). Representative objects created by segmenting the nuclei signal show the visible difference between the nuclei before (C), and after (D) respectively. The histograms of the nuclei volume (E) and aspect ratio (F) reveal that clearing results in a 3-fold decrease in volume, while the nuclei become slightly more elongated. For (E), $n_{\text{before}}= 3567$ and $n_{\text{after}}= 11783$. For (F), $n_{\text{before}}= 1703$ and $n_{\text{after}}= 255$. All data comes from $n=4$ samples.

Over the last five years, several new techniques for staining, clearing, and mounting whole organs have been developed to overcome the limitations of BABB, in part motivated by the race to decipher neuronal circuits (under the BRAIN initiative). Some rely on matching the tissue's refractive index using aqueous solutions (Scale⁶⁹, SeeDB⁷⁰), which preserve fluorescence strength and minimize morphological deformation. Yet Scale is limited to refractive index up to 1.35, well below the heart's refractive index at 1.5⁷¹ and proved insufficient in my experiments (data not shown). Another recent technique termed Clarity goes further by hybridizing the tissue with a hydrogel before solubilizing the cell membranes and staining⁷². This long process often takes more than a month and is incompatible with our goal to develop a high-throughput assay. These results encouraged me to carry out the high resolution imaging of the ECM without clearing. Using standard confocal microscopy and high NA oil objectives, high quality images can be obtained within 20-25 μm deep in sample mounted in PBS.

The thickness of the compact layer of the myocardium (the outer layer without trabeculae) in the left ventricle increases from 25 μm at HH stage 24 to 40 μm at stage HH 34⁷³. So achieving a good signal within the first 20 μm is sufficient to carry out a structural characterization of the ECM.

3.4.3 The left ventricle myocardium is vascularized between day 5 and day 9 (stages HH 28 - 35)

In the early stages of cardiac morphogenesis, the myocardium is avascular and increases in mass through the formation of trabeculae. The vascularization of the heart starts with the invasion of cells from the sinus venosus (the part of the embryonic heart emptying into the right atrium) over the epicardium and into the myocardium at stage HH27 (day 5)^{74,75}. These cells, joined by endocardial cells forming “blood-islands” in the myocardium, form a coronary plexus which slowly covers the

entire myocardium starting from the dorsal atrioventricular grooves. Then “capillary-like” structures connect to the aorta by day 7.5 (stage HH32), triggering the remodeling of the coronary plexus into a network of coronary arteries, veins, and capillaries⁷⁶⁻⁷⁸.

The transformation of the myocardium from a single layer of avascular CMs to a highly aligned, multilayered, vascularized tissue is the goal that cardiac tissue engineers aim to achieve in the laboratory. Thus, I observed the development of the coronary vasculature in the ventral left ventricle through this period to determine which stage would be the most appropriate template for future scaffolds for cardiac engineering (Figure 2.5). FN is essential during vascular morphogenesis⁷⁹ and is an early marker of capillary formation⁸⁰. I fixed and stained hearts for FN at 5, 7, and 9 day of incubation to reveal the presence and structure of capillaries.

At day 5, FN forms small bundles of fibers interspaced between CMs, following the main direction of alignment (Figure 3.5 A). At day 7, tubular structures become visible revealing the creation of capillary tubes, which have a FN-rich basement membrane (Figure 3.5 B). Finally at day 9, the myocardium has an extensive array of capillaries, supplying each CMs directly with oxygen and nutrients (Figure 3.5 C). A single slice of the 3D image z-stack shows a lumen with two endothelial nuclei between aligned CMs (Fig. 3.3.D). The striation in the actin stain are characteristic of the sarcomeres in the contractile myofibers. During this period, I can observe the formation of the coronary plexus from day 5 to day 7 as cells migrate from the epicardium and endocardium into the myocardium, then the creation of a network of capillaries from day 7 to day 9 as blood start flowing through the coronary plexus.

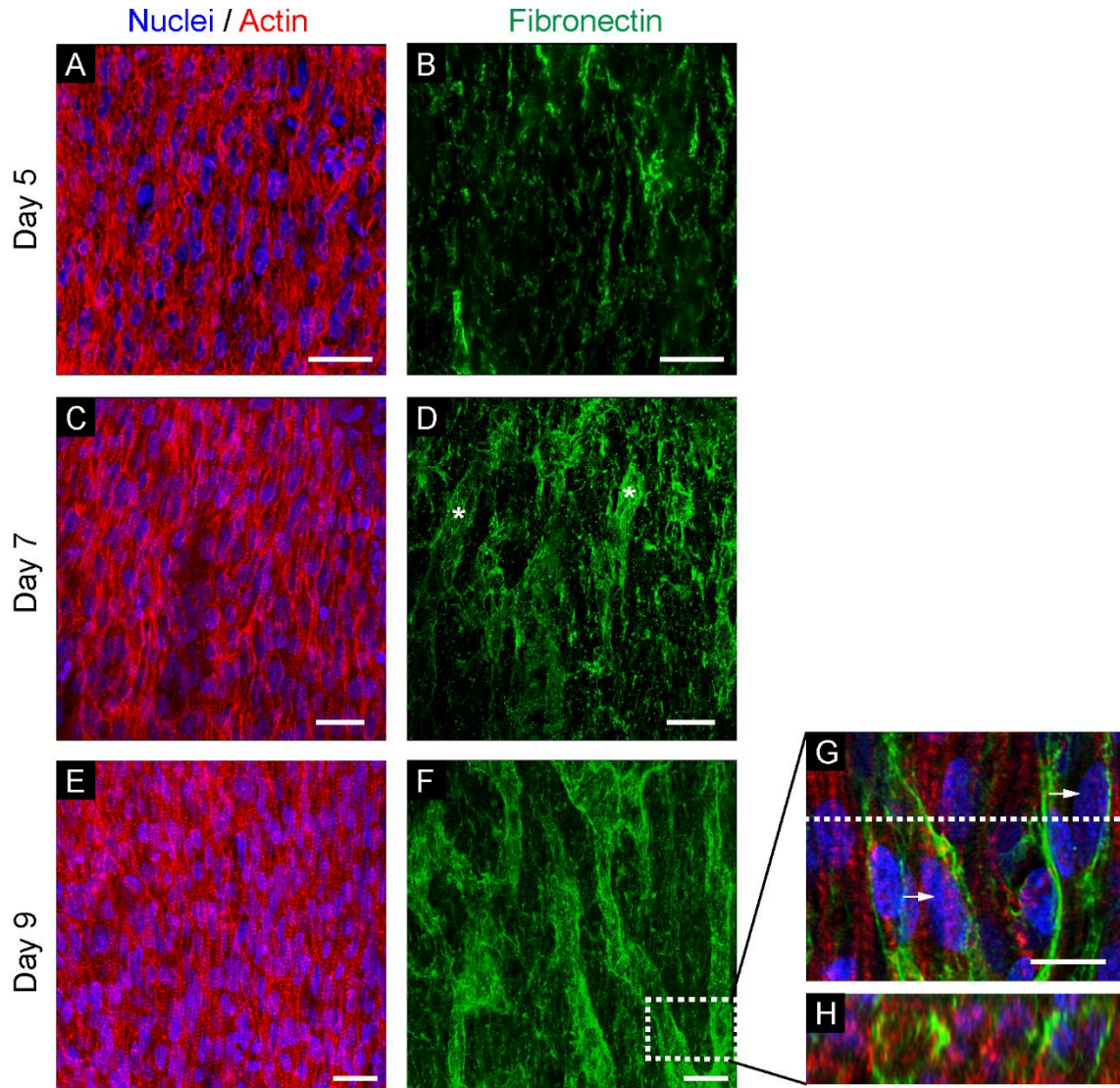


Figure 3.5. Vascularization of the myocardium between day 5 and day 9 of development. Maximum intensity projections of 3D image z-stacks of chick embryonic left ventricles at different stages reveal the formation of the capillary network. (A) At day 5, actin staining show the poor alignment of CM cytoskeleton. (B) Thin FN fibers are regularly located between CMs, following the main direction of alignment. (C) At day 7, the actin cytoskeleton shows distinct striations, which are a mark of well organized myofibrils. (D) Large, tubular FN structures (stars) are evidence of the preliminary capillary lumens. (E) At day 9, CM are very well aligned with distinct sarcomeres seen in regular actin striations. (F) FN staining reveals a full network of capillaries. (G) A close-up of day 9 myocardium shows the nuclei of endothelial cells (white arrows). (H) Circular lumens are visible in a cross-section. Scale bars = 20 μm (A-F) and 10 μm (G,H).

My goal is to provide design parameters for tissue engineering scaffolds, which can promote the growth of cardiac tissue from a stage similar to day 5 to a strongly aligned and vascularized tissue

seen on day 9. Moreover, I do not want to confound ECM cues that are linked to vasculogenesis with those linked to myogenesis. This is why I select day 5 (stage HH 28) as the best time to study the myocardial ECM in an avascular environment.

3.4.4 Laminin and fibronectin, but not collagen type IV are found in the prevascular myocardium of the ventral left ventricle of 5 day-old chick embryos.

I am interested in a range of ECM proteins, in particular basement membrane proteins such as FN, LAM, and collagen type IV. There is documented evidence that they play a great role during cardiac morphogenesis, by enabling the migration of endothelial and vascular smooth muscle cells⁴⁰ and promoting CM proliferation²⁰. I am targeting this analysis to obtain parameters for scaffold design, and so I am most interested in the ECM proteins for which I have the best tools in the laboratory^{81,82}. I dissected, fixed, and stained the left ventricles from day 5 chick embryos (\approx stage HH 28) for sarcomeric α -actinin, LAM, FN, and COL1 (Figure 2.4).

Using confocal microscopy, I obtained 3D images from the epicardium through the compact outer layer of the myocardium. Cross-sections reveal that there is a sharp border between the epicardium and the myocardium, marked by α -actinin staining (Figure 3.6 a), and a well-defined basement membrane, which is rich in LAM (Figure 3.6 b), and also contains FN (Figure 3.6 c) and COL1 (Figure 3.6 d). Cells in the epicardium present an actin cytoskeleton characteristic of the epithelium (Figure 3.6 e), and are wrapped by sheets of LAM and COL1 (Figure 3.6 f, h), with an intricate network of FN fibers (Figure 3.6 g). Just below the epicardium, the myocardium is the densest

(Figure 3.6 i), with little LAM (Figure 3.6 j), sparse FN fibers that are aligned with the main orientation of the CMs (Figure 3.6 k), and traces of COL1 (Figure 3.6 l). Finally,

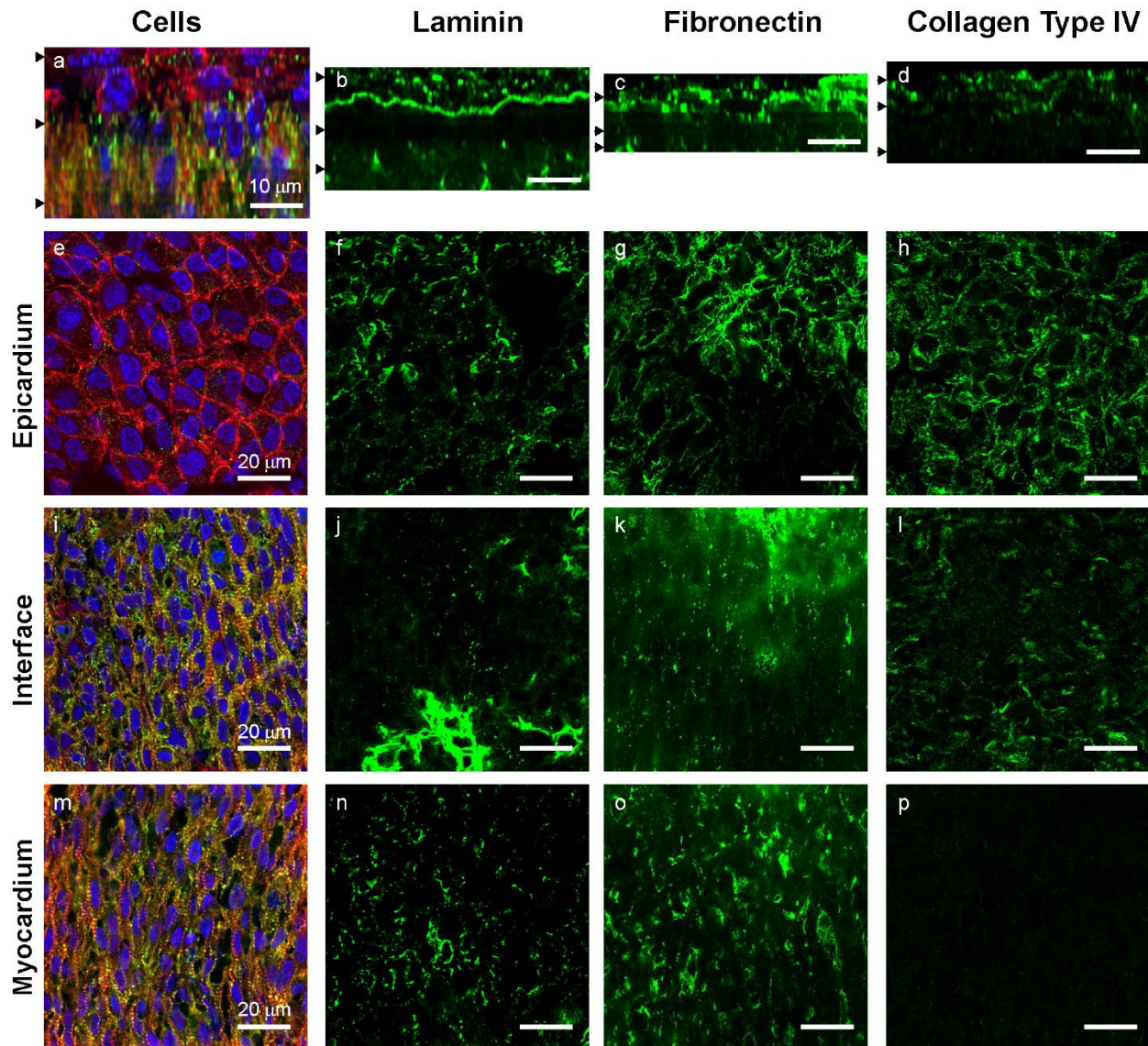


Figure 3.6. Spatial expression of laminin, FN, and collagen type IV in the left ventricle of 5 day – old chick embryos.

Hearts of 5-day old chick embryos were dissected, fixed, and stained for nuclei (blue), actin (red) and either α -actinin, LAM, FN, or COL1 (green). (a-d) Cross-sections of 3D z-stacks with black arrowheads marking the location of each slice for (e-h), (i-l), and (m-p) from top to bottom. Scale bars = 10 μ m. (e-p) Single slices of 3D z-stacks with scale bars = 20 μ m.

deeper in the myocardium, there are intercellular spaces in the tissue (Figure 3.6 m), which are filled with LAM (Figure 3.6 n) and FN (Figure 3.6 o). However, there was no COL1 signal at this depth in the myocardium (Figure 3.6 p).

The great spatial disparities in the LAM, FN, and collagen IV signals make the distinction between epicardium and myocardium easily discernable, even without relying on the α -actinin signal. The absence of collagen IV staining in the myocardium at this early stage is not surprising: although it is an essential component of the fetal cardiac ECM (with one study measuring its contribution to 8% of the total weight of ECM²⁰), collagen IV only appears after LAM, as a late marker of maturation of the coronary capillaries⁸⁰. To better understand the relationship of the ECM and the myocardium at this stage, I then look at the colocalization of FN and LAM in greater detail.

3.4.5 Fibronectin and laminin are colocalized in intercellular spaces in the avascular myocardium

I focus on the LAM and FN matrices in the ventral left ventricle of 5 day old chick embryos. I stained samples for LAM and FN simultaneously to study the colocalization of these two essential basement membrane proteins. Cross-sections of 3D images show that CMs with aligned actin cytoskeleton are present directly beneath the epicardium's basement membrane, which is identified by a very strong LAM staining (Figure 3.7). In the epicardium, cells are surrounded by a dense mat of FN fibers with some sheets of LAM. The FN network is seen below the epicardial cells and connected with the LAM-rich basement membrane. Just below the basement membrane, small fibers of FN with dots of LAM are visible. Very quickly as we go deeper in the myocardium, small

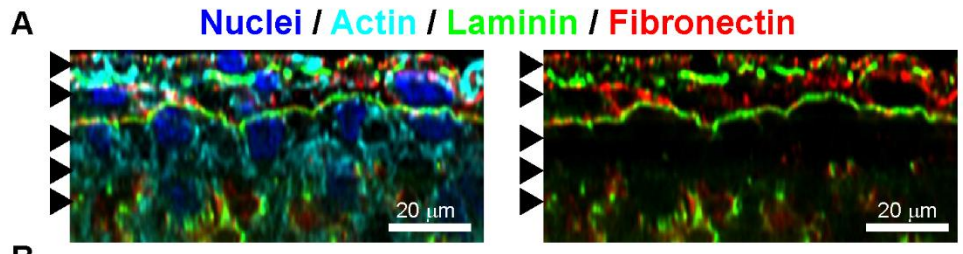
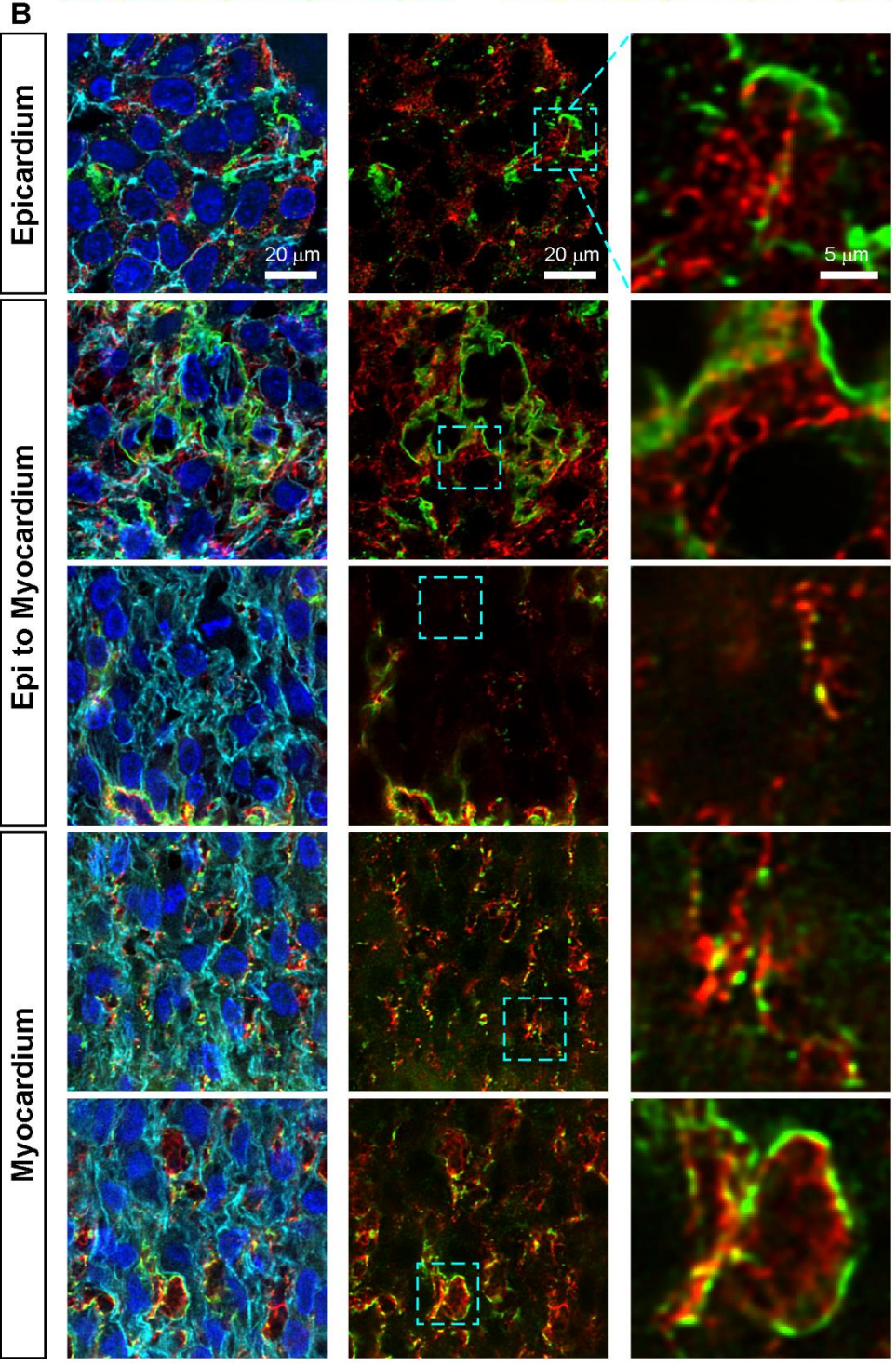


Figure 3.7.
Colocalization of FN and Laminin in the myocardium in the left ventricle of 5 day old chick embryos
Cross-section of a 3D image with black arrows marking the location of several images.



Each row shows deeper slices of the tissue stained for the nuclei (blue), F-actin (cyan), LAM (green), and FN (red). The left column shows the merged images with all the signals, the middle only LAM and FN. The right column contains images of enlarged areas of the FN and LAM matrices indicated by dotted cyan squares in the middle column.

acellular cavities are visible. They grow as we reach $\sim 10 \mu\text{m}$ within the myocardium: there the CMs are less aligned and large LAM-coated gaps are filled with a network of FN fibers.

The intercellular spaces filled with ECM that I observed at this stage have been previously described by Icardo *et al.* who hypothesized that continuous synthesis of ECM within the myocardium leads to an increase of the hydrostatic pressure and to the formation of these intercellular spaces⁸³. Deep in the myocardium, they might also be signs of the underlying trabeculae and the beginning of the trabeculated myocardium. Alternatively, these intercellular spaces could be a prelude to the invasion of vascular cells as FN is known to serve as tracks to guide the development of new vessels during coronary vasculogenesis⁸⁰. It is likely that these ECM-filled acellular cavities serve multiple roles. These features are present in all the samples studied, thus I hypothesize that they are an important part of cardiac morphogenesis at this stage. To proceed with the analysis of myocardial ECM cues, I decided to focus on the $\sim 5 - 10 \mu\text{m}$ of myocardium just below the epicardium.

3.4.6 Quantitative characterization of the fibronectin and laminin matrices

I used Imaris to segment the FN and LAM matrices in the top 5-10 μm of the myocardium of the ventral left ventricle of 5 day-old embryos and extract structural parameters. First, I segmented the ECM signal to create “surfaces” (3D objects created by Imaris based on a chosen threshold and described by a set of statistics such as volume, orientation, channel intensity, etc...) and sorted the surfaces according to their volume in three categories: small ($< 10 \mu\text{m}^3$), medium ($\geq 10 \mu\text{m}^3$ and $< 100 \mu\text{m}^3$), and large ($\geq 100 \mu\text{m}^3$) (Table 3.1). In representative z-stacks for each protein, I see that small ECM elements are predominant while large elements are occasionally present in the FN matrix but

never in LAM (Figure 3.8 A). I found that the total volume of FN is made of 34% of small elements, 50 % of medium, and 16 % of large while LAM contains 77% small and 23% medium (Figure 3.8 B).

	Small ($< 10 \mu\text{m}^3$)	Medium ($\geq 10 \ \& \ < 100 \mu\text{m}^3$)	Large ($\geq 100 \mu\text{m}^3$)
FN (n = 11)	0.34±0.09	0.5±0.08	0.16±0.13
LAM (n = 6)	0.77±0.11	0.23±0.11	

Table 3.1. Distribution of the volume of ECM elements.

To characterize spatial organization in 3D, I calculated for each voxel of the 3D z-stack the distance to the nearest ECM “surface”. The local maxima of these values represent half the spacing between ECM “surface” (Figure 3.9 A). I find that the mode for FN is 1.6 μm versus 2.2 μm for LAM (Figure 3.9 B). This distribution also reflects the lesser amount of LAM stain observed compared to FN, and so greater spacing generally between LAM bundles. However, local maxima with an intensity below 2 (i.e. a distance to ECM below 2 μm) are often found within intricate bundles of ECM. The actual spacing experienced by CMs is better represented by values above 3 μm . One important issue with this measure is the border effect, predominant in the right tail of the distribution.

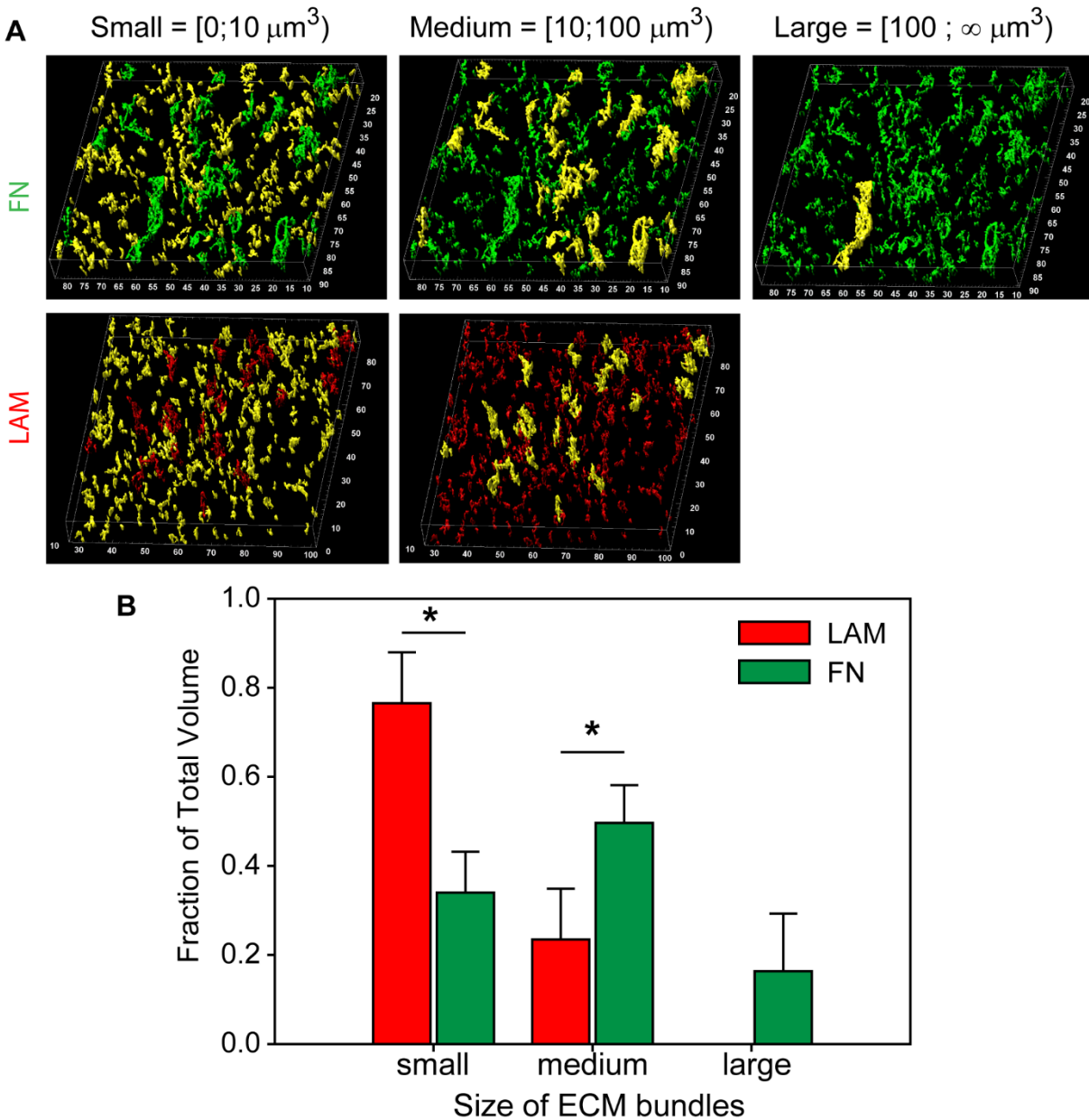


Figure 3.8. Quantitative characterization of laminin and fibronectin volume distribution.

(A) 3D representation of the FN and LAM elements segmented using Imaris are sorted into three categories based on their volume (elements in the representative z-stacks are highlighted in yellow when they match the category). (B) Bar chart of the fraction of total volume that small, medium, large elements represent. Bars = mean \pm standard deviation. * = $p < 0.01$ based on t-test. Data from 11 and 6 samples was gathered for FN and LAM respectively. The total number of ECM elements is 3534 for FN, 1613 for LAM.

Consider a point at the top of the volume imaged in a sample, where the “distance to ECM” is only computed based on the proximity of ECM bundles in the same plane and below this point. If I had

imaged even just 1 μm more above, any ECM bundle present could only have decreased the “distance to ECM” value at this point. Beyond this limitation, the “distance to ECM” measure is a simple and easy to interpret parameter to describe the 3D spatial organization of the ECM in the myocardium.

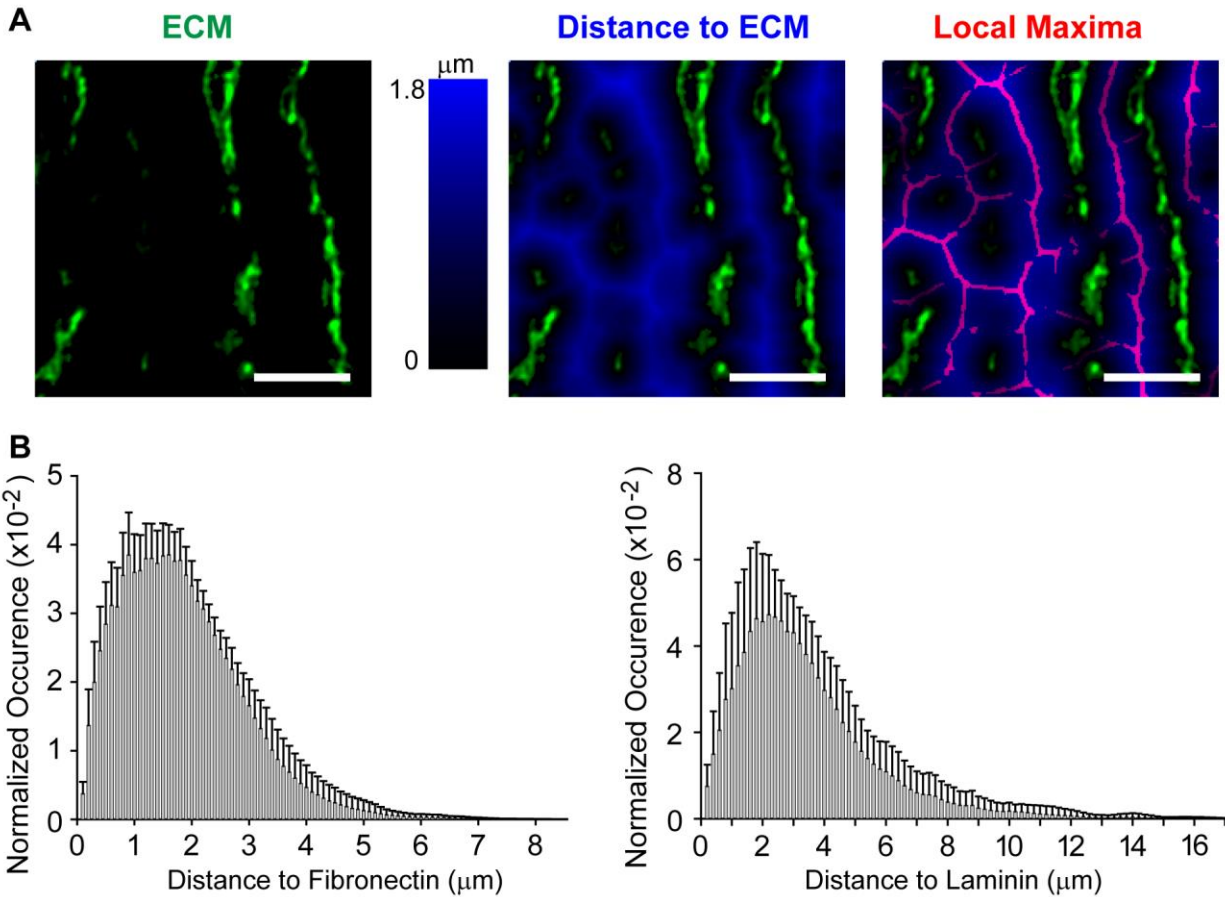


Figure 3.9. Characterization of ECM spacing in 3D.

(A) The ECM signal is used to calculate the “distance to ECM”, a new channel where the intensity of each voxel is equal to the shortest distance to the ECM in μm . The local maxima of the “distance to ECM” is a simple way to describe spacing in 3D. Scale bars = 4 μm . (B) Histograms of distance to FN and LAM, where the bars are mean + standard deviation for this bin across all samples.

Further, I created “filaments” (3D objects created by Imaris using a threshold as well as skeletonization to segment fibrous structures) following the skeleton of the FN signal to extract additional information. The diameter of FN fibers was $0.54 \pm 0.19 \mu\text{m}$ with an average length of 0.86

$\pm 0.63 \mu\text{m}$ (Figure 3.10 A, B). In this analysis, a fiber is defined as a segment of FN between two intersections, meaning that two long fibers connecting at their middle will be counted as four fibers of half the length. Thus, most small fibers counted are often segments in large bundles of FN. When I look at fibers with a length above $1 \mu\text{m}$ (31% of all fibers), I find that they are overall aligned in the main direction of the myocardium (Figure 3.10 C).

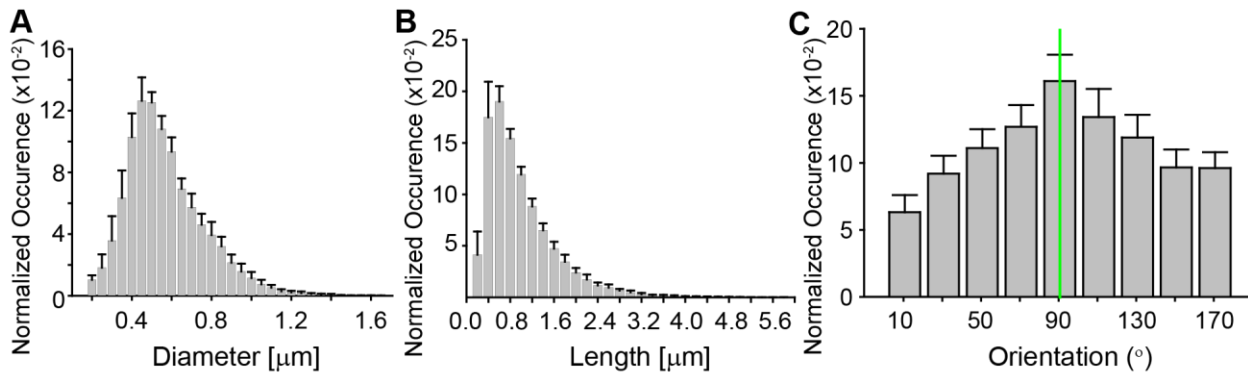


Figure 3.10. Structural characterization of the fibronectin fibers.

(A) Histogram of fiber diameter across all samples. (B) Histogram of fiber length, which is defined as the length of segments between two intersections. (C) Histogram of fiber orientation angle, for fibers with length $> 1 \mu\text{m}$. The fibers are centered on the main direction of myofiber orientation (green line) at 90° . $n = 92160$ for (A,B), 28968 for (C).

I can quickly deduce from our analysis simple criteria to build biomimetic scaffolds: a pattern of aligned FN fibers with $0.5 \mu\text{m}$ diameter, $1 \mu\text{m}$ length, spaced every $3 \mu\text{m}$ is a quick implementation of the data (Table 3.2). To design more complex ECM scaffolds, we should aim to reproduce the distribution of small and large bundles of fibers as well as the spread of orientation, length, and diameter of the native FN fibers.

Measuring structural parameters using immunostaining and confocal microscopy has several limitations. First, it is impossible to estimate the total amount of protein within the volume of myocardium imaged. Accurate measures of the protein mass requires mass spectroscopy. The volume or intensity of the fluorescent signal are poor estimation of the amount of protein as they rely heavily

on the quality of staining. Second, the results of the data analysis are dependent in some part on the parameters used in the image segmentation algorithms. I used the same parameters for imaging and processing all samples. To go further, artificial images covering a range of feature sizes should be processed with different parameters to determine the robustness of the image segmentation.

	Laminin	Fibronectin
Volume of ECM bundles	75% S 25% M	35% S 50% M 15% L
Spacing	4 μm	3 μm
Diameter		0.5 μm
Length		0.9 μm
Orientation		myofiber $\pm 50^\circ$

Table 3.2. Design criteria for biomimetic ECM scaffolds based on the study of the embryonic myocardium.

A lasting question regarding the structural analysis carried out here is: how much resolution is needed? The smallest features I can measure with confocal microscopy are at least $\sim 150 - 200$ nm wide in the focal plane of the objective. Does the structure of the FN molecule matter? Single FN strands are 2 nm wide⁸⁴ with domains that uncoil under stress to reveal cryptic binding domains. There is significant evidence that the nanoscale structure of FN in particular plays a key role in regulating diverse cell behaviors^{85,87,89} and the same effect is likely to be observed in many other ECM components. Thus, a perfectly tuned cell microenvironment must rely on nanometer resolution. However, in an engineering context, with the goal to build scaffolds for regenerating cardiac muscle, I am bound by the limits of the fabrication technique. As I discuss in chapter 4, the hydrogel micropatterning technique we developed is accurate down to feature sizes of $\approx 2 \mu\text{m}$. Any improvement

of the resolution below our current 200 nm limit will have no effect on scaffold fabrication and will also require the use of more complex analysis techniques such as SEM or STORM, which are time consuming and not easily applicable to study the structure in 3D.

3.5 Conclusion

In this chapter, we demonstrated the use of whole-mount microscopy to study the architecture of the whole embryonic heart using refractive index matching. Whole-heart imaging enables the creation of complex 3D model of the embryonic organ: already, scaffolds based on the 5 day old heart were bioprinted in alginate using a breakthrough technique called FRESH⁶⁴. It sidestepped the limitations of BABB by carrying out high resolution imaging of the ECM in the top 20 μm of the myocardium, without clearing with BABB. I found that FN and LAM remain major components of the myocardium throughout cardiomyogenesis from day 5 to day 9, while collagen IV could not be detected in the myocardium at day 5. FN is also a great marker of vascularization, and the basement membrane of the endothelium stains brightly for it: I can observe the progression of the coronary plexus and the development of full-fledge capillaries. After choosing to study the avascular myocardium at day 5, I used well established image analysis and segmentation algorithms to extract critical information regarding the FN and LAM matrices. 2D studies using images of the FN matrix as a template are already being carried out by a colleague, Ivan Batalov. Future experiments will be able to systematically investigate the effect of specific features (e.g. fiber length, diameter, orientation) of the FN and LAM matrices on cardiac tissue growth *in vitro* and relate it to cardiomyogenesis *in ovo*.

Chapter 4 Development of a technique to encode directional ECM cues onto a hydrogel to guide chick cardiomyocyte alignment

4.1 Abstract

The native embryonic ECM cannot be extracted and used as a scaffold. To provide immature CMs, obtained by differentiating human PSCs, with ECM cues inspired by our study of the embryonic myocardium, we need to build a biomimetic scaffold from the bottom-up. However, while many tools based on soft lithography have been used to create complex ECM patterns with micrometer size features in 2D, 3D cardiac tissues have instead relied on homogenous bulk hydrogels.

To bridge the gap between 2D and 3D techniques, I describe in this chapter a novel technique to micropattern ECM cues onto hydrogels. I characterized the quality of the pattern and found it to be within 10% of the intended feature size. I then investigated the effect of hydrogel composition on the alignment of chick primary CMs in response to 20x20 FN lines. Competition between adhesive proteins and remodeling of the FN lines modulate the alignment of cells on each hydrogel. High concentration COL1 (6 mg/mL) was selected as the best substrate to maximize CM alignment to the micropatterned ECM cues. This is the first step to be able to encode micrometer size ECM patterns into 3D.

4.2 Introduction

The ECM of the embryonic myocardium is unique and plays a significant role in the transformation that the heart undergoes during myogenesis. Going from a thin layer of CMs to a

multilayered, compact, and vascularized myocardium is the goal of cardiac tissue engineering. This is why I aim to build scaffolds that mimic the embryonic cardiac ECM, as I hypothesize that they will guide cardiac tissue growth *in vitro*.

In 3D, casting hydrogels loaded with human CMs is a common approach to build cardiac constructs. In particular, there are several well established platforms, which achieved good cardiac function and maturation: the Biowire, developed by the groups of Dr. Radisic and Dr. Keller, is a construct of collagen and Matrigel built around a suture to guide alignment and paced with electrical field stimulation at an increasing rate⁸⁶; the Engineered Heart Tissues developed by the group of Drs. Zimmermann and Eschenhagen are rings of COL1 and matrigel⁹³ or fibrin and matrigel^{96,97} that are set around silicone posts to provide passive tension; the human cardiac patches created by the group of Dr. Bursac are meshes of fibrin and Matrigel⁹⁰ (Table 4.1). These approaches have led to the maturation of human cardiac constructs by the combination of bulk hydrogel casting and electrical or mechanical stimuli. There is no control over the structure and composition of the scaffolds at the cell level: it is impossible to add ECM cues derived from the study of the native ECM.

Approach	Composition	Reference
Biowire	2.1 mg/mL Collagen I + 10% Matrigel	86
Cardiac patch	2 mg/mL Fibrin + 10% Matrigel	88,90–92
Engineered Heart Tissue	0.45-0.95 mg/mL Collagen I + 5-15% Matrigel	93–95
	5 mg/mL fibrin + 10% Matrigel	96–98

Table 4.1. Hydrogel composition used to build 3D functional cardiac tissue using established techniques.

A step toward providing cells with specific ECM cues is the use of decellularized organs. Decellularized adult hearts from pigs⁴⁹, mouse⁹⁹, rats²⁷ and humans³⁰ have been used as structural scaffolds or as homogenous hydrogels. Although this is the fastest path to create scaffolds that

recapitulate the complex biochemical composition of the native environment, it is not applicable to the embryonic ECM. First, gathering enough embryonic material for large scale tissue engineering would require hundreds of samples. Second, using human embryonic material is obviously out of the question. Finally, the decellularization protocols are still not completely characterized and the resulting ECM scaffolds show great variability from batch to batch⁵². We need tools to build ECM scaffolds that mimic the structure and composition of the embryonic ECM from the bottom-up.

In 2D, soft lithography has been used effectively to create micrometer sized pattern of ECM proteins and control the formation of contractile fibers. Patches of FN microcontact-printed on PDMS with different shapes were created to impose specific border conditions to the CMs and control sarcomere formation^{100,101}. Forcing the cell to adopt a specific aspect ratio by designing rectangular adhesive patches modifies nuclear shape and increases contractile force generation^{68,102}. However, the ECM patterns are always fixed to the substrate and thus the knowledge acquired with these well designed experiments cannot be used in 3D.

In this chapter, I describe a technique that allows the transfer of micrometer scale ECM patterns onto hydrogels. I leverage the unique feature of surface-initiated assembly⁸²: the ability to release microcontact-printed ECM proteins from the substrate. I first microcontact print FN in a standard pattern of 20 μm wide by 20 μm spacing lines (20x20) onto a glass coverslip coated with poly(N-isopropyl acrylamide) (PIPAAm). PIPAAm is thermoreversible and dissolves in water, enabling the transfer of the ECM pattern to other substrates. Thus, the complex 3D organization of ECM cues found *in vivo* can be recapitulated layer-by-layer with the same precision expected in 2D from soft lithography approaches. First, I characterized the fidelity of the transfer technique by

measuring pattern features before and after transfer. Then, I evaluated the capacity of micropatterned hydrogels to guide the formation of cardiac sheets from chick primary CMs. Alignment is a major predictor of function in cardiac tissue and I optimized the composition of the hydrogel to maximize CM alignment with the 20x20 FN pattern. I tested a range of concentration of COL1, fibrin, and Matrigel, inspired by the successes of 3D hydrogel casting in the literature (Table 4.2). I found that high concentration COL1 is the optimal substrate to present micropatterned ECM cues to promote cardiac alignment.

	Concentration (mg/mL)				X	Matrigel (mg/mL)	
Collagen I	1.5	3	4.5	6		0	
Fibrin	2	10	20			1	

Table 4.2. Hydrogel composition tested to maximize cardiac alignment.

4.3 Materials & Methods

4.3.1 Hydrogel casting

All the hydrogel solutions were prepared on ice. Matrigel aliquots were thawed on ice 30 min prior to casting the gel. All solutions and reagents were kept on ice. Collagen I (High concentration rat tail, Corning) was prepared according to manufacturer's instructions. Briefly the stock COL1 / acetic acid solution was neutralized with 10x PBS and NaOH to induce gelation. Fibrinogen (Bovine, Sigma) was dissolved at specific concentrations in dH₂O with 10 mM HEPES and pH = 7.4 at 37° C for 1 hr. Fibrin gels were formed by mixing the fibrinogen solution 9:1 with a thrombin solution to obtain 2, 10, or 20 mg/mL final concentration with 0.1 U/mL of thrombin. To make hydrogels containing 1 mg/mL Matrigel, fibrinogen or COL1 solutions at a higher concentration were made and mixed with Matrigel just before casting. 50 µL of each solution was cast in 9mm diameter Fastwells set on clean and sterile glass coverslips in the biohood. The gels were left at least 1 hr in the incubator at 37° C. Then the gels were brought back in the biohood and the Fastwells were delicately removed. Gels were left to dry completely under the flow of the biohood, which usually required 1hr 30 min – 2hrs.

4.3.2 Transferring ECM patterns onto hydrogels

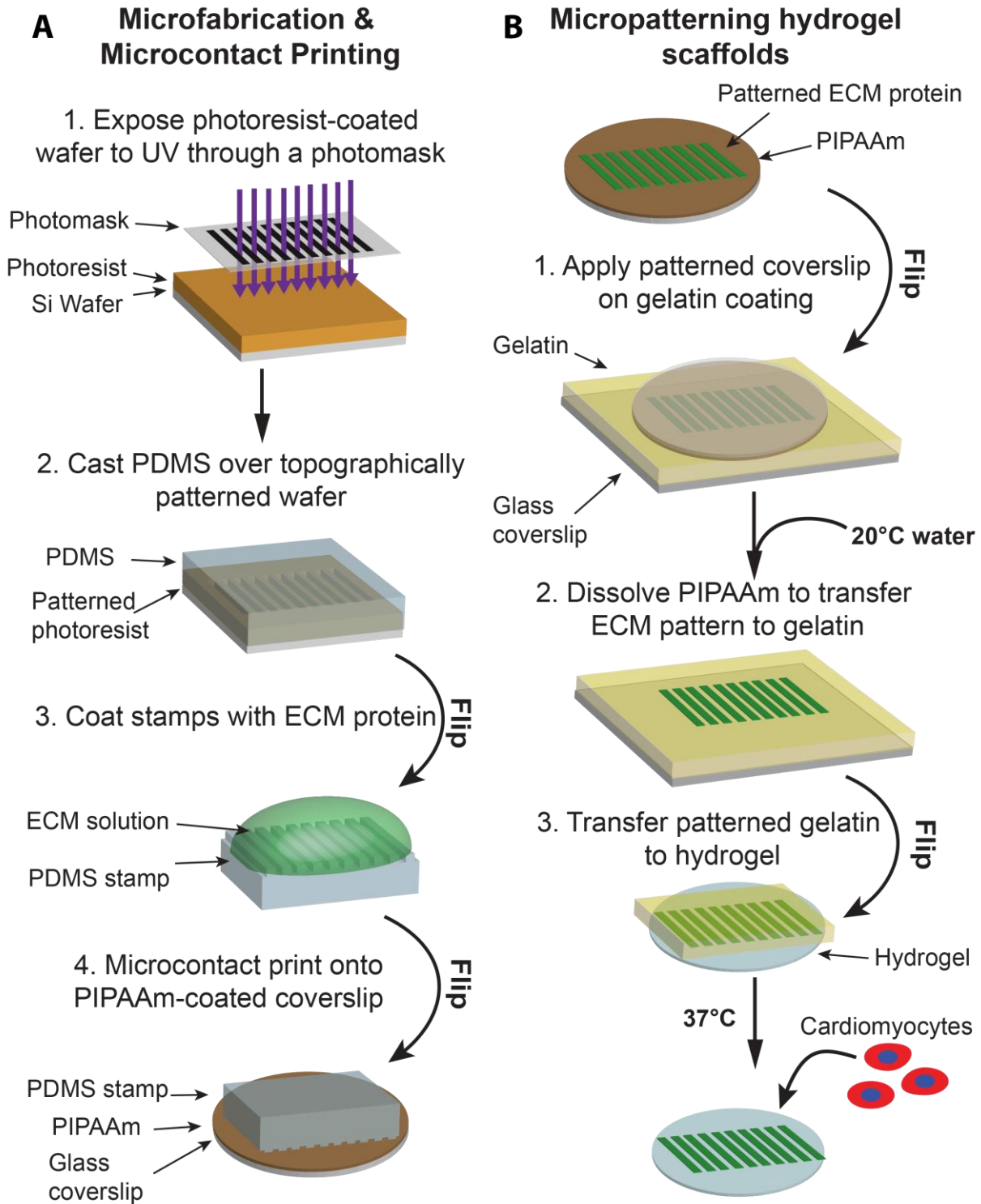


Figure 4.1. Micropatterning ECM cues onto hydrogel scaffolds.

First, I created PDMS stamps using standard photolithography. 42x55 mm N2 glass coverslips (ThermoFisher) were spincoated with the photoresist Megaposit SPR200-3.0 (Microchem) at 5000 rpm for 15 s. Then they were baked at 150° C for 90s. A custom UV exposure system was calibrated and used to expose the photoresist to UV for 55s through a chrome photomask with a 20 µm by 20 µm line pattern (Figure 4.1 A1). The coated glass coverslips were baked post-exposure for an additional 90s at 150°C. Finally, the photoresist was developed in the solution MF-26A for 40s then rinse with dH₂O.

PDMS Sylgard 184 (Dow Corning) was prepared by mixing the base and curing agent in a 10:1 ratio and poured over the patterned photoresist. The PDMS was allowed to cure for at least 4 hrs at 65°C then the part above the pattern was cut out to create a PDMS stamp (Figure 4.1 A2). All experiments in this chapter used PDMS stamps made from a unique photoresist template, thus I expect the features of the PDMS stamps to have the exact same dimensions.

The PDMS stamp was “inked” for 1 hr at room temperature with a protein solution: 50 µg/mL FN (human plasma, Corning #356008) with 30% conjugated to Alexa Fluor 546 – maleimide as described previously⁸² (Figure 4.1 A3). A PIPAAm-coated glass coverslip was prepared by adding 200 µL of a 10% w/v PIPAAm (Polysciences, # 25189-55-3, Mw = 40,000) solution in butanol. The coverslip was spincoated at 6000 rpm for 1 min, then left to dry for 30 min before the next step. I microcontact printed the protein by putting the stamp into conformal contact with a PIPAAm-coated glass coverslip for 30 min (Figure 4.1 A4). The stamps were gently peeled off to reveal the coverslip micropatterned with FN lines. The coverslip was then flipped onto a 20% w/v gelatin gel and dipped into 20°C water (Figure 4.1 B1). The PIPAAm dissolved and released the protein pattern on the gelatin

(Figure 4.1 B2). Finally, a piece of gelatin was cut and melted over a dried hydrogel at 37°C for 45 min (Figure 4.1 B3). After washing off the gelatin four times with warm PBS, the micropatterned hydrogels were inspected using a macrozoom laser-scanning confocal Nikon AZ-C2 with 10 x magnification (NA = 0.45). Hydrogels with bad transfer were discarded (\approx 10-20% per batch); the rest were UV-treated for 15 min while in PBS. Finally, PBS was removed and the ECM-patterned hydrogels were ready to be seeded with cells (Figure 4.1 B4).

4.3.3 Chick primary cardiomyocyte isolation and culture

White Leghorn chick eggs were purchased from Eichner's Farm Market (Wexford, PA) and incubated for 8 days at 37° C and 50-60% humidity. On the day of the experiment, eggs were cracked and the embryos put in warm PBS. The hearts were dissected and the ventricles isolated. Once 7 – 15 ventricles had been selected (1 set of ventricles \approx 700,000 cells), they were cut about 20 times with scissors, then stirred on a hot plate at 37° C with 3 mL of TrypLE Express. After 10 min, the supernatant, containing dead cells and blood was discarded. Then, 3 mL of fresh TrypLE Express were added and the tissues incubated for 5 min. At the end of the incubation period, the supernatant was added through a 40 μ m cell strainer to 30 mL of cold seeding media (SM = M199, 10% Heat-inactivated FBS, 1% Pen/strep). This step was repeated 5 times total. Before the fifth and last incubation, the remaining tissues were pipetted up and down to further break them. The entire solution was then put through the strainer. The cell solution was spun at 100 g for 10 min and the pellet resuspended in 15 mL of SM. The cells were preplated twice 45 min in a T75 tissue culture flask to remove fibroblasts that adhere faster than CMs. Finally, the CM-enriched cells were ready to

be seeded in SM. 24 hrs after seeding, media was changed to maintenance media (MM = M199, 2% Heat-inactivated FBS, 1% Pen/strep). MM was then refreshed every two days. For all fibrin hydrogels, 10 mg/mL aprotinin (from bovine lung, Sigma-Aldrich, #A3428) was added to seeding and maintenance media.

4.3.4 Fixing and immunostaining

After four days in culture, samples were briefly washed with warm PBS with calcium and magnesium then fixed for 15 min in PBS with 4% formaldehyde and 0.05 % Triton X-100. Samples were then rinsed with PBS three times before blocking for 30 min at room temperature in PBS with 10% bovine serum albumin or 5% goat serum. Samples were stained in two steps: the primary incubation contained PBS, 10% bovine serum albumin, and 1:200 antibody against sarcomeric α -actinin (mouse monoclonal, Sigma), 1:200 antibody against FN (rabbit monoclonal, Sigma) for 1 hr at room temperature; following three 5 min washes in PBS, the secondary incubation was carried out with 1:200 Alexa Fluor 546 goat anti-rabbit IgG (ThermoFisher) and 1:200 Alexa Fluor 488 goat anti-mouse IgG (ThermoFisher) for 1 hr. After three more washes, the samples were mounted with Prolong Gold (ThermoFisher) on glass slides

4.3.5 Image acquisition and analysis

Samples were imaged on an inverted Zeiss LSM700 laser-scanning confocal microscope with a 20x objective (0.8 NA) and a 63x oil objective (1.4 NA). For each sample, between 4 and 6 fields of view were acquired, using the optimal pinhole size, a 1 μ m step size between each slice of the z-stack capturing the whole thickness of the cell layer. The analysis was carried out in Matlab : briefly, a

maximum intensity projection was created for each z-stack and a mask of the CMs using the α -actinin signal was created; then vectors based on the local alignment of actin were calculated for each point within the mask using a fingerprint enhancement algorithm^{26,103,104}; finally, the orientational order parameter was defined as the maximal eigenvalue of the orientation tensor of these vectors (Figure 4.2). The code also relies on the Bio-Formats library¹⁰⁵ to easily access the metadata of proprietary file format such as .lsm, .lif, and .nds. The custom Matlab code is found in Appendix B.

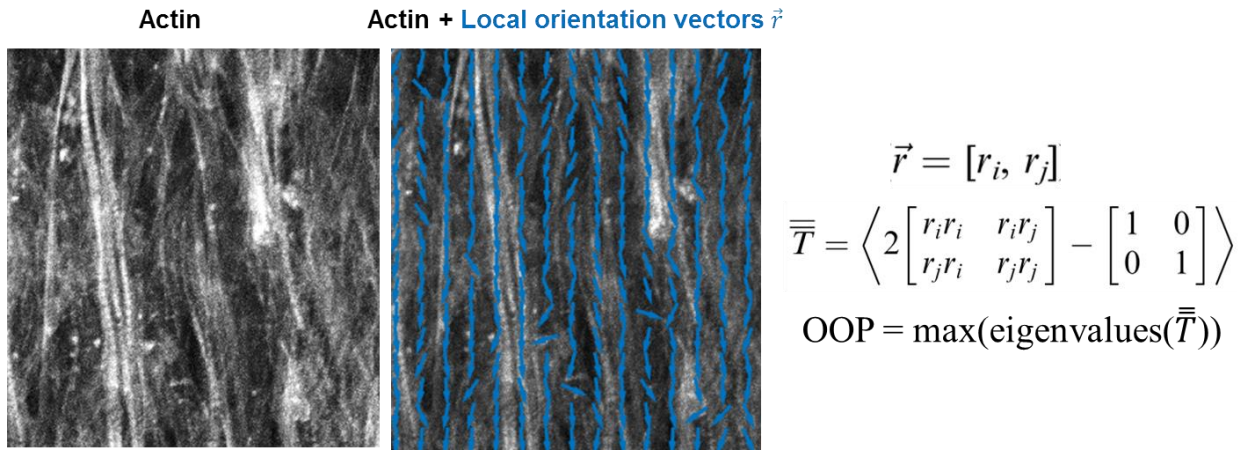


Figure 4.2. Calculation of the orientational order parameter. First, a maximum intensity projection is created from 3D confocal images of the actin cytoskeleton. Then, I use Matlab to calculate local orientation vectors based on intensity gradient. Finally, the orientational order parameter is obtained by determining the maximal eigenvalue of the tensor T . Adapted from Grosberg et al.¹⁰⁶

4.3.6 Experimental design and statistics

For pattern fidelity, all FN patterns were created with PDMS stamps coming from a unique photoresist template. I counted the width of 3 lines in each field of view, with 3 fields of view per sample, and at least 4 samples per condition, created in two batches.

For the orientational order parameter, at least five samples for each condition were studied by carrying out at least three experiments with two samples per condition. Samples were removed from

the analysis for several reasons: physical harm during experiment, aberrant cell density, unexplained loss of FN pattern, CM coverage <15%. All results were analyzed using Sigmaplot. Two way ANOVA followed by Holm-Sidak multiple comparison was carried out to assess the significance ($p < 0.05$) vs. PDMS and for each hydrogel concentration with vs. without Matrigel.

4.4 Results & Discussion

4.4.1 Patterning fibronectin lines on hydrogels with high fidelity

I characterized a new technique to embed ECM cues onto hydrogels. It relies on standard photolithography and μ CP to create a pattern of ECM proteins in 2D with great resolution (Figure 4.1 A). While traditional μ CP is usually the last step in substrate fabrication, μ CP on PIPAAm-coated coverslips, a thermoresponsive polymer, enables the subsequent transfer of the protein pattern to another substrate (Figure 4.3 A). I transfer the protein first to gelatin, and then to a hydrogel composed of COL1, fibrin, or Matrigel. I find this process to be reliable and reproducible with ~ 80% success rate (data not shown).

Substrate	Line Width (μ m)	P<0.05 vs. PIPAAm
<i>Before:</i>		
PIPAAm	20.6 \pm 0.7	
<i>After:</i>		
Fibrin 2 mg/mL	19.3 \pm 1.5	Yes
Fibrin 2 mg/mL + Matrigel	19.7 \pm 0.8	Yes
Fibrin 20 mg/mL	20.2 \pm 0.4	Yes
Fibrin 20 mg/mL + Matrigel	19.0 \pm 1.3	No
Collagen I 1.5 mg/mL	19.8 \pm 1.0	Yes
Collagen I 1.5 mg/mL + Matrigel	19.9 \pm 0.6	Yes
Collagen I 6 mg/mL	19.5 \pm 1.2	Yes
Collagen I 6 mg/mL + Matrigel	19.6 \pm 0.9	Yes

Table 4.3. Line width of fibronectin lines before and after transfer to different substrates

To recapitulate the complex native ECM structure, a scaffold fabrication technique must provide micrometer resolution and accuracy. To optimize and characterize our technique, I use an artificial pattern of FN lines, 20 μ m wide with 20 μ m spacing (20x20), which has shown the ability to induce the formation of highly aligned tissue on PDMS^{26,102,107}. I measured the width of the FN

lines before and after transfer onto hydrogels of different composition to quantify the morphological changes caused by the process (Figure 3.2). The FN lines are well preserved on all

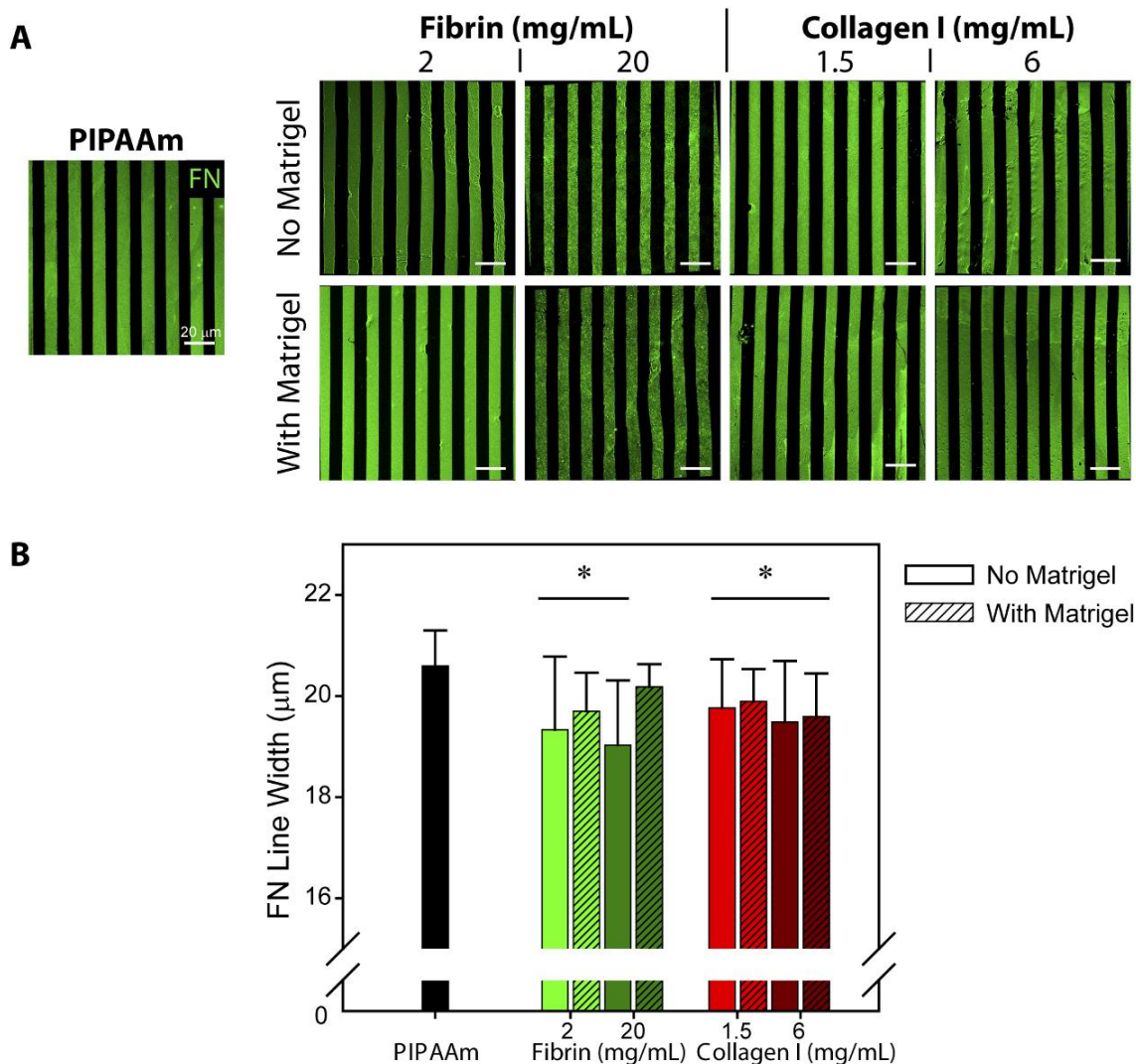


Figure 4.3. Fidelity of Pattern Transfer.

(A) 20 μm wide FN lines (green) with 20 μm spacing were μCP on PIPAAm-coated coverslips. Confocal images of the fluorescently conjugated protein show that the lines were well preserved after transfer on hydrogels composed of fibrin (2 and 20 mg/mL), COL1 (1.5 and 6 mg/mL), with or without the addition of Matrigel (1 mg/mL). Scale bars = 50 μm. (B) Histogram (mean + standard deviation) of FN line width before and after transfer. * = $p < 0.05$ vs. PIPAAm. $n = 180$ for PIPAAm, $n = 27$ for all other substrates.

substrates (Figure 4.3 B). The FN lines were significantly narrower after transfer (except for 20 mg/mL fibrin with Matrigel) than on PIPAAm (Table 4.3). This is an expected effect of μCP on PIPAAm followed by release: FN molecules adsorbed to the PDMS stamp are under strain when microcontact-

printed on PIPAAm; when PIPAAm dissolves, the molecules assemble as a fiber and some of the strain is released^{81,82}, which leads to significant contraction of free-floating fibers assembled by surface-initiated assembly. Here, the protein patterned PIPAAm is put into contact with gelatin before release, which limits the amount of shrinkage observed by in the line width. The changes observed during transfer represent less than 10% of the original width. This technique can be used to accurately pattern ECM proteins onto hydrogels with great spatial resolution.

4.4.2 High concentration collagen I maximizes cardiomyocyte alignment with FN lines

I compare the effect of several hydrogel compositions on the ability of chick primary CMs to align with 20x20 FN lines. To do this, I seeded chick CMs isolated from the ventricles of 8 day old embryos and cultured them for four days on micropatterned hydrogels. Qualitative observation with the confocal microscope reveal that for all composition of fibrin hydrogels, alignment is very poor and far removed from the strong anisotropy seen on PDMS controls (Figure 4.4 A). However on COL1 – based hydrogels, two different behaviors are clearly visible: the tissue is very poorly aligned on hydrogels containing Matrigel, while there is consistent anisotropy without. The orientational order parameter (OOP) is a measure of the overall anisotropy of the actin cytoskeleton: it is 1 when all the actin fibers are perfectly aligned, and 0 when the tissue is completely isotropic (Table 4.4). OOP is consistently high on PDMS (Figure 4.4 B). On fibrin, it is always lower than 0.5 with strong variability. On COL1 without Matrigel, OOP is above 0.6 but drops below 0.4 with the addition of Matrigel. To obtain the strongest and most consistent alignment, I identify 6 mg/mL COL1 as the ideal substrate.

		Collagen I				Fibrin			PDMS
mg/mL		1.5	3	4.5	6	2	10	20	
Matrigel	0	0.62±0.21	0.65±0.18	0.63±0.07	0.75±0.1	0.46±0.18	0.41±0.14	0.46±0.14	0.92±0.02
	1	0.32±0.13	0.41±0.2	0.37±0.17	0.43±0.13	0.24±0.14	0.34±0.17	0.3±0.15	

Table 4.4. Orientational order parameter (mean ± standard deviation) of chick CMs on different substrates. Best composition framed in red.

Our results come in sharp contrast to previous successful approaches to engineer cardiac tissue from the literature. The Biowire, cardiac patch, and Engineered Heart Tissue all use 10% Matrigel, often observing that it is essential for the tissues to develop significant contractile forces⁹³. Further, the concentration of fibrin or COL1 used in the literature is significantly lower than the ones I chose in this study (see Table 4.1). Higher amount of ECM was found to limit tissue compaction and remodeling and decrease conduction velocity and contractility. To interpret these results, we need to look at the unique aspects of our technique for scaffold fabrication. The hydrogel is a substrate on top of which are displayed microscale ECM cues for the cells. Alignment of the CMs in this context is driven by their capacity to read the ECM cues and follow them. Adhesion is the key regulator in our system: as on 2D PDMS substrates patterned with FN lines, it is the contrast between very adhesive and less adhesive regions that provide directional guidance to the cells. However, 3D tissues built from casting hydrogels loaded with cells depend on anisotropic mechanical strains and specific border conditions to control alignment: gels are cast around posts or sutures and as cells remodel and pull on

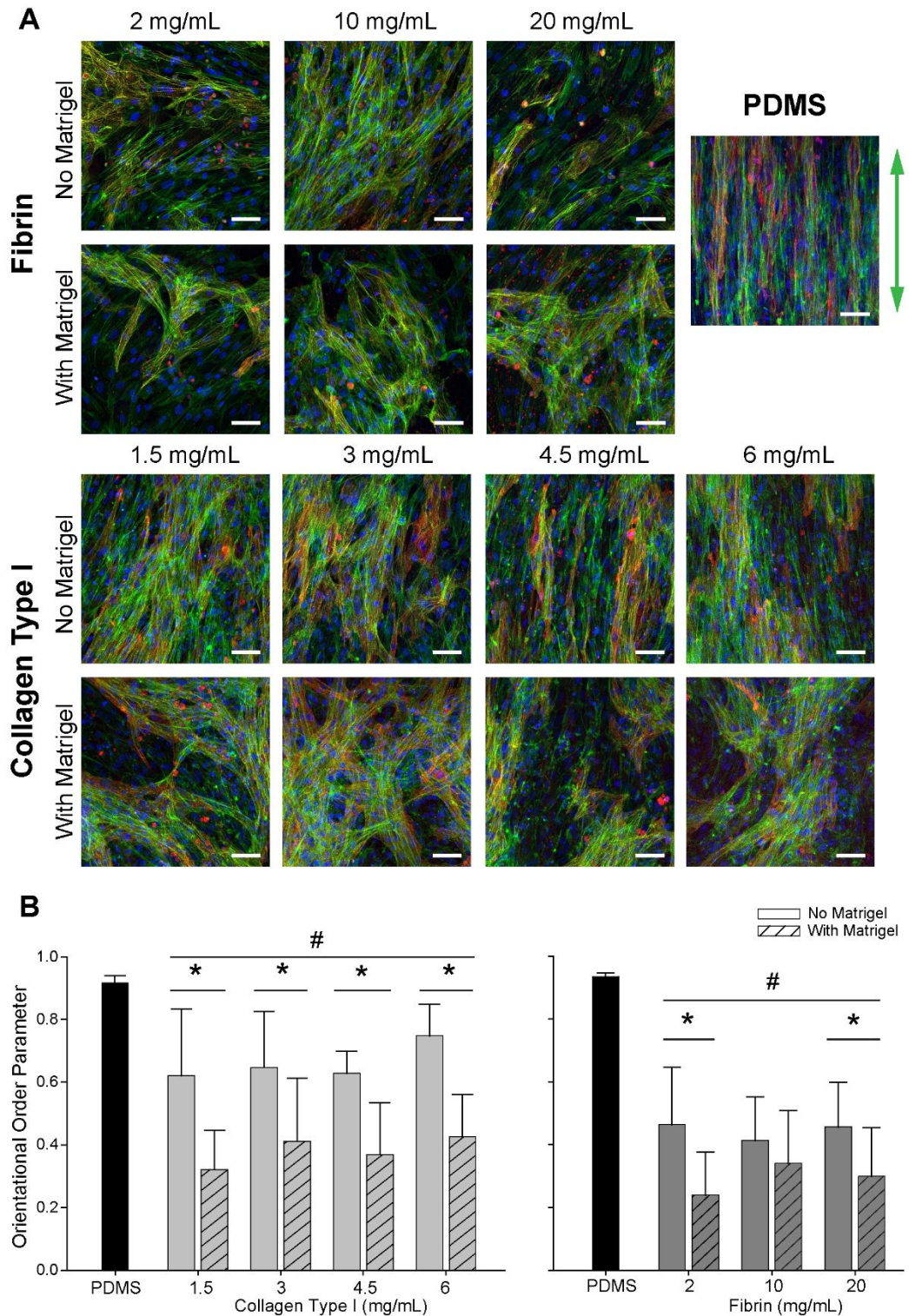


Figure 4.4. Chick primary CMs align on micropatterned ECM scaffolds.

(A) Grid of confocal fluorescence images of chick cells after 4 days of culture on hydrogels of different compositions and on PDMS, stained for nuclei (blue), actin (green), α -actinin (red). Scale bars = 50 μ m. (B) Histograms (mean + standard deviation) of the orientational order parameter of the actin cytoskeleton on each substrate. * = $p < 0.05$ vs. Matrigel, # = $p < 0.05$ vs. PDMS. $n \geq 5$.

the gels, the building tension forces them to align. In 3D hydrogels, the scaffolds must be easy to remodel and foster tissue compaction and organization. Thus, Matrigel helps cell spreading and remodeling. Low concentration of fibrin or COL1 makes 3D hydrogels that are light, with low hydrostatic pressure, and compact significantly as cardiac tissues. In our system, low concentration COL1 (< 1.5 mg/mL) were too fragile to be manipulated and had very poor quality of ECM pattern transfer.

4.4.3 Remodeling and competition of adhesive patterns cause loss of alignment

To better understand the mechanisms driving the alignment on hydrogels of different composition, I stained for FN after culture and observed what remained of the patterned ECM cues under high magnification. In fibrin-based hydrogels without Matrigel, I found that FN was well preserved despite very low alignment of the CMs. On samples with Matrigel, the FN was completely remodeled and only bright strands remained of the original 20x20 lines (Figure 4.5 A). On collagen-based hydrogels, the FN lines are preserved, and I can see FN fibers pulled off the substrate by the cells (Figure 4.5 B). On PDMS controls, the FN pattern is visible beyond a lot of bright FN fibers, either made by pulling material from the substrate or by the cells creating their own (Figure 4.5 C). Thus the addition of Matrigel has two different actions leading to decreased alignment of the chick CMs. First, it competes with the FN cues for adhesion, even without remodeling. This is the case on collagen-based hydrogels that are not remodeled but still show poor OOP with Matrigel. Matrigel is often used to promote adhesion of cells in a wide range of application. It is composed mostly of LAM,

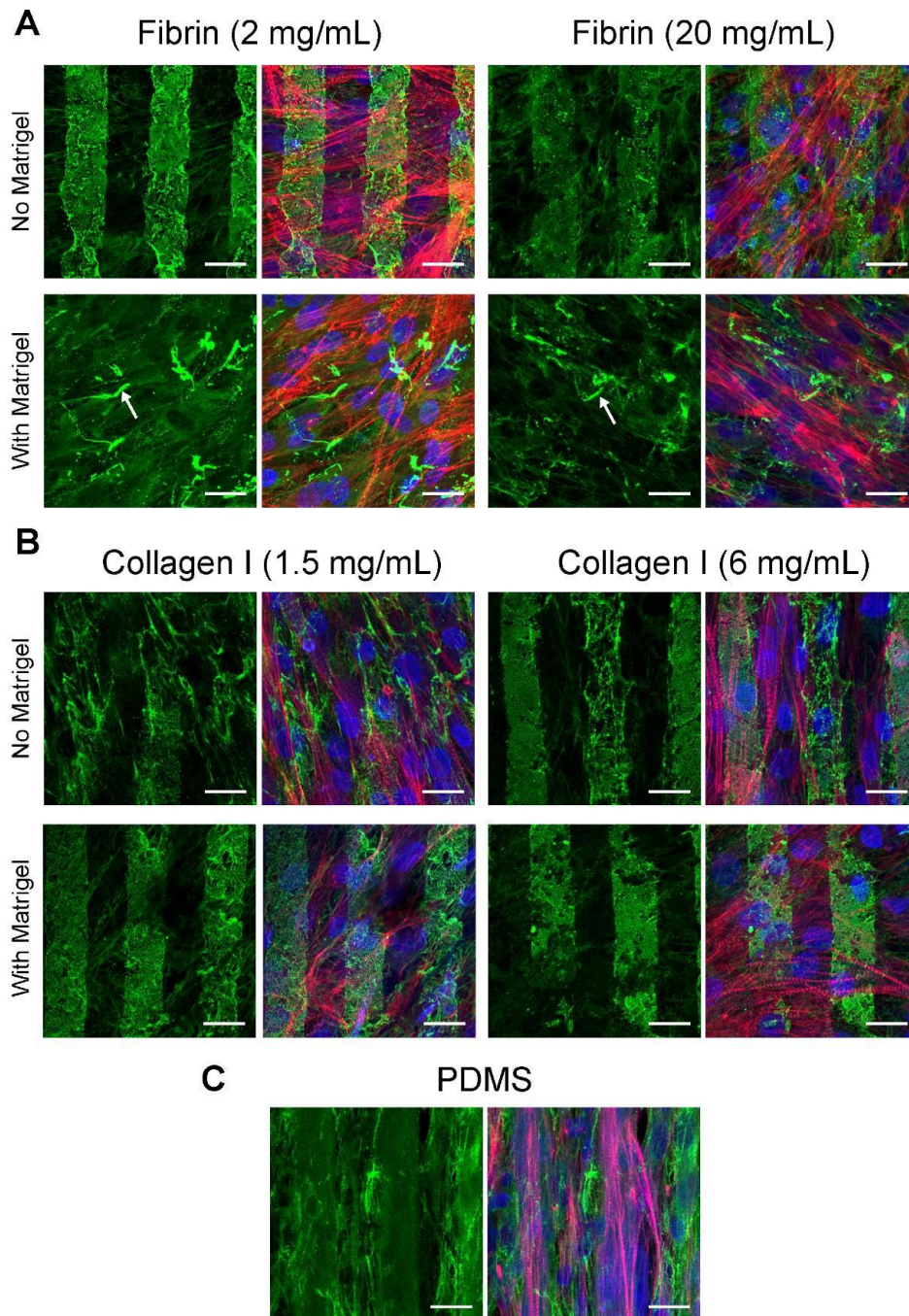


Figure 4.5. Remodeling of the fibronectin lines after culture.

Confocal images of chick primary CMs grown for 4 days on hydrogels patterned with 20x20 FN lines. Samples were stained for nuclei (blue), actin (red), FN (green). (A) FN + Matrigel hydrogels only show small fibers left of the original 20x20 lines (white arrows). Fibrin hydrogels preserved the pattern but show no alignment. (B) The FN lines are present on all collagen I-based hydrogels although there is no alignment on COL1 + Matrigel. (C) PDMS controls promote great alignment. Scale bars = 20 μ m.

COL1, and entactin, but also contains small amount of FN, and other component of the basement membrane¹⁰⁸.

The ability of CMs to bind to specific ECM components vary significantly with their maturity: while neonatal CMs are able to bind equally well to LAM, FN, COL1, and COL1, adult CMs lose the ability to bind to all but LAM and COL1^{42,109}. In our own experience, chick primary CMs attach more readily to FN than collagen type I. Thus, the addition of Matrigel dramatically reduces the contrast between very adhesive and less adhesive bands of the pattern and limit the alignment of cells along the FN lines.

This competition for cell binding is also at play on fibrin-based hydrogels. Fibrin and FN both present RGD sites that can bind to common integrins¹¹⁰, which decreases the anisotropy generated by the line pattern. Fibrin is also readily remodeled by cells, in particular by cardiac fibroblasts that still remain in the cells isolated from the chick ventricles. Moreover, fibrin is part of the provisional matrix during wound healing and is known to foster remodeling and angiogenesis¹¹¹. I found that despite the addition of aprotinin, hydrogels made of 40 mg/mL fibrin seeded with chick primary CMs dissolved almost completely due to remodeling (data not shown). This suggests that the high concentration of provisional proteins found in fibrin + Matrigel hydrogels can promote remodeling and lead to the loss of the original pattern of FN lines.

Considering these issues points to alternative solutions to improve CM alignment past the direct optimization of hydrogel composition. Several MMP inhibitors can be tested to minimize remodeling of the FN lines¹¹². Antibodies against specific integrins can be added to the medium to block cell-ECM interactions and artificially increase the perceived difference between adhesive and less

adhesive bands on the hydrogel. As I plan to stack aligned cardiac sheets to create 3D multilayered tissues, I expect to supplement the guidance given by the micropatterned ECM cues with a standard mechanical anisotropy by attaching two ends of the sheets to posts.

4.5 Conclusion

In this chapter, I demonstrated the use of a novel technique to transfer ECM patterns onto hydrogels with high fidelity. I found that the dimensions were preserved during transfer within 10% of the original 20 μm wide lines. Using this technique, I created aligned cardiac sheets with chick primary CMs. I tested a range of hydrogel composition to maximize CM alignment. I found that on high concentration COL1 (6mg/mL), the FN lines consistently drive high alignment with little remodeling of the hydrogel or the FN. Thus, 6 mg/mL COL1 hydrogels are the best platform to present complex ECM cues to cardiac cells. In chapter 4, I use this knowledge to create aligned and functional human cardiac tissue.

Chapter 5 Creation of aligned human cardiac tissue

5.1 Abstract

The use of human PSC-derived CMs enables us to build physiologically relevant tissues and to focus on the most important criteria for cardiac tissue engineering: contractile force generation. In this chapter, I grow human cardiac sheets on the ideal hydrogel substrate identified in chapter 3. I first characterize their alignment then measured contractile stresses with the muscular thin film (MTF) assay. Twitch stresses between 2.6 and 28.3 kPa correspond to what has been reported in the literature and are of the same order of magnitude as those measured in adult cardiac muscle. Human cardiac sheets can also be stacked up to 4-layer high to create multilayered constructs. I show in this chapter that I can encode microscale ECM pattern onto cardiac sheets and rebuild layer-by-layer functional 3D cardiac tissues with some control over the spatial organization of ECM cues.

5.2 Introduction

Advances in derivation, culture, and differentiation of human embryonic and induced PSCs have driven cardiac tissue engineering ever closer to clinical relevance over the last decade. Although it remains a long and labor-intensive process, the rise of xenofree culture protocols^{113,114} and monolayer differentiation schemes⁹ has lowered the bar for the adoption of human PSC culture by many laboratories. This switch to human CMs has led to the recent focus on promoting cardiac maturation, as PSC-derived CMs are more plastic and immature than the neonatal CMs that have been traditionally used from rat or mouse model¹⁰.

Compared to the chick primary CMs I used in chapter 3, human PSC-derived CMs have many advantages. First, although the avian heart follows the same developmental plan as the human heart, there are major physiological differences between chick and human CMs: avian CMs do not form T-tubules, a mark of maturity in human CMs⁴⁴. Second, while differentiating human PSCs is more labor-intensive than harvesting fertile eggs, it allows the use of very high purity ($\approx 98\%$) CMs following metabolic¹¹⁵ or surface marker-based selection¹¹⁸.

A pure population of human CMs lets us focus on the goal of cardiac tissue engineering: reproducing *in vitro* the contractile forces generated by adult human cardiac tissues. To do this, I seed human CMs onto the optimal substrate identified in chapter 3: 6 mg/mL COL1 hydrogel patterned with 20x20 FN lines. I first characterize the alignment of the CMs relative to the FN lines and found that it varied significantly as the thickness of the tissue, and the distance to the FN pattern, increased. I adapted the MTF assay^{10,26,116,117} by cutting the patterned hydrogels into rectangular shapes that could be peeled of the underlying coverslip and electrically stimulated. I measured the stresses generated by single cardiac sheets under different stimulation rate. Finally, I demonstrated the creation of 3D multilayered cardiac constructs by stacking up to 4 individual cardiac sheet. Double layer constructs could also be used in the thin film assay to measure stresses under stimulation.

This chapter demonstrates the use of the hydrogel patterning technique to grow functional human cardiac muscle *in vitro*, with results on par with the literature. Beyond the ability to engineer and stack cell sheets, I can, for the first time, encode ECM cues with micrometer precision into a 3D construct. This study will lead to the creation of complex biomimetic scaffolds and will allow

researchers to leverage the role of specific ECM patterns, well understood in 2D, toward building better 3D cardiac tissue.

5.3 Materials & Methods

5.3.1 *Stem cell culture and differentiation*

I use the human embryonic stem cell line HES3 given generously by the laboratory of Prof. Peter Van Der Meer at the University of Groningen, Netherlands. The line has been modified to express GFP – Nkx2.5, which is an early marker of cardiac progenitors, but is not used for this purpose in our study. Maintenance culture is carried out on Matrigel (GFR Matrigel, Corning) in Essential 8 Medium (E8 - ThermoFisher, #A1517001) with 1:1000 Mycozap (Lonza). At day -3, HES3 cells are seeded at 215,000 cells per well in a 6 well plate (Figure 5.1A). At day 0, when cells reach $\approx 75\%$ confluence, they are washed with PBS and the media is changed to RPMI 1640 (ThermoFisher, #11875093) with B-27 supplement minus Insulin (ThermoFisher, #A1895601). The first day, 100 ng/mL of Activin A, 10 ng/mL of FGFb, 3 μ M CHIR99021 and 1% v/v Knockout Serum Replacer (KSR) are added. At day 1 of differentiation, the cells are washed then the media is replaced with fresh RPMI/B27 and 5 ng/mL BMP4, 5 ng/mL FGFb. After the 9th day of differentiation, cells are grown in Chemically Defined Medium with 3 components (CDM3¹¹⁵) made of RPMI

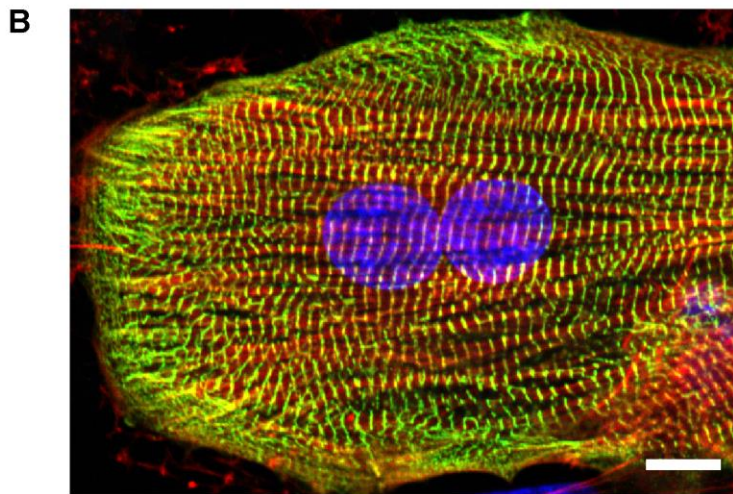
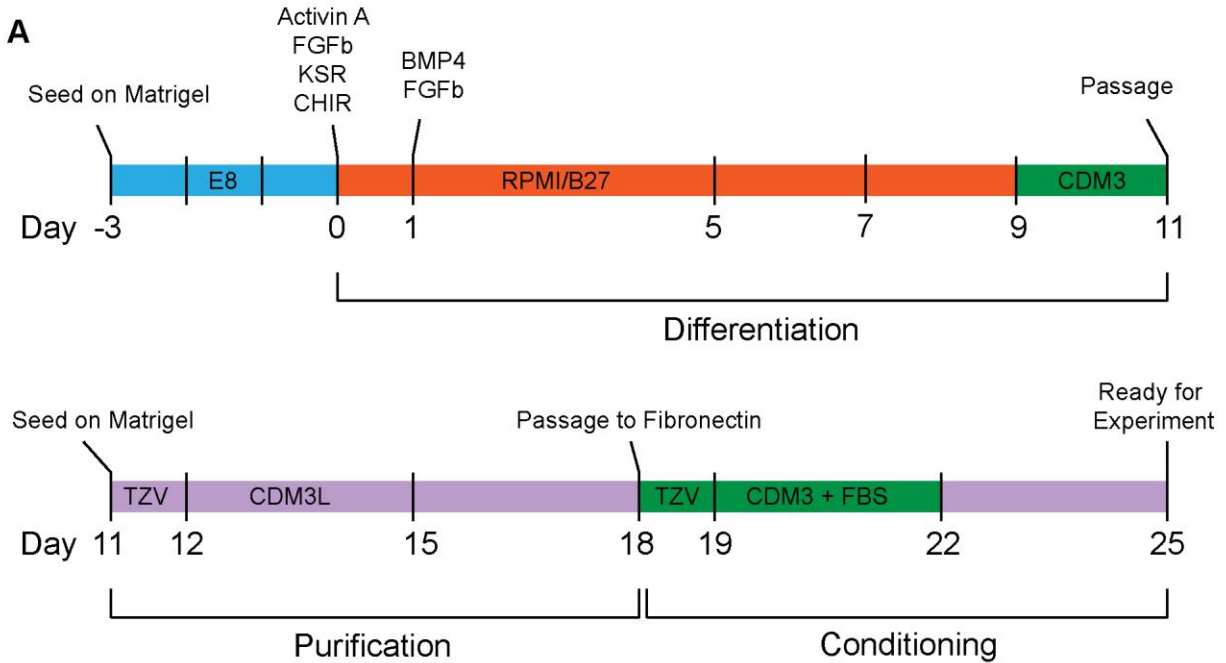


Figure 5.1. Stem cell differentiation, purification, and conditioning.

(A) Timeline of stem cell culture and differentiation. E8 (blue) = Essential 8; CDM3 (green) = Chemically Defined Medium with 3 components; TZV = addition of 2 μ M of thiazovivin to the medium. CDM3L (purple) = CDM3 without glucose and with sodium DL-lactate; RPMI/B27 (orange) = RPMI 1640 Medium without Insulin + B27 supplements; FBS = addition of 10% Fetal Bovine Serum to the medium. The total process takes 28 days. (B) Image of purified HES3-derived CMs grown for 4 days on COL1 hydrogel stained for nuclei (blue), actin (red), α -actinin (green). Scale bar = 10 μ m.

1640, 500 μ g/mL *O.sativa*-derived recombinant human albumin (Sigma-Aldrich, #A0237), and 213 μ g/mL L-ascorbic acid 2-phosphate sesquimagnesium salt hydrate (Sigma-Aldrich, #A8960).

After differentiation, the cells are dissociated with TrypLE Express Enzyme (ThermoFisher, #12604021) at 37°C for 15 min. Differentiated cells are then centrifuged at 200g for 7 min and resuspended in CDM3L : CDM3 with RPMI 1640 without glucose (ThermoFisher, #11879020) and 5 M sodium DL lactate. CDM3L enables metabolic purification of the cell population as only CMs can use sodium DL lactate as an alternate source of energy. 2 μ M thiazovivin (TZV) is always added for the first 24 hrs after passaging CMs. After a week of purification, CMs are passaged to plates that were liquid coated with FN (30 μ g/mL in 1 mL per well for 1 hour at room temperature). 10% fetal bovine serum (FBS) is added to CDM3 to allow the cells to attach and spread for the first 4 days. After one week of conditioning on FN, the cells are ready to be used for an experiment. Conditioning on FN is essential for the cells to be able to adhere to the hydrogel scaffolds. Purified CMs develop large myofibrils and beat spontaneously starting after 10 days of differentiation and until at least 50 days in culture (Figure 5.1B).

For each batch of cells, a preliminary experiment was carried out to determine the optimal cell seeding density which was between 275,000 and 350,000 cells / cm². The surface area seeded for each hydrogel was limited to 0.76 cm² by using a ring made of the cut core of a 1.5mL microcentrifuge tube and a slab of PDMS (1:10 Sylgard 184 to Sylgard 527). Thus, cells were counted before centrifugation at 200g for 7 min, then resuspended to reach the appropriate density in 400 μ L of CDM3 + TZV + 15% FBS per sample. The day after seeding and every three days thereafter, the medium is replaced with CDM3 + 10% FBS. The ring of PDMS is removed after the first day.

5.3.2 *Stacking cardiac sheets*

Two days after seeding, cardiac sheets are gently peeled off the glass coverslip and transferred with a spatula above another cardiac sheet in a well without medium. The cardiac sheet is flushed off the spatula with 200 μ L of fresh CDM3/FBS medium. Then the sheets are delicately aligned. For the 4-layer constructs, each round COL1 hydrogel had a thin section cut off to mark the orientation of the FN pattern before seeding. The cardiac sheets are kept in contact using a block of 1% agarose (1cm x 1cm) which had been incubated at room temperature with CDM3/FBS for 1 hr prior. About 500 μ L of CDM3/FBS are immediately added to the well and the samples are incubated for 2 hrs. Then, 1 extra mL is added to each well. The agarose block is removed the next day and medium changed. To build 4-layer constructs, a layer was added every day.

Double-sided hydrogels were prepared in two steps. First, a PIPAAm coverslip with FN lines is set on a hot plate at 37° C. Quickly, a COL1 solution is prepared and pipetted on the warm coverslip, then the coverslip is immediately put in the incubator. This step is very sensitive: if the collagen solution is too cold, PIPAAm dissolves too fast and the FN pattern is lost, if the coverslip is too warm, it will denature collagen I. After 1 hr in the incubator, the Fastwell is removed and the gel left to dry in the biohood (see Chapter 4). The orientation and quality of the FN lines are marked using confocal microscopy. Then another pattern of FN lines is transferred on top of the hydrogel using gelatin as described earlier.

5.3.3 Muscular thin film assay

After drying the round COL1 gels, a rectangular shape was carved out of half of the disc (\approx 2.5 mm wide by 4 mm long) (Figure 5.2). Great care was paid to aligning the FN pattern on the gelatin gel with the length of the rectangular thin film of collagen I. Then, the gelatin was melted and the samples prepared as described in Chapter 4. After four days of culture, medium was removed and replaced with 37°C Tyrode's solution. A blade was used to gently cut the cells around the thin film. A picture taken at this stage was used to measure the length of the rectangular piece of collagen I. Finally, the rectangular piece of the cardiac sheet was peeled off the underlying glass coverslip with tweezers. Most samples would contract spontaneously.

For the MTF assay, samples were left to equilibrate in Tyrode's for 30min. Then I used a heated stage custom-built by Rebecca Duffy and TJ Hinton to keep the sample at 37°C while on the stage of a stereomicroscope mounted with a DSLR camera. I used a Grass stimulator (Grass Technologies) linked to two parallel platinum electrodes immersed in Tyrode's to pace the sample using field stimulation. All samples were stimulated at 50 V, using a square wave with a duration of 10 ms. I recorded 15 s of spontaneous contractions, then 15 s at each 1 Hz step from 1 to 5 Hz. The .mov files were converted to AVI and opened using ImageJ. I tracked the tip of the thin film over five contractions for each step as described elsewhere^{116,119}. By measuring the length of the projection of the bent MTF, I can deduce the radius of curvature. I adapted a Matlab code originally written by Grosberg *et al.*¹⁰⁶ to calculate the stress developed by the cells as a function of curvature, cell thickness, substrate thickness and stiffness. To calculate twitch stress, I subtracted the fully relaxed stress (at diastole without electrical stimulation) from the peak stress under stimulation.

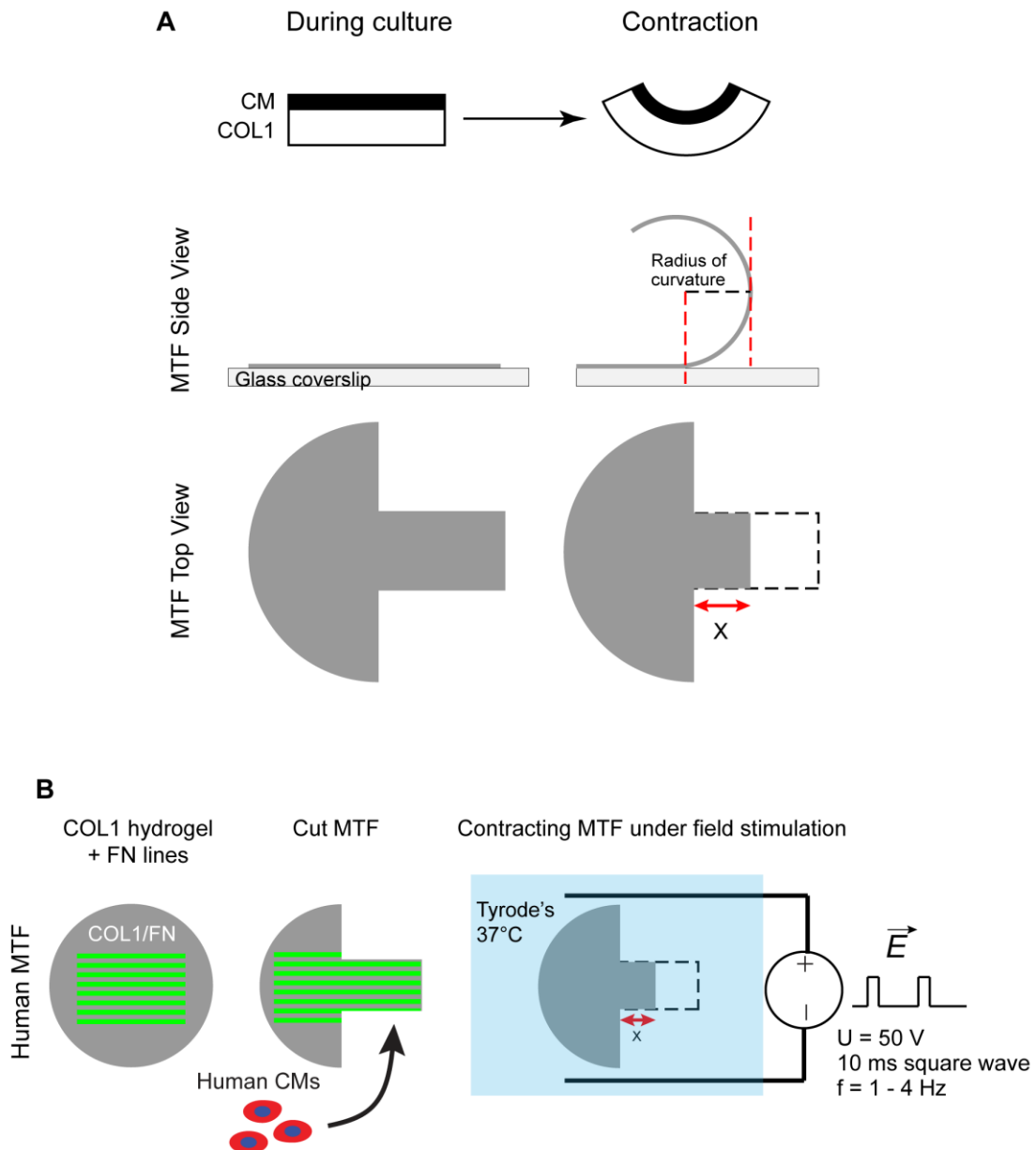


Figure 5.2. Measuring contractile forces using the muscular thin film assay.

(A) Schematic of the MTF assay. A bi-layer thin film made of a contractile cell sheet and elastomeric substrate bends when the cells contract. The radius of curvature can be estimated by measuring the projection X when imaging the MTF from above, then used to calculate cell-generated stresses. (B) Schematic of the setup used in this dissertation. COL1 hydrogels patterned with FN lines were cut to rectangles then seeded with human CMs. After culture, stresses were measured under field stimulation at different rates.

5.3.4 Immunohistochemistry and fluorescence microscopy

After culture, samples are fixed in PBS with calcium, magnesium, and 4% formaldehyde for 15 min. Samples were then incubated for 30 min with PBS and 10% bovine serum albumin (BSA) for blocking. For single sheets, each staining incubation was carried out at room temperature for one hour while multilayer constructs were incubated overnight at 4°C. Primary staining consisted of PBS with 10% BSA, and 1:200 mouse anti-sarcomeric α -actinin antibodies. Secondary staining had 1:200 Alexa Fluor 488 goat anti-mouse, as well as 3/200 Alexa Fluor 633 Phalloidin. Three washes of 5 min in PBS were carried out after each incubation. 1 drop of NucBlue was added to the second wash after the secondary stain to stain nuclei. Samples were mounted on microscope slides with Prolong Gold Mounting reagent. Immunostained samples were imaged with a Zeiss LSM700 laser scanning confocal microscope using a 20x objective (NA = 0.8).

5.3.5 Orientational order parameter analysis

The analysis relied on the same algorithms described in Chapter 3 to determine the orientational order parameter using Matlab (see Appendix B). However, to better determine the effect of the distance to the patterned FN, the calculations were made for each slice of each z-stack and not on maximum intensity projection. The parameters measured are: mean, standard deviation, median, and mode of the actin orientation angles, OOP, and CM coverage. To manipulate the complicated data (6 experiments x 3 samples x 6 fields of view x 6 slices x 8 statistics), I exported the results to a PivotTable in Microsoft Excel. CM coverage was used to calculate the average thickness of the tissue.

I summed CM coverage for each slice in z of the field of view and divided by the total area of the field of view. This is the equivalent thickness of the same volume of CMs filling the entire surface area.

5.3.6 Characterization of collagen type I hydrogels

COL1 hydrogels were made by batch of 6 hydrogels. Up to 4 batches were made on the same day. At least two COL1 gels per day were selected as controls. They were treated as the FN-patterned samples: gelatin was melted then washed off and the controls were UV treated for 15 min.

To measure thickness, controls were then mounted on a microscope slide in PBS with a Fastwell silicone ring. I acquired 3D z-stack using second harmonic generation of COL1 at 830 nm excitation with a Leica SP5 multiphoton microscope and a 25x water objective (NA = 0.95). Using ImageJ, I measured the thickness of the COL1 hydrogels in cross-sections of three field of view per sample.

To measure stiffness, Rachele Palchesko-Simko and I used an MFP-3D-BIO atomic force microscope (Asylum Research) with nitride probe and a pyramidal tip (TR400PSA, Asylum Research) to obtain force curves during indentation at three different locations per sample. I fit the curves with the Hertz model to estimate the Young's modulus of the hydrogel^{120,121,125}.

5.4 Results & Discussion

5.4.1 Growth and alignment of human cardiac sheets

HES3-CMs purified then conditioned on FN adhered well on COL1 hydrogels. After four days in culture, they formed highly contractile cardiac sheets. I imaged the actin cytoskeleton and measured the orientational order parameter. When looking at a projection of the whole thickness of

the tissue, alignment seems very poor; bright actin fibers with poor alignment at the top of the tissue hide the dimmer aligned fibers at the bottom. So I measured OOP as a function of depth inside the tissue, starting at the very bottom, in direct contact with the FN pattern (Figure 5.3). In a representative sample, OOP = 0.69 just 1 μm away from the FN pattern, with the histogram of actin orientation angles showing a nice peak, and decreases to OOP = 0.4 4 μm above the FN pattern (Figure 5.3 A). This is partly due to the preference human PSC-derived CMs have for cell-to-cell over cell-to-substrate interactions. I often observed cells initially spreading after a day on the substrate before aggregating together when cell density increases. Instead of a tissue with an even thickness, this creates valleys and mounts where the peaks are far removed from the substrate and are highly isotropic (see 4 μm image, Figure 5.3 A). This corresponds to previous findings that the alignment of CMs with a substrate quickly decreases with distance from the substrate¹²². For all experiments, sample thickness ranged from 3 μm to 6 μm so that the $n = 21$ for $z \in [0 - 3]$, $n = 18$ for $z = 4$, $n = 9$ for $z = 5$, and $n = 4$ for $z = 6$ (Figure 5.3 B). There is considerable variability of OOP between each batch of differentiated CMs: for example samples from experiment 1 all have high OOP while experiment 3 samples have very low OOP. Significant improvement of the cell source can be made to promote reproducible alignment.

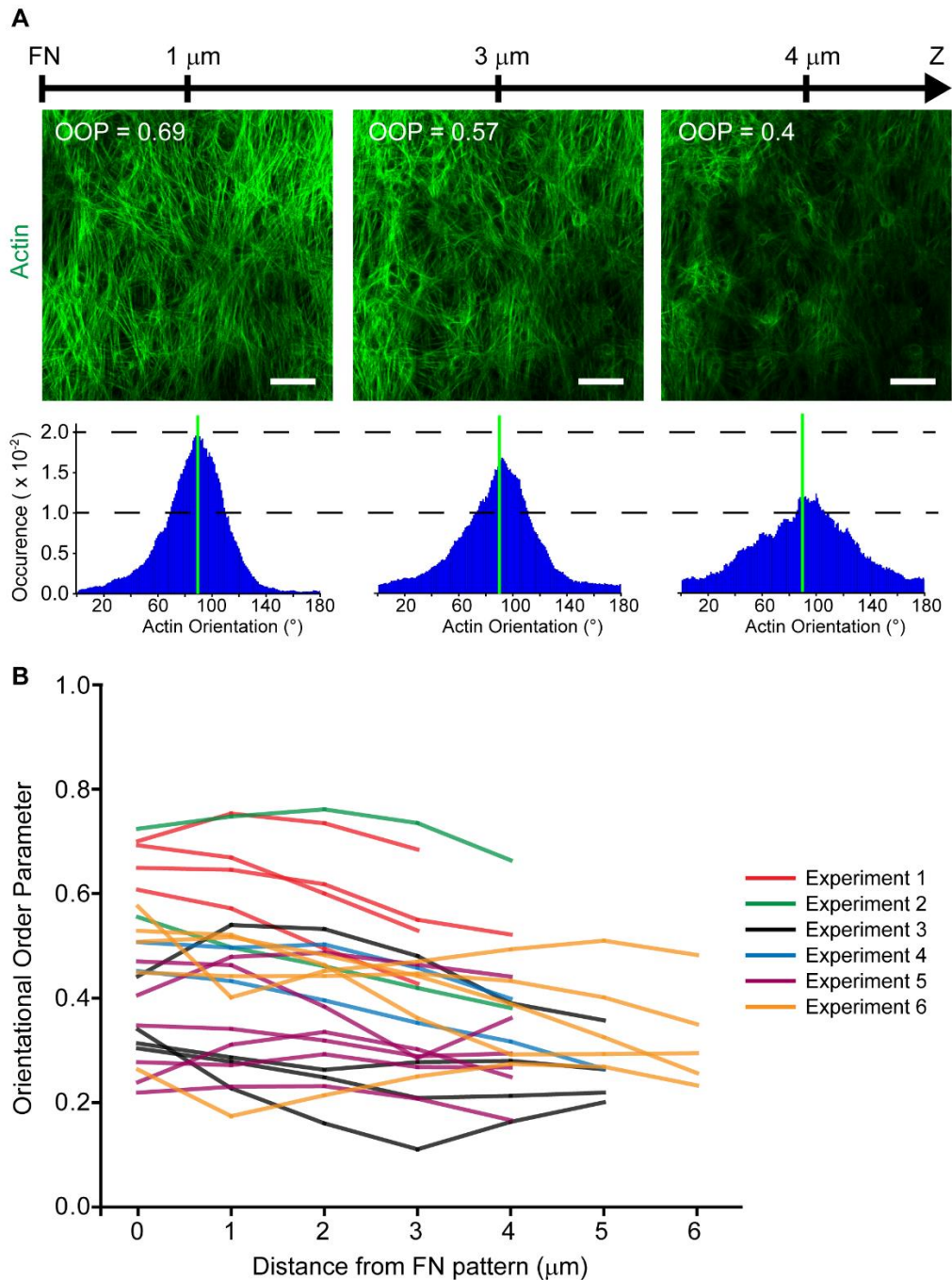


Figure 5.3. Alignment of human cardiomyocytes on collagen I hydrogels micropatterned with fibronectin lines.

(A) Illustration of the decrease of OOP with increasing distance from FN pattern. 1 μm above the FN pattern, the actin cytoskeleton is well aligned with OOP = 0.69 and a sharp peak in the histogram of actin orientation angles centered on the FN lines (green line). As we look deeper into the tissue and reach 4 μm from the FN lines, OOP decreases to 0.4. Scale bars are 50 μm . (B) Graph of OOP as a function of distance from the FN pattern, shown for each sample, with experiment color code. There is great overall variability but small variability within each experiment. For example, all samples from experiment 1 have OOP > 0.6 and all samples from experiment 5 have OOP < 0.5. N = 23.

The capacity of CMs to adhere, spread, and align on the FN-patterned collagen I hydrogels was found to be highly dependent on the cells used. First, I selected the HES3 line for these experiments after trying out two other cell lines (an iPSC line obtained from the laboratory of Prof. Wu at Stanford, and a HUES9 cell line from Dr. Peter Van den Meer) that were unable to align or even spread consistently on our substrates (data not shown). Second, differences from batch to batch account for most of the spread in OOP. Finally, proper conditioning is essential: cells used directly after purification without conditioning could not adhere to the substrates and conditioning on gelatin or COL1 led to completely isotropic tissues. Thus, a systematic investigation of CMs derived from many cell lines, with a focus on OOP and integrin expression, could help shed light on what drives a specific cell line to align to ECM patterns. Conditioning can also be optimized by varying protein concentration, or protein composition. Finally, while FN plays an important role in the embryo and during cardiac morphogenesis, there are many spliced variants, not all of them with knockouts that are embryonically lethal^{79,123,124}. So the choice of patterned ECM could be further refined by selecting a stage-matched FN, which cells from a specific line, with a certain conditioning, expressing the appropriate integrins, would best align to.

Furthermore, the long term structure and function of cardiac sheets depends on the continuous remodeling of the ECM. I expect human CMs, and the small percentage of non-CMs in the cell population, to slowly remodel the FN pattern and the underlying COL1 hydrogel as well as produce their own ECM. Over the time required for muscle maturation (2 to 3 weeks), the FN pattern will be modified and the ECM composition change, which could potentially decrease alignment. In this work, I did not notice significant changes in the FN pattern or COL1 hydrogel after up to 7 days in culture.

However, long term observation is required to determine the extent of ECM remodeling with human CMs culture.

5.4.2 Measuring contractile force generation with the muscular thin film assay

Contractile force generation is the major criteria by which to compare engineered cardiac tissues with human adult cardiac tissues. To measure the stresses generated by the HES3-CMs, I adapted the MTF assay^{26,102}: the FN-patterned COL1 hydrogels were cut into rectangular strips before seeding; the strips can be peeled off the glass coverslip and contract when stimulated by an electric field. I can then measure the radius of curvature of the strips and deduce the stresses generated by the cell layer. To do this, I first studied the mechanical properties of the COL1 hydrogels. I measured their stiffness using AFM and their thickness using multiphoton microscopy. For their Young's modulus, I found that the variability within one sample was greater than batch-to-batch variability (Figure 5.4 A). The modulus was 280.3 ± 79.9 μm for all samples (Table 5.1). The thickness of the COL1 gels was 21.2 ± 2.6 μm across all batches (Figure 5.4 B). For all following calculations of contractile forces, I used the modulus and thickness measured for the same batch of COL1 hydrogels.

Date	Thickness (μm)	Young's modulus (kPa)
1/15/2016	-	279.4 ± 70.2
1/29/2016	21.9 ± 1.4	253.9 ± 59.1
2/1/2016	19.6 ± 2.2	284.5 ± 88.3
2/6/2016	23.0 ± 2.3	299.9 ± 92.4

Table 5.1. Young's modulus and thickness of collagen I hydrogels made on different days.

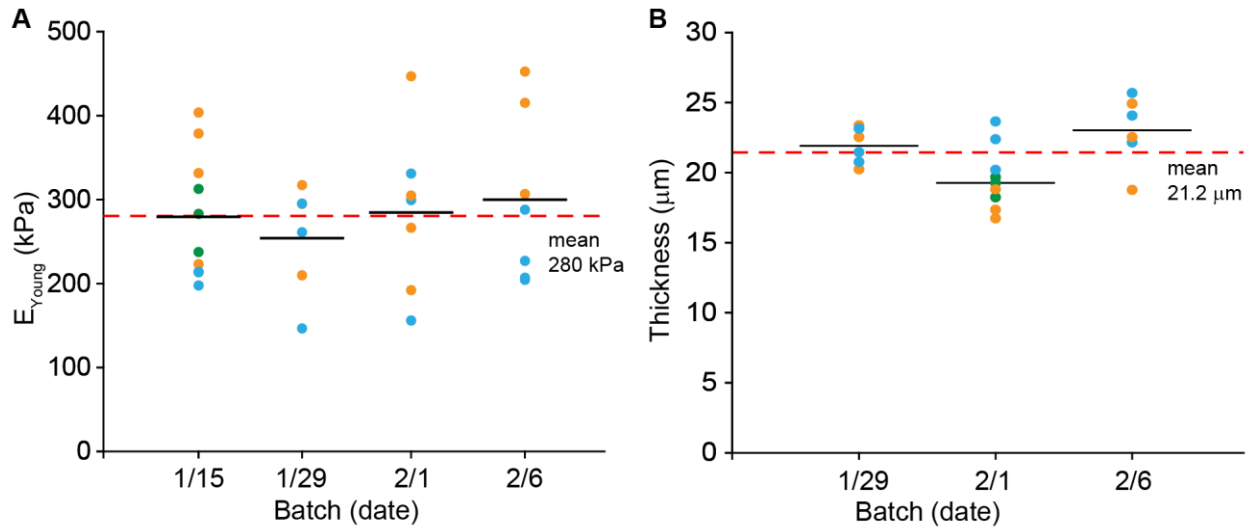


Figure 5.4. Young's modulus and thickness of COL1 hydrogels.

(A) Dot plot of the Young's Modulus measured using the AFM. Each dot is a different measure; measures from the same day with the same color are from the same sample. The mean of each batch is indicated with a black line while the overall mean is the red dotted line. (B) Dot plot of COL1 thickness. At least two samples per batch were assessed for (A, B) and three measures per sample.

I used a DSLR camera to capture the contraction of the MTFs under dark field illumination.

The movement has a large amplitude (Figure 5.5 A), which is visible with the naked eye. The peak stresses generated by the samples range from 2.6 kPa to 28 kPa (Table 5.2). All samples exhibited decreasing amplitude as the rate of stimulation increased (Figure 5.5 B). Twitch stress (peak stress minus fully relaxed stress) varies little as the rate increases across all samples (Figure 5.5 C).

Sample	1 Hz	2 Hz	3 Hz	4 Hz
1	27.1	28.3	25.6	21.1
2	6.9	6.7	6.7	6.1
3	2.6	2.5	2.9	3.5
4	17.6	17.9	18.7	19.9
5	16.9	15.7	16.4	17.3

Table 5.2. Twitch stress of cardiac MTF under stimulation (kPa).

However, there is a lot of difference between samples. The precision can be improved by fixing and staining samples right after stimulation to correct for differences in CM coverage and thickness. In many samples, the amplitude of contraction was too large and led the tip of the film to roll back and hit against the main body of the sample. This effect limits the total amplitude of contraction and the samples were removed from the analysis. Thus, I anticipate that repeating the experiment with shorter thin films would prevent the film from rolling back on itself and provide measurement of even higher stresses.

I find that the stresses measured are in the range observed by others using human ESC-derived CMs (11.8 kPa active stresses were reported in fibrin-based cardiac patches by Bursac *et al.*⁹⁰, 4 kPa was reported in 3D tissues made from cardiac bodies by Kensah *et al.*¹²⁶). The values measured in this study also compare positively to published literature using neonatal and adult rat cells^{10,116,127}. They are of the same order of magnitude as active forces measured in human adult heart (20-45 kPa¹²⁸). However, I did not observe the positive force-frequency relationship of human myocardium: in the adult left ventricle, isometric twitch tension was measured at 15 kPa at 1Hz, and increased with frequency until a peak of 44 kPa at 2.9 Hz¹²⁸. It is likely that our MTF will require long term maturation before exhibiting the same force-frequency response. Moreover, in our system, the contraction is auxotonic: as during the heart's beating, the contracting CMs shorten against an increasing load. The frank-starling law governs pressure-volume in the heart during the contraction cycle. At the scale of individual cells, it is seen as the increase of the active stress generated by a CM when its resting length increases¹²⁹. Here, as the frequency increases, the MTF does not have time to reach its relaxed state and so each contraction starts with already shortened CMs.

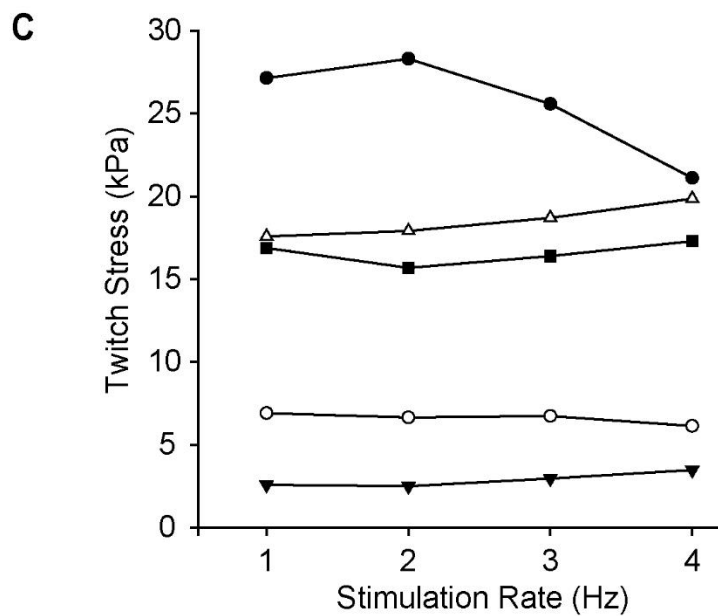
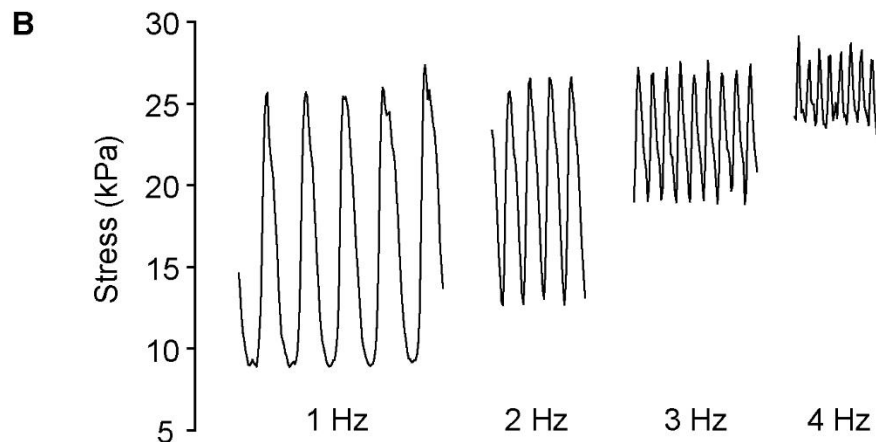
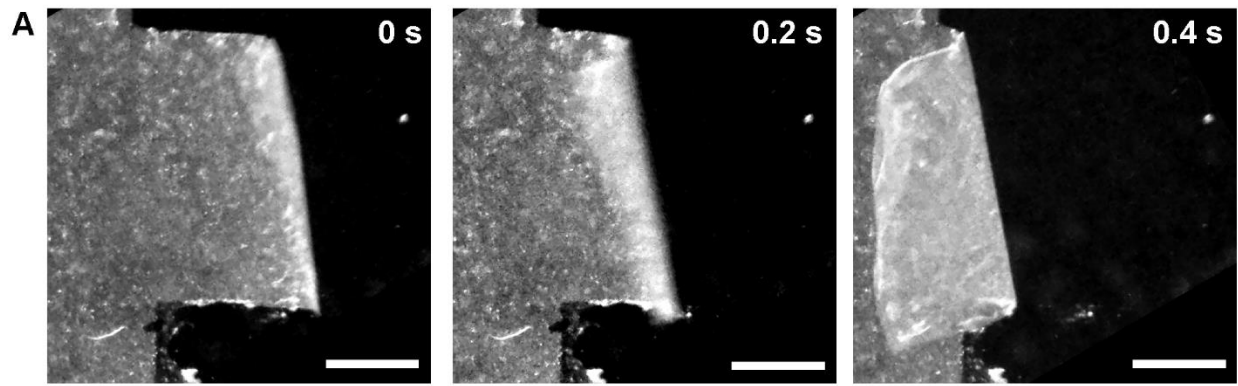


Figure 5.5. Contractile force generation by cardiac sheets under field stimulation.
 (A) Still frames of a sheet of CMs seeded on a FN-patterned COL1 hydrogel at 0s, 0.2, and 0.4 s of contraction, paced at 1 Hz. Scale bars = 1 mm. (B) Graphs of stress vs. time for the sample in (A) at 1, 2, 3, and 4 Hz. (C) Graph of twitch stress (Peak minus relaxed stress) showing mean \pm standard deviation for $n=5$ samples stimulated at 1 to 4 Hz.

As others have noted¹³⁰, there is no definitive method to compare forces generated by engineered cardiac constructs across different modalities. So it is important to understand the limitations of this assay. First, the very strong curvature of the samples stretches the limit of the model which works best for small radii of curvature. Second, although using AFM force curves to measure the Young's modulus of a hydrogel is a well-established technique in the literature^{121,125,131}, it is not a direct predictor of the mechanical behavior of the hydrogel at the tissue scale: in particular, the Young's modulus of individual COL1 fibrils assessed by AFM reaches $\approx 5-10$ GPa¹³¹, 3 orders of magnitude above what I measured for the hydrogel. Further, collagen fibers reorganize under strain so that strains measured locally always underrepresent global strains¹³². I could improve the model by taking into account the increased complexity and non-linearity of the COL1 hydrogel compared to PDMS.

5.4.3 Stacking micropatterned hydrogels to create multilayered cardiac constructs with precise control of the 3D geometry of ECM cues

To build 3D cardiac constructs, I seeded individual substrates then stacked them one-by-one to leave time for the cells to adhere to the COL1 hydrogel from the layer above. I found that up to 4 layers can be stacked (Figure 5.6). To demonstrate that the orientation of each layer can be controlled, I create parallel and orthogonal stacks of cardiac sheets (Figure 5.6 A and B respectively). I found that with practice I could achieve a final orientation within 10° of the intended orientation. Yet, moving and aligning the layer with tweezers and spatula can cause defects (Figure 5.6 A – Top View). The final construct is composed of about 15% cells and 85% COL1 hydrogel in volume (Figure 5.6 C). However, I found that cells in stacked

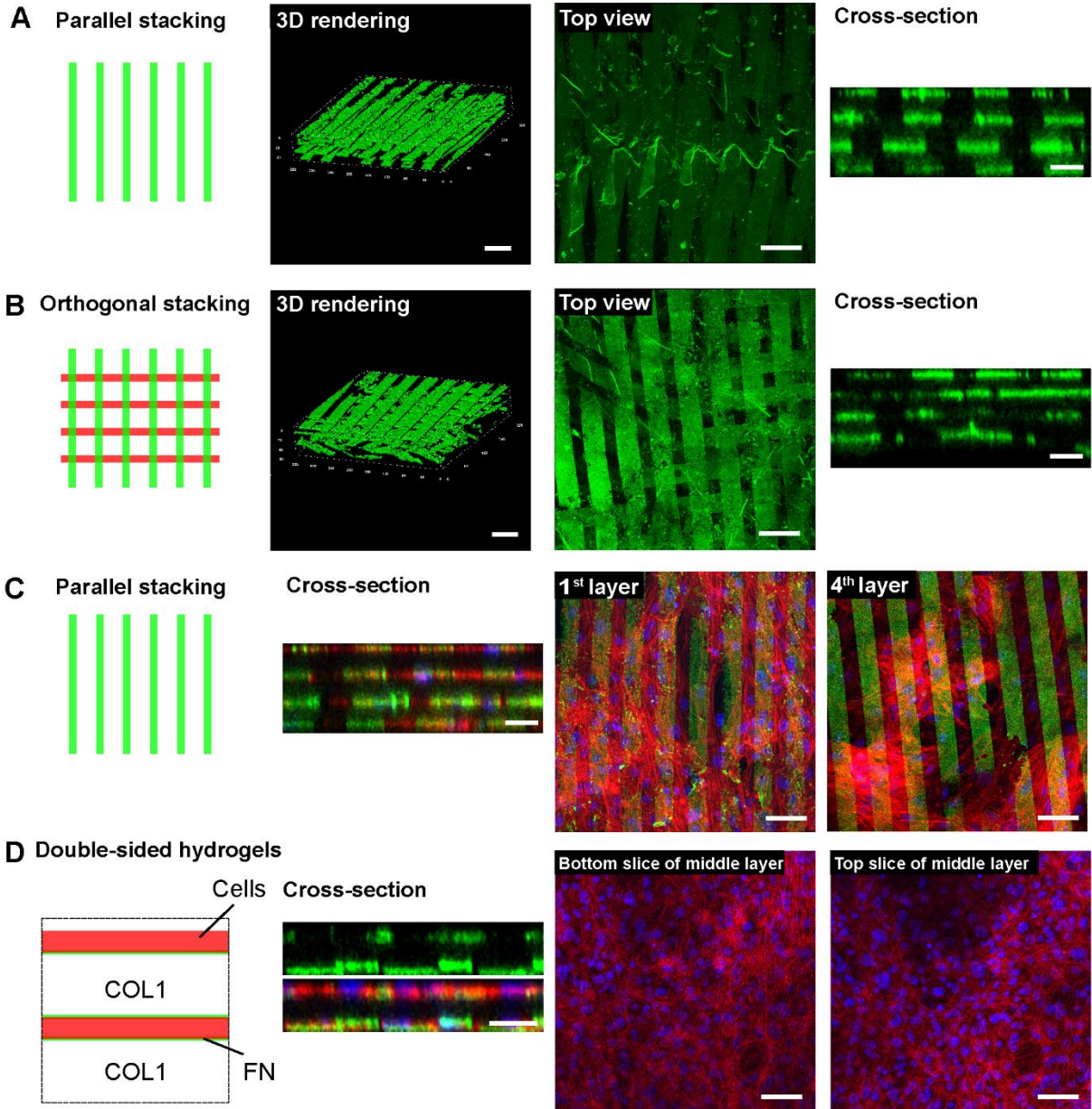


Figure 5.6. Creation of multilayered cardiac constructs. Individual cardiac sheets can be stacked one by one to reach four. (A) and (B) show the FN in parallel and orthogonal stacks respectively. (C) Cells in a parallel stack show poor alignment on the top layer. (F) FN lines patterned on both sides of the hydrogel do not improve alignment. Scale bars = 20 μm for all cross-sections, 50 μm for all other images.

constructs were poorly aligned. There are two likely causes. The first is that stacking requires longer culture time, and each layer spends a different amount of time as a single layer. CMs that stayed in culture on the substrate too long were prone to aggregating or detaching. This would explain the bright

clumps of cells in the top layer, which was added last (Figure 5.6 C - 4th layer). Second, the cells in the middle are presented with FN lines below but a homogenous COL1 hydrogel above. This contributes to the loss of alignment.

To promote CM alignment, I created COL1 hydrogels with micropatterned FN lines on both sides (Figure 5.6 D). Two-layer constructs made with these double-sided gels displayed directional ECM cues above and below the cell layer. However, looking at single slices at the bottom and at the top of this cell layer, I observe the same behavior occurring with individual cardiac sheets: the actin cytoskeleton is aligned at the bottom but near isotropic at the top of the cell layer, despite having FN lines on both sides. I hypothesize that the CMs gain their orientation within the first two days of culture, during which they actively reorganize their cytoskeleton. When I stack the cardiac sheets after two days, the CMs have already settled and the addition of FN lines on top of the tissue is not enough to force their reorientation. This indicates that if I can improve the initial alignment of individual cardiac sheets, stacking will not decrease significantly.

5.4.4 Multilayered constructs can be used in the muscular thin film assay

Double-layer constructs could be used in the MTF assay. In this system, the inner cell layer contributes some negligible shortening while the top cell layer is responsible for the bending of the thin film. I calculated the stresses generated by the construct by modeling the thin film as a single layer of cells on top of a COL1 hydrogels twice as thick. I observe a similar trend that with single layer constructs: peak stress increases with stimulation rate (Figure 5.6 A). Due to the small amplitude of contraction, fluctuations due to manual tracking accuracy introduce visible noise in the signal (Figure

5.6 B). Further experiments are required to determine if twitch stress is always lower in multilayer constructs.

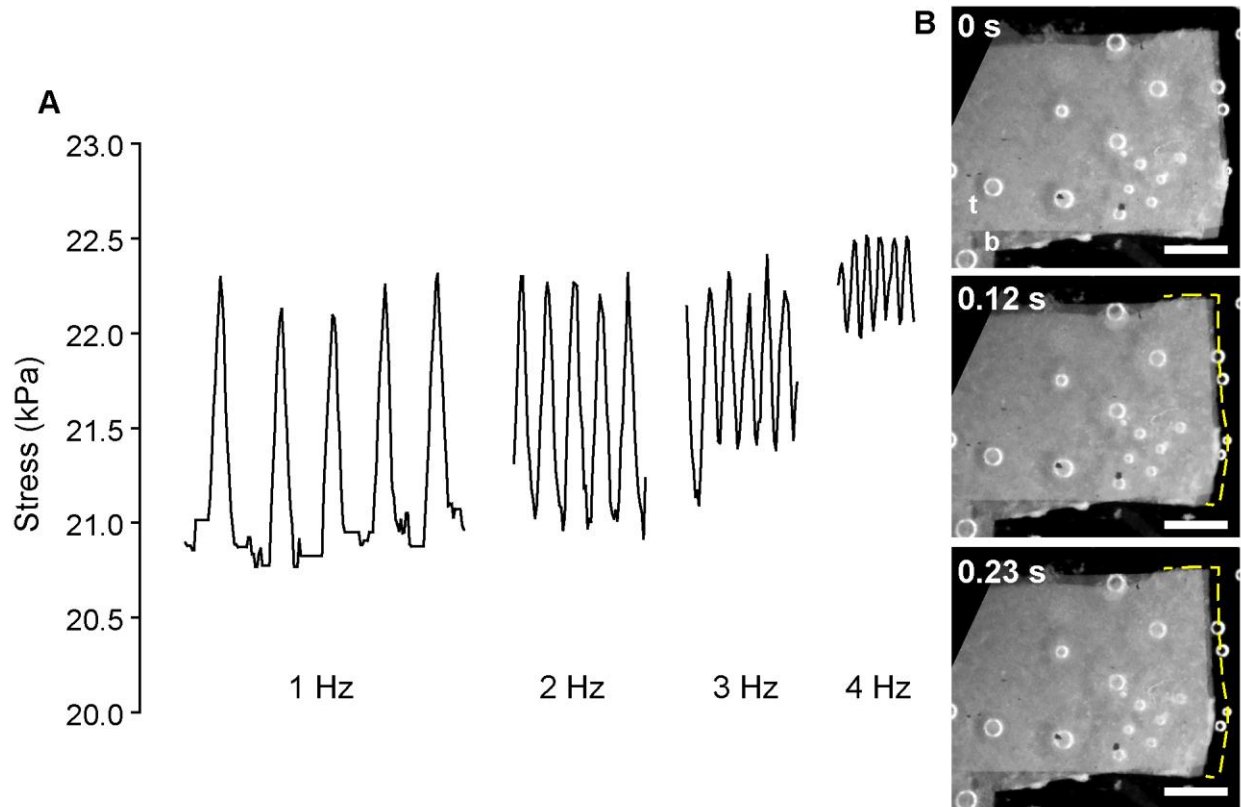


Figure 5.7. Stimulated contraction of two-layer cardiac constructs. (A) Graph of the stresses generated during contraction of a double layer construct under different stimulation rates. (B) Dark field images show the amplitude of the contraction. At 1Hz, the contraction between 0 s and 0.23 s is seen by comparing to the yellow dotted outline (sample at 0s). Scale bars = 1 mm.

Being able to characterize the contraction mechanics of multilayered constructs with this well-established assay will enable the study of more complex cardiac structures. The orientation in the myocardium is not constant across the thickness but shifts by $\approx 90^\circ$ between the epicardium and endocardium¹⁵. This shift is essential to organ function. The immediate next step is to stack cardiac sheets at varying angles to mimic the heart's native structure and study their contraction under different stimulation rate.

5.5 Conclusion

In this chapter, I applied the platform built in chapter 3 toward building physiologically relevant human cardiac tissue. Human PSC-derived CMs aligned on the optimal high concentration COL1 hydrogel micropatterned with 20x20 lines of FN. To obtain consistently high alignment, the source of CMs must be optimized with care (cell line, method of conditioning, reproducibility from batch to batch). I adapted the MTF assay to measure contractile stresses generated by single layer cells under electrical stimulation. Individual layers can be stacked with good accuracy to create 3D cardiac constructs. And in a first, I was able to measure contractile forces generated by a multilayer cardiac tissue. Although more work remains in order to be able to stack 4-layer constructs with good alignment throughout, this study will enable the creation of 3D cardiac constructs with biomimetic orientation and the characterization of their contractile properties.

Chapter 6 Summary and future directions

6.1 Summary

In this dissertation, I proposed for a new paradigm for cardiac tissue engineering: we are using human PSC-derived CMs, which are embryonic-like cells, to replicate *in vitro* the process of myogenesis, which only occurs in the human embryo; so we need to learn from the embryo and, in particular, from the ECM of the embryonic myocardium. Building scaffolds to follow the template of the embryonic ECM requires more applicable knowledge of its structure and composition and a new fabrication technique that can encode ECM cues in 3D with micrometer precision. In chapter 3, I derived a set of structural parameters that can be used to build biomimetic scaffolds: 0.5 μm diameter FN fibers, 1 μm long, organized in bundles spaced every 4-8 μm . In chapter 4, I leveraged surface-initiated assembly to micropattern FN lines onto hydrogels. I showed that the technique was accurate and reproducible, and optimized hydrogel composition to maximize chick CMs alignment. In chapter 5, I created human cardiac sheets using ESC-derived CMs. The human tissues generated strong contractile forces in this first implementation of the MTF assay using natural hydrogels. Finally, I showed that our system can be used to study the contractility of multilayered cardiac constructs and even achieved 4-layer tissues. These results pave the way to the design of complex embryo-mimetic ECM scaffolds to engineer mature and functional human cardiac muscle *in vitro*.

6.2 Limitations and future directions

The techniques developed here cover the essential steps to building biomimetic ECM scaffolds. The immediate goal for future work should be to test our hypothesis: an artificial pattern of FN and LAM matching the parameters defined in chapter 3 should be seeded with human CMs for long term culture; maturation and function should be assessed by measuring contractile force generation, calcium handling, and gene expression.

To do this, the cell source needs to be optimized. Different cell lines should be tested, with different conditioning methods, and their integrin expression analyzed. A better understanding of the mechanisms driving cell alignment on our scaffolds will enable the growth of more aligned 3D constructs. Second, the stacking protocols need to be improved to achieve a high reliability and a better control over the final 3D architecture of the micropatterned ECM cues. Additional experiments to study the contractile force generation of multilayer constructs are also required to determine how it can be related or predicted by single layer mechanics.

To fully test our hypothesis, a single experiment will not suffice. In this dissertation, I tackled each challenge separately : ECM analysis, micropatterned scaffold fabrication, and creation of human 3D cardiac tissue. However, each part needs to be considered with the whole goal in mind. First, I carried out the analysis of the ECM without knowing what parameters and features are actually the most impactful: does FN fiber length matter? Is it just secondary to fiber diameter and spacing? Would CMs sense the difference between 0.4 and 0.6 μm diameter? What is the appropriate resolution? These questions can only be answered by starting a cyclic approach to scaffold design: a range of parameters should be tested *in vitro* and the results used to further refine the ECM analysis, in order to create

better scaffolds, etc.... I hope that this work enabled the quick-cycle experimentation toward the fabrication of functional cardiac tissues and the generation of applicable knowledge and proven scaffold design principles.

While I attempt to create a new path for cardiac tissue engineering, there is a lot to learn from already successful 3D approaches. Electrical and mechanical stimuli are very potent tools to improve contractile force generation of engineered cardiac muscle. Long term culture, and biochemical cues (i.e. growth factors) have also been used successfully to promote cardiac maturation¹². Achieving the growth of adult-like myocardium *in vitro* will require the synergistic use of all types of inputs, beyond the biomimetic ECM cues I have focused on. I expect that biomimetic scaffolds inspired by the embryonic ECM will be seeded with human CMs, then incubated in a bioreactor providing perfusion and oxygen as well as a combination of electrical and mechanical stimuli, for several weeks.

Finally, I take a look back at the original hypothesis: ECM cues in terms of structure and composition can guide embryonic-like cells to form mature and functional tissue. Our experience with human stem cells and cardiac differentiation has demonstrated the difficulty of assigning an exact stage to the phenotype of these cells. They are neither adult nor embryonic. While they share the plasticity we expect from embryonic cells, they do not recognize FN without first being conditioned to it. This requires a change of perspective: we need to provide immature cells with immature ECM cues. I expect that this problem will need to be approached from both ends, to find the middle ground where the cells can best read the ECM cues presented to them, and those ECM cues can guide them to maturation.

6.3 Contribution to the field

The work described in this dissertation has been prepared with the intent of publishing in peer-reviewed journals. Results from Chapter 3 will be submitted with minimum modification to the journals of *In Vitro Cellular & Developmental Biology* or *Matrix Biology*. Results from Chapters 4 and 5, with some additional experiments to measure contractile force generation of multilayered constructs, will be combined in a single publication submitted to *Acta Biomaterialia* or *Biomaterials*. A review of cardiac physiology and cardiac tissue engineering has already been published as a book chapter⁸. Moreover, this work has led to many presentations at conferences including six talks as first author (Appendix A).

Beyond the scope of this dissertation, all the work required to develop a reproducible scaffold fabrication technique led to many parallel projects. Dr. John Szymanski, Dr. Yan Sun, and I coauthored a study demonstrating a novel use of the surface-initiated assembly technique that enabled the patterning of ECM proteins onto substrates with complex topography such as sand-paper. The study was published in *Nature Methods* and featured on the cover¹²² (Appendix C). The next step of transferring FN patterns on a gelatin gel was initially thought of in order to implant ECM meshes *in vivo*. This has become an ambitious project led by Dr. Alkiviadis Tsamis to use ECM meshes as nanomechanical biosensors to measure strain during morphogenesis; the results will soon be submitted for publication in the journal *Nature Materials*.

The protocols developed to carry out the analysis of the ECM in chapter 3 were also critical to two different projects in our laboratory. A 3D model of the embryonic heart was created based on images of the whole-heart cleared in BABB. The heart was printed in alginate using a new FRESH

bioprinting technique published in *Science Advances* (Appendix D). Moreover, Ivan Batalov used high resolution images of the FN matrix in the myocardium to create biomimetic patterns of FN that he is testing in 2D.

6.4 Conclusions

The work presented here dramatically expands the parameter space that can be investigated for cardiac tissue engineering. By enabling the use of micrometer ECM cues for 3D constructs, researchers can start to apply the knowledge derived from decades of research in 2D toward engineering functional muscle *in vitro*. Beyond the physical stimuli and bulk hydrogels that are regularly used, we can now add a new dimension of control of the cell environment at the micrometer scale. This will enable the fabrication from the bottom-up of scaffolds that can recapitulate much more of the complexity of the native ECM than has been possible so far. Finally, the study of the embryonic ECM provides a great starting point toward the creation of biomimetic ECM scaffolds.

References

1. Go, A. S. *et al.* Heart Disease and Stroke Statistics--2014 Update: A Report From the American Heart Association. *Circulation* 129:e28–e292, 2014.
2. Laflamme, M. A., and C. E. Murry. Heart regeneration. *Nature* 473:326–35, 2011.
3. Bergmann, O., R. D. Bhardwaj, S. Bernard, S. Zdunek, F. Barnabé-Heider, S. Walsh, J. Zupicich, K. Alkass, B. A. Buchholz, H. Druid, S. Jovinge, and J. Frisén. Evidence for cardiomyocyte renewal in humans. *Science* 324:98–102, 2009.
4. UNOS. Transplant Trends by Organ Type. , 2015.at <https://www.unos.org/data/transplant-trends/#transplants_by_organ_type+year+2015>
5. Segers, V. F. M., and R. T. Lee. Stem-cell therapy for cardiac disease. *Nature* 451:937–42, 2008.
6. Clifford, D. M., S. A. Fisher, S. J. Brunskill, C. Doree, A. Mathur, S. Watt, and E. Martin-Rendon. Stem cell treatment for acute myocardial infarction. *Cochrane database Syst. Rev.* 2:CD006536, 2012.
7. Passier, R., L. W. van Laake, and C. L. Mummery. Stem-cell-based therapy and lessons from the heart. *Nature* 453:322–9, 2008.
8. Jallerat, Q., J. M. Szymanski, and A. W. Feinberg. Nano- and Microstructured ECM and Biomimetic Scaffolds for Cardiac Tissue Engineering. In: *Bio-inspired Materials for Biomedical Engineering*. Hoboken, NJ, USA: John Wiley & Sons, Inc., 2014, pp. 195–226.
9. Batalov, I., and A. W. Feinberg. Differentiation of Cardiomyocytes from Human Pluripotent Stem Cells Using Monolayer Culture. *Biomark. Insights* 10:71–6, 2015.
10. Feinberg, A. W., C. M. Ripplinger, P. van der Meer, S. P. Sheehy, I. Domian, K. R. Chien, and K. K. Parker. Functional differences in engineered myocardium from embryonic stem cell-derived versus neonatal cardiomyocytes. *Stem cell reports* 1:387–96, 2013.
11. Ribeiro, M. C., L. G. Tertoolen, J. A. Guadix, M. Bellin, G. Kosmidis, C. D’Aniello, J. Monshouwer-Kloots, M.-J. Goumans, Y. Wang, A. W. Feinberg, C. L. Mummery, and R. Passier. Functional maturation of human pluripotent stem cell derived cardiomyocytes in vitro--correlation between contraction force and electrophysiology. *Biomaterials* 51:138–50, 2015.
12. Yang, X., L. Pabon, and C. E. Murry. Engineering adolescence: maturation of human pluripotent stem cell-derived cardiomyocytes. *Circ. Res.* 114:511–23, 2014.
13. Harvey, R. P. Patterning the vertebrate heart. *Nat. Rev. Genet.* 3:544–56, 2002.
14. Sedmera, D., T. Pexieder, M. Vuillemin, R. P. Thompson, and R. H. Anderson. Developmental patterning of the myocardium. *Anat. Rec.* 258:319–37, 2000.
15. Savadjiev, P., G. J. Strijkers, A. J. Bakermans, E. Piuze, S. W. Zucker, and K. Siddiqi. Heart wall myofibers are arranged in minimal surfaces to optimize organ function. *Proc. Natl. Acad. Sci. U. S. A.* 109:9248–53, 2012.
16. Buckingham, M., S. Meilhac, and S. Zaffran. Building the mammalian heart from two sources of myocardial cells. *Nat. Rev. Genet.* 6:826–35, 2005.
17. Dierickx, P., P. A. Doevendans, N. Geijsen, and L. W. van Laake. Embryonic template-based generation and purification of pluripotent stem cell-derived cardiomyocytes for heart repair. *J. Cardiovasc. Transl. Res.* 5:566–80, 2012.

18. Levkau, B., M. Schäfers, J. Wohlschlaeger, K. von Wnuck Lipinski, P. Keul, S. Hermann, N. Kawaguchi, P. Kirchhof, L. Fabritz, J. Stypmann, L. Stegger, U. Flögel, J. Schrader, J. W. Fischer, J. Fischer, P. Hsieh, Y.-L. Ou, F. Mehrhof, K. Tiemann, A. Ghanem, M. Matus, J. Neumann, G. Heusch, K. W. Schmid, E. M. Conway, and H. A. Baba. Survivin determines cardiac function by controlling total cardiomyocyte number. *Circulation* 117:1583–93, 2008.
19. Zhou, J., H. Y. Kim, J. H.-C. Wang, and L. A. Davidson. Macroscopic stiffening of embryonic tissues via microtubules, RhoGEF and the assembly of contractile bundles of actomyosin. *Development* 137:2785–94, 2010.
20. Williams, C., K. P. Quinn, I. Georgakoudi, and L. D. Black. Young developmental age cardiac extracellular matrix promotes the expansion of neonatal cardiomyocytes in vitro. *Acta Biomater.* 10:194–204, 2013.
21. Little, C. D., and B. J. Rongish. The extracellular matrix during heart development. *Experientia* 51:873–82, 1995.
22. Rozario, T., and D. W. DeSimone. The extracellular matrix in development and morphogenesis: a dynamic view. *Dev. Biol.* 341:126–40, 2010.
23. Whitesides, G. M., E. Ostuni, S. Takayama, X. Jiang, and D. E. Ingber. Soft lithography in biology and biochemistry. *Annu. Rev. Biomed. Eng.* 3:335–73, 2001.
24. Perl, A., D. N. Reinhoudt, and J. Huskens. Microcontact Printing: Limitations and Achievements. *Adv. Mater.* 21:2257–2268, 2009.
25. Martínez, E., A. Lagunas, C. A. Mills, S. Rodríguez-Seguí, M. Estévez, S. Oberhansl, J. Comelles, and J. Samitier. Stem cell differentiation by functionalized micro- and nanostructured surfaces. *Nanomedicine (Lond).* 4:65–82, 2009.
26. Feinberg, A. W., A. Feigel, S. S. Shevkopyas, S. Sheehy, G. M. Whitesides, and K. K. Parker. Muscular thin films for building actuators and powering devices. *Science (80-)*. 317:1366–70, 2007.
27. Ott, H. C., T. S. Matthiesen, S.-K. Goh, L. D. Black, S. M. Kren, T. I. Netoff, and D. A. Taylor. Perfusion-decellularized matrix: using nature’s platform to engineer a bioartificial heart. *Nat. Med.* 14:213–21, 2008.
28. Wang, B., A. Borazjani, M. Tahai, A. L. D. J. Curry, D. T. Simionescu, J. Guan, F. To, S. H. Elder, and J. Liao. Fabrication of cardiac patch with decellularized porcine myocardial scaffold and bone marrow mononuclear cells. *J. Biomed. Mater. Res. A* 94:1100–10, 2010.
29. Duan, Y., Z. Liu, J. O’Neill, L. Q. Wan, D. O. Freytes, and G. Vunjak-Novakovic. Hybrid gel composed of native heart matrix and collagen induces cardiac differentiation of human embryonic stem cells without supplemental growth factors. *J. Cardiovasc. Transl. Res.* 4:605–15, 2011.
30. Godier-Furnémont, A. F. G., T. P. Martens, M. S. Koeckert, L. Wan, J. Parks, K. Arai, G. Zhang, B. Hudson, S. Homma, and G. Vunjak-Novakovic. Composite scaffold provides a cell delivery platform for cardiovascular repair. *Proc. Natl. Acad. Sci. U. S. A.* 108:7974–9, 2011.
31. Severs, N. J. The cardiac muscle cell. *Bioessays* 22:188–99, 2000.
32. Bergmann, O., and S. Jovinge. Cardiac regeneration in vivo: Mending the heart from within? *Stem Cell Res.* 13:523–531, 2014.
33. Sultana, N., L. Zhang, J. Yan, J. Chen, W. Cai, S. Razzaque, D. Jeong, W. Sheng, L. Bu, M. Xu, G.-Y. Huang, R. J. Hajjar, B. Zhou, A. Moon, and C.-L. Cai. Resident c-kit(+) cells in the heart are not cardiac stem cells. *Nat. Commun.* 6:8701, 2015.

34. Xin, M., E. N. Olson, and R. Bassel-Duby. Mending broken hearts: cardiac development as a basis for adult heart regeneration and repair. *Nat. Rev. Mol. Cell Biol.* 14:529–41, 2013.
35. Schleich, J. M., T. Abdulla, R. Summers, and L. Houyel. An overview of cardiac morphogenesis. *Arch. Cardiovasc. Dis.* 106:612–623, 2013.
36. Martinsen, B. J. Reference guide to the stages of chick heart embryology. *Dev. Dyn.* 233:1217–37, 2005.
37. Sedmera, D., and T. McQuinn. Embryogenesis of the heart muscle. *Heart Fail. Clin.* 4:235–245, 2008.
38. Vunjak-novakovic, G., N. Tandon, A. Godier, R. Maidhof, A. Marsano, T. P. Martens, and M. Radisic. Challenges in Cardiac Tissue Engineering. *Tissue Eng.* 16:, 2010.
39. Weber, K. T. Cardiac interstitium in health and disease: the fibrillar collagen network. *J. Am. Coll. Cardiol.* 13:1637–52, 1989.
40. Lockhart, M., E. Wirrig, A. Phelps, and A. Wessels. Extracellular matrix and heart development. *Birth Defects Res. A. Clin. Mol. Teratol.* 91:535–50, 2011.
41. Hanson, K. P., J. P. Jung, Q. a. Tran, S.-P. P. Hsu, R. Iida, V. Ajeti, P. J. Campagnola, K. W. Eliceiri, J. M. Squirrell, G. E. Lyons, and B. M. Ogle. Spatial and temporal analysis of extracellular matrix proteins in the developing murine heart: a blueprint for regeneration. *Tissue Eng. Part A* 19:1132–43, 2013.
42. Borg, T. K., K. Rubin, E. Lundgren, K. Borg, and B. Obrink. Recognition of extracellular matrix components by neonatal and adult cardiac myocytes. *Dev. Biol.* 104:86–96, 1984.
43. Hamburger, V., and H. L. Hamilton. A series of normal stages in the development of the chick embryo. *J. Morphol.* 88:49–92, 1951.
44. Brette, F., and C. Orchard. T-tubule function in mammalian cardiac myocytes. *Circ. Res.* 92:1182–92, 2003.
45. Zak, R. Cell proliferation during cardiac growth. *Am. J. Cardiol.* 31:211–9, 1973.
46. Li, F., M. McNelis, and K. Lustig. Hyperplasia and hypertrophy of chicken cardiac myocytes during posthatching development. *Am. J. Physiol. - Regul. Integr. Comp. Physiol.* , 1997.at <<http://ajpregu.physiology.org/content/273/2/R518.short>>
47. Anversa, P., G. Olivetti, P. G. Bracchi, and A. V Loud. Postnatal development of the M-band in rat cardiac myofibrils. *Circ. Res.* 48:561–8, 1981.
48. Romano, N. H., D. Sengupta, C. Chung, and S. C. Heilshorn. Protein-engineered biomaterials: nanoscale mimics of the extracellular matrix. *Biochim. Biophys. Acta* 1810:339–49, 2011.
49. Remlinger, N. T., P. D. Wearden, and T. W. Gilbert. Procedure for decellularization of porcine heart by retrograde coronary perfusion. *J. Vis. Exp.* e50059, 2012.doi:10.3791/50059
50. Badylak, S. F., D. Taylor, and K. Uygun. Whole-organ tissue engineering: decellularization and recellularization of three-dimensional matrix scaffolds. *Annu. Rev. Biomed. Eng.* 13:27–53, 2011.
51. Crapo, P. M., T. W. Gilbert, and S. F. Badylak. An overview of tissue and whole organ decellularization processes. *Biomaterials* 32:3233–43, 2011.
52. Akhyari, P., H. Aubin, P. Gwanmesia, M. Barth, S. Hoffmann, J. Huelsmann, K. Preuss, and A. Lichtenberg. The quest for an optimized protocol for whole-heart decellularization: a comparison of three popular and a novel decellularization technique and their diverse effects on crucial extracellular matrix qualities. *Tissue Eng. Part C. Methods* 17:915–26, 2011.

53. Sicari, B. M., J. L. Dziki, and S. F. Badylak. Strategies for functional bioscaffold-based skeletal muscle reconstruction. *Ann. Transl. Med.* 3:256, 2015.
54. Su, Z., H. Ma, Z. Wu, H. Zeng, Z. Li, Y. Wang, G. Liu, B. Xu, Y. Lin, P. Zhang, and X. Wei. Enhancement of skin wound healing with decellularized scaffolds loaded with hyaluronic acid and epidermal growth factor. *Mater. Sci. Eng. C. Mater. Biol. Appl.* 44:440–8, 2014.
55. Badylak, S. F., D. O. Freytes, and T. W. Gilbert. Reprint of: Extracellular matrix as a biological scaffold material: Structure and function. *Acta Biomater.* 23 Suppl:S17–26, 2015.
56. Swinehart, I. T., and S. F. Badylak. Extracellular matrix bioscaffolds in tissue remodeling and morphogenesis. *Dev. Dyn.* 245:351–60, 2016.
57. Seif-Naraghi, S. B., D. Horn, P. J. Schup-Magoffin, and K. L. Christman. Injectable extracellular matrix derived hydrogel provides a platform for enhanced retention and delivery of a heparin-binding growth factor. *Acta Biomater.* 8:3695–703, 2012.
58. Li, F., X. Wang, J. M. Capasso, and A. M. Gerdes. Rapid transition of cardiac myocytes from hyperplasia to hypertrophy during postnatal development. *J. Mol. Cell. Cardiol.* 28:1737–46, 1996.
59. Jung, J. P., J. M. Squirrell, G. E. Lyons, K. W. Eliceiri, and B. M. Ogle. Imaging cardiac extracellular matrices: a blueprint for regeneration. *Trends Biotechnol.* 30:233–40, 2012.
60. Kim, H. Y., and L. A. Davidson. Punctuated actin contractions during convergent extension and their permissive regulation by the non-canonical Wnt-signaling pathway. *J. Cell Sci.* 124:635–46, 2011.
61. Besseling, T. H., J. Jose, and A. van Blaaderen. Methods to calibrate and scale axial distances in confocal microscopy as a function of refractive index. 8, 2014.at <<http://arxiv.org/abs/1404.3952>>
62. Sedmera, D. Function and form in the developing cardiovascular system. *Cardiovasc. Res.* 91:252–9, 2011.
63. Dowsey, A. W., J. Keegan, and G.-Z. Yang. Cardiac-motion compensated MR imaging and strain analysis of ventricular trabeculae. *Med. Image Comput. Comput. Assist. Interv.* 10:609–16, 2007.
64. Hinton, T. J., Q. Jallerat, R. N. Palchesko, J. H. Park, M. S. Grodzicki, H. Shue, M. H. Ramadan, A. R. Hudson, and A. W. Feinberg. Three-dimensional printing of complex biological structures by freeform reversible embedding of suspended hydrogels. *Sci. Adv.* 1:e1500758, 2015.
65. Miller, C. E., R. P. Thompson, M. R. Bigelow, G. Gittinger, T. C. Trusk, and D. Sedmera. Confocal imaging of the embryonic heart: how deep? *Microsc. Microanal.* 11:216–23, 2005.
66. Ahnfelt-Rønne, J., M. C. Jørgensen, J. Hald, O. D. Madsen, P. Serup, and J. Hecksher-Sørensen. An improved method for three-dimensional reconstruction of protein expression patterns in intact mouse and chicken embryos and organs. *J. Histochem. Cytochem.* 55:925–30, 2007.
67. Dahl, K. N., A. J. S. Ribeiro, and J. Lammerding. Nuclear shape, mechanics, and mechanotransduction. *Circ. Res.* 102:1307–18, 2008.
68. Bray, M.-A. P., W. J. Adams, N. A. Geisse, A. W. Feinberg, S. P. Sheehy, and K. K. Parker. Nuclear morphology and deformation in engineered cardiac myocytes and tissues. *Biomaterials* 31:5143–50, 2010.
69. Hama, H., H. Kurokawa, H. Kawano, R. Ando, T. Shimogori, H. Noda, K. Fukami, A.

- Sakaue-Sawano, and A. Miyawaki. Scale: a chemical approach for fluorescence imaging and reconstruction of transparent mouse brain. *Nat. Neurosci.* 14:1481–8, 2011.
70. Ke, M.-T., S. Fujimoto, and T. Imai. SeeDB: a simple and morphology-preserving optical clearing agent for neuronal circuit reconstruction. *Nat. Neurosci.* 16:1154–61, 2013.
 71. Tsenova, V., and E. V. Stoykova. Refractive index measurement in human tissue samples. , 2003.doi:10.1117/12.519584
 72. Chung, K., J. Wallace, S.-Y. Kim, S. Kalyanasundaram, A. S. Andalman, T. J. Davidson, J. J. Mirzabekov, K. A. Zalocusky, J. Mattis, A. K. Denisin, S. Pak, H. Bernstein, C. Ramakrishnan, L. Grosenick, V. Gradinaru, and K. Deisseroth. Structural and molecular interrogation of intact biological systems. *Nature* 497:332–7, 2013.
 73. Sedmera, D., T. Pexieder, V. Rychterova, N. Hu, and E. B. Clark. Remodeling of chick embryonic ventricular myoarchitecture under experimentally changed loading conditions. *Anat. Rec.* 254:238–52, 1999.
 74. Red-Horse, K., H. Ueno, I. L. Weissman, and M. A. Krasnow. Coronary arteries form by developmental reprogramming of venous cells. *Nature* 464:549–53, 2010.
 75. Riley, P. R., and N. Smart. Vascularizing the heart. *Cardiovasc. Res.* 91:260–8, 2011.
 76. Reese, D. E. Development of the Coronary Vessel System. *Circ. Res.* 91:761–768, 2002.
 77. Wada, A. M., S. G. Willet, and D. Bader. Coronary vessel development: a unique form of vasculogenesis. *Arterioscler. Thromb. Vasc. Biol.* 23:2138–45, 2003.
 78. Majesky, M. W. Development of coronary vessels. *Curr. Top. Dev. Biol.* 62:225–59, 2004.
 79. Astrof, S., and R. O. Hynes. Fibronectins in vascular morphogenesis. *Angiogenesis* 12:165–75, 2009.
 80. Rongish, B. J., G. Hinchman, M. K. Doty, H. S. Baldwin, and R. J. Tomanek. Relationship of the extracellular matrix to coronary neovascularization during development. *J. Mol. Cell. Cardiol.* 28:2203–15, 1996.
 81. Feinberg, A. W., and K. K. Parker. Surface-initiated assembly of protein nanofabrics. *Nano Lett.* 10:2184–91, 2010.
 82. Szymanski, J. M., Q. Jallerat, and A. W. Feinberg. ECM protein nanofibers and nanostructures engineered using surface-initiated assembly. *J. Vis. Exp.* e51176, 2014.doi:10.3791/51176
 83. Icardo, J. M., and A. Fernandez-Terán. Morphologic study of ventricular trabeculation in the embryonic chick heart. *Acta Anat. (Basel).* 130:264–74, 1987.
 84. Erickson, H. P., N. Carrell, and J. McDonagh. Fibronectin molecule visualized in electron microscopy: a long, thin, flexible strand. *J. Cell Biol.* 91:673–78, 1981.
 85. Ohashi, T., D. P. Kiehart, and H. P. Erickson. Dynamics and elasticity of the fibronectin matrix in living cell culture visualized by fibronectin-green fluorescent protein. *Proc. Natl. Acad. Sci. U. S. A.* 96:2153–8, 1999.
 86. Nunes, S. S., J. W. Miklas, J. Liu, R. Aschar-Sobbi, Y. Xiao, B. Zhang, J. Jiang, S. Massé, M. Gagliardi, A. Hsieh, N. Thavandiran, M. A. Laflamme, K. Nanthakumar, G. J. Gross, P. H. Backx, G. Keller, and M. Radisic. Biowire: a platform for maturation of human pluripotent stem cell-derived cardiomyocytes. *Nat. Methods* 10:781–7, 2013.
 87. Diao, J., A. J. Maniotis, R. Folberg, and E. Tajkhorshid. Interplay of mechanical and binding properties of Fibronectin type I. *Theor. Chem. Acc.* 125:397–405, 2010.
 88. Bian, W., N. Badie, H. D. Himel, and N. Bursac. Robust T-tubulation and maturation of cardiomyocytes using tissue-engineered epicardial mimetics. *Biomaterials* 35:3819–28, 2014.

89. Cao, L., M. K. Zeller, V. F. Fiore, P. Strane, H. Bermudez, and T. H. Barker. Phage-based molecular probes that discriminate force-induced structural states of fibronectin in vivo. *Proc. Natl. Acad. Sci. U. S. A.* 109:1–6, 2012.
90. Zhang, D., I. Y. Shadrin, J. Lam, H.-Q. Xian, H. R. Snodgrass, and N. Bursac. Tissue-engineered cardiac patch for advanced functional maturation of human ESC-derived cardiomyocytes. *Biomaterials* 34:5813–20, 2013.
91. Liao, B., N. Christoforou, K. W. Leong, and N. Bursac. Pluripotent stem cell-derived cardiac tissue patch with advanced structure and function. *Biomaterials* 32:9180–7, 2011.
92. Christoforou, N., B. Liao, S. Chakraborty, M. Chellapan, N. Bursac, and K. W. Leong. Induced pluripotent stem cell-derived cardiac progenitors differentiate to cardiomyocytes and form biosynthetic tissues. *PLoS One* 8:e65963, 2013.
93. Zimmermann, W.-H., K. Schneiderbanger, P. Schubert, M. Didié, F. Münzel, J. F. Heubach, S. Kostin, W. L. Neuhuber, and T. Eschenhagen. Tissue engineering of a differentiated cardiac muscle construct. *Circ. Res.* 90:223–30, 2002.
94. Eschenhagen, T., C. Fink, U. Remmers, H. Scholz, J. Wattchow, J. Weil, W. Zimmermann, H. H. Dohmen, H. Schäfer, N. Bishopric, T. Wakatsuki, and E. L. Elson. Three-dimensional reconstitution of embryonic cardiomyocytes in a collagen matrix: a new heart muscle model system. *FASEB J.* 11:683–94, 1997.
95. Naito, H., I. Melnychenko, M. Didié, K. Schneiderbanger, P. Schubert, S. Rosenkranz, T. Eschenhagen, and W.-H. Zimmermann. Optimizing engineered heart tissue for therapeutic applications as surrogate heart muscle. *Circulation* 114:I72–8, 2006.
96. Hansen, A., A. Eder, M. Bönstrup, M. Flato, M. Mewe, S. Schaaf, B. Aksehirlioglu, A. P. Schwoerer, A. Schwörer, J. Uebeler, and T. Eschenhagen. Development of a drug screening platform based on engineered heart tissue. *Circ. Res.* 107:35–44, 2010.
97. Schaaf, S., A. Shibamiya, M. Mewe, A. Eder, A. Stöhr, M. N. Hirt, T. Rau, W.-H. Zimmermann, L. Conradi, T. Eschenhagen, and A. Hansen. Human engineered heart tissue as a versatile tool in basic research and preclinical toxicology. *PLoS One* 6:e26397, 2011.
98. Hirt, M. N., J. Boeddinghaus, A. Mitchell, S. Schaaf, C. Börnchen, C. Müller, H. Schulz, N. Hubner, J. Stenzig, A. Stoehr, C. Neuber, A. Eder, P. K. Luther, A. Hansen, and T. Eschenhagen. Functional improvement and maturation of rat and human engineered heart tissue by chronic electrical stimulation. *J. Mol. Cell. Cardiol.* 74:151–61, 2014.
99. Lu, T.-Y., B. Lin, J. Kim, M. Sullivan, K. Tobita, G. Salama, and L. Yang. Repopulation of decellularized mouse heart with human induced pluripotent stem cell-derived cardiovascular progenitor cells. *Nat. Commun.* 4:2307, 2013.
100. Parker, K. K., J. Tan, C. S. Chen, and L. Tung. Myofibrillar architecture in engineered cardiac myocytes. *Circ. Res.* 103:340–2, 2008.
101. Salick, M. R., B. N. Napiwocki, J. Sha, G. T. Knight, S. A. Chindhy, T. J. Kamp, R. S. Ashton, and W. C. Crone. Micropattern width dependent sarcomere development in human ESC-derived cardiomyocytes. *Biomaterials* 35:4454–64, 2014.
102. Feinberg, A. W., P. W. Alford, H. Jin, C. M. Ripplinger, A. A. Werdich, S. P. Sheehy, A. Grosberg, and K. K. Parker. Controlling the contractile strength of engineered cardiac muscle by hierarchical tissue architecture. *Biomaterials* 33:5732–41, 2012.
103. Kovese, P. MATLAB and Octave Functions for Computer Vision and Image Processing at <<http://www.peterkovese.com/matlabfns/#fingerprints>>
104. Pong, T., W. J. Adams, M.-A. Bray, A. W. Feinberg, S. P. Sheehy, A. A. Werdich, and K. K. Parker. Hierarchical architecture influences calcium dynamics in engineered cardiac

- muscle. *Exp. Biol. Med. (Maywood)*. 236:366–73, 2011.
105. Bio-Formats, the solution for reading proprietary microscopy image data and metadata at <<http://www.openmicroscopy.org/site/products/bio-formats>>
 106. Grosberg, A., P. W. Alford, M. L. McCain, and K. K. Parker. Ensembles of engineered cardiac tissues for physiological and pharmacological study: heart on a chip. *Lab Chip* 11:4165–73, 2011.
 107. Nawroth, J. C., H. Lee, A. W. Feinberg, C. M. Ripplinger, M. L. McCain, A. Grosberg, J. O. Dabiri, and K. K. Parker. A tissue-engineered jellyfish with biomimetic propulsion. *Nat. Biotechnol.* 30:792–7, 2012.
 108. Hughes, C. S., L. M. Postovit, and G. A. Lajoie. Matrigel: a complex protein mixture required for optimal growth of cell culture. *Proteomics* 10:1886–90, 2010.
 109. Bird, S. D., P.A.Doevendans, M.A.van Rooijen, A.Brutel de la Riviere, R. J. Hassink, R. Passier, and C. L. Mummery. The human adult cardiomyocyte phenotype. *Cardiovasc. Res.* 58:423–34, 2003.
 110. Elangbam, C. S., C. W. Qualls, and R. R. Dahlgren. Cell adhesion molecules--update. *Vet. Pathol.* 34:61–73, 1997.
 111. Davis, G. E., and D. R. Senger. Endothelial extracellular matrix: biosynthesis, remodeling, and functions during vascular morphogenesis and neovessel stabilization. *Circ. Res.* 97:1093–107, 2005.
 112. Spinale, F. G. Myocardial matrix remodeling and the matrix metalloproteinases: influence on cardiac form and function. *Physiol. Rev.* 87:1285–342, 2007.
 113. Mordwinkin, N. M., P. W. Burridge, and J. C. Wu. A review of human pluripotent stem cell-derived cardiomyocytes for high-throughput drug discovery, cardiotoxicity screening, and publication standards. *J. Cardiovasc. Transl. Res.* 6:22–30, 2013.
 114. Burridge, P. W., S. Thompson, M.A. Millrod, S. Weinberg, X. Yuan, A. Peters, V. Mahairaki, V. E. Koliatsos, L. Tung, and E. T. Zambidis. A universal system for highly efficient cardiac differentiation of human induced pluripotent stem cells that eliminates interline variability. *PLoS One* 6:e18293, 2011.
 115. Burridge, P. W., E. Matsa, P. Shukla, Z. C. Lin, J. M. Churko, A. D. Ebert, F. Lan, S. Diecke, B. Huber, N. M. Mordwinkin, J. R. Plews, O. J. Abilez, B. Cui, J. D. Gold, and J. C. Wu. Chemically defined generation of human cardiomyocytes. *Nat. Methods* 11:855–60, 2014.
 116. Alford, P. W., A. W. Feinberg, S. P. Sheehy, and K. K. Parker. Biohybrid thin films for measuring contractility in engineered cardiovascular muscle. *Biomaterials* 31:3613–21, 2010.
 117. Domian, I. J., M. Chiravuri, P. van der Meer, A. W. Feinberg, X. Shi, Y. Shao, S. M. Wu, K. K. Parker, and K. R. Chien. Generation of functional ventricular heart muscle from mouse ventricular progenitor cells. *Science* 326:426–9, 2009.
 118. Lin, B., J. Kim, Y. Li, H. Pan, X. Carvajal-Vergara, G. Salama, T. Cheng, Y. Li, C. W. Lo, and L. Yang. High-purity enrichment of functional cardiovascular cells from human iPS cells. *Cardiovasc. Res.* 95:327–35, 2012.
 119. Sun, Y., R. Duffy, A. Lee, and A. W. Feinberg. Optimizing the structure and contractility of engineered skeletal muscle thin films. *Acta Biomater.* 9:7885–94, 2013.
 120. Engler, A. J., M. A. Griffin, S. Sen, C. G. Bönnemann, H. L. Sweeney, and D. E. Discher. Myotubes differentiate optimally on substrates with tissue-like stiffness: pathological implications for soft or stiff microenvironments. *J. Cell Biol.* 166:877–87, 2004.

121. Young, J. L., and A. J. Engler. Hydrogels with time-dependent material properties enhance cardiomyocyte differentiation in vitro. *Biomaterials* 32:1002–9, 2011.
122. Sun, Y., Q. Jallerat, J. M. Szymanski, and A. W. Feinberg. Conformal nanopatterning of extracellular matrix proteins onto topographically complex surfaces. *Nat. Methods* 12:134–6, 2015.
123. Yamada, K. M., and K. Olden. Fibronectins--adhesive glycoproteins of cell surface and blood. *Nature* 275:179–84, 1978.
124. Astrof, S., A. Kirby, K. Lindblad-Toh, M. Daly, and R. O. Hynes. Heart development in fibronectin-null mice is governed by a genetic modifier on chromosome four. *Mech. Dev.* 124:551–8, 2007.
125. Engler, A. J., C. Carag-Krieger, C. P. Johnson, M. Raab, H.-Y. Tang, D. W. Speicher, J. W. Sanger, J. M. Sanger, and D. E. Discher. Embryonic cardiomyocytes beat best on a matrix with heart-like elasticity: scar-like rigidity inhibits beating. *J. Cell Sci.* 121:3794–802, 2008.
126. Kensah, G., A. Roa Lara, J. Dahlmann, R. Zweigerdt, K. Schwanke, J. Hegermann, D. Skvorc, A. Gawol, A. Azizian, S. Wagner, L. S. Maier, A. Krause, G. Dräger, M. Ochs, A. Haverich, I. Gruh, and U. Martin. Murine and human pluripotent stem cell-derived cardiac bodies form contractile myocardial tissue in vitro. *Eur. Heart J.* 34:1134–46, 2013.
127. Eschenhagen, T., and W. H. Zimmermann. Engineering myocardial tissue. *Circ. Res.* 97:1220–31, 2005.
128. Mulieri, L. A., G. Hasenfuss, B. Leavitt, P. D. Allen, and N. R. Alpert. Altered myocardial force-frequency relation in human heart failure. *Circulation* 85:1743–50, 1992.
129. Iribe, G., M. Helmes, and P. Kohl. Force-length relations in isolated intact cardiomyocytes subjected to dynamic changes in mechanical load. *Am. J. Physiol. Heart Circ. Physiol.* 292:H1487–97, 2007.
130. Liao, B., D. Zhang, and N. Bursac. Functional cardiac tissue engineering. *Regen. Med.* 7:187–206, 2012.
131. Wenger, M. P. E., L. Bozec, M. A. Horton, and P. Mesquida. Mechanical properties of collagen fibrils. *Biophys. J.* 93:1255–63, 2007.
132. Roeder, B. A., K. Kokini, and S. L. Voytik-Harbin. Fibril microstructure affects strain transmission within collagen extracellular matrices. *J. Biomech. Eng.* 131:031004, 2009.

Appendix A List of publications and presentations

1. PUBLICATIONS

a. Peer-reviewed articles

- Tsamis A, Jallerat Q, Szymanski JM, Feinberg AW. "Fibronectin Nanomechanical Biosensors for Cell-Generated Tissue Strains during Embryonic Morphogenesis". *In preparation*.
- Jallerat Q, Palayekar V, Monroe M, Begur G, Feinberg AW. "Micro-Patterning Directional ECM Cues in Hydrogel-Based Scaffolds for Cardiac Tissue Engineering". *In preparation*.
- Jallerat Q, Feinberg AW. "Characterization of the Cardiac ECM during Embryonic Development using Whole-mount Multiphoton Microscopy". *In preparation*
- Batalov I, Jallerat Q, Kim S, Feinberg AW. "Biomimetic Micropatterns Based on the Embryonic Heart for 2D Cardiac Tissue Engineering". *In preparation*.
- Sun Y*, Jallerat Q*, Szymanski JM*, Feinberg AW. (2015). "Conformal Nanopatterning of Extracellular Matrix Proteins onto Topographically Complex Surfaces". *Nature Methods*, 12(2), 134-136. doi: 10.1038/nmeth.3210 ** Selected for cover art - February 2015 **
- Hinton TJ, Jallerat Q, Palchesko RN, Park JH, Grodzicki MS, Shue HJ, Ramadan MH, Hudson AR, Feinberg AW. (2015). "Three-Dimensional Printing of Complex Biological Structures by Freeform Reversible Embedding of Suspended Hydrogels". *Science Advances*, 1(9), e1500758. doi: 10.1126/sciadv.1500758
- Szymanski JM, Jallerat Q, Feinberg AW. (2014). "ECM Protein Nanofibers and Nanostructures Engineered Using Surface-Initiated Assembly". *Journal of visualized experiments: JoVE*, (86), e51176-e51176. doi: 10.3791/51176
- * denotes equal contribution

b. Book chapters

- Jallerat Q, Szymanski JM, Feinberg AW. (2014). "Nano-and Microstructured ECM and Biomimetic Scaffolds for Cardiac Tissue Engineering". In *Bio-Inspired Materials for Biomedical Engineering* (pp. 195-226). Eds: Kirschner, Brennan. John Wiley & Sons.
- Palchesko RN, Sun Y, Zhang L, Szymanski JM, Jallerat Q, Feinberg AW. (2013). "Nanofiber Biomaterials". In *Springer Handbook of Nanomaterials* (pp. 977-1010). Springer.

2. PRESENTATIONS

- Jallerat Q, Palayekar V, Monroe M, Feinberg AW. (2016). “Micro-Patterning Directional Fibronectin Cues onto Hydrogel Scaffolds for Cardiac Tissue Engineering”. World Biomaterials Congress, Montreal, CA. (Oral)
- Jallerat Q, Palayekar V, Monroe M, Feinberg AW. (2015). “Micro-Patterning Directional ECM Cues in Hydrogel-Based Scaffolds for Cardiac Tissue Engineering”. *89th American Chemical Society Colloid & Surface Science Symposium*, Pittsburgh, PA. (Oral)
- Jallerat Q, Palayekar V, Monroe M, Feinberg AW. (2015). “Micro-Patterning Directional ECM Cues in Hydrogel-Based Scaffolds for Cardiac Tissue Engineering”. *Society for Biomaterials Annual Meeting*, Charlotte, NC. (Oral)
- Jallerat Q, Palayekar V, Monroe M, Begur G, Feinberg AW. (2015). “Engineering Myocardium Based on Biomimetic ECM Scaffolds”. *McGowan Institute for Regenerative Medicine Retreat*, Farmington, PA. (Poster)
- Jallerat Q, Palayekar V, Monroe M, Begur G, Feinberg AW. (2015). “Micro-Patterning Directional ECM Cues in Hydrogel-Based Scaffolds for Cardiac Tissue Engineering”. *Tissue Engineering and Regenerative Medicine International Society World Congress*, MA. (Oral)
- Jallerat Q, Sun Y, Szymanski JM, Feinberg AW. (2014). “Conformal Nanopatterning of Extracellular Matrix Proteins onto Topographically Complex Surfaces”. *Biomedical Engineering Society Annual Meeting*, San Antonio, TX. (Poster)
- Jallerat Q, Feinberg AW. (2014). “Micro-Patterning Directional ECM Cues in Hydrogel-Based Scaffolds for Cardiac Tissue Engineering”. *Biomedical Engineering Society Annual Meeting*, San Antonio, TX. (Oral)
- Jallerat Q, Feinberg AW. (2014). “Embedding Directional ECM Cues onto Hydrogels for Cardiac Tissue Engineering”. *Gordon Research Conference in Signal Transduction by Engineered Extracellular Matrices*, Boston, MA. (Poster)
- Jallerat Q, Feinberg AW. (2014). “Engineering Myocardium Using Biomimetic ECM Scaffolds”. *Center for the Mechanics and Engineering of Cellular Systems Monthly Meeting Meeting*, Carnegie Mellon University, Pittsburgh, PA. (Oral)
- Jallerat Q, Feinberg AW. (2014). “Engineering Myocardium Based on Biomimetic ECM Scaffolds”. *McGowan Institute for Regenerative Medicine Retreat*, Farmington, PA. (Poster)
- Jallerat Q, Feinberg AW. (2013). “3D Characterization of the Fibronectin Matrix in the Embryonic Heart Using Whole-Mount Confocal Microscopy”. *Biomedical Engineering Society Annual Meeting*, Seattle, WA. (Poster)
- Jallerat Q, Feinberg AW. (2013). “Engineering Myocardium Based on Biomimetic ECM Scaffolds”. *McGowan Institute for Regenerative Medicine Retreat*, Farmington, PA. (Poster)
- Jallerat Q, Feinberg AW. (2012). “Regenerating Vascularized Myocardium Using Biomimetic ECM Scaffolds”. *Dowd-ICES Seminar*, Carnegie Mellon University, Pittsburgh, PA. (Oral)
- Jallerat Q, Feinberg AW. (2012). “Engineering Myocardium Based on Biomimetic ECM Scaffolds”. *McGowan Institute for Regenerative Medicine Retreat*, Farmington, PA. (Poster)

Jallerat Q, Feinberg AW. (2011). “Regenerating Vascularized Myocardium Using Biomimetic ECM Scaffolds”. *Dowd-ICES Seminar*, Carnegie Mellon University, Pittsburgh, PA. (Oral)

Appendix B Matlab code

Below is the Matlab Code used to detect the orientation of the actin cytoskeleton of human cardiomyocytes in Chapter 4.

```

% actinDetectMulti_slice_by_slice_QJ

% This script analyzes z-stacks from samples stained for F-actin and  $\alpha$ -actinin. It detects the
orientation of the actin cytoskeleton in each slice of each z-stack.
% It filters the results based on the  $\alpha$ -actinin signal (i.e orientation of all cells or
orientation of cardiomyocytes only).
% NB: this code does not calculate any averages for the whole sample. It
% enables the observation of all the data.

% It exports everything to a .mat file which contains all the
% not-aggregated data. .mat files for several experiments can be
% concatenated and transformed to a Pivot Table in excel to sort the data
% interactively

% Arguments: list of image files (Zeiss format .lsm), the channel number
% for actin and  $\alpha$ -actinin

% Returns: For each single slice - actin orientation angles mode, mean, standard
%          deviation, median, percent actin area, percent  $\alpha$ -actinin area,
%          orientational order parameter
%

% Required functions:
% max_projections.m
% actinDetectTest.m
% actinDetectSlice.m
% OOP.m
% descriptive_stats.m
% mask_actinin.m
% and all functions from Fingerprint Detection algorithm (Peter Kovesi)

% Created by Quentin Jallerat
% Regenerative Biomaterials & Therapeutics Group
% Department of Biomedical Engineering
% Carnegie Mellon University

% Updated March 2016 by Quentin Jallerat

```

Ask user for number of samples

```

ExpInfo = inputdlg({'Number of samples:', 'Experiment title:', 'actin layer number:', ' $\alpha$ -actinin
layer number:'}, 'Input', 1, {'1', 'actin alignment', '2', '3'});
Nb_of_samples = str2num(ExpInfo{1});
actinLayerNumber = str2num(ExpInfo{3});
actininLayerNumber = str2num(ExpInfo{4});

%exp_title = ['E:\Dropbox(RBG)\Cardiac Tissue Engineering\Image Processing\MATLAB\DATA\'
ExpInfo{2}];
exp_title = ExpInfo{2};

```

```

%Prepare data structure : save all stats in one file with one array for
%each slices and one for the whole sample. Within this array, we need to
%split into two tables that can be used as Pivot Tables in Excel: one will
%contain the filename of the image, the experiment, sample, position, slice
%it belongs to and the other will have filename and all the measured stats
%n alignment. Another file will contain a huge array of all the angles
%measured.

```

```

%cell(samples, Field of view FOV, Slices, Stats)
% 6 , 7, 8 are picked to be >= max
Slices_stats = cell(Nb_of_samples, 6 , 7 , 8);
Slices_names = cell(Nb_of_samples, 6, 7);
Samples_stats = cell(Nb_of_samples, 8);
Samples_names = cell(1,Nb_of_samples);

channel = str2num(ExpInfo{3}); % actinLayerNumber
info = {};
rootfolder = 'D:\Dropbox (RBG)\Cardiac Tissue Engineering\Experiments\';

```

Get files for each sample and save them under a cell array

```

for spl=1:Nb_of_samples
    message = sprintf('select files for sample %i',spl);

[file,path]=uigetfile({'*.*'; '*.ism'; '*.TIF'; '*.tif'; '*.bmp'; '*.jpg'},message,rootfolder, 'Multiselect', 'on');
    file_list{spl,1}=path;
    rootfolder = path;
    file_list{spl,2}= file;
    sample = file{1};
    disp(sample(1:10));
end

```

Loop for each sample

```

tic;
for spl=1:Nb_of_samples

    sample = file_list{spl,2};
    if ~isa(sample, 'char')
        Nb_of_FOV = int32(length(sample));
    else
        Nb_of_FOV = 1;
    end
    sample

    TotalArea_cm = 0;

```

```

% Loop over each image for sample #i
for fov = 1:Nb_of_FOV

    % Initialize file names
    if Nb_of_FOV == 1
        stack_name = sample(:);
        image_file = [file_list{spl,1} sample];
    else
        stack_name = sample{fov};
        sample_name = [exp_title '_' stack_name(1:12)];
        image_file = [file_list{spl,1} sample{fov}];
    end

    % Open the image file using OpenMicroscopyEnvironment Bioformats
    % which provide standardized methods to access the data for all
    % file formats.
    lsm = bfopen(image_file);

    % Load metadata
    info = lsm{1,4}; % Load OME metadata
    PixelSize = str2double(info.getPixelsPhysicalSizeX(0));
    width = int32(str2double(info.getPixelsSizeX(0)));
    % Define blksize (should be 3/pixelSize based on recommendation)
    blksize = floor(3/PixelSize);
    %fprintf('Image resolution: %5.5f px/μm\n\n', 1/PixelSize);

    % Get actin z-stack
    ChannelCount = info.getChannelCount(0);
    [PlaneCount,~] = size(lsm{1,1}); % PlaneCount = z-slice x channels in bioformat metadata
    structure
    Nb_of_Slices = int32(PlaneCount/ChannelCount);
    %[Width,Height] = size(image{1,1});

        MIP = max_projection(lsm{1,1}(:,1),info, [ actinLayerNumber, actininLayerNumber
]);

    % To make sure the threshold used to segment the actinin and actin
    % signal is the same for each slice of a z-stack, we will set 1
    % pixel in each slice to the max intensity for this channel
    % Genius idea from Ivan Batalov

    maxActinPx = max(max(MIP(:,:,1)));
    maxSarcomerePx = max(max(MIP(:,:,2)));

    % Allocate memory for All_angles once for each sample
    if ~exist('Slice_angles','var')
        Slice_angles = zeros(width*width,Nb_of_FOV,Nb_of_Slices);
    end

    % Set threshold for actin for all the samples

```

```

if ~exist('thresh','var')
    thresh = actinDetectTest(lsm{1,1}{actinLayerNumber +
2*ChannelCount,1},blksize,PixelSize);
end

```

Get orientation for each slice and each location

```

for s = 1:Nb_of_Slices

    % Here we mask the actin and actinin signal. The masks are
    % transformed / eroded/dilated to represent the actual coverage
    % of cardiomyocytes / code by Ivan Batalov
    actin = lsm{1,1}{actinLayerNumber + (s - 1)*ChannelCount,1};
    sarcomeres = lsm{1,1}{actininLayerNumber + (s - 1)*ChannelCount,1};

    if ~isa(sarcomeres, 'double')
        sarcomeres = double(sarcomeres);
        actin = double(actin);
    end

    actin(1,1) = maxActinPx;
    sarcomeres(1,1) = maxSarcomerePx;

    [imSizeX,imSizeY] = size(sarcomeres);

    threshold = (0.1*max(sarcomeres(:))+0.9*min(sarcomeres(:)));
    actinThreshold = (0.05*max(actin(:))+0.95*min(actin(:)));
    d = floor(1.5*blksize);

    sarcomereMask = bwmorph(sarcomeres > threshold, 'open');
    actinMask = bwmorph(actin > actinThreshold, 'open');
    sarcomeres_border = bwmorph(sarcomereMask, 'remove');
    actin_border = bwmorph(actinMask, 'remove');

    disk = strel('disk', d, 0);
    sarcomereMask = sarcomereMask | imdilate(sarcomeres_border, disk);
    actinMask = actinMask | imdilate(actin_border, disk);

    % erode 60%, because cells' area is higher than sarcomere coverage
    sarcomereMask = bwmorph(sarcomereMask, 'erode', floor(d*0.6));
    actinMask = bwmorph(actinMask, 'erode', floor(d*0.6));
    actinMask = actinMask | sarcomereMask; % expand actin mask to include sarcomere mask
    ActinAreaFraction = nnz(actinMask)/((imSizeX-20)*(imSizeY-20));
    ActininAreaFraction = nnz(sarcomereMask)/((imSizeX-20)*(imSizeY-20));
    [~, orientation] = actinDetectSlice(actin,blksize,thresh,width,sarcomereMask);

    if ActininAreaFraction > 0

        % Keep non-zero values only
        nonzero_orientation = orientation(orientation ~=0);

        % Get descriptive stats

```

```

[Mean, Std, Median, ~, Mode] = descriptive_stats(nonzero_orientation,180);
ActinAreaFraction = length(nonzero_orientation)/((width-20)*(width-20));
OrientationOrderParameter = OOP(nonzero_orientation);

% store stats and names for all slices
slice_name = sprintf([stack_name(1:end-4) ' z=%i'],s);
Slices_stats(spl,fov,s,:) = {slice_name
,ActinAreaFraction,Mean,Std,Median,Mode,OrientationOrderParameter,ActininAreaFraction};
Slices_names(spl,fov,s) = {slice_name};
else

% store stats and names for all slices
slice_name = sprintf([stack_name(1:end-4) ' z=%i'],s);
Slices_stats(spl,fov,s,:) = {slice_name ,0,0,0,0,0,0,0};
Slices_names(spl,fov,s) = {slice_name};
end

% Gather angles
Slice_angles(:,fov,s) = orientation;

end

```

```
end
```

```

%Flatten and remove null values from slice_angles
Slice_angles = Slice_angles(:);
Slice_angles = Slice_angles(Slice_angles~=0);

[Mean, Std, Median, ~, Mode] = descriptive_stats(Slice_angles,180);
ActinAreaFraction = length(Slice_angles)/Nb_of_FOV/Nb_of_Slices/((width-20)*(width-20));

%angles here should be in radians, cause cos() and sin() functions are
%used
OrientationOrderParameter = OOP(Slice_angles);
Samples_stats (spl,:) =
{sample_name,ActinAreaFraction,Mean,Std,Median,Mode,OrientationOrderParameter, []};

%Save all angles for the sample for record keeping
save([sample_name '_angles.mat'],'slice_angles');
Samples_names{spl}=sample_name;
clear slice_angles

end
save([exp_title '_stats.mat'],'Slices_stats', 'Samples_stats', 'Samples_names');
fclose('all');
clearvars thresh;
toc;

```



```

function [ all_orientation , cm_orientation] = actinDetectSlice(
actin,blksize,thresh,Size,sarcomereMask )
%actinDetectSlice returns the list of orientation angles for all cells and for cardiomyocytes
only for a single image
% - Performs actinDetect on a single slice and returns the list of non zero
%   angles
% - If sarcomereMask exists, it also returns cm_orientation

% Adapted from:
% Peter Kovesi
% School of Computer Science & Software Engineering
% The University of Western Australia
% pk at csse uwa edu au
% http://www.csse.uwa.edu.au/~pk
% January 2005

% Identify ridge-like regions and normalise image
% disp('Normalizing Image and Creating Mask' )
[normim, mask] = ridgesegment(actin, blksize, thresh);
show(mask,2);
show(normim,1);

% Determine ridge orientations
% disp('Calculating Ridge Orientations' )
[orientim, reliability] = ridgeorient(normim, 1, 3, 3);
plotridgeorient(orientim, 20, actin, 3)
show(reliability,4)

% Only keep orientation values with a reliability greater than 0.5
reliability_binary = reliability>0.5;

% Remove 10 pixel wide border where orientation values are not accurate
reliability_binary(:,1:1:10) = 0;
reliability_binary(1:1:10,:) = 0;
reliability_binary(:,Size-10:1:Size) = 0;
reliability_binary(Size-10:1:Size,:) = 0;

% Multiply orientation angles by the binary mask image to remove
% data where there are no cells
newmask = mask.*reliability_binary;
show(newmask,5)
orientim = orientim.*newmask;

% Get cm_orientation only if sarcomereMask exists
if ~isempty(sarcomereMask)
    cm_mask = newmask.*sarcomereMask;
    show(cm_mask,6)
    cm_orientim = orientim.*cm_mask;
    show(cm_orientim,7)
else
    cm_orientim = [];
end

```

```

% Convert 2D-array to 1D vector
all_orientation = orientim(:);
cm_orientation = cm_orientim(:);

end

```

Published with MATLAB® R2015a

```

function [ thresh ] = actinDetectTest( image ,blksize, PixelSizeX )
%actinDetectTest Choose parameters thresh for actinDetect
% Runs actinDetect on 1 slice to determine optimal parameters for
% analysis

% Adapted from Adam W. Feinberg

thresh = 0;

% Identify ridge-like regions and normalise image
index = 0;
while index < 1;
% % Threshold of standard deviation to decide if a block is a ridge region
thresh = input('Enter Threshold (0.1 - 0.2): ');
disp('Normalizing Image and Creating Mask' )
[normim, mask] = ridgesegment(image, blksize, thresh);
normim_fig=figure;
imshow(normim,[]);
mask_fig=figure;
imshow(mask,[]);

% Determine if normalization and mask look good, click on image to
% accept or press any key to enter new values
w = input('Accept Threshold (yes = 1, no = 0): ');
if w == 1
disp('Image threshold accepted' )
index = 1;
else
disp('Re-analyze imaging...')
end
end

return

end

```

Published with MATLAB® R2015a

```

function [ MIP ] = max_projection( image, info , channels)
%max_projection Create a matrix with channels based on a maximum intensity projection of
%image (OME format) along Z
% info = metadata for the image
% image = structure created when opening an image with Bioformats : bfoopen(...){idx,1}
% channels = [2,3] to get only channels 2 and 3

% Create 4-D Matrix
ChannelCount = info.getChannelCount(0);
PlaneCount = info.getPlaneCount(0)/ChannelCount;
[Height, width] = size(image{1});

MIP = zeros (Height,width,PlaneCount,length(channels));
% bioformats stores all the channels consecutively (C=1,Z=1),(C=2,Z=1) then (C=1,Z=2)
for plane = 1:PlaneCount
    for j = 1:length(channels)
        MIP(:,:,plane,j) = image{ChannelCount*(plane-1)+channels(j)};
    end
end
size(MIP)

% Z-project for each channel
MIP = squeeze(max(MIP,[],3));

if ~isa(MIP, 'double'),
    MIP=double(MIP);
end
end

```

Published with MATLAB® R2015a

```

function [ Mean, Std, Median, n, Mode ] = descriptive_stats( Angles, Nbins )
%descriptive_stats Returns mean, standard deviation, median, normalized histogram with Nbins bins
and mode
% Angles need to be a column vector of values in radians

% Convert radians to degrees
if max(Angles)<= pi
    Angles_deg = Angles / pi * 180;
else Angles_deg = Angles;
end

% Calculate stats for entire sample

Mean = mean(Angles_deg);
Std = std(Angles_deg);
Median = median(Angles_deg);

% Create histogram
[n,xout] = hist( Angles_deg , Nbins );

```

```

dx = xout(2)-xout(1);           % calc a single bin width
n = n / sum( n*dx );           % normalize histogram to have area of 1

% Find mode
[~,I] = max(n);
Mode = xout(I);

end

```

Published with MATLAB® R2015a

```

function [ Orientational_order_parameter ] = OOP( nonzero_orientation )
% OOP calculate orientational order parameter of a matrix
%
%     Use this function to get orientational order parameter of actin stained
%     images
%
% Inputs = nonzero_orientation (array of the nonzero orientation angles)
% which can be in rad or degrees
% NB: cos and sin functions need radians
%
% Outputs = Orientational_order_parameter

% Make sure the input is in radians
if max(nonzero_orientation)>pi;
    disp('Conversion to radians')
    nonzero_orientation = deg2rad(nonzero_orientation);
end

%Tensor Method for Orientational Order Parameter
%Calculate x and y components of each vector r
Vectors(1,:) = cos(nonzero_orientation);
Vectors(2,:) = sin(nonzero_orientation);

%Calculate the Orientational Order Tensor for each r and the average
%Orientational Order Tensor (OOT_Mean)
for i=1:2
    for j=1:2
        OOT_All(i,j,:)=Vectors(i,:).*Vectors(j,:);
        OOT_Mean(i,j) = mean(OOT_All(i,j,:));
    end
end

%Normalize the orientational Order Tensor (OOT), this is necessary to get the
%order parameter in the range from 0 to 1
OOT = 2.*OOT_Mean-eye(2);
%Find the eigenvalues (orientational parameters) and
%eigenvectors (directions) of the Orientational Order Tensor
[~,orient_parameters]=eig(OOT);
%orientational order parameters is the maximal eigenvalue, while the
%direcoter is the corresponding eigenvector
Orientational_order_parameter = max(max(orient_parameters));

```

```
end
```

[Published with MATLAB® R2015a](#)

```
%Script to create Pivot table from an array of stats from each slice across
%many locations/samples/experiments

% Requires cell2piv.m by Daniel Moran

%load the .mat files created by actinDetectMulti_slice_by_slice
%sequentially and rename them... here 'HCM***' = name of experiments
HCM23_stats=Slices_stats;
HCM23_names=Samples_names;

HCM29d_stats=Slices_stats;
HCM29d_names=Samples_names;

HCM30b_stats=Slices_stats;
HCM30b_names=Samples_names;

HCM33a_stats=Slices_stats;
HCM33a_names=Samples_names;

HCM34b_stats=Slices_stats;
HCM34b_names=Samples_names;

HCM35b_stats=Slices_stats;
HCM35b_names=Samples_names;
```

Assemble matrix such that dim1 = experiments, dim2=samples, dim3 = field of view, dim4 = slice in z-stack, dim5 = stats

```
number_of_experiment = 6;
HCM_stats = cell(number_of_experiment,8,6,7,8);
for sp1 = 1:size(HCM23_stats,1)
    for FOV = 1:6
        for z = 1:7
            HCM_stats(1,sp1,FOV,z,:)=HCM23_stats(sp1,FOV,z,:);
        end
    end
end

for sp1 = 1:size(HCM29d_stats,1)
    for FOV = 1:6
        for z = 1:7
            HCM_stats(2,sp1,FOV,z,:)=HCM29d_stats(sp1,FOV,z,:);
        end
    end
end
```

```

        end
    end
end

for sp1 = 1:size(HCM33a_stats,1)
    for FOV = 1:6
        for z = 1:7
            HCM_stats(4,sp1,FOV,z,:)=HCM33a_stats(sp1,FOV,z,:);
        end
    end
end

for sp1 = 1:size(HCM30b_stats,1)
    for FOV = 1:6
        for z = 1:7
            HCM_stats(3,sp1,FOV,z,:)=HCM30b_stats(sp1,FOV,z,:);
        end
    end
end

for sp1 = 1:size(HCM34b_stats,1)
    for FOV = 1:6
        for z = 1:7
            HCM_stats(5,sp1,FOV,z,:)=HCM34b_stats(sp1,FOV,z,:);
        end
    end
end

for sp1 = 1:size(HCM35b_stats,1)
    for FOV = 1:6
        for z = 1:7
            HCM_stats(6,sp1,FOV,z,:)=HCM35b_stats(sp1,FOV,z,:);
        end
    end
end
end

```

Flatten array to size x 6: one column each for experiment, sample, field of view, slice, and statistic

```

HCM_stats_pivot = cell2piv( HCM_stats,
{'HCM23', 'HCM29d', 'HCM30b', 'HCM33a', 'HCM34b', 'HCM35b'}, 1:8, 1:6, 1:7, ...
    {'slice_name'
, 'PercentActinArea', 'Mean', 'Std', 'Median', 'Mode', 'OrientationOrderParameter', 'CM_coverage'}, ...
    {'Experiment', 'Sample', 'FOV', 'Z', 'Stats'});

% Remove empty rows
HCM_stats_pivot(all(cellfun('isempty', HCM_stats_pivot(:,6)), 2), :) = [];

```

Rework HCM_stats_pivot to add sample_names

```

for i = 1:size(HCM_stats_pivot,1)
    sample_number = str2double(HCM_stats_pivot{i,2});
    if ~isnan(sample_number)
        switch HCM_stats_pivot{i,1}
            case 'HCM23'
                HCM_stats_pivot{i,2}=HCM23_names{sample_number};

            case 'HCM29d'
                HCM_stats_pivot{i,2}=HCM29d_names{sample_number};

            case 'HCM30b'
                HCM_stats_pivot{i,2}=HCM30b_names{sample_number};

            case 'HCM33a'
                HCM_stats_pivot{i,2}=HCM33a_names{sample_number};

            case 'HCM34b'
                HCM_stats_pivot{i,2}=HCM34b_names{sample_number};

            case 'HCM35b'
                HCM_stats_pivot{i,2}=HCM35b_names{sample_number};
        end
    end
end
end

```

Save

```

save HCM_stats_pivot.mat

xlswrite('HCM Pivot.xlsx',HCM_stats_pivot,'TableStats','A1');

```

Published with MATLAB® R2015a

Appendix C Peer-reviewed article 1

Below is an article that was published in Nature Methods and selected for cover art in the February 2015 issue¹²². The work leveraged the surface-initiated assembly technique to enable ECM patterning of substrates with complex topography (e.g. high aspect ratio ridges, sandpaper...).

Conformal nanopatterning of extracellular matrix proteins onto topographically complex surfaces

Yan Sun^{1,2,4}, Quentin Jallerat^{1,4}, John M Szymanski^{1,4} & Adam W Feinberg^{1,3}

Our Patterning on Topography (PoT) printing technique enables fibronectin, laminin and other proteins to be applied to biomaterial surfaces in complex geometries that are inaccessible using traditional soft lithography techniques. Engineering combinatorial surfaces that integrate topographical and biochemical micropatterns enhances control of the biotic-abiotic interface. Here, we used this method to understand cardiomyocyte response to competing physical and chemical cues in the microenvironment.

The nano- and microscale patterning of biomaterial surfaces has enabled the development of advanced systems to control cell structure and function. Specifically, engineering topographical, chemical and/or mechanical cues in defined geometries can directly regulate cell adhesion, morphology, cytoskeletal organization and cell-cell interactions. The technology to do this is based primarily on photolithographic techniques to create nano- or micropatterned masters (typically silicon wafers) that are then replica molded to make topographically patterned surfaces in other materials such as hydrogels and elastomers. These are used directly for cell culture or are formed into stamps and microfluidic systems to pattern extracellular matrix (ECM) proteins, growth factors and other bioactive molecules onto surfaces¹. Researchers have shown that these nanometer- and micrometer-scale patterns of topography and biochemistry can each align cells, organize anisotropic tissue sheets and modulate gene expression profiles^{2,3}. There is also evidence of the synergistic effect of combining these patterned cues into an integrated surface, such as for the enhanced alignment of neurons⁴ and endothelial cells⁵. However, to date, the ability to independently engineer microtopography and patterned chemistry into hierarchically structured surfaces has been limited due to the technical challenge of chemical patterning onto rough surfaces.

Here we report the Patterning on Topography (PoT) printing technique, which is able to directly transfer ECM proteins in defined

geometries from a smooth release surface onto a microtopographically complex surface while substantially maintaining pattern fidelity (Fig. 1a and Online Methods). Briefly, thermally sensitive poly(*N*-isopropylacrylamide) (PIPAAm) is spin-coated onto glass coverslips (Fig. 1a, step 1, and Supplementary Fig. 1); then an ECM protein is patterned onto the PIPAAm using microcontact printing (μ CP) with a polydimethylsiloxane (PDMS) stamp (Fig. 1a, step 2). Next, a topographically patterned surface is brought into contact with the ECM patterned PIPAAm-coated coverslip (Fig. 1a, step 3), submerged in distilled water at 40 °C and slowly cooled to room temperature. As the PIPAAm transitions through its lower critical solution temperature at ~35°C, the PIPAAm swells and pushes the patterned ECM protein as an ~5-nm thick layer^{6,7} onto the adjacent, topographically patterned surface where it adheres due to hydrophobic interactions (Fig. 1a, step 4). As the PIPAAm continues to swell, it eventually dissolves (Fig. 1a, step 5) and the PoT-printed surface can be used for cell seeding and culture (Fig. 1a, step 6).

The unique capabilities of PoT printing to pattern ECM proteins on topographically patterned surfaces are clearly demonstrated when compared to standard μ CP and protein coatings adsorbed from solution. To show this, we used PDMS either spin coated onto glass coverslips as a flat control surface or cast against A4 paper, 150-grit sandpaper or 220-grit sandpaper. These surfaces were chosen because the heterogeneous distribution of feature width, depth and morphology enabled us to simultaneously evaluate the ability to pattern a wide range of microscale feature dimensions. We examined the full range of test surfaces and used confocal imaging and three-dimensional (3D) rendering to evaluate PoT printing fidelity (Fig. 1b and Supplementary Fig. 2). As expected, the spin-coated PDMS surface could be patterned with PoT or μ CP, with no discernible difference. In comparison, even the A4 paper was rough enough to present challenges to μ CP, resulting in a collapse of the line pattern and gaps in pattern transfer that caused a loss of fidelity. Results were worse on the rougher 220- and 150-grit sandpaper surfaces, with fibronectin (FN) transferred in patches and large gaps on the order of hundreds of micrometers. In contrast, the PoT-printed surfaces had well-transferred and conformal FN lines that maintained pattern fidelity and followed surface contours, even on the sandpaper surfaces (Fig. 1b and Supplementary Fig. 2).

Next, we used PoT to pattern ECM protein lines onto micro-ridges with defined geometries to determine the limits of the technique. Test surfaces with 20- μ m-wide, 20- μ m-spaced microridges demonstrated that we could PoT print up to 37 μ m deep, a depth-to-width aspect ratio of 1.85 (Supplementary Fig. 3). The FN lines were conformal to the ridge tops, the bottoms of the trenches and the vertical sidewalls, even on undercuts. Further, we could PoT print on deeper, 48- μ m microridges with a 2.4 aspect ratio corresponding to nearly 500% strain of

¹Department of Biomedical Engineering, Carnegie Mellon University, Pittsburgh, Pennsylvania, USA. ²School of Biological Science and Medical Engineering, Beihang University, Beijing, China. ³Department of Materials Science and Engineering, Carnegie Mellon University, Pittsburgh, Pennsylvania, USA. ⁴These authors contributed equally to this work. Correspondence should be addressed to A.W.F. (feinberg@andrew.cmu.edu).

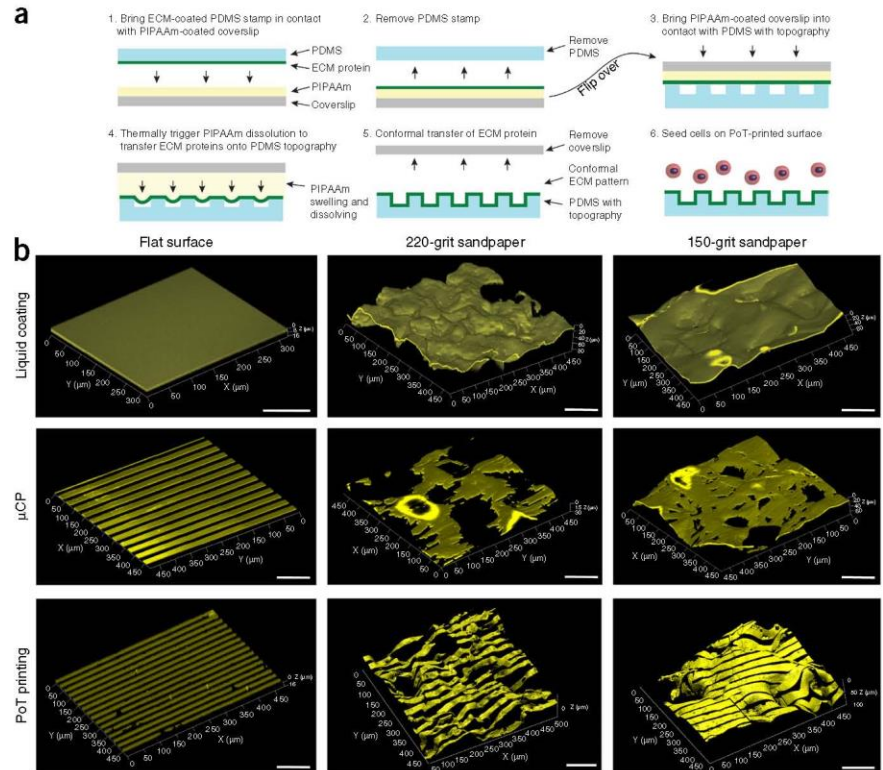
Figure 1 | PoT printing transfers nano- and micropatterns of ECM proteins onto microtopographically patterned surfaces.

(a) A schematic of the PoT process.

(b) Representative 3D confocal images of flat PDMS controls and PDMS negatives of the indicated surfaces coated with FN adsorbed from solution, microcontact printed (μ CP) with 20- μ m-wide, 20- μ m-spaced FN lines or PoT printed with 20- μ m-wide, 20- μ m-spaced FN lines. Scale bars are 100 μ m.

the FN; however, there were gaps in the FN on the sidewalls (see **Supplementary Note** for further discussion on PoT limitations). Varying feature dimensions demonstrated PoT printing on microridges from 2 μ m wide, 2 μ m spaced and 2.5 μ m deep up to 200 μ m wide, 200 μ m spaced and 36 μ m deep (**Supplementary Fig. 4**), and we expect that smaller (sub-micron) and larger features can also be patterned based on the sandpaper results (**Fig. 1b** and **Supplementary Fig. 2**). We also validated that other ECM proteins, including laminin and collagen type IV, could be PoT printed and that multiple proteins could be combined, such as FN and laminin lines orthogonal to each other and 45° to the microridges (**Supplementary Fig. 5**). Although we refer to PoT as a nanopatterning technique because the transferred ECM proteins are ~5 nm thick^{6,7}, we verified that PoT can also print conformal FN lines 100–500 nm wide and 5 μ m spaced on 15- μ m deep microridges (**Supplementary Fig. 6**). Finally, control experiments confirmed (i) that μ CP of the FN lines using a PDMS stamp with a low Young's modulus ($E \sim 50$ kPa) to better conform to the microridges failed to achieve results comparable to PoT (**Supplementary Fig. 7**) and (ii) that FN lines could also be PoT printed on stiffer photoresist microridges (**Supplementary Fig. 8**; see **Supplementary Note** for further discussion on μ CP techniques compared to PoT).

Next, we used PoT printing to investigate cell response to surfaces presenting orthogonal topographic and chemical guidance



cues. This is important for applications such as cardiac tissue engineering, where cardiomyocytes (CMs) can be engineered into anisotropic two-dimensional (2D) tissues using surfaces with either microridges⁸ or micropatterned^{9,10} FN lines. But what happens when CMs are presented with both alignment cues? Control 20- μ m-wide, 20- μ m-spaced microridges uniformly coated with FN and seeded with chick CMs resulted in cell alignment parallel to the microtopography (**Fig. 2a**). In contrast, CMs seeded on microridges with orthogonal PoT printed FN lines followed the FN lines despite having to traverse relatively large topographic features (**Fig. 2b,c** and **Supplementary Fig. 9**). Notably, the CMs were able to spread and deform around the microridges (**Fig. 2d–i**) while displaying a characteristic sarcomeric structure (**Supplementary Fig. 10**). To quantify this difference in cell response, we analyzed actin alignment relative to the microridges and FN lines (**Fig. 2j–l**). On the

uniformly FN-coated surface, CMs aligned in parallel with the underlying microridges (**Fig. 2j**). However, on the PoT-printed surface with 5- μ m microridges, CMs aligned with the underlying FN lines (**Fig. 2k**). As

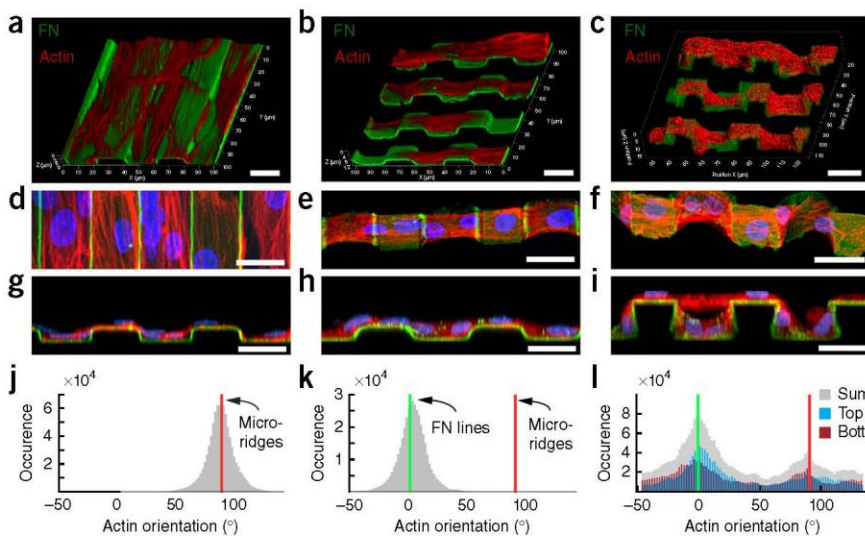


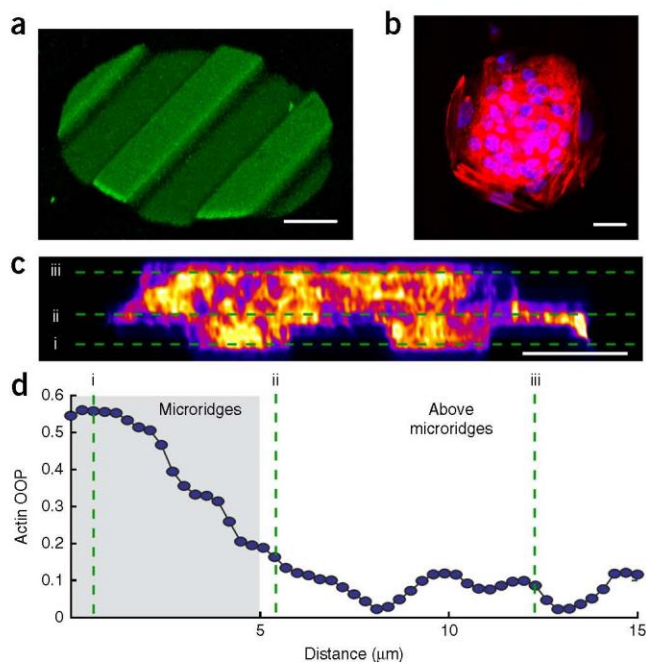
Figure 2 | PoT-printed surfaces direct cell alignment. (a) 20- μ m-wide, 20- μ m-spaced and 5- μ m-tall PDMS microridges uniformly coated with FN (green) and seeded with CMs stained for actin (red). (b,c) 20- μ m-wide FN lines PoT printed orthogonal to microridges that were 5 μ m (b) and 15.5 μ m (c) tall. (d–f) Top-down view of a subregion of the surfaces in a–c with CMs additionally stained for nuclei (blue). (g–i) Cross-sections of the areas in d–f. (j–l) Histograms of actin orientation angle for CMs in d–f. Images are representative of $n = 3$ samples for each depth. Scale bars are 20 μ m.

Figure 3 | Circular areas patterned onto microridges to investigate the interplay between micropatterned topography and chemistry. (a) 3D rendering of a 100- μm -diameter FN circle on top of 20- μm -wide, 20- μm -spaced, 5- μm -tall PDMS microridges. (b) Fluorescent image of CMs on the 100- μm -diameter FN circle stained for nuclei (blue) and actin (red). (c) Cross-section of the cardiac microtissue in **b** where CMs are classified as (i) in the microridges, (ii) just above the microridges or (iii) well above the microridges. (d) Quantification of the actin orientational order parameter (OOP) through the thickness of the cardiac microtissue in **a** and **c**. Images are representative of $n = 10$ samples for each condition. Scale bars are 20 μm .

the depth increased, CM alignment became bimodal, with cells on the ridge tops continuing to align to the FN lines and cells in the trenches shifting alignment 90° to the microtopography (Fig. 2l and Supplementary Fig. 9). This demonstrated that CM response was depth dependent, and cross-sectional views suggested that adhesion to the ridge sidewalls influenced this process (Fig. 2i). When vertical sidewalls were not present and changes in height were more gradual, such as for FN lines PoT printed on a PDMS replica of a 220-grit sandpaper, CM alignment followed the protein pattern (Supplementary Fig. 11). Control experiments confirmed that stability in culture and cell response to PoT-printed FN lines were similar to standard μCP FN lines (Supplementary Fig. 12).

Finally, we used PoT-printed FN circles to produce spatially variable guidance cues where the circle edge changed from being parallel to orthogonal to the underlying microridges at a $\pi/2$ interval. To do this, we patterned an array of 100- μm -diameter FN circles on 20- μm -wide, 20- μm -spaced and 5- μm -tall microridges (Fig. 3a). As expected, the FN circles conformally coated the ridge tops, sidewalls and trench bottoms, and the seeded CMs formed a cardiac microtissue that covered the entire surface (Fig. 3b). The microtissue was $\sim 15 \mu\text{m}$ thick, with distinct differences in CM alignment based on vertical position (Fig. 3c). Analysis of actin alignment (Fig. 3d and Supplementary Fig. 13) showed that CMs in the grooves were aligned to the microridges, those above the microridges were aligned to the edge of the FN circle, and those above that appeared completely isotropic, with no apparent guidance from the aligned CMs below. Increasing the diameter of the FN circle from 100 μm to 250 or 500 μm (Supplementary Figs. 14 and 15) showed that CM alignment to the edge of the FN circle extended $\sim 100 \mu\text{m}$ from the periphery. Although this is a basic example of combining spatially variable microtopographical and chemical cues, it clearly demonstrates (i) that in our system patterned FN over-rides topography in terms of CM alignment and (ii) that CM alignment to either cue depends on direct physical contact, and there is limited ability of CMs to propagate the alignment to neighboring cells.

PoT provides a methodology to probe how cells respond to competing topographical and chemical cues and to engineer surfaces that maximize a given behavior, such as organization of CM into an aligned cardiac tissue. Looking forward, PoT printing enables improved control over the cellular microenvironment, which will be useful for understanding basic cell-surface interactions as well as engineering more advanced biomaterial surfaces where topography and chemistry can be independently optimized.



METHODS

Methods and any associated references are available in the [online version of the paper](#).

Note: Any Supplementary Information and Source Data files are available in the online version of the paper.

ACKNOWLEDGMENTS

We acknowledge financial support from China Scholarship Council (CSC) for State Scholarship Fund No. [2008]3027 (Y.S.), the Carnegie Mellon University Dowd-ICES Fellowship (Q.J.), the NIH Biomechanics in Regenerative Medicine T32 training grant (T32EB003392) and the Bertucci Graduate Fellowship (J.M.S.) and the NIH Director's New Innovator Award (DP2HL117750) (A.W.F.).

AUTHOR CONTRIBUTIONS

A.W.F. conceived and supervised the project. A.W.F. and Y.S. designed the experiments. Y.S., Q.J. and J.M.S. performed the experiments. A.W.F., Q.J., J.M.S. and Y.S. analyzed the data and wrote the paper.

COMPETING FINANCIAL INTERESTS

The authors declare competing financial interests: details are available in the [online version of the paper](#).

Reprints and permissions information is available online at <http://www.nature.com/reprints/index.html>.

- Whitesides, G.M., Ostuni, E., Takayama, S., Jiang, X.Y. & Ingber, D.E. *Annu. Rev. Biomed. Eng.* **3**, 335–373 (2001).
- Bettinger, C.J., Langer, R. & Borenstein, J.T. *Angew. Chem. Int. Ed.* **48**, 5406–5415 (2009).
- Falconnet, D., Csucs, G., Michelle Grandin, H. & Textor, M. *Biomaterials* **27**, 3044–3063 (2006).
- Greene, A.C., Washburn, C.M., Bachand, G.D. & James, C.D. *Biomaterials* **32**, 8860–8869 (2011).
- Feinberg, A.W. et al. *J. Biomed. Mater. Res. A* **86A**, 522–534 (2007).
- Szymanski, J.M., Jallerat, Q. & Feinberg, A.W. *J. Vis. Exp.* **86**, e51176 (2014).
- Feinberg, A.W. & Parker, K.K. *Nano Lett.* **10**, 2184–2191 (2010).
- Chung, C.-Y. et al. *FASEB J.* **25**, 851–862 (2011).
- Feinberg, A.W. et al. *Biomaterials* **33**, 5732–5741 (2012).
- Feinberg, A.W. et al. *Science* **317**, 1366–1370 (2007).

ONLINE METHODS

Fabrication of microtopographically modified surfaces. Polydimethylsiloxane (PDMS, Sylgard 184, Dow-Corning) was mixed in a 10:1 base resin-to-curing agent ratio, degassed and then used to create the different microtopographically modified surfaces in this study. Smooth control surfaces were fabricated by spin-coating the PDMS on 25-mm-diameter glass coverslips at 4,000 r.p.m. and cured at 65 °C for 4 h to create ~15- μ m-thick films¹¹. Surfaces with random microtopographies were fabricated by creating PDMS replicas (negatives) of A4 printer paper and 220-grit and 150-grit sandpaper. To do this, a 4 × 4-cm square of the paper was placed into the bottom of a 10-cm petri dish and PDMS was poured on top to an approximate thickness of 0.5 cm. The PDMS was cured at 65 °C for 4 h, peeled off and then cut into 1 × 1-cm squares. Surfaces with microridge topographies were fabricated by using photolithography according to previously published methods^{7,11}. The materials used for photolithography varied depending on the photoresist layer thickness. For photoresist layers with a thickness between 2 and 10 μ m, SPR 220.3 photoresist (Microchem) was spin-coated onto glass wafers. Thicker photoresist layers between 10 and 40 μ m were prepared by spin-coating SU-8 2015 photoresist (Microchem) onto silicon wafers. SU-8 2050 photoresist (Microchem) was spin-coated onto silicon wafers to generate photoresist layers thicker than 40 μ m. All photoresist layers were exposed to UV light through a transparency photomask and then developed using SU8 developer or MF-26A developer (SU8 and SPR respectively, Microchem) to create SU-8 or SPR microridges on top of silicon or glass wafers. Patterned wafers were then coated with PDMS to a thickness of 0.5 cm, cured at 65 °C for 4 h, peeled off and then cut into 1 × 1-cm squares.

Uniform coating and microcontact printing (μ CP) of ECM proteins. For uniform protein coatings adsorbed from solution, the PDMS substrates were sonicated in 50% ethanol for 30 min and dried by nitrogen. The ECM protein fibronectin (FN) (Corning, catalog number 356008) was diluted to a concentration of 50 μ g/mL in distilled water; 40% of the FN was conjugated to Alexa Fluor 488 fluorescent dye (Life Technologies). A 300- μ L droplet of FN solution was incubated on the PDMS substrates for 15 min, rinsed two times with distilled water and then dried under nitrogen. For μ CP, PDMS stamps with microridges 20 μ m wide, 20 μ m spaced and 2 μ m tall were fabricated using photolithography as described above for the microtopographically modified surfaces. PDMS stamps were sonicated in 50% ethanol for 30 min and dried by nitrogen, incubated with FN solution for 1 h, rinsed two times with distilled water and then dried under nitrogen. The μ CP of laminin (LAM, Invitrogen) and collagen type IV (COL IV, Sigma) were performed similarly except both were diluted to working concentrations of 100 μ g/mL in distilled water. The PDMS substrates to be patterned were UV/ozone treated for 15 min and then brought into conformal contact with the PDMS stamps for 5 min. Gentle pressure by lightly tapping the back of the PDMS stamps with tweezers was used to ensure contact.

Patterning on Topography (PoT) printing of ECM proteins. The PoT printing process is a modification of surface-initiated assembly⁷ where the release of the ECM protein occurs directly

onto a microtopographically structured surface. To do this, we first spin-coated 25-mm-diameter glass coverslips with a 10% poly(*N*-isopropylacrylamide) (PIPAAm, Polysciences, Inc.) in 1-butanol (w/v) solution at 6,000 r.p.m. To PoT print features with a depth-to-width aspect ratio higher than 0.5, we increased the thickness of the PIPAAm layer by spin-coating glass coverslips with a 40% PIPAAm in 1-butanol (w/v) solution at 2,000 r.p.m. PIPAAm layer thickness was determined by first spin-coating PIPAAm at different concentrations and then making a small scratch through the PIPAAm layer with a razor blade. Next, we used atomic force microscopy (AFM, MFP3D, Asylum Research) in air using AC mode with AC160TS-R3 cantilevers (Olympus Corporation) to scan over the scratch. The thickness of the PIPAAm layer was then quantified using the IGOR Pro software environment (WaveMetrics, Inc.). Prior to PoT printing, the PIPAAm-coated coverslips were sterilized using high-intensity UV light for 15 min. Fluorescently labeled FN, LAM and COLIV were then patterned onto the PIPAAm-coated coverslips by μ CP with various geometries, including (i) 20- μ m-wide, 20- μ m-spaced lines; (ii) 100- μ m-diameter circles; (iii) 250- μ m-diameter circles and 500- μ m-diameter circles. Next, PDMS substrates with microtopography on the surface were sterilized using high-intensity UV light for 15 min and placed in conformal contact with the protein-patterned PIPAAm coverslips for 10 min. Making sure to keep the PDMS stamp and PIPAAm surface in contact, the samples were placed within the well of a 6-well plate, 40 °C sterile distilled water was poured onto the stamp and PIPAAm and then the plate was placed in a 37 °C incubator for at least 3 h to allow time for water to enter the channels or spaces and diffuse into the PIPAAm. The plate was then removed from the incubator and placed in the biosafety cabinet at room temperature for 1 h to dissolve the PIPAAm layer and release the ECM patterns onto the PDMS substrates. Once the PIPAAm dissolved, the PDMS and coverslip were no longer attached and the PoT-printed PDMS substrate could then be removed and used for cell culture or analysis. We also tested the ability to PoT print onto very stiff substrates by placing an SPR 220.3 master mold containing 20- μ m-wide, 20- μ m-spaced and 3- μ m-tall microridges into conformal contact with a PIPAAm-coated coverslip patterned with 20- μ m-wide and 20- μ m-spaced FN lines. For all experiments, PoT-printed substrates that had defects due to poor contact with the PIPAAm-coated coverslip or to improper water penetration within the topography were discarded. At least three samples per condition were used for imaging and cell seeding.

Cardiomyocyte isolation and culture. Chick cardiomyocytes (CMs) were isolated from day 7–8 (HH stages 30–32) White Leghorn embryos and are not considered live vertebrate animals under PHS policy. For each isolation, 7–15 hearts were dissected, cut into small pieces and digested in 3 mL of 0.05% Trypsin-EDTA (Sigma-Aldrich) for 7 min. The supernatant was carefully collected, added to seeding medium (M199 medium, 10% heat-inactivated FBS, 1% penicillin/streptomycin) and filtered through a 40- μ m cell strainer to isolate individual cells. The 7-min incubation was repeated three times so that the hearts were completely digested while minimizing cytotoxicity by long exposure to trypsin. The cell solution was then centrifuged at 50g for 10 min and resuspended in 30 mL of seeding medium. Fibroblasts were removed by selective adhesion by pre-plating successively for

45-min incubations in T75 cell culture flasks. The supernatant, enriched in CMs, was centrifuged at 50g for 10 min then resuspended in seeding medium at 7.5×10^5 cells/mL. PDMS substrates were placed in a 6-well plate, 200 μ L of the cell suspension was pipetted on top and incubated for 2 h to allow cells to attach and then the wells were filled with additional seeding medium. On the next day, the medium was replaced with a maintenance medium containing a reduced level of 2% heat-inactivated FBS to minimize fibroblast proliferation.

Fluorescent staining and imaging. The CMs and ECM proteins were fluorescently labeled to analyze the surface structure and cell response. The FN (human, Corning, catalog number 356008) was fluorescently labeled before use with fluorescent dyes, either Alexa Fluor 546 maleimide or Alexa Fluor 488 carboxylic acid, succinimidyl ester (Life Technologies), according to published methods¹². The fluorescently labeled FN was combined with unlabeled FN at a volume concentration of 40%. PDMS surfaces PoT printed with LAM or COL IV were fluorescently stained using monoclonal primary antibodies (Sigma, catalog number L9393 for LAM, C1926 for COL IV) followed by staining using Alexa Fluor 488-conjugated goat anti-mouse secondary antibodies (Life Technologies, catalog number A-11001). The CMs were cultured for 2 days, removed from the incubator, briefly washed with 37 °C PBS and then fixed for 15 min in 4% paraformaldehyde with 0.05% Triton X-100. Next, samples were blocked for 1 h with 5% goat serum and then incubated with 1:200 DAPI, 1:100 primary monoclonal antibody against sarcomeric alpha-actinin (Sigma, catalog number A7811) and 1:60 Phalloidin conjugated to Alexa Fluor 633 (Life Technologies) for 2 h at 37 °C. Samples were subsequently washed three times for 10 min in PBS and then incubated with goat anti-mouse secondary antibody conjugated to Alexa Fluor 488 for 2 h at 37 °C. Finally, samples were washed three times for 10 min in PBS and mounted against No. 1.5 glass coverslips with Prolong Gold (Life Technologies). Substrates were imaged using a Zeiss LSM 700 laser scanning confocal microscope with 40 \times (NA = 1.3) and 63 \times (NA = 1.4) oil immersion objectives or a Leica SP5 multiphoton microscope with a 25 \times (NA = 0.95) water immersion objective. 3D image stacks were deconvolved using AutoQuant X3 (Media Cybernetics, Inc.). Image processing and 3D rendering were performed using Zen 2010 (Zeiss), ImageJ image processing software (NIH) and Imaris (Bitplane, Inc.).

Image analysis of actin alignment. The alignment of actin filaments was analyzed using a modified ridge detection algorithm according to previously published methods¹³. Briefly, Phalloidin-labeled images of actin filaments were captured as z-stacks for CMs on the PoT-printed surfaces. The 8-bit gray scale images were normalized and an orientation vector map was generated from the pixel intensity gradients. These orientation vectors were found parallel to the actin filaments and used to generate a histogram where cytoskeletal anisotropy was designated as a distinct peak at a specific angle. For deeper microridges, sub z-stacks for the top and bottom halves of the samples were created and analyzed. The 2D orientational order parameter (OOP) was used as a measure of alignment⁹, with a scale from 0 to 1, 0

indicating complete isotropic orientation and 1 indicating perfect anisotropic orientation.

PoT printing of nanoscale ECM patterns. To fabricate FN nanofibers with a submicron width, we used a Photonic Professional GT 3D printer (Nanoscribe GmbH). Briefly, a master mold containing 250- μ m-long, 5- μ m-wide, 2- μ m-high and 500-nm-spaced features was first designed in AutoCAD (Autodesk Inventor) and exported into DeScribe 2.0 software. The master mold was then 3D printed using IP-L photoresist. Unexposed regions were then removed by immersion in a PGMEA developer solution (Microchem). PDMS stamps containing the negative of the master mold (yielding 500-nm-wide features) were prepared by casting the PDMS pre-polymer solution over the master mold as previously mentioned. To accurately assess their nanoscale dimensions, the FN was μ CP onto PIPAAm-coated glass coverslips and scanned using AFM in air using AC mode with AC160TS-R3 cantilevers (Olympus Corporation). High-resolution AFM images were obtained using a scan size of 1,024 \times 1,024 lines over a scan area of 8 μ m \times 8 μ m. The nanofiber width was quantified using the IGOR Pro software environment (WaveMetrics, Inc.).

Stability of PoT-printed ECM patterns in culture. PDMS-coated coverslips were either μ CP or PoT printed with 20- μ m-wide and 20- μ m-spaced FN lines that were fluorescently labeled as previously described. All substrates were treated with 1% Pluronic F-127 (Sigma-Aldrich) for 15 min, washed three times with PBS and then placed in separate wells of a 6-well plate. For each condition, three coverslips were seeded with 50,000 C2C12 mouse myoblasts (ATCC, CRL-1772) per well in growth medium (DMEM, 10% FBS, 1% penicillin/streptomycin, 1% L-glutamine) while three coverslips were kept in growth medium without cells. After 3 days in culture, all samples were fixed and cell samples were stained for nuclei and F-actin and imaged as described earlier. C2C12 cells were authenticated and certified mycoplasma-free by the manufacturer.

Fabrication of low Young's modulus PDMS stamps for μ CP. To determine the depth-to-width aspect ratio at which μ CP is unable to pattern topographical surfaces, we fabricated low Young's modulus PDMS stamps as described previously¹¹. Briefly, stamps with an elastic modulus of \sim 50 kPa were prepared by mixing Sylgard 184 and Sylgard 527 in a 10:1 ratio (w:w). Sylgard 184 was prepared as described previously while Sylgard 527 was prepared by mixing equal parts of A and B components per manufacturer's instructions. The 10:1 mixture of Sylgard 184 and Sylgard 527 was then cast over a SPR 220.3 master mold and cured at 65 °C for 4 h. Prior to casting, the SPR 220.3 master mold was silanized (PlusOne Repel-Silane ES, GE Healthcare) in a vacuum desiccator for at least 4 h. After curing, the stamps were peeled off of the master mold, coated with FN as previously described and then μ CP orthogonally onto PDMS microridges.

11. Palchesko, R.N., Zhang, L., Sun, Y. & Feinberg, A.W. *PLoS ONE* **7**, 1–13 (2012).

12. Klotzsch, E. *et al. Proc. Natl. Acad. Sci. USA* **106**, 18267–18272 (2009).

13. Bray, M.-A.P. *et al. Biomaterials* **31**, 5143–5150 (2010).

Appendix D Peer-reviewed article 2

Below is an article published in *Sciences Advances* describing a breakthrough bioprinting technique called FRESH. My contribution was limited to imaging, staining, and cell culture. The article features a direct and simple application of the microscopic study of the whole embryonic heart in chapter 3 : I created CAD models from the 3D confocal images , which were then bioprinted in alginate at a 20:1 scale.

Three-dimensional printing of complex biological structures by freeform reversible embedding of suspended hydrogels

Thomas J. Hinton,¹ Quentin Jallerat,¹ Rachele N. Palchesko,¹ Joon Hyung Park,¹ Martin S. Grodzicki,¹ Hao-Jan Shue,¹ Mohamed H. Ramadan,² Andrew R. Hudson,¹ Adam W. Feinberg^{1,3*}

2015 © The Authors, some rights reserved; exclusive licensee American Association for the Advancement of Science. Distributed under a Creative Commons Attribution License 4.0 (CC BY). 10.1126/sciadv.1500758

We demonstrate the additive manufacturing of complex three-dimensional (3D) biological structures using soft protein and polysaccharide hydrogels that are challenging or impossible to create using traditional fabrication approaches. These structures are built by embedding the printed hydrogel within a secondary hydrogel that serves as a temporary, thermoreversible, and biocompatible support. This process, termed freeform reversible embedding of suspended hydrogels, enables 3D printing of hydrated materials with an elastic modulus <500 kPa including alginate, collagen, and fibrin. Computer-aided design models of 3D optical, computed tomography, and magnetic resonance imaging data were 3D printed at a resolution of ~200 μm and at low cost by leveraging open-source hardware and software tools. Proof-of-concept structures based on femurs, branched coronary arteries, trabeculated embryonic hearts, and human brains were mechanically robust and recreated complex 3D internal and external anatomical architectures.

INTRODUCTION

Over the past decade, the additive manufacturing (AM) of biomaterials has transitioned from a rapid prototyping tool used in research and development into a viable approach for the manufacturing of patient-specific medical devices. Key to this is the ability to precisely control structure and material properties in three dimensions and tailor these to unique anatomical and physiological criteria based on computed tomography (CT) and magnetic resonance imaging (MRI) medical imaging data. First-in-human applications include customized polyetherketoneketone bone plates for the repair of large cranial defects (1, 2) and polycaprolactone bioresorbable tracheal splints for pediatric applications (3). The enabling three-dimensional (3D) printing technologies are primarily based on selective laser sintering of metal, ceramic, or thermoplastic microparticles; fused deposition modeling of thermoplastics, or on photopolymerization of photosensitive polymer resins (4, 5), and have tremendous growth potential for surgical and medical devices (4, 6) and scaffolds for tissue repair (7, 8). However, these approaches are limited in their ability to 3D print very soft materials such as elastomers, gels, and hydrogels that are integral components of many medical devices and are required for most future applications in tissue engineering and regenerative medicine (9, 10). Specifically, biological hydrogels composed of polysaccharides and/or proteins are a class of materials that are challenging to 3D print because they must first be gelled in situ during the fabrication process and then supported so that they do not collapse or deform under their own weight. Although the need for support materials is common across many AM techniques, it is particularly difficult for these soft biological hydrogels, where the elastic modulus is <100 kPa and there is a narrow range of thermal, mechanical, and chemical conditions that must be met to prevent damage to the materials and potentially integrated cells.

Current approaches for the 3D printing of biological hydrogels have achieved important advances but are still in need of significant

improvement (9, 11). For example, syringe-based extrusion has been used to 3D print polydimethylsiloxane (PDMS) elastomer and alginate hydrogel into multiple biological structures including the ear (12) and aortic heart valve (13, 14). Other research teams have demonstrated the direct bioprinting of fibrin (15, 16), gelatin (17), and mixtures of proteins derived from decellularized tissues (18) or cast extracellular matrix (ECM) gels around dissolvable templates (19). These results have expanded the range of materials that can be used and demonstrated the ability to incorporate and print live cells. There are also commercially available bioprinters from Organovo (20–22) and EnvisionTEC (7, 23) that have expanded the accessibility of bioprinters beyond the groups that custom build their own systems. However, the complexity of microstructures and the 3D anisotropy that can be created remain limited; often, the structures printed are simple square lattices, similar to stacked Lincoln Logs, which do not recapitulate the microstructure of real tissues.

As a field, significant improvements are still needed in terms of the ability to directly manufacture using biologically relevant hydrogels, controlling microstructure and anisotropy in 3D, and expanding biological AM research by driving down the cost of entry while increasing the quality and fidelity of the printing process. Our goal was to specifically address five major challenges including (i) deposition and cross-linking of soft biomaterials and viscous fluids with elastic moduli of <100 kPa, (ii) supporting these soft structures as they are printed so that they do not collapse or deform, (iii) anisotropically depositing the material to match the microstructure of real tissue, (iv) removing any support material that is used, and (v) keeping cells alive during this whole process using aqueous environments that are pH-, ionic-, temperature-, and sterility-controlled within tight tolerances (24–26).

RESULTS AND DISCUSSION

Using a thermoreversible support bath to enable freeform reversible embedding of suspended hydrogels

Here, we report the development of a 3D bioprinting technique termed freeform reversible embedding of suspended hydrogels (FRESH).

¹Department of Biomedical Engineering, Carnegie Mellon University, Pittsburgh, PA 15213, USA. ²Department of Chemistry, Carnegie Mellon University, Pittsburgh, PA 15213, USA. ³Department of Materials Science and Engineering, Carnegie Mellon University, Pittsburgh, PA 15213, USA.

*Corresponding author. E-mail: feinberg@andrew.cmu.edu

FRESH uses a thermoreversible support bath to enable deposition of hydrogels in complex, 3D biological structures and is implemented using open-source tools, serving as a highly adaptable and cost-effective biological AM platform. The key innovation in FRESH is deposition and embedding of the hydrogel(s) being printed within a second hydrogel support bath that maintains the intended structure during the print process and significantly improves print fidelity (Fig. 1, A and B, and movie S1). The support bath is composed of gelatin microparticles that act like a Bingham plastic during the print process, behaving as a rigid body at low shear stresses but flowing as a viscous fluid at higher shear stresses. This means that, as a needle-like nozzle moves through the bath, there is little mechanical resistance, yet the hydrogel being extruded out of the nozzle and deposited within the bath is held in place. Thus, soft materials that would collapse if printed in air are easily maintained in the intended 3D geometry. This is all done in a sterile, aqueous, buffered environment compatible with cells, which means cells can be extruded out of the printer nozzle with the hydrogel and maintain viability. Once the entire 3D structure is FRESH printed, the temperature is raised to a cell-friendly 37°C, causing the gelatin support bath to melt in a nondestructive manner. Although Wu *et al.* (27) previously described 3D printing of a hydrogel ink within a hydrogel support bath for omnidirectional printing, the fugitive ink was designed to leave microchannels within a permanent support bath that was ultravioletly cross-linked afterward to repair nozzle-induced damage. In contrast, FRESH enables the direct 3D printing of biologically relevant hydrogel inks including alginate, fibrin, collagen type I, and Matrigel within a fugitive support bath designed to be removed afterward.

FRESH is implemented on a MakerBot Replicator modified with a custom syringe-based extruder designed for precision hydrogel deposition. All plastic parts to convert the MakerBot into a bioprinter are printed in polylactic acid (PLA) using the stock thermoplastic extruder,

which is then replaced with the custom syringe-based extruder [the STL (stereolithography) file can be downloaded from <http://3dprint.nih.gov/>]. Our syringe-based extruder uses the stepper motor, taken from the original extruder, to move the plunger of a 3-ml syringe via a direct gear drive (fig. S1). The overall size and mass is comparable to the original extruder and, once mounted, integrates seamlessly with the MakerBot hardware and software, requiring only calibration of the number of motor steps that extrudes a given volume of fluid. Typically, we use a 150- μm -diameter stainless steel needle on the end of the syringe, but a range of needle diameters can be selected to control the volume of material being extruded.

The FRESH support bath consists of a slurry of gelatin microparticles processed to have a Bingham plastic rheology. To do this, we blended a solid block of gelatin hydrogel to break up the material into microparticles and then centrifuged it to remove the supernatant and produce the final slurry (fig. S2). Increasing the blending time decreases microparticle size (Fig. 1C), with a blending time of 120 s producing microparticles with a mean Feret diameter of $55.3 \pm 2 \mu\text{m}$ (Fig. 1D). Rheometry confirmed that the gelatin slurry that was blended for 120 s behaved like a Bingham plastic (Fig. 1E), not yielding until a threshold shear force is reached. Maintaining the gelatin slurry at room temperature ($\sim 22^\circ\text{C}$) preserves these rheological properties. For FRESH, the gelatin support slurry is loaded into a container of sufficient size to hold the part to be printed. In addition to its rheological and thermoreversible properties, gelatin was selected as the support bath material because it is biocompatible (28, 29). This is important, as it is unlikely that 100% of the gelatin is removed during the release process because it is a denatured form of collagen type I that can self-associate and bind to polysaccharides and other ECM proteins such as fibronectin (30, 31). Thus, it is unlikely that any small amount of residual gelatin will negatively affect cell integration and may actually enhance adhesion through integrin binding (32).

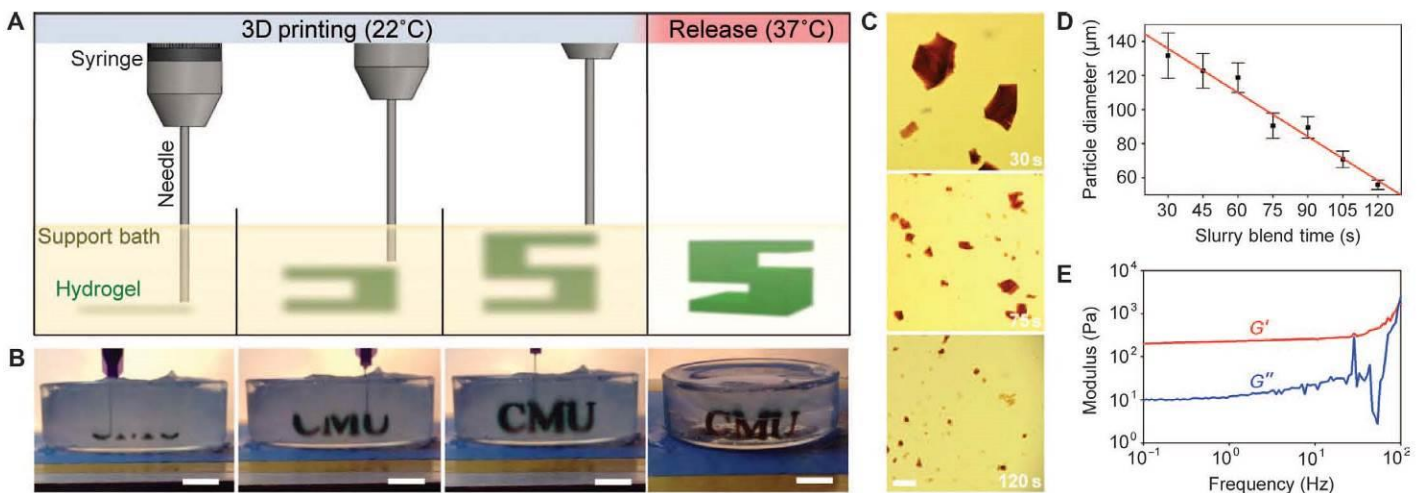


Fig. 1. FRESH printing is performed by depositing a hydrogel precursor ink within the thermoreversible support bath consisting of gelatin microparticles and initiating gelling in situ through one of multiple cross-linking mechanisms. (A) A schematic of the FRESH process showing the hydrogel (green) being extruded and cross-linked within the gelatin slurry support bath (yellow). The 3D object is built layer by layer and, when completed, is released by heating to 37°C and melting the gelatin. (B) Images of the letters “CMU” FRESH printed in alginate in Times New Roman font (black) and released by melting the gelatin support (gray material in the petri dish). When the gelatin support melts the change in optical properties, convective currents and diffusion of black dye out of the alginate make it appear that the letters are deforming, although they are not. (C) Representative images of gelatin particles produced by blending for 30, 75, or 120 s. (D) The mean Feret diameter of gelatin particles as a function of blending time from 30 to 120 s ($n > 1000$ per time point; the red line is a linear fit and error bars indicate SD). (E) Rheological analysis of storage (G') and loss (G'') modulus for gelatin support bath showing Bingham plastic behavior. Scale bars, 1 cm (B) and 1 mm (C).

Characterization of 3D printed hydrogels using FRESH

FRESH works by extruding the liquid phase material from the syringe into the support bath, where the material must rapidly gel into a filament without diffusing away. This gelation process occurs via rapid cross-linking of the polymer molecules into a network, and the cross-linking mechanism depends on the hydrogel being 3D printed. We have validated this process using fluorescently labeled alginate cross-linked by divalent cations (0.16% CaCl_2) added to the support bath. A representative alginate filament embedded in the support bath illustrates that the gelatin microparticles are moved out of the way but still influence the surface morphology of the filament (Fig. 2A). As the alginate gels, there are visible “spurs” that form in between microparticles. However, these are not necessarily a problem in the context of a larger 3D printed structure because filaments fuse together to form the 3D printed part and thus these spurs may actually enhance this process by better bridging filaments. For this representative filament, the diameter of the extrusion was $199 \pm 41 \mu\text{m}$ (Fig. 2B). However, the diameter of the extruded hydrogel filament depends on a large number of factors including the hydrogel being printed and its cross-linking kinetics, gel-

atin microparticle size, nozzle diameter, extruder translation speed, and flow rate. Thus, similar to 3D printing of most materials, the resolution and morphology of a print depend on a number of machine settings and require optimization for each material used.

Although the properties of single filaments are important, it is the ability of filaments to fuse into larger-scale structures that is required for 3D printing. Metal and plastic 3D printing typically produces parts that are <100% solid, creating an external skin that is infilled using a repeating geometric structure with a defined porosity. For FRESH, we used rectilinear and octagonal infill algorithms to generate patterns of interconnected alginate filaments (Fig. 2, C to H). The rectilinear infill is a simple square lattice structure (Fig. 2C) that we FRESH printed at a $500\text{-}\mu\text{m}$ pitch (Fig. 2D). Confocal imaging and 3D rendering demonstrate that there is interconnectivity between filaments in the x , y , and z axes (Fig. 2E). The octagonal infill is a more complex pattern of squares and octagons (Fig. 2F) that we FRESH printed at a $750\text{-}\mu\text{m}$ pitch (Fig. 2G). A 3D rendering again demonstrates the interconnectivity between filaments in the x , y , and z axes (Fig. 2H). It should be noted that the fidelity of these infill patterns is comparable to that

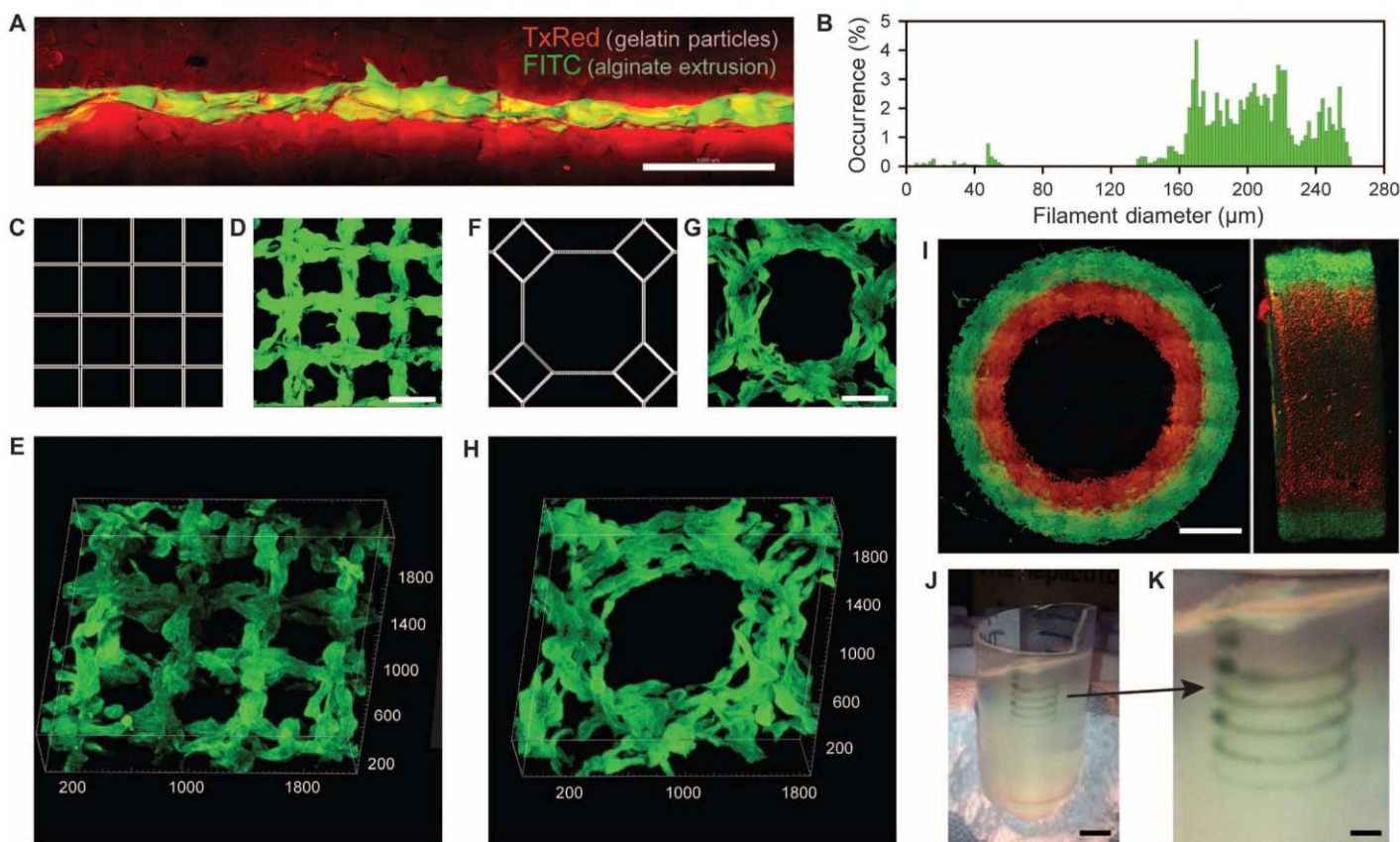


Fig. 2. Analysis of the hydrogel filaments and structures fabricated using FRESH. (A) A representative alginate filament (green) embedded within the gelatin slurry support bath (red). (B) Histogram of the diameter of isolated alginate filaments within the gelatin support bath showing a range from 160 to 260 μm . (C to E) A standard square lattice pattern commonly used for infill in 3D printing FRESH printed in fluorescent alginate (green) and viewed (D) top down and (E) in 3D. (F to H) An octagonal infill pattern FRESH printed in fluorescent alginate (green) and viewed (G) top down and (H) in 3D. (I) Example of a two-material print of coaxial cylinders in red and green fluorescently labeled alginate with a continuous interface shown in top down and lateral cross sections. (J) An example of a freeform, nonplanar FRESH print of a helix shown embedded in the gelatin support bath. (K) A zoomed-in view of the helix demonstrating that FRESH can print in true freeform and is not limited to standard layer-by-layer planar fabrication. Scale bars, 1 mm (A), 500 μm (D and G), 2 mm (I), 10 mm (J), and 2.5 mm (K).

achieved using the stock thermoplastic extruder to print the same geometries in PLA, and further improvements are anticipated by performing FRESH on better hardware with optimized print parameters.

FRESH can also be used to 3D print complex multimaterial parts and in nonplanar geometries. Dual syringe-based extruders can be mounted onto the MakerBot (fig. S1) and directly leverage the dual-extruder printing capability built into the software to alternate between extruders (movie S2). To demonstrate dual-material printing, we printed two different fluorescently labeled alginates in concentric cylinders. Multiphoton imaging shows distinct layers, each 1 mm wide, integrated together throughout a 3-mm thickness (Fig. 2I). Uniquely, FRESH is also not limited to standard layer-by-layer 3D printing and can freeform deposit material in 3D space with high fidelity as long as the extruder does not pass through previously deposited material. This is demonstrated by printing a single filament along a helical path (Fig. 2, J and K, and movie S3). This is a continuous, single filament with the extruder simultaneously moving in x , y , and z , showing the ability to deposit material in highly anisotropic structures in all three axes.

3D printing of complex biological structures

FRESH was next used to print complex biological structures based on medical imaging data to demonstrate its capability to fabricate complex geometries. Further, we wanted to validate that prints were mechanically robust and could be formed from multiple types of protein and polysaccharide hydrogels. First, a human femur from CT data (Fig. 3A) was scaled down to a length of ~35 mm and a minimum diameter of ~2 mm and FRESH printed in alginate (Fig. 3B). The 3D printed femur only mimicked the external structure (surface) of the real femur and had a solid infill. Applying uniaxial strain showed that the femur could undergo ~40% strain and recover elastically (Fig. 3C and movie S4), validating that there was mechanical fusion between the printed alginate layers. Further, the femur could be bent in half and elastically recover and, when strained to failure, fractured at an oblique angle to the long axis of the bone, confirming that failure was not due to layer delamination (movie S5). Next, we created a simple bifurcated tube in CAD (computer-aided design) to demonstrate the ability to FRESH print a hollow structure (fig. S3A). We used both the femur

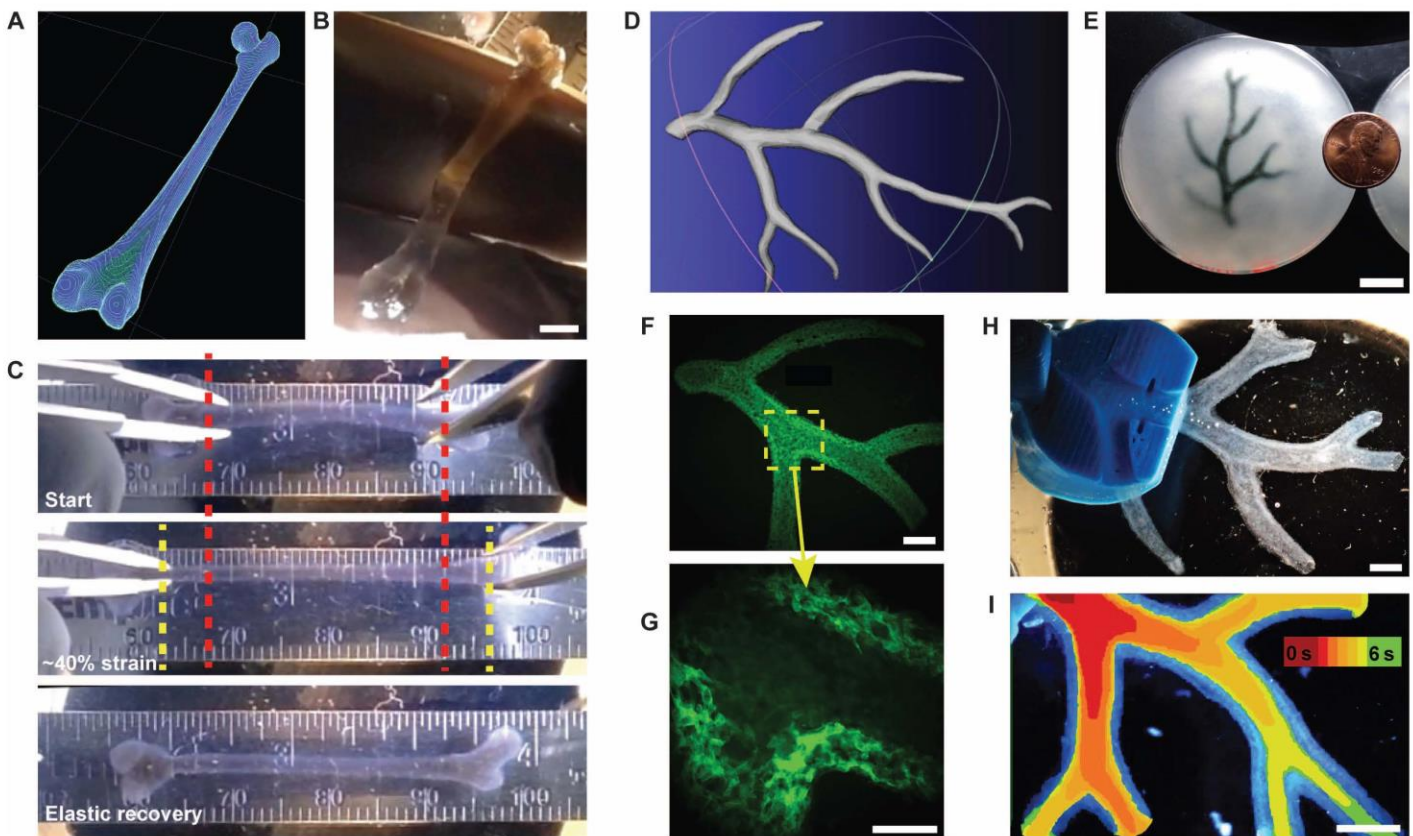


Fig. 3. FRESH printing of biological structures based on 3D imaging data and functional analysis of the printed parts. (A) A model of a human femur from 3D CT imaging data is scaled down and processed into machine code for FRESH printing. (B) The femur is FRESH printed in alginate, and after removal from the support bath, it closely resembles the model and is easily handled. (C) Uniaxial tensile testing of the printed femur demonstrates the ability to be strained up to 40% and elastically recover. (D) A model of a section of a human right coronary arterial tree from 3D MRI is processed at full scale into machine code for FRESH printing. (E) An example of the arterial tree printed in alginate (black) and embedded in the gelatin slurry support bath. (F) A section of the arterial trees printed in fluorescent alginate (green) and imaged in 3D to show the hollow lumen and multiple bifurcations. (G) A zoomed-in view of the arterial tree shows the defined vessel wall that is <1 mm thick and the well-formed lumen. (H) A dark-field image of the arterial tree mounted in a perfusion fixture to position a syringe in the root of the tree. (I) A time-lapse image of black dye perfused through the arterial tree false-colored at time points of 0 to 6 s to show flow through the lumen and not through the vessel wall. Scale bars, 4 mm (B), 10 mm (E), 2.5 mm (F), 1 mm (G), and 2.5 mm (H and I).

and bifurcated tube to show that other ECM hydrogels including collagen type I and fibrin can be FRESH printed with comparable fidelity to alginate (fig. S3, B to D, and movie S6). Printing multiple copies of the same bifurcated tube continuously for 4 hours also confirmed that the platform was thermally stable and that support bath rheological properties did not change over this period (fig. S3, C and D). Further, sheets of C2C12 myoblasts suspended in a mixture of fibrinogen, collagen type I, and Matrigel were printed at 20°C under sterile conditions and showed 99.7% viability by LIVE/DEAD staining (fig. S4, A and B). Multiday studies using C2C12 myoblasts and MC3T3 fibroblasts showed that cells were well distributed in 3D (fig. S4, C and E, respectively) and, over a 7-day culture period, formed a high-density cellular network (fig. S4, D and F, respectively). These examples demonstrate that FRESH can 3D print mechanically robust parts with biomimetic structure (Fig. 3C) and high repeatability (fig. S3, C and D) from a range of ECM hydrogels including collagen, fibrin, and Matrigel (figs. S3 and S4) and with embedded cells (fig. S4).

Additional mechanical characterization was performed by creating cast and 3D printed alginate dog bones (fig. S5A) and subjecting them to uniaxial tensile testing to generate stress-strain curves (fig. S5B), with the linear region from 5 to 20% strain used to calculate the elastic modulus (fig. S5C). Alginate is widely used in the tissue engineering field, and our results were comparable to those previously reported (33), although our gels were stiffer because of higher alginate and calcium concentrations. The cast alginate had a strain-to-failure of $42 \pm 8\%$ (fig. S5D), about two times that of the 3D printed alginate, and an elastic modulus of 446 ± 72 kPa (fig. S5E), about nine times that of the 3D printed alginate. Part of this difference is because the 3D printed alginate dog bones were printed with 50% infill, effectively reducing the true cross-sectional area and introducing internal voids that initiated cracks at lower strains. Normalizing for the 50% infill by taking the cross-sectional area as half of that measured externally increased the elastic modulus from 51 ± 14 kPa to 102 ± 27 kPa, which is $\sim 25\%$ of the cast alginate modulus. The lower mechanical properties of the 3D printed alginate were expected because the layer-by-layer fabrication approach is known to impart defects and material anisotropy (34, 35). However, these results, in combination with the straining of the 3D printed femur, demonstrate the mechanical fusion between printed layers and show that FRESH can be used to fabricate soft structures with mechanical integrity.

We next evaluated the ability to fabricate a more complex, perfusable structure using MRI data of part of the right coronary artery vascular tree and creating a hollow lumen with a wall thickness of <1 mm (Fig. 3D) (36). This was FRESH printed to scale with an overall length from trunk to tip of ~ 4.5 cm and contained multiple bifurcations with 3D tortuosity (Fig. 3E and movie S7). Arterial trees printed using fluorescent alginate confirmed that the internal lumens and bifurcations were well formed (Fig. 3F) and that a wall thickness of <1 mm and lumen diameters of 1 to 3 mm were achieved (Fig. 3G). Detailed structural analysis comparing the 3D model (fig. S6A) to the 3D printed arterial tree (fig. S6B) showed good fidelity and accurate anatomical structure with $<15\%$ variation in overall length and width and angles of the major bifurcations within $\leq 3^\circ$. Analysis of the wall thickness and lumen diameter confirmed that the 3D model (fig. S6C) was comparable to the 3D printed arterial tree (fig. S6D), although the printed wall thickness was increased and the lumen diameter decreased to ensure mechanical integrity of the overall vessel network for perfusion studies. A custom fixture to hold

the arterial tree was 3D printed in PLA (Fig. 3H and fig. S7) and used to perfuse the print. Black dye pumped through the arterial tree confirmed that it was patent and manifold and that hydrogel density was sufficient to prevent diffusion through the wall (Fig. 3I and movie S8). Similar to the mechanical testing of the femur (Fig. 3C) and dog bones (fig. S5), the minimal diffusion through the arterial wall confirmed that the alginate layers were well fused together, forming a solid structure.

Finally, we evaluated the ability to FRESH print 3D biological structures with complex internal and external architectures that would be extremely challenging or impossible to create using traditional fabrication techniques. First, we selected a day 5 embryonic chick heart (Fig. 4A) because of the complex internal trabeculations. We fixed and stained the heart for cell nuclei, F-actin, and fibronectin and generated a 3D optical image using confocal microscopy (Fig. 4B). The 3D optical image was then thresholded, segmented, and converted into a solid model for 3D printing (Fig. 4C and fig. S8). The diameter of the actual embryonic heart (~ 2.5 mm) was scaled up by an order of magnitude (~ 2.5 cm) to better match the resolution of the printer and FRESH printed using fluorescently labeled alginate. The printed heart was then imaged using a multiphoton microscope to generate a cross section through the structure (Fig. 4D) showing internal trabeculation comparable to that in the model (Fig. 4C). Comparing the 3D model, G-code machine path, and final printed alginate heart (fig. S9, A to C) showed good co-registration of primary features when overlaid on one another (fig. S9, D to F). A dark-field image of the whole 3D printed heart provided further validation of print fidelity and the ability to fabricate complex internal structures down to the submillimeter length scale (Fig. 4E). Dimensional analysis comparing the 3D heart model (fig. S9G) to the 3D printed heart (fig. S9H) demonstrated nearly identical length, width, and size of major internal structures with $<10\%$ variability. Overlaying images of the 3D model and printed heart helped further visualize the co-registration of the internal trabeculations and other anatomical features (fig. S9I). This embryonic heart is a good example of the types of structures that can be 3D printed with FRESH but are not possible to fabricate using traditional approaches because of the complex internal architecture.

To create complex external surface structures, we used an MRI image of the human brain (Fig. 4F) because of the intricate folds in the cortical tissues. A high-resolution view of the 3D brain model shows the surface in detail (Fig. 4G); however, the internal structure of the brain was solid infill. The embryonic heart model was scaled up in size, whereas the human brain model was scaled down to 3 cm in length to evaluate the resolution limits of the printer and reduce print times. The model of the exterior surface of the human brain was 3D printed using alginate, and different regions including the frontal and temporal lobes of the cortex and the cerebellum were well defined (Fig. 4H). Visualization of the brain surface was enhanced with black dye and revealed structures corresponding to the major folds of the cerebral cortex in the 3D model (Fig. 4I and movie S9). A more detailed comparison confirmed the similar morphology of multiple surface folds of the cerebral cortex between the 3D model and the 3D printed brain (fig. S10). Together, both the 3D printed embryonic heart and brain demonstrate the unique ability of FRESH to print hydrogels with complex internal and external structures.

Looking forward, can we leverage these FRESH bioprinting capabilities to engineer soft hydrogel scaffolds for advanced tissue engineering

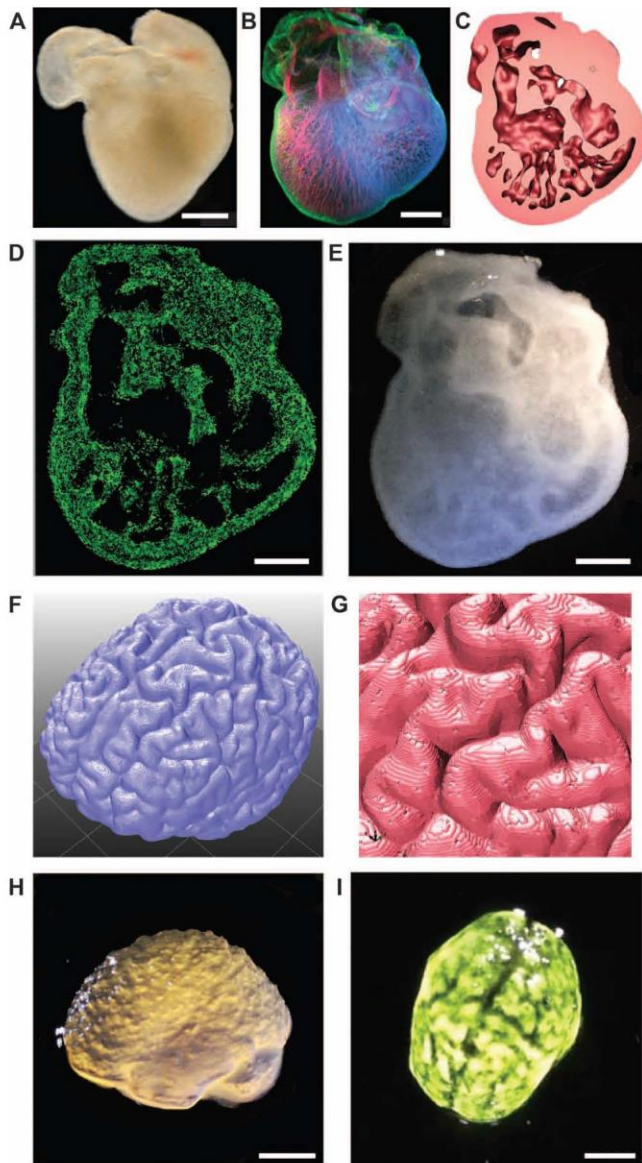


Fig. 4. FRESH printed scaffolds with complex internal and external architectures based on 3D imaging data from whole organs. (A) A dark-field image of an explanted embryonic chick heart. (B) A 3D image of the 5-day-old embryonic chick heart stained for fibronectin (green), nuclei (blue), and F-actin (red) and imaged with a confocal microscope. (C) A cross section of the 3D CAD model of the embryonic heart with complex internal trabeculation based on the confocal imaging data. (D) A cross section of the 3D printed heart in fluorescent alginate (green) showing recreation of the internal trabecular structure from the CAD model. The heart has been scaled up by a factor of 10 to match the resolution of the printer. (E) A dark-field image of the 3D printed heart with internal structure visible through the translucent heart wall. (F) A 3D rendering of a human brain from MRI data processed for FRESH printing. (G) A zoomed-in view of the 3D brain model showing the complex, external architecture of the white matter folds. (H) A lateral view of the brain 3D printed in alginate showing major anatomical features including the cortex and cerebellum. The brain has been scaled down to ~3 mm in length to reduce printing time and test the resolution limits of the printer. (I) A top down view of the 3D printed brain with black dye dripped on top to help visualize the white matter folds printed in high fidelity. Scale bars, 1 mm (A and B) and 1 cm (D, E, H, and I).

applications? In terms of complex scaffold design, our results demonstrate the ability to fabricate a wide range of 3D biological structures based on 3D imaging data with spatial resolution and fidelity that match or exceed previous results. Further, this is directly done with natural biopolymers such as alginate, fibrin, and collagen type I, which are cross-linked by ionic, enzymatic, and pH/thermally driven mechanisms, respectively. This flexibility in materials used and architectures printed defines a new level of capability for the AM of soft materials. The square and octagonal infill patterns (Fig. 2, C to H) show results comparable to those achieved with thermoplastics (for example, PLA) printed on the stock MakerBot Replicator printer we used, suggesting that we may be limited by the hardware. We anticipate that higher resolution is possible using higher-precision printers, smaller-diameter needles, and gelatin slurries with a smaller particle diameter. Cost is also an important consideration for the future expansion of 3D bioprinting as a tissue biofabrication platform, as commercially available and custom-built printers currently cost more than \$100,000 and/or require specialized expertise to operate (7, 17, 20–23, 27). In contrast, FRESH is built on open-source hardware and software and the gelatin slurry is low cost and readily processed using consumer blenders. To emphasize the accessibility of the technology, we implemented FRESH on a \$400 3D printer (Printrbot Jr, movie S10) and the STL file to 3D print the custom syringe-based extruder can be downloaded from <http://3dprint.nih.gov/>. It should be acknowledged that the direct bioprinting of functional tissues and organs requires further research and development to become fully realized, and a number of companies and academic laboratories are actively working toward this goal. The low cost of FRESH and the ability to 3D print a range of hydrogels should enable the expansion of bioprinting into many academic and commercial laboratory settings and accelerate important breakthroughs in tissue engineering for a wide range of applications, from pharmaceutical testing to regenerative therapies.

MATERIALS AND METHODS

Modification of a MakerBot Replicator for syringe-based extrusion

All 3D printing was performed using a MakerBot Replicator (MakerBot Industries) modified with a syringe-based extruder (fig. S1A). To do this, we removed the stock thermoplastic extruder assembly from the plastic *x*-axis carriage and replaced it with a custom-built syringe pump extruder (fig. S1, B and C). The syringe pump extruder was designed to use the NEMA-17 stepper motor from the original MakerBot thermoplastic extruder and mount directly in place of the extruder on the *x*-axis carriage. The syringe pump extruder was printed in acrylonitrile butadiene styrene and PLA plastic using the thermoplastic extruder on the MakerBot before its removal. By using the same stepper motor, the syringe pump extruder was natively supported by the software that came with the printer. The design for the syringe pump extruder can be downloaded as an STL file from <http://3dprint.nih.gov/> that can be printed on any RepRap or MakerBot 3D printer. In addition to a single extruder configuration, multiple syringe pump extruders could be mounted in a dual-extruder configuration, enabling 3D printing of multiple materials at one time (fig. S1D). No software modifications were necessary to operate the printer in single- or dual-extruder modes, aside from settings corresponding to nozzle diameter, filament diameter, and “start/end” G-code found in the software responsible for controlling the 3D printer.

Preparation and analysis of gelatin slurry support bath

To create the gelatin slurry support bath, we mixed 150 ml of 4.5% (w/v) gelatin (Type A, Thermo Fisher Scientific) in 11 mM CaCl₂ (Sigma-Aldrich) into a solution and then gelled it for 12 hours at 4°C in a 500-ml mason jar (Ball Inc.). Next, 350 ml of 11 mM CaCl₂ at 4°C was added to the jar and its contents were blended (at “pulse” speed) for a period of 30 to 120 s on a consumer-grade blender (Osterizer MFG) (fig. S2A). Then, the blended gelatin slurry was loaded into 50-ml conical tubes (fig. S2B) and centrifuged at 4200 rpm for 2 min, causing slurry particles to settle out of suspension (fig. S2C). The supernatant was removed and replaced with 11 mM CaCl₂ at 4°C. The slurry was vortexed back into suspension and centrifuged again. This process was repeated until no bubbles were observed at the top of the supernatant, which indicated that most of the soluble gelatin was removed. At this point, gelatin slurries could be stored at 4°C. For FRESH printing, the slurry was poured into a petri dish or a container large enough to hold the object to be printed (fig. S2D). Any excess fluid was removed from the gelatin slurry support bath using Kimwipes (Kimberly-Clark), which produced a slurry material that behaved like a Bingham plastic. All 3D printing was performed using gelatin blended for 120 s.

To measure the effect of blend time on gelatin particle size, we blended the gelatin for periods of 30, 45, 60, 75, 90, 105, and 120 s. Blend times longer than 120 s were not used because the gelatin particles began to entirely dissolve into the solution. For each blend time analyzed, 500 µl of slurry was removed and diluted to 10 ml with 11 mM CaCl₂ and 0.1% (w/v) black food coloring (McCormick & Co.). Then, 140 µl of each diluted sample was mounted on a coverslip and imaged with a digital camera (D7000 SLR, Nikon) mounted on a stereomicroscope with oblique illumination (SMZ1000, Nikon). For each image, ImageJ (National Institutes of Health) (37) was used to enhance contrast, convert to LAB color space, and apply a lightness threshold. ImageJ was then used to count particles and measure their Feret diameters, areas, and circumferences using the “analyze particle” function. Linear regression of particle diameter as a function of time was performed using SigmaPlot 11 (Systat Software Inc.).

To measure the rheological properties of the gelatin slurry support bath, we blended the gelatin for 120 s and then prepared it as described for the FRESH 3D printing process. The slurry was loaded onto a Gemini 200 Rheometer with a 40-mm, 4° cone (Malvern) and analyzed in frequency sweep from 0.001 to 100 Hz at 150-µm separation and 25°C. The storage (G') and loss (G'') moduli were measured and recorded in Microsoft Excel and plotted using SigmaPlot 11.

Preparation of hydrogel inks for 3D printing

A solution of 2.0% (w/v) sodium alginate (FMC BioPolymer), 0.02% (w/v) 6-aminofluorescein [fluorescein isothiocyanate (FITC), Sigma], 0.022% (w/v) 1-ethyl-3-(3-dimethylaminopropyl)carbodiimide (Sigma), and 0.025% (w/v) sulfo-*N*-hydroxysuccinimide (Sigma) in distilled water was prepared and stirred for 48 hours at 20°C to prepare fluorescently labeled alginate for 3D printing. Unreacted FITC was removed from FITC-labeled alginate by five consecutive 12-hour dialysis shifts against 2% (w/v) sodium alginate at 4°C in dialysis cassettes (Slide-A-Lyzer 3.5k MWCO, Thermo Fisher). After dialysis, 100 µl of FITC-labeled alginate was added to a 10-ml solution of 4% (w/v) sodium alginate, 0.4% (w/v) hyaluronic acid (Sigma), and 0.1% (w/v) black food coloring (for visualization during

printing) to create a fluorescently labeled alginate ink. Fluorescent alginate prints were imaged using a Leica SP5 multiphoton microscope with a 10× [numerical aperture (NA) = 0.4] objective and a 25× (NA = 0.95) water immersion objective. Higher-magnification images were obtained using a Zeiss LSM 700 confocal microscope with a 63× (NA = 1.4) oil immersion objective. Bimaterial prints and arterial tree prints were imaged using a Nikon AZ-C2 macro confocal microscope with a 1× (NA = 0.1) objective. 3D image stacks were deconvolved with AutoQuant X3 and processed with Imaris 7.5 (Bitplane Inc.).

To prepare fibrinogen for 3D printing of fibrin constructs, we prepared a solution of fibrinogen (10 mg/ml; VWR), 0.5% (w/v) hyaluronic acid (Sigma), 1% (w/v) bovine serum albumin (Sigma), 10 mM sodium HEPES (Sigma), and 1× phosphate-buffered saline (PBS; VWR) and loaded it into a syringe for printing. To ensure cross-linking of the fibrinogen into fibrin once printed in the support bath, we supplemented the baths with thrombin (0.1 U/ml; VWR). Fibrin prints were released from the bath material by incubation at 37°C for at least 1 hour (fig. S3C).

For 3D printing of collagen, rat tail collagen type I (BD Biosciences) at concentrations ranging from 8.94 to 9.64 mg/ml in 0.02 N acetic acid was used as received without further modification. To ensure cross-linking of collagen into a gel after extrusion, the support bath was supplemented with 10 mM HEPES to maintain a pH of ~7.4 and neutralize the acetic acid. After printing, scaffolds were incubated at 37°C for at least 1 hour to further cross-link the collagen (fig. S3D) and melt the support bath.

For 3D printing of cellularized constructs, components of a multi-component ECM ink were prepared at 4°C under sterile conditions in a biosafety cabinet. The ECM ink consisted of a solution of collagen type I (2 mg/ml; BD Biosciences), Matrigel (0.25 mg/ml; BD Biosciences), fibrinogen (10 mg/ml; VWR), 0.5% (w/v) hyaluronic acid, 1% (w/v) bovine serum albumin (Sigma), 10 mM sodium HEPES (Sigma), and 1× PBS (VWR), which was prepared and thoroughly mixed at 4°C. This specific protein and polysaccharide mixture was experimentally determined to quickly gel while maintaining viability of printed cells. C2C12 myoblasts or MC3T3-E1.4 cells were suspended in media at a concentration of 8×10^6 cells/ml and diluted 1:4 with the ECM mixture to create a final concentration of 2×10^6 cells/ml. The cellularized ink was then loaded into a sterile syringe used in the 3D printer. To ensure cross-linking of the ECM-based ink once printed, we supplemented the support bath with 10 mM HEPES and thrombin (0.1 U/ml).

The FRESH 3D printing process

Digital 3D models for FRESH prints were created using 3D imaging data or designed using SolidWorks software (Dassault Systèmes). The files for the human femur and coronary artery tree were downloaded from the BodyParts3D database (36). The model of the human brain was provided under creative commons licensing by A. Millns (Inition Co.). The 3D digital models were opened in MeshLab (<http://meshlab.sourceforge.net/>) to be exported in the STL file format. For the 3D model of the coronary artery tree, only the outer surface was provided by the BodyParts3D database; hence, the arterial tree was resampled to create a smaller daughter surface with inverted normals. When both surfaces were combined, a hollow model with internal and external surfaces with a wall thickness of ~1 mm resulted, which was exported as an STL file for printing.

All STL files were processed by Skeinforge (<http://fabmetheus.crsndoo.com/>) or KISSlicer (www.kisslicer.com/) software and sliced into 80- μm -thick layers to generate G-code instructions for the 3D printer. G-code instruction sets were sent to the printer using ReplicatorG (<http://replicat.org/>), an open-source 3D printer host program.

Hydrogel precursor inks were first drawn into a 2.5-ml syringe (Model 1001 Gastight Syringe, Hamilton Company) with a 150- μm -ID (inside diameter), 0.5-inch stainless steel deposition tip needle (McMaster-Carr) used as the nozzle to perform FRESH printing. The syringe was then mounted into the syringe pump extruder on the 3D printer (fig. S1, B and C). A petri dish or similar container large enough to hold the part to be printed was filled with the gelatin slurry support bath and manually placed on the build platform, and the container was held in place using a thin layer of silicone grease. The tip of the syringe needle was positioned at the center of the support bath in x and y and near the bottom of the bath in z before executing the G-code instructions. It is important to initiate FRESH 3D printing within 30 s of placing the syringe extruder in the support bath to avoid excessive cross-linking of material and clogging in the nozzle. Scaffolds were printed in a temperature-controlled room at $22 \pm 1^\circ\text{C}$ over a period of 1 min to 4 hours depending on the size and complexity of the printed construct as well as the ink used. For cellularized constructs, sterility was maintained by printing in a biosafety cabinet. Embedded constructs were heated to 37°C directly on the printer's platform, placed on a dry bath, or placed inside an incubator to liquefy the support bath and release a print after FRESH. Once the gelatin was melted, alginate prints were rinsed with 11 mM CaCl_2 and stored at 4°C . Once the gelatin was melted for collagen and fibrin prints, the objects were rinsed with $1\times$ PBS and stored at 4°C . For multicomponent ECM prints containing cells, scaffolds were rinsed with the appropriate culture medium based on the incorporated cell types and incubated at 37°C .

Cell culture and fluorescent staining

All reagents were purchased from Life Technologies unless otherwise specified. The MC3T3-E1.4 fibroblast cell line and prints containing MC3T3 cells [CRL-2593, American Type Culture Collection (ATCC)] were cultured in α -MEM (minimum essential medium) supplemented with 10% fetal bovine serum (FBS; Gibco Labs), penicillin (100 U/ml), and streptomycin (100 $\mu\text{g}/\text{ml}$). The C2C12 myoblast cell line and prints containing C2C12 cells (CRL-1722, ATCC) were cultured at 37°C under 5% CO_2 in Dulbecco's modified Eagle's medium supplemented with 10% (v/v) FBS, 1% (v/v) L-glutamine (200 mM), penicillin (100 U/ml), and streptomycin (100 $\mu\text{g}/\text{ml}$), based on published methods (38).

Cell viability after FRESH printing was assessed by performing a LIVE/DEAD assay (Life Technologies) on prints containing C2C12 cells (fig. S4, A and B). Each print was first washed with Opti-MEM media containing 2% FBS and 2% 10,000-U penicillin-streptomycin solution and incubated at 37°C under 5% CO_2 for 30 min. The prints were then removed from the incubator, rinsed with $1\times$ PBS, incubated in 2 ml of PBS with 2 μl of calcein AM and 4 μl of ethidium homodimer per sample for 30 min, and then imaged on a Zeiss LSM 700 confocal microscope. The number of live and dead cells in each of the five images per three independent samples was counted and the percent viability was calculated by dividing the number of live cells by the number of total cells per image.

Prints containing cells were cultured for up to 7 days and analyzed at 1- and 7-day time points to verify cell survival and growth. After 1 and 7 days of culture, printed sheets were rinsed with $1\times$ PBS (supplemented with 0.625 mM MgCl_2 and 0.109 mM CaCl_2) at 37°C , fixed in 4% (w/v) formaldehyde (Polysciences Inc.) for 15 min, and then washed three times in $1\times$ PBS. Fixed prints were incubated for 12 hours in a 1:200 dilution of 4',6-diamidino-2-phenylindole (DAPI; Life Technologies) and a 3:200 dilution of phalloidin conjugated to Alexa Fluor 488 (Life Technologies). Prints were then washed three times in PBS and mounted with ProLong Gold antifade reagent (Life Technologies) between a microscope glass slide and an NI.5 glass coverslip. The mounted samples were stored at room temperature and protected from light for 12 hours to allow the ProLong reagent to cure. Prints were imaged using a Leica SP5 multiphoton microscope with a $10\times$ (NA = 0.4) objective and a $25\times$ (NA = 0.95) water immersion objective. 3D image stacks were deconvolved with AutoQuant X3 and processed with Imaris 7.5.

Perfusion of 3D printed coronary arterial tree

To evaluate whether the 3D printed arterial tree was manifold, we mounted it in a custom-made 3D printed perfusion fixture (fig. S7, A and B). A solution of 11 mM CaCl_2 (Sigma) and 0.1% (w/v) black food coloring was injected into the root of the tree using a standard 3-ml syringe (BD Biosciences) with a 150- μm -ID, 0.5-inch needle, and the tip at the end of each branch was cut off to permit outflow. Perfusion was captured with a digital camera (D7000 SLR, Nikon) mounted on a stereomicroscope with oblique illumination (SMZ1000, Nikon).

Creation of a 3D model of the heart of a 5-day-old chick embryo

The 3D model of the embryonic chick heart was generated from 3D optical imaging data of a fluorescently labeled 5-day-old heart. Fertilized eggs of White Leghorn chicken were incubated at 37°C and 50% humidity for 5 days to do this. Then, the embryo [Hamburger-Hamilton stage 27 to 28 (39)] was explanted and the heart (ventricles, atria, and outflow tract) was dissected and fixed for 15 min in PBS with calcium, magnesium, and 4% formaldehyde. After being washed in PBS, the heart was blocked and permeabilized for 2 hours at 37°C in PBS with 0.1% Triton X-100 and 5% goat serum. Two steps of immunostaining were carried out overnight at 4°C . The first stain used dilutions of 1:200 DAPI, 3:100 phalloidin conjugated to Alexa Fluor 633 (Life Technologies), and 1:100 anti-fibronectin primary antibody (mouse, Sigma-Aldrich). After being extensively washed in PBS, the samples were stained with a 1:100 dilution of goat anti-mouse secondary antibody conjugated to Alexa Fluor 546 (Life Technologies). Samples were then washed and dehydrated by immersion in successive solutions of PBS with an increasing concentration of isopropyl alcohol as previously described (40). Finally, the samples were cleared by transferring to a solution of 1:2 benzyl alcohol/benzyl benzoate (BABB) to match the refractive index of the tissue. The transparent sample was mounted in BABB and imaged with a Nikon AZ-C2 macro confocal microscope with a $5\times$ objective (NA = 0.45).

The 3D image stack was deconvolved using AutoQuant X3 and processed with Imaris 7.5, MATLAB (MathWorks), and ImageJ. The DAPI (fig. S8A), actin (fig. S8B), and fibronectin (fig. S8C) channels were merged to obtain an image with the simultaneously well-defined trabeculae and outer wall of the heart (fig. S6D). A detailed mask of the heart showing the trabeculae was created by segmenting the averaged signals using a high-pass threshold (fig. S8E). A rough mask

showing the bulk of the heart was obtained using a low-pass threshold (fig. S8F). Next, the Imaris “Distance Transform” XTension was used on the bulk mask to create a closed shell of the outer wall of the heart. The high-detail mask and the mask of the closed shell were combined to obtain a complex model of the heart with detailed trabeculae and a completely closed outer wall (fig. S6G). The final model was smoothed and segmented using Imaris to preserve a level of detail adequate for 3D printing (fig. S8H). A 3D solid object was created by exporting the smoothed model as an STL file using the Imaris XT module and the “Surfaces to STL” XTension for MATLAB (fig. S8, I and J).

Mechanical characterization

Mechanical characterization comparing 3D printed and cast alginate constructs was performed using uniaxial tensile testing, adapted from our previously published method for characterizing soft PDMS (41). Briefly, tensile bar strips (dog bones) of 4% (w/v) alginic acid in 11 mM CaCl₂ were either 3D printed using the FRESH method or cast into laser-cut acrylic molds consisting of a grip section (7 × 10 mm), a reduced section (3.45 × 25 mm), and ~1 mm thickness. The 3D printed strips were fabricated with a 250-μm-diameter nozzle in a slurry containing 11 mM CaCl₂. Settings for the 3D printed strips were 100-μm layers, 50% octagonal infill, and 1 perimeter. The width and thickness of each test strip were individually measured before mechanical analysis. Uniaxial tensile testing (*n* = 6 of each type) was performed on an Instron 5943 (Instron) at a strain rate of 5 mm/min until failure. The elastic modulus of each sample was determined from the slope of the linear region of the stress-strain curves from 5 to 20% (or until failure, if it failed before 20%).

SUPPLEMENTARY MATERIALS

Supplementary material for this article is available at <http://advances.sciencemag.org/cgi/content/full/1/9/e1500758/DC1>

- Fig. S1. Modification of an open-source 3D printer for FRESH printing.
 Fig. S2. Preparation of the gelatin slurry support bath.
 Fig. S3. Examples of 3D printed bifurcated tubes using alginate, fibrin, and collagen.
 Fig. S4. 3D printed sheets of cells and ECM.
 Fig. S5. Mechanical characterization of cast and 3D printed alginate dog bones using uniaxial tensile testing.
 Fig. S6. A comparison of the 3D model and 3D printed arterial tree to assess print fidelity.
 Fig. S7. A 3D printed perfusion fixture for the right coronary arterial tree.
 Fig. S8. Generation of a 3D model of the embryonic heart from confocal microscopy.
 Fig. S9. A comparison of the 3D model and 3D printed embryonic heart to assess print fidelity.
 Fig. S10. A comparison of the 3D model and 3D printed brain.
 Movie S1. Time lapse of FRESH printing and heated release of the “CMU” logo.
 Movie S2. FRESH printing using the dual syringe pump extruders.
 Movie S3. Out-of-plane FRESH printing of a helix.
 Movie S4. Uniaxial strain of a FRESH printed femur model showing elastic recovery.
 Movie S5. Strain to failure of a FRESH printed femur.
 Movie S6. FRESH printing of soft collagen type I constructs.
 Movie S7. Time-lapse video of a coronary arterial tree being FRESH printed.
 Movie S8. Perfusion of a FRESH printed coronary arterial tree.
 Movie S9. Visualization of the 3D structure of a FRESH printed brain model.
 Movie S10. Modification of a sub-4000 3D printer for FRESH printing.

REFERENCES AND NOTES

1. A. M. Shah, H. Jung, S. Skirboll, Materials used in cranioplasty: A history and analysis. *Neurosurg. Focus* **36**, E19 (2014).
2. FDA 510(k) summary statement for Osteofab Patient Specific Cranial Device. Report Number K121818, Center for Devices and Radiological Health (2013), http://www.accessdata.fda.gov/cdrh_docs/pdf12/K121818.pdf (viewed 10/11/15).

3. D. A. Zopf, S. J. Hollister, M. E. Nelson, R. G. Ohye, G. E. Green, Bioresorbable airway splint created with a three-dimensional printer. *N. Engl. J. Med.* **368**, 2043–2045 (2013).
4. S. K. Bhatia, S. Sharma, 3D-printed prosthetics roll off the presses. *Chem. Eng. Prog.* **110**, 28–33 (2014), www.aiche.org/sites/default/files/cep/20140528.pdf (viewed 10/12/15).
5. J. R. Tumbleston, D. Shrivanyants, N. Ermoshkin, R. Januszewicz, A. R. Johnson, D. Kelly, K. Chen, R. Pinschmidt, J. P. Rolland, A. Ermoshkin, E. T. Samulski, J. M. DeSimone, Additive manufacturing. Continuous liquid interface production of 3D objects. *Science* **347**, 1349–1352 (2015).
6. J. N. Fullerton, G. C. M. Frodsham, R. M. Day, 3D printing for the many, not the few. *Nat. Biotechnol.* **32**, 1086–1087 (2014).
7. C. H. Lee, S. A. Rodeo, L. Ann Fortier, C. Lu, C. Erskan, J. J. Mao, Protein-releasing polymeric scaffolds induce fibrochondrocytic differentiation of endogenous cells for knee meniscus regeneration in sheep. *Sci. Transl. Med.* **6**, 266ra171 (2014).
8. B. Derby, Printing and prototyping of tissues and scaffolds. *Science* **338**, 921–926 (2012).
9. S. V. Murphy, A. Atala, 3D bioprinting of tissues and organs. *Nat. Biotechnol.* **32**, 773–785 (2014).
10. I. Martin, P. J. Simmons, D. F. Williams, Manufacturing challenges in regenerative medicine. *Sci. Transl. Med.* **6**, 232fs16 (2014).
11. G. Sinha, Cell presses. *Nat. Biotechnol.* **32**, 716–719 (2014).
12. M. S. Manno, Z. Jiang, T. James, Y. Lin Kong, K. A. Malatesta, W. O. Soboyejo, N. Verma, D. H. Gracias, M. C. McAlpine, 3D printed bionic ears. *Nano Lett.* **13**, 2634–2639 (2013).
13. L. A. Hockaday, K. H. Kang, N. W. Colangelo, P. Y. C. Cheung, B. Duan, E. Malone, J. Wu, L. N. Girardi, L. J. Bonassar, H. Lipson, C. C. Chu, J. T. Butcher, Rapid 3D printing of anatomically accurate and mechanically heterogeneous aortic valve hydrogel scaffolds. *Biofabrication* **4**, 035005 (2012).
14. B. Duan, L. A. Hockaday, K. H. Kang, J. T. Butcher, 3D bioprinting of heterogeneous aortic valve conduits with alginate/gelatin hydrogels. *J. Biomed. Mater. Res. A* **101A**, 1255–1264 (2013).
15. X. Cui, T. Boland, Human microvasculature fabrication using thermal inkjet printing technology. *Biomaterials* **30**, 6221–6227 (2009).
16. T. Xua, C. A. Gregory, P. Molnara, X. Guia, S. Jalotab, S. B. Bhadurib, T. Bolanda, Viability and electrophysiology of neural cell structures generated by the inkjet printing method. *Biomaterials* **27**, 3580–3588 (2006).
17. D. B. Kolesky, R. L. Truby, A. Sydney Gladman, T. A. Busbee, K. A. Homan, J. A. Lewis, 3D bioprinting of vascularized, heterogeneous cell-laden tissue constructs. *Adv. Mater.* **26**, 3124–3130 (2014).
18. F. Pati, J. Jang, D.-H. Ha, S. Won Kim, J.-W. Rhie, J.-H. Shim, D.-H. Kim, D.-W. Cho, Printing three-dimensional tissue analogues with decellularized extracellular matrix bioink. *Nat. Commun.* **5**, 3935 (2014).
19. J. S. Miller, K. R. Stevens, M. T. Yang, B. M. Baker, D.-H. T. Nguyen, D. M. Cohen, E. Toro, A. A. Chen, P. A. Galie, X. Yu, R. Chaturvedi, S. N. Bhatia, C. S. Chen, Rapid casting of patterned vascular networks for perfusable engineered three-dimensional tissues. *Nat. Mater.* **11**, 768–774 (2012).
20. F. Marga, K. Jakob, C. Khatiwala, B. Shepherd, S. Dorfman, B. Hubbard, S. Colbert, G. Forgacs, Toward engineering functional organ modules by additive manufacturing. *Biofabrication* **4**, 022001 (2012).
21. K. Jakob, C. Norotte, F. Marga, K. Murphy, G. Vunjak-Novakovic, G. Forgacs, Tissue engineering by self-assembly and bio-printing of living cells. *Biofabrication* **2**, 022001 (2010).
22. C. Norotte, F. S. Marga, L. E. Niklason, G. Forgacs, Scaffold-free vascular tissue engineering using bioprinting. *Biomaterials* **30**, 5910–5917 (2009).
23. A. Lantada, in *Handbook on Advanced Design and Manufacturing Technologies for Biomedical Devices*, A. D. Lantada, Ed. (Springer US, New York, 2013), pp. 261–275.
24. F. P. W. Melchels, M. A. N. Domingos, T. J. Klein, J. Malda, P. J. Bartolo, D. W. Huttmacher, Additive manufacturing of tissues and organs. *Prog. Polym. Sci.* **37**, 1079–1104 (2012).
25. S. Tasoglu, U. Demirci, Bioprinting for stem cell research. *Trends Biotechnol.* **31**, 10–19 (2013).
26. I. T. Ozbolat, Y. Yu, Bioprinting toward organ fabrication: Challenges and future trends. *IEEE Trans. Biomed. Eng.* **60**, 691–699 (2013).
27. W. Wu, A. DeConinck, J. A. Lewis, Omnidirectional printing of 3D microvascular networks. *Adv. Mater.* **23**, H178–H183 (2011).
28. J. M. Dang, K. W. Leong, Natural polymers for gene delivery and tissue engineering. *Adv. Drug Deliv. Rev.* **58**, 487–499 (2006).
29. S. Young, M. Wong, Y. Tabata, A. G. Mikos, Gelatin as a delivery vehicle for the controlled release of bioactive molecules. *J. Control. Release* **109**, 256–274 (2005).
30. E. Engvall, E. Ruoslahti, E. J. Miller, Affinity of fibronectin to collagens of different genetic types and to fibrinogen. *J. Exp. Med.* **147**, 1584–1595 (1978).
31. Y. A. Antonov, N. P. Lashko, Y. K. Glotova, A. Malovikova, O. Markovich, Effect of the structural features of pectins and alginates on their thermodynamic compatibility with gelatin in aqueous media. *Food Hydrocoll.* **10**, 1–9 (1996).
32. J.-S. Chun, M.-J. Ha, B. S. Jacobson, Differential translocation of protein kinase C ϵ during HeLa cell adhesion to a gelatin substratum. *J. Biol. Chem.* **271**, 13008–13012 (1996).
33. J. L. Drury, R. G. Dennis, D. J. Mooney, The tensile properties of alginate hydrogels. *Biomaterials* **25**, 3187–3199 (2004).

34. A. Bellini, S. Güçeri, Mechanical characterization of parts fabricated using fused deposition modeling. *Rapid Prototyping J.* **9**, 252–264 (2003).
35. A. Farzadi, M. Solati-Hashjin, M. Asadi-Eydivand, N. A. Abu Osman, Effect of layer thickness and printing orientation on mechanical properties and dimensional accuracy of 3D printed porous samples for bone tissue engineering. *PLoS One* **9**, e108252 (2014).
36. N. Mitsuhashi, K. Fujieda, T. Tamura, S. Kawamoto, T. Takagi, K. Okubo, BodyParts3D: 3D structure database for anatomical concepts. *Nucleic Acids Res.* **37**, D782–D785 (2009).
37. C. A. Schneider, W. S. Rasband, K. W. Eliceiri, NIH image to ImageJ: 25 years of image analysis. *Nat. Methods* **9**, 671–675 (2012).
38. Y. Sun, R. Duffy, A. Lee, A. W. Feinberg, Optimizing the structure and contractility of engineered skeletal muscle thin films. *Acta Biomater.* **9**, 7885–7894 (2013).
39. V. Hamburger, H. L. Hamilton, A series of normal stages in the development of the chick embryo. *J. Morphol.* **88**, 49–92 (1951).
40. H. Y. Kim, L. A. Davidson, Punctuated actin contractions during convergent extension and their permissive regulation by the non-canonical Wnt-signaling pathway. *J. Cell Sci.* **124**, 635–646 (2011).
41. R. N. Palchesko, L. Zhang, Y. Sun, A. W. Feinberg, Development of polydimethylsiloxane substrates with tunable elastic modulus to study cell mechanobiology in muscle and nerve. *PLoS One* **7**, e51499 (2012).

Acknowledgments: We thank M. Blank for technical assistance with uniaxial tensile testing. **Funding:** This work was supported in part by the NIH Director's New Innovator Award (DP2HL117750) and the NSF CAREER Award (1454248). **Author contributions:** T.J.H., Q.J., and A.W.F. designed the research, analyzed data, and wrote the paper. T.J.H., Q.J., J.H.P., M.S.G., H.-J.S., R.N.P., M.H.R., and A.R.H. performed the research. **Competing interests:** Carnegie Mellon University has filed for patent protection on the technology described herein, and T.J.H. and A.W.F. are named as inventors on the patent. **Data and materials availability:** The data presented here are available from <http://dx.doi.org/10.5061/dryad.tp4cp>. The 3D STL models of the syringe pump extruder and the embryonic chick heart are available at <http://3dprint.nih.gov/>.

Submitted 10 June 2015

Accepted 2 September 2015

Published 23 October 2015

10.1126/sciadv.1500758

Citation: T. J. Hinton, Q. Jallerat, R. N. Palchesko, J. H. Park, M. S. Grodzicki, H.-J. Shue, M. H. Ramadan, A. R. Hudson, A. W. Feinberg, Three-dimensional printing of complex biological structures by freeform reversible embedding of suspended hydrogels. *Sci. Adv.* **1**, e1500758 (2015).

Appendix E Book chapter

Here is the book chapter summarizing the key elements of cardiac physiology to consider and the different ways cardiac tissue engineering attempts to replicate it *in vitro*.

**NANO- AND
MICROSTRUCTURED ECM AND
BIOMIMETIC SCAFFOLDS FOR
CARDIAC TISSUE ENGINEERING****QUENTIN JALLERAT and JOHN M. SZYMANSKI***Department of Biomedical Engineering, Carnegie Mellon University,
Pittsburgh, PA, USA***ADAM W. FEINBERG***Department of Biomedical Engineering, Department of Materials Science and
Engineering, Carnegie Mellon University, Pittsburgh, PA, USA***12.1 INTRODUCTION**

Cardiovascular disease (CVD) has become the principal cause of death in the developed world, causing one in three US deaths in 2009 (787,931 total) [1]. The most common form of CVD is coronary heart disease, where the coronary vasculature supplying the heart tissue with oxygen and nutrients becomes occluded. When starved of oxygen for too long, it causes a heart attack, or myocardial infarction (MI), where the cardiomyocytes (CMs) die and are unable to regenerate. MI was responsible for one in six US deaths in 2009, and associated health care costs amounted to \$195.2 billion [1]. This demonstrates the increasing burden of CVD on the society. Moreover, patient morbidity leads to a considerable decrease in their standard of living. To address this issue, significant basic and clinical research efforts are focused on the development of strategies to restore cardiac function.

Therapies to treat MI and heart failure face unique challenges, chief among them is the absence of natural regeneration in adult cardiac tissue. CM proliferation, important during development, nearly disappears after birth [2]. Instead, postnatal myocardial growth is mostly due to CM maturation and enlargement, termed

hypertrophy, which can bring a 20-fold increase in cell size [3]. Recent findings suggest that there is a basal level of CM proliferation even in adults, but fewer than 1% are replaced every year, meaning more than 50% of CMs are sustained throughout our lifetime [4]. After injury, the percentage of CM proliferation near the infarct site rises to 3%, but it is insufficient to naturally recover cardiac function [5]. Damaged myocardium is then further remodeled during the acute inflammatory response and is eventually replaced by hypoxic and noncontractile scar tissue. Therapeutic approaches aim to recover full or partial cardiac function, either by inducing the formation of viable cardiac tissue or by compensating for the damaged tissue with medical devices.

With disease progression or recurrent MI, patients eventually suffer heart failure, characterized by the inability to pump enough blood to the body. A heart transplant is the gold standard for treatment, and while it is estimated that 40,000 patients could benefit, there are only about 2200 donor hearts available each year [6]. To address the urgent need for circulatory assist, devices such as total artificial hearts and left ventricular assist devices have been developed [7]. These mechanical pumps work short term, but have serious limitations as they can trigger thrombosis, leading to blood clots that circulate to the brain or the lungs, block small arteries, and induce stroke or embolism. Furthermore, excessive shear stress within these mechanical assist devices can damage the blood cells, causing hemolysis. Thus, survival is improved only for ~5 years, with these devices used predominantly for bridge to transplantation instead of destination therapy for heart failure [8]. More recently, stem cells have been used in an attempt to regenerate and repair damaged heart tissue [9–13]. Stem cell therapy can effectively modulate the effects of the acute inflammatory response after a heart attack via the release of paracrine factors that reduce CM death and preserve functional myocardium that would otherwise be remodeled to form scar tissue [11]. However, long-term outcomes are hindered by the inability to recover the bulk of cardiac muscle lost during MI. More than 90% of stem cells injected into the infarct die after a week in the hostile environment with little to no new muscle formation or functional integration [11]. Additionally, exogenous cells introduced into the complex cardiac environment have the potential to create arrhythmia due to inadequate electromechanical coupling [14].

Cardiac tissue engineering has emerged as a promising solution to address these challenges and produce functional cardiac tissue. While approaches vary, typically, polymer scaffolds are engineered to provide physical and chemical cues that guide the behavior of cardiac cells and instruct them to proliferate, differentiate, and eventually assemble into a viable tissue. The primary goal is to develop a construct with dense, anisotropic cardiac muscle that has electromechanical function on par with ventricular myocardium. The ultimate tissue engineering application is to repair an MI in a patient, by either replacing the damaged tissue with an *in vitro*-engineered cardiac muscle graft or implanting a scaffold *in vivo* that promotes endogenous repair. Additionally, engineered cardiac muscle has great utility as an *in vitro* model system of cardiac function, enabling researchers to test the effects of drugs for safety and toxicity, as well as discover new compounds to treat a range of CVD. To inform scaffold design, cardiac tissue engineering draws from cardiac anatomy and physiology, advances in stem cell biology and, most importantly, from a better

understanding of the heart's native scaffold, the extracellular matrix (ECM). The ECM is essential to cardiac structure and function and it helps provide and transduce the physical and chemical cues required by cardiac cells to maintain tissue homeostasis. For these reasons, researchers have developed a range of technologies to engineer scaffolds that mimic the cardiac ECM in order to achieve the production of functional cardiac constructs. Cardiac tissue engineering, by using bio-inspired scaffolds to induce tissue growth, has the potential to treat CVD in millions of patients every year.

In this chapter, we provide an overview of the heart and the biomimetic approaches used to engineer cardiac muscle tissue. We first describe the unique structure and function of cardiac muscle (myocardium), discuss how this dictates scaffold design, and then define the benchmarks used to evaluate the performance of engineered cardiac tissue. Next, we present the different techniques researchers have developed to fabricate tissue-engineered cardiac scaffolds that mimic ECM cues observed in the heart. For each case, we discuss the relevant physical, mechanical and/or chemical properties and the particular advantages and limitations of the approach. Finally, we discuss the persistent challenges to engineering functional cardiac tissue and the future directions of the field.

12.2 STRUCTURE AND FUNCTION OF THE MYOCARDIUM

12.2.1 Multiscale Hierarchy of the Contractile Apparatus

The myocardium features a complex hierarchical organization that spans from the molecular to tissue scales, encompassing eight orders of spatial magnitude (Figure 12.1). At the nanometer scale, contractile forces rely on the interaction of molecular motors composed of actin and myosin filaments organized into overlapping bands that form the basic contractile unit termed the sarcomere. Sarcomeres assemble into cytoskeletal filaments termed myofibrils that span the entire CM cell body, and myofibrils within CMs bundle in parallel to form aligned contractile structures. The 2–4 billion CMs in the heart are cylindrical in shape, with a length to width aspect ratio of 7:1, and are longitudinally connected end to end by specialized structures, termed intercalated disks, that mechanically and electrically couple the cells into multicellular, contractile myofibers [3,15]. At the tissue scale, the heart consists of lamellar-like layers of aligned cardiac myofibers wrapped around the heart to form the walls of the ventricles and the atria. In the left ventricle, which sends the blood to the body through the systemic circulation, myofiber orientation varies linearly throughout the thickness of the ventricular wall (Figure 12.2). This architecture is responsible for translating the uniaxial contraction of individual cells into an actual reduction in the volume of the heart chambers during a pumping cycle. Thus, it is the coordinated action of billions of actin–myosin molecular motors at the nanometer scale, each generating piconewton forces, that produces tissue-scale forces up to 10 mN/mm² of myocardium [16,17]. Engineered cardiac constructs need to reproduce the complex hierarchical structure of the myocardium in order to provide clinically relevant contractile forces.

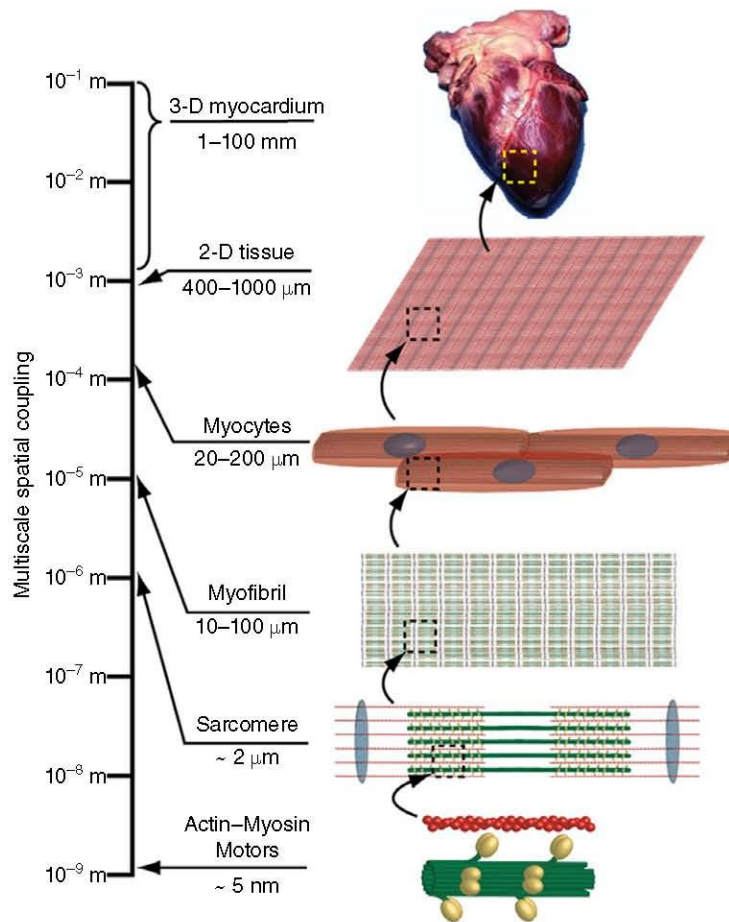


FIGURE 12.1 A schematic of the multiscale hierarchy of the myocardium. The generation of macroscale forces requires a precise architecture spanning eight orders of spatial magnitude from nanometers up to centimeters. Actin–myosin molecular motors are organized as overlapping filaments that are assembled into sarcomeres, which in turn form myofibrils spanning an entire cell. Myocytes are mechanically and electrically coupled via intercalated disks to form multicellular myofibers that are organized into aligned 2-D sheets. The ventricles in the heart are composed of overlapping myocyte sheets forming lamellar-like layers.

12.2.2 Mechanical Anisotropy

The complex arrangement of aligned myofibers gives the myocardium highly anisotropic mechanical properties. For example, the native myocardium of the left ventricle of a rat has a Young's modulus of 157 ± 84 kPa parallel and 84 ± 8 kPa perpendicular to the myofibers (Figure 12.3), with similar values reported for human and porcine hearts [18–22]. The importance of the mechanical properties and anisotropy is illustrated by the profound alterations observed in disease states. In a rat

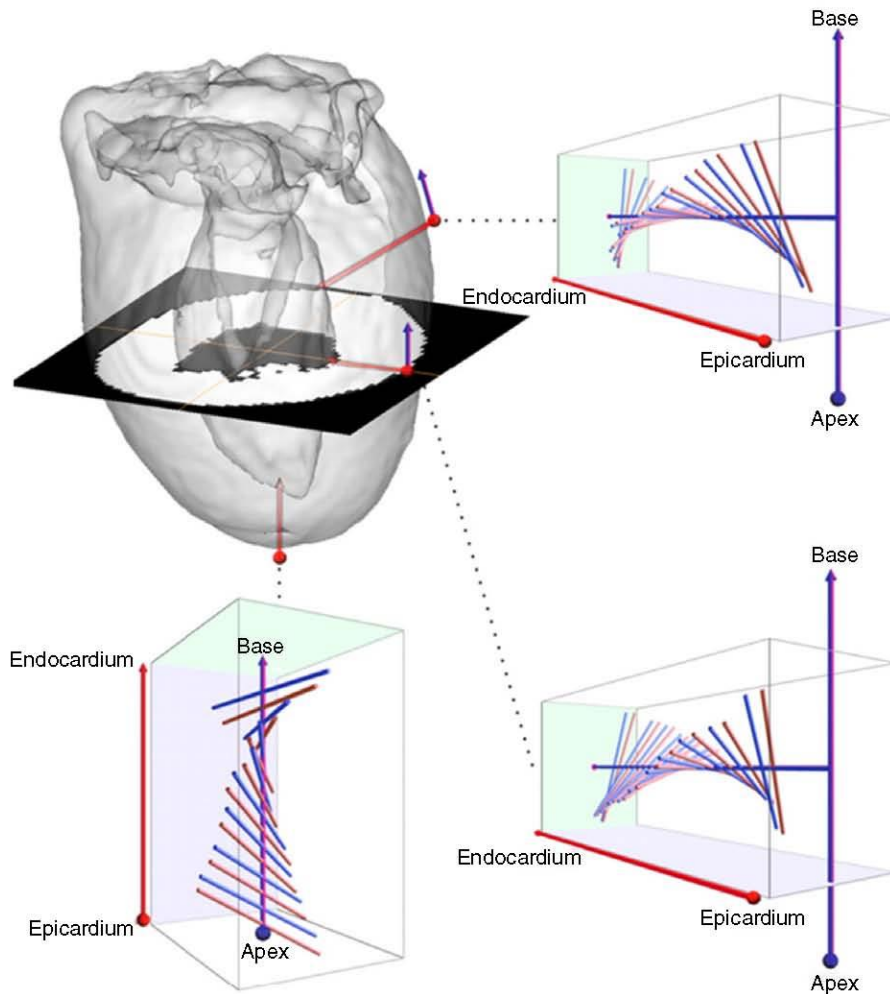


FIGURE 12.2 Myofiber orientation in a rat heart. The orientation of the myofibers was reconstructed by fitting a generalized helicoid model to an MRI dataset. The schematic of the heart shows the three areas of observation (red penetrating arrows) at the base, equator, and apex (clockwise from top right). At each location, the orientation of the myofibers through the myocardium, from endocardium (innermost layer) to the epicardium (outermost) is shown. Myofiber orientation was reconstructed (blue rods) by interpolating orientations obtained from MRI data (red rods). MRI, magnetic resonance imaging. (Reprinted with permission from Reference 141.)

model of MI, ventricular stiffness increased twofold at 6 weeks after the MI, while the scar tissue within the MI became completely isotropic in mechanical properties [23]. *In vitro*, CMs cultured on substrates stiffer than normal myocardium have demonstrated a decreased beating frequency, further suggesting that ventricular stiffening can adversely affect CM contraction and cardiac function [24]. This indicates that in order to achieve therapeutic success, scaffolds for cardiac tissue

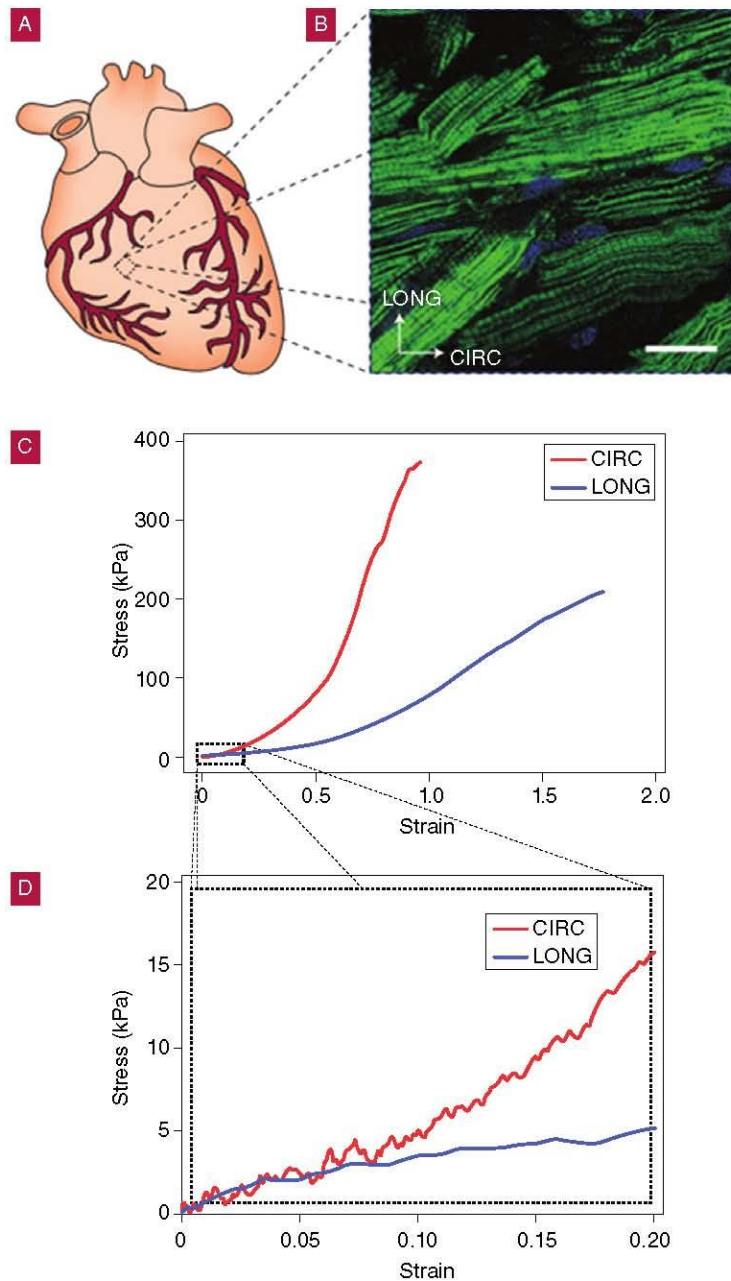


FIGURE 12.3 Mechanical and structural characteristics of the myocardium. The typical arrangement of aligned myofibers gives the myocardium highly anisotropic tensile properties. (A) A schematic representation of a mammalian heart. (B) Confocal microscopy image of the right ventricular myocardium of an adult rat showing the oriented myofibers, labeled for F-actin (green) and cell nuclei (blue). (C,D) Uniaxial tensile stress–strain plots of right ventricular myocardium along the circumferential and longitudinal direction illustrates the mechanical anisotropy (C, full range to demonstrate failure properties; D, physiologic regime). Scale bar in (B) is 50 μm . CIRC and LONG stand for circumferential and longitudinal axes, respectively. (Reprinted with permission from Reference 18.) (See insert for color representation of the figure.)

engineering must match the unique mechanical properties of the native myocardium. Specifically, CMs contract $\sim 10\%$ during the cardiac cycle in order to empty the ventricle and eject blood. Achieving this deformation in an engineered cardiac tissue requires that the effective elastic modulus of the combined cells and scaffold be closely matched to the native myocardium.

12.2.3 Innervation and the Conduction System

The heart has a complex control system to regulate heart rate and the contraction cycle, and like every muscle, the heart is densely innervated. Heart rate and cardiac output are influenced by a network of afferent and efferent neurons that extend to the brain and the spinal cord, as well as interconnected neurons within the heart [25]. However, direct control of heart rate originates in the sinoatrial (SA) node, a group of cells in the right atria that initiate each contraction of the heart by regularly and autonomously depolarizing (Figure 12.4) [26,27]. Electrical signals generated in the SA node propagate as an action potential through the myocardium via the gap junctions, which are intercellular ion channels that transmit electrical potentials via Ca^{2+} flux. The arrangement of CMs in aligned myofibers accounts for the anisotropic electrical properties, with faster action potential propagation longitudinally than

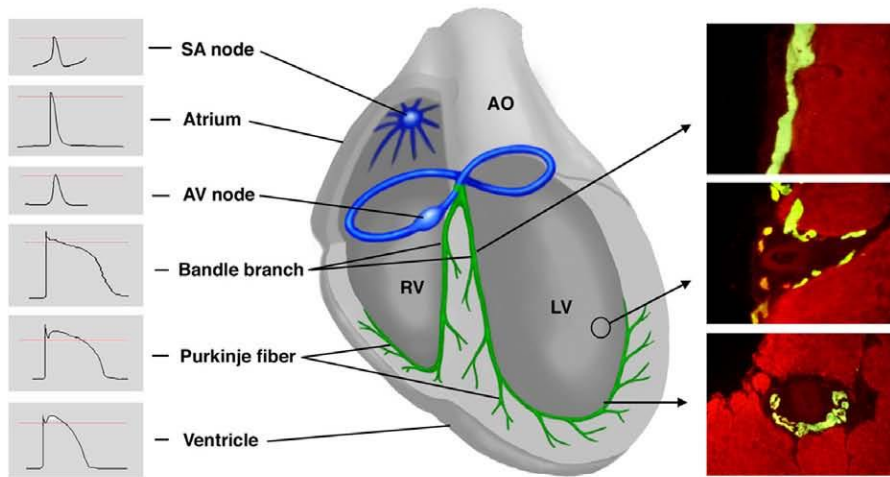


FIGURE 12.4 The cardiac conduction system. (A) Representative action potentials for components of the conduction system in the chick heart illustrated in (B). The action potentials originating in the SA node undergo several transformations as they travel through the atria, the AV node, and finally the Purkinje fibers and the ventricles. Panels on the right show the Purkinje fibers (green) within the myocardium (red) at different locations in the ventricles. (C) Subendocardial Purkinje fibers. (D) Branch point from subendocardial Purkinje fibers. (E) Intramural Purkinje fibers. AO, aorta; AV, atrioventricular; LV, left ventricle; RV, right ventricle; SA, sinoatrial. (Reproduced with permission from Reference 26.) (See insert for color representation of the figure.)

transverse [28]. From the atria, the action potential reaches the atrioventricular (AV) node, which connects to a ring of CMs that loops between the ventricles and the atria. The AV node slows conduction by introducing a delay to ensure enough time for the atria to empty into the ventricles. The action potential is then transmitted to the ventricular conduction system, which comprises the Purkinje fibers. The specialized CMs of the Purkinje fibers have higher conduction speed in order to rapidly distribute the action potential throughout the ventricles so that they can contract synchronously. Together, the nerves, nodes, and ventricular conduction system coordinate and regulate contraction to meet systemic needs. However, disease states can disrupt normal contraction and cause an arrhythmia, which can be fatal. Loss of synchrony, whether due to genetic defect or tissue remodeling after MI, prevents coordinated contraction of the ventricles, thus reducing or eliminating blood flow [25,29,30]. For cardiac tissue engineering, grafts intended to replace infarcted scar tissue must integrate successfully with the native neuronal and conduction systems and synchronize with the viable myocardium in order to improve cardiac function. Failure to do so will create a pro-arrhythmic interface between the graft and the patient's myocardium. It remains to be determined how difficult it is to achieve this integration, as there are no clinical trials of engineered tissue grafts that have yet been conducted in humans.

12.2.4 Vascularization

The CMs in the heart are constantly contracting, creating a high metabolic demand that requires a large supply of oxygen and nutrients. To meet this need, the heart is the most vascularized organ in the body with capillaries spaced $\sim 20 \mu\text{m}$, which maximizes mass transport to and from the CMs [31]. The coronary vasculature forms an extremely intricate vessel network branching throughout the myocardium from the $\sim 6 \text{ mm}$ diameter coronary artery to the $\sim 10 \mu\text{m}$ diameter capillaries (Figure 12.5). The high capillary density means each CM is in contact with endothelial cells from at least one capillary [32]. While endothelial cells line the capillaries, larger vessels are supported by pericytes and smooth muscle cells that line the outer perimeter and maintain vessel integrity and vasoactivity. These vascular cells represent a significant fraction of the total number of cells in the heart and have an essential role in regulating CM function. In the context of cardiac tissue engineering, tissues must have sufficient CM density to generate contractile force and high capillary density to provide adequate nutrient transport in three-dimensional (3-D) constructs. For example, cell density of more than $5 \times 10^5 \text{ cells/mm}^3$ is observed in the adult rat myocardium, of which $\sim 17\%$ are cardiac vascular cells (endothelial cells and pericytes) [33,34]. The cardiac endothelium, in particular, can regulate cardiac function via paracrine signaling between endothelial cells and CMs [35,36]. For example, when cultured with endothelial cells *in vitro*, CMs showed improved survival rate and contractile performance [37]. In cardiac tissue engineering, it is important to account for the coronary vascular system in terms of nutrient mass transport to highly metabolic CMs, as well as specific cardiac endothelium–CM signaling. Recapitulating both aspects is likely necessary in order to achieve clinically relevant CM density and function.

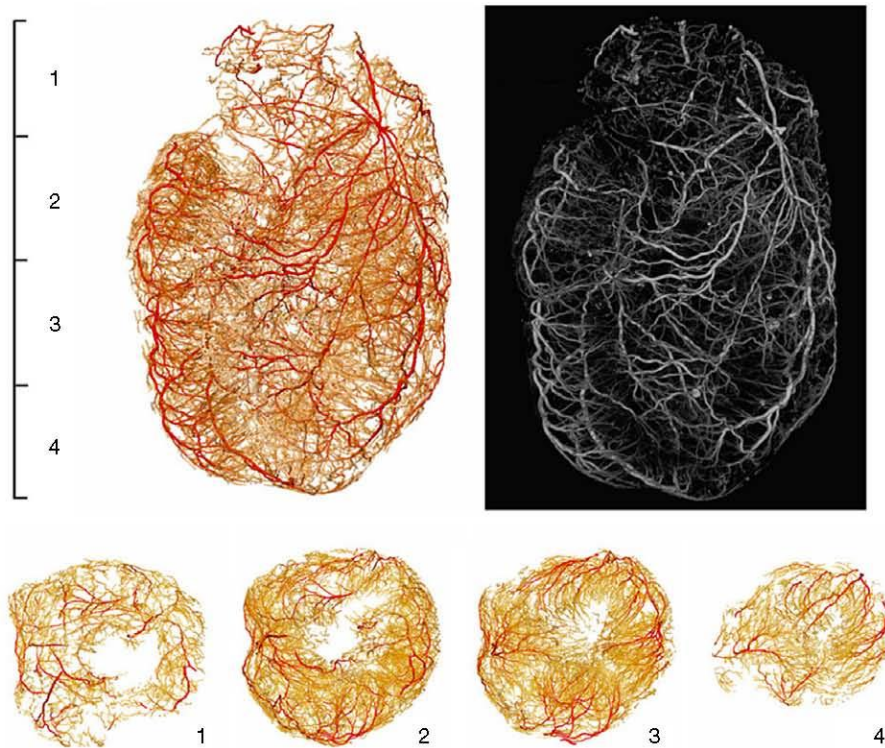


FIGURE 12.5 The whole vasculature of an adult rat heart was reconstructed (top left) from micro-CT data (top right). Transverse sections obtained in four planes (below) show the penetrating network of capillaries. The color of the rendered vessels corresponds to the intensity of the voxels in the original dataset. (Reprinted with permission from Reference 142.) (See insert for color representation of the figure.)

12.2.5 Extracellular Matrix

The cardiac ECM is a 3-D network of fibrillar proteins and glycosaminoglycans (GAGs) that provides structural support and serves as an essential substrate for physical and chemical signaling. Each cell type in the heart contributes in some way to the synthesis, assembly, and remodeling of the ECM in their local environment. However, cardiac fibroblasts are the primary cell type involved in the maintenance of the ECM and represent 64% of the total number of cells in the adult rat heart, though they account for only $\sim 18\%$ of the cardiac volume [33,38]. Cells interact with the ECM through integrin receptors on their membrane that can bind to the ECM and form a mechanical linkage to the cytoskeleton within the cell. Through this binding interaction, cells can exert mechanical forces on the ECM to migrate through their environment or to manipulate and assemble the surrounding ECM. In order to remodel the ECM, cells also release specialized enzymes, the matrix metalloproteinases (MMPs), which can cleave specific ECM components [39].

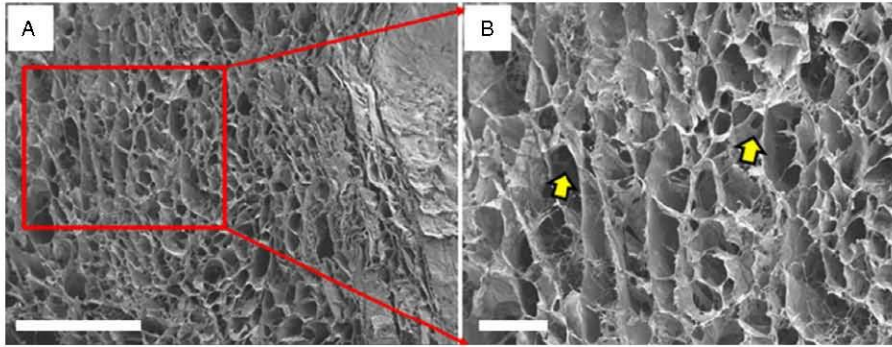


FIGURE 12.6 Scanning electron microscopy (SEM) images of porcine myocardium after decellularization using the detergent sodium dodecyl sulfate (SDS). (A) Cross-section view shows the porous topography. Scale bar is 400 μm . (B) At higher magnification, the intricate network of interconnecting pores (yellow arrows) throughout the ECM is visible. Scale bar is 100 μm . (Adapted with permission from Reference 20.)

There are a large number of proteins within the cardiac ECM that contribute to its structural, mechanical, and chemical properties. The first element of the ECM interacting directly with the CMs is the basement membrane, a thin protein layer composed mostly of laminin, fibronectin, collagen type IV, and perlecan, a basement membrane-specific heparan sulfate [40,41]. The basement membrane acts as a selective barrier for soluble factors, as well as a linkage to the structural fibers of the extracellular environment. Beyond the basement membrane, collagens type I and III provide tensile strength and maintain the shape of the heart while also distributing the contractile forces to the whole organ [42–44]. They form a complex weave that surrounds bundles of adjacent CMs and long coiled strands aligned with the main myofiber orientation [45]. Each CM is tethered to the collagen matrix by costameres, protein assemblies that link the sarcomeres to integrin receptors to the ECM, which prevent slippage or injury under excessive loading [44,46]. Additionally, the myocardium contains the structural fiber elastin, a cross-linked, flexible protein that is highly expressed in blood vessel walls and contributes to the heart's elasticity [20]. Structurally, the cardiac ECM has characteristics of the fibrillar and laminar components, featuring an interconnected network of small pores, organized very tightly around cardiac cells. For example, the average pore diameter was 21.4 μm in decellularized porcine myocardium (Figure 12.6) [20]. The fibrillar proteins also exhibit a wide range of diameters, ranging from $\sim 1 \mu\text{m}$ for elastin, from 10 nm to 10 μm for collagen type I, and from 5 nm to 1 μm for fibronectin [47–49].

The importance of the ECM in normal cardiac function is highlighted by the maladaptive changes that occur in structure and composition with disease and aging. For example, the ECM collagen content and the diameter of the collagen fibers increase with age. This contributes to loss of elasticity (i.e., increase in stiffness) and is associated with a higher risk of CVD [42]. Furthermore, abnormal turnover of ECM proteins such as collagens, fibronectins, and laminins due to increased MMP

activity is observed in many cardiomyopathies [50]. The ECM is also important in wound healing in the heart. During the acute phase of MI, the normal cardiac ECM is replaced by a provisional fibrin-based matrix. In the chronic phase, a dense, collagen type I-rich scar tissue is formed that is stiffer and has lost the mechanical anisotropy of the healthy tissue, which further hinders cardiac contraction [23,51]. Thus, the cardiac ECM is a key model system for designing cardiac tissue engineering scaffolds, and further highlights the need to recapitulate properties of the healthy ECM in order to produce viable cardiac constructs.

12.3 BIO-INSPIRED DESIGN REQUIREMENTS OF CARDIAC TISSUE ENGINEERING SCAFFOLDS

The structure and function of the myocardium as highlighted in Section 12.1 forms the basis from which we can implement the bio-inspired design of cardiac tissue engineering scaffolds. While the myocardium contains complex contractile, electrical, and vascular networks, it is the cardiac ECM that integrates these together into a functional tissue system. Thus, it is the cardiac ECM that many researchers look to as a design template for building biomimetic scaffolds. Significant research has focused on the structural, mechanical, and biochemical characteristics of the ECM and methods to recapitulate a subset of these properties using synthetic or naturally derived polymer scaffolds.

Porosity is a key component of scaffolds because CMs need to be able to infiltrate and couple together into a dense network to form functional myocardium, requiring a network of interconnected pores. In scaffolds that cannot be easily remodeled by the cells, the absolute minimum size for pores is the size of a cell, which based on measurements of the decellularized myocardium is $\sim 20 \mu\text{m}$ [20]. Because the myocardium is cell dense, the scaffold must have high porosity or be able to be resorbed or remodeled by the cells to achieve a high porosity. Based on the ECM density in the heart, this requires a scaffold porosity of $>90\%$ to sustain high cell density, ensure homogenous cell seeding, and support oxygen and nutrients mass transport essential to the function of cardiac tissue. In the case of low porosity or very small pore size, specialized techniques such as the use of medium perfusion, are required for efficient cell seeding and oxygen and nutrients delivery to the bulk of the scaffold.

The cardiac ECM is composed of protein fibers such as collagen type I and III, fibronectin, and elastin, which are organized in parallel with the myofibers and provide alignment cues to the constituent CMs. It is important to recapitulate the structural characteristics of these fibers because CMs, like all cells, respond to physical structures in the nanometer to micrometer range via a contact guidance effect. The key physical attributes of ECM fibers are the diameter (typically ranging from 5 nm to 10 μm), spatial density, and 3-D orientation. Thus, scaffolds with fibers or fiber-like features that mimic the structure of the cardiac ECM can be effective for the alignment of CMs and other cardiac cells into anisotropic tissues.

In the myocardium, cardiac cells are tightly connected to the ECM via integrin receptors, and this adhesive binding is necessary for survival and function. For

example, disruption of fibronectin binding, observed in mice without the integrin $\alpha_5\beta_1$, is embryonically lethal [52]. The specific ECM protein composition and organization is also important, as fibronectin, which is expressed at higher levels during cardiac development, has been shown to foster cardiac progenitor cell differentiation into CMs [53]. Cardiac tissue engineering scaffolds composed of ECM proteins typically have intrinsic ligands for integrin receptors to bind cells, comparable with the native ECM. However, synthetic materials, polysaccharides, and other non-ECM protein materials must be modified in some way to add cell adhesive motifs. Typically, this is achieved by grafting or adsorbing polypeptides or whole ECM proteins (such as fibronectin) to the materials as either a surface or bulk modification.

In the heart, cells remodel the cardiac ECM continuously to allow for myofiber formation, angiogenesis, and high cell density. For example, collagens are completely replaced every 160–240 days and noncollagen proteins are replaced 10 times as fast [54]. It is essential that cardiac tissue engineering scaffolds degrade in a controlled manner in order for cells to organize and maintain their own ECM. Scaffolds made from native components of the ECM can readily be remodeled by cells because they already express the appropriate enzymes, such as MMPs. For synthetic materials, remodeling can be achieved by using biodegradable polymers that cleave by hydrolysis and/or integrating enzyme-cleavable domains, comparable with the MMP-degradable sites in ECM proteins. Moreover, the kinetics of scaffold degradation should be coordinated with ECM production and remodeling to match the rate of muscle formation and maintain structural integrity throughout the process.

Finally, scaffolds need to integrate with the electrical and mechanical properties of the cardiac environment. For example, constructs must exhibit high fatigue resistance by reversibly withstanding mechanical strains of $\sim 13\%$ over a large number of contraction–relaxation cycles, millions if grafted in the actual heart [55,56]. Scaffolds also need to match the mechanical compliance and anisotropy of the myocardium to promote CM alignment and contractility. Based on rat and human myocardium, the Young's modulus should be in the range of 10 kPa to 1 MPa and be higher in the myofiber direction than transverse. The CMs must also be aligned uniaxially within each lamellar layer, for example 50% of the CMs in the rat right ventricle are aligned within $\pm 20^\circ$ of the mean alignment direction [18]. Furthermore, scaffolds must not negatively impact the electrical properties of cardiac tissue, in particular, it must have similar conduction velocity and anisotropy to native myocardium and the impedance should be low to avoid hindering contraction and causing necrotic/hypoxic myocardium [57].

12.4 APPROACHES TO FABRICATING ECM BIOMIMETIC SCAFFOLDS

12.4.1 Porous Scaffolds

Fabricating scaffolds with an interconnected network of pores is the most straightforward way to obtain a thick 3-D structure that can be seeded with cells throughout and sustain high cell density. For cardiac tissue engineering, porogen leaching and

lyophilization are the methods that have produced the best results. In porogen leaching, a polymer solution is mixed with a porogen (e.g., salts or sugars) and polymerized. The porogen is then dissolved using a solvent, which creates voids within the polymer matrix. By controlling the size and density of porogen particles, scaffolds can be engineered with pore sizes ranging from one to hundreds of micrometers and porosities of up to 95% of the scaffold volume [58]. For example, Radisic *et al.* used sodium chloride (NaCl) particles as porogens to fabricate poly(glycerol sebacate) (PGS) scaffolds with interconnected pores between 75 and 150 μm in diameter and 90% porosity (Figure 12.7A) [59]. These scaffolds allowed seeding of CMs and cardiac fibroblasts at high density *in vitro* and when implanted in a mice model of MI, acellular porous PGS scaffolds were readily invaded by host cells and supported the formation of new blood vessels [59,60]. Porogen leaching also can be adapted to provide more control over the macroscale architecture of the scaffold. For example, Madden *et al.* engineered porous scaffolds that combined regularly spaced polycarbonate (PC) rods and poly(methyl methacrylate) (PMMA) beads in order to create an array of parallel channels in the poly(2-hydroxyethyl methacrylate-co-methacrylic acid) (pHEMA-co-MAA) hydrogel scaffold (Figure 12.7B) [61]. The result was a high-porosity scaffold with an array of 60- μm wide channels in place of the rods that fostered CM bundle formation and 30- μm pores in place of the beads that improved neovascularization in an infarct model.

Lyophilization, or freeze-drying, is another method for creating porous scaffolds, and is most commonly used for naturally derived biopolymers. To do this, a polymer dissolved in water is frozen and then exposed to near vacuum to sublimate the ice crystals that formed during the freezing process, leaving behind pores. This technique can be used with polysaccharides such as alginate to produce scaffolds with tunable pore size and mechanical properties (Figure 12.7C) [62]. Furthermore, polysaccharide scaffolds can be chemically modified with cell-adhesive proteins found in the ECM. For example, alginate scaffolds with $\sim 100\text{-}\mu\text{m}$ pores fabricated by lyophilization were modified with the integrin-binding peptide arginine-glycine-aspartic acid (RGD), and heparin-binding protein (HBP) [63]. Culturing CMs on the alginate-RGD-HBP scaffolds resulted in increased expression of sarcomeric α -actinin, indicating increased muscle volume compared with CMs cultured on nonmodified alginate scaffolds. Additionally, lyophilization can be used to engineer scaffolds with anisotropic pore structures by controlling thermal gradients during the freezing process. For example, when a collagen-GAG solution is frozen in a Teflon cylinder between two copper plates, the difference in thermal conductivity between copper and Teflon creates a unidirectional pore structure. After freeze-drying, these scaffolds had elongated pores up to 243 μm in diameter, with an aspect ratio of up to 12.6:1, which promoted alignment and beating of the human CM cell line HL-1 *in vitro* (Figure 12.7D) [64].

As described, porogen leaching and lyophilization are techniques commonly used to fabricate scaffolds with controllable porosity. In general, scaffolds are produced with isotropic microstructure, although recent work has demonstrated that a degree of anisotropy can be engineered into the scaffolds using more advanced techniques. While promising results have been obtained with these methods, it

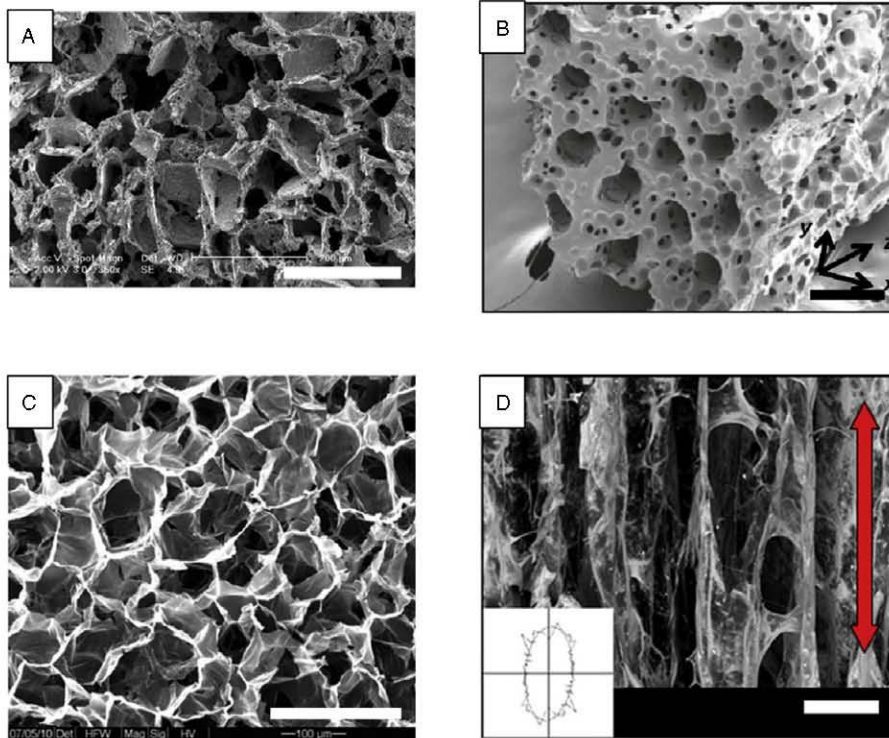


FIGURE 12.7 SEM images of porous scaffolds for cardiac tissue engineering. (A) PGS scaffolds were created by salt leaching. NaCl particles were incorporated in PGS polymer solution during polymerization then dissolved in water to leave 75- to 150- μm pores. Scanning electron micrographs reveal an extensive network of interconnected pores. Scale bar is 200 μm . (B) pHEMA-co-MAA hydrogel scaffold were fabricated using an array of rods PC as well as PMMA beads. After dissolution of the porogen, the network of interconnected 30- μm pores promoted angiogenesis, while the 60- μm diameter channels induced the formation of myocyte bundles. Scale bar is 100 μm . (C) Alginate sponges were made by freeze-drying a solution of cross-linked alginate. Scaffolds with 97- μm pores were modified with binding peptides to improve cell adhesion. Scale bar is 200 μm . (D) Anisotropic collagen-GAG scaffolds were fabricated using freeze-drying. To obtain elongated pores, the solution was frozen in a Teflon cylinder between two copper plates. The arrow marks the scaffold's axis. Insert shows the best fit ellipse to the average pore shape. Scale bar is 200 μm . (Adapted with permission respectively from References 59, 61, 63, and 143.)

remains to be seen whether the high degree of anisotropy seen in the native myocardium can be replicated. Furthermore, these techniques provide limited control of scaffold architecture at the micrometer and nanometer scales. Whether it is necessary to engineer the scaffold to mimic the ECM at this scale is still an active area research, but should be considered as a potential limitation in the context of cardiac tissue engineering.

12.4.2 Micro- and Nanofiber Scaffolds

Major components of the cardiac ECM, including collagen type I and III, are found in the form of fibers of varying diameter and length. Engineering scaffolds with fibrillar topography is an essential approach to mimic the cardiac ECM because fiber diameter has been shown to affect cell attachment, migration, and spreading [65]. Electrospinning is the most common technique used to produce fibrillar scaffolds for cardiac tissue engineering using a wide range of synthetic and natural materials, while rotary jet spinning and surface-initiated assembly are two newer techniques that offer additional control over scaffold properties.

Electrospinning employs a strong electrical field to draw a fiber from an electrically charged polymer solution ejected through a needle onto a grounded collector (see Reference 66 for an in-depth review). The relative simplicity of electrospinning has fostered the development of multiple approaches to control scaffold composition, fiber size, and architecture. Stationary collectors can be used to generate isotropic scaffolds while rotating collectors such as disks or mandrels can be used to generate aligned, anisotropic scaffolds [67–69]. For example, Shin *et al.* used a stationary collector to generate an isotropic scaffold consisting of 250-nm diameter polycaprolactone fibers that supported myofibril formation and contractility of cultured CMs [70]. To generate anisotropy, Zong *et al.* generated an isotropic scaffold which consists of 1- μm diameter poly(L-lactide) (PLA) fibers (Figure 12.8A), which were uniaxially stretched after electrospinning and promoted alignment of cultured CMs (Figure 12.8B) [71]. The electrospinning process can also be tailored to control scaffold mechanical properties. For example, Amoroso *et al.* used a rotating mandrel that was translating at varying speed along its longitudinal axis to control the number of overlapping fibers in the scaffold and mimic the bending stiffness of a heart valve [69]. The composition of the polymer solution used in electrospinning also has a direct effect on fiber diameter and the electrical and mechanical properties. In one example, increasing the ratio of poly(aniline) to gelatin solution reduced the diameter of electrospun fibers from 803 to 61 nm, while increasing the tensile modulus from 499 to 1384 MPa [72]. The scaffolds demonstrated significantly more proliferation of cardiac myoblasts compared with glass or tissue culture-treated plastic substrates. Poly(aniline) is also a conductive polymer and thus can be used to modify the electrical properties of engineered scaffolds. For example, rat CMs cultured on electrospun poly(L-lysine)-poly(aniline) scaffolds supported greater CM viability when the cells were electrically stimulated to contract [73]. Electrospinning is also capable of creating scaffolds with a range of fiber diameters nanometer to micrometer scales, similar to the cardiac ECM where diameters range from 5-nm fibronectin fibrils to 10- μm collagen type I fibers. To achieve this, multiple polymer solutions can be coelectrospun and collected on the same surface to obtain a range of fiber characteristics. For example, 50- to 500- μm diameter poly(lactic-co-glycolic acid) fibers were electrospun together with 2- to 4- μm diameter fibrin fibers to create multiscale scaffolds (Figure 12.8C,D), which promoted expression of the CM markers sarcomeric α -actinin, troponin, and tropomyosin in mesenchymal stem cells [74].

Electrospinning is a popular technique to create micro- and nanofiber scaffolds that mimic the size of fibers found in the cardiac ECM. However, there are a number

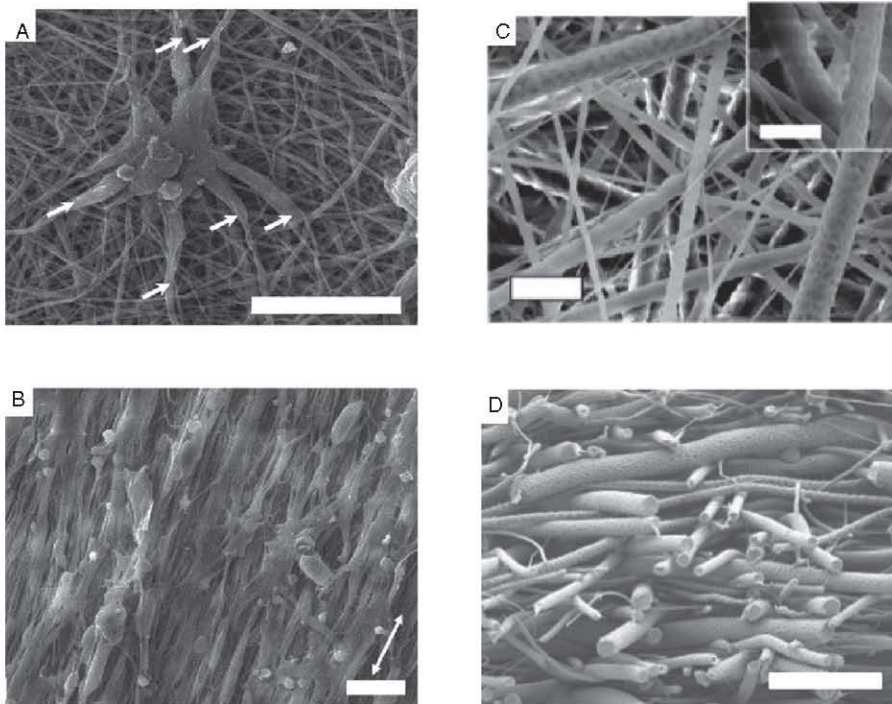


FIGURE 12.8 Electrospinning of anisotropic and multiscale scaffolds. Adult rat CMs were seeded on electrospun scaffolds of PLA that were (A) isotropic or (B) anisotropic due to being uniaxially stretched. Arrows in (A) show the filopodia-like structure that the cells create to spread on the scaffold while the arrow in (B) indicates the main fiber orientation that CMs follow. SEM images, scale bars are 40 μm . Another application of electrospinning is the fabrication of multiscale scaffolds. (C) Two solutions of polycaprolactone of different concentrations were electrospun simultaneously on the same collector to produce fibers with two mean diameters, 3.3 μm and 0.6 μm . Scale bars are 10 μm and 5 μm (insert). (D) SEM cross-sections show the ECM-like range of fiber diameters. Scale bar is 40 μm . (Adapted with permission from References 71 and 144.)

of limitations that are important to consider. First, electrospinning does not produce a specific fiber diameter; rather it produces scaffolds with a distribution of fiber diameters. Whether this is an issue depends on a number of factors, including the sensitivity of cells of interest to fiber morphology. Second, electrospinning produces scaffolds that are typically dense fiber mats, which results in relatively low porosities and pore sizes that are smaller than cells, limiting infiltration. One approach to solve this issue has been the incorporation of electrospun poly(glycolic acid) fibers within a freeze-dried collagen-GAG scaffold, which increased the mechanical stiffness and improved the ability to culture cardiac stem cells [75]. Third, electrospinning of synthetic polymers can mimic the size of ECM fibers, but not the cell-adhesive motifs that bind integrins, in these cases it is necessary to coat the fibers with an

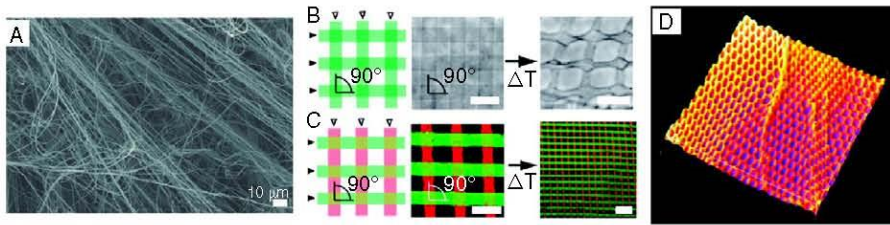


FIGURE 12.9 Alternatives to electrospinning to create micro- and nanofiber scaffolds. Rotary jet spinning uses a high-speed rotating spindle to draw fibers from synthetic and natural materials. (A) SEM images of gelatin fibers show a high degree of alignment. Surface-initiated assembly is a technique that mimics cell-mediated assembly and provides control of the scaffold nano- to macroscale structure and composition. (B) Schematic (left) and optical phase image (right) of two patterns of 20- μm width by 20- μm spacing fibronectin lines microcontact-printed orthogonally onto PIPAAm. After some time (ΔT) in cooling water, the mesh termed nanofabric is released and maintains its shape. (C) The same pattern was created with fibronectin (green) and laminin (red) and was released as a bicomponent nanofabric (right) showing that SIA can be used to control the architecture and composition of biomimetic ECM nanofabrics. (D) Three-dimensional, false-colored rendering of a fibronectin mesh with 20- μm wide elliptical holes observed by scanning electron microscopy. The nanofabric shows fishnet-like ripples. Scale bars are 40 μm in B and C and 100 μm for the released bicomponent nanofabrics. X, Y axes are 360 μm in D. (Adapted with permission from References 77 and 78.) (See insert for color representation of the figure.)

ECM protein or related cell-adhesive peptide. Finally, electrospinning uses strong electrical fields that make it incompatible with some materials, and some polymers will not form fibers under the spinning conditions. This has led to the development of alternative fiber spinning techniques that can produce nano- and microfibers with similar diameters, but from a different range of materials. For example, rotary jet spinning (RJS) uses a high-speed rotating spindle to create strong centrifugal forces that push a polymer solution through an integrated nozzle [76]. The spun fibers such as PLA are assembled inside a cylindrical collector with a high degree of anisotropy and have been shown to support CM attachment and uniaxial alignment [77]. RJS works with synthetic polymers such as PLA, polyacrylic acid, and polyethylene glycol (PEG) and natural biopolymers such as gelatin (Figure 12.9A), and represents one of the alternative fiber spinning techniques being developed to address some of the limitation of electrospinning.

While the cardiac ECM contains a variety of nano- and microfibers, cells do not assemble these using fiber spinning techniques such as those typically used for manmade materials. Rather, ECM protein fibers are polymerized using a range of receptor-mediated and enzymatically driven processes. For example, fibronectin fibers are assembled on the cell membrane using integrin receptors in a process termed fibrillogenesis [49]. The integrin receptors bind fibronectin dimers and actin-based contraction unfolds the dimers and exposes cryptic fibrillogenesis sites that bind adjacent fibronectin dimers. Certain ECM protein fibers such as fibronectin, laminin, and collagen type IV cannot be fabricated using most known fiber spinning

techniques, but mimicking the way cell assembles these ECM fibers may be an alternative approach. Recently, Feinberg *et al.* developed a technique termed surface-initiated assembly (SIA) that enables the fabrication of ECM protein nanofibers with control of the nano- to macroscale fiber organization and composition [78]. In SIA, fibronectin is adsorbed to polydimethylsiloxane (PDMS) where it unfolds due to hydrophobic surface interactions. The unfolded fibronectin with exposed, cryptic fibrillogenesis domains is then transferred to a sacrificial surface, which can be dissolved to release the assembled fibronectin fibers. This process mimics cell-mediated assembly of the ECM, where integrins bound to the cytoskeleton are used to unfold fibronectin dimers to expose their self-binding (fibrillogenesis) sites [48]. SIA can create freestanding, nanometer-thick ECM protein nanofibers (Figure 12.9B) and nanofabrics (Figure 12.9D), using single or multiple ECM proteins such as fibronectin, laminin, fibrinogen, and collagens type I and IV. A unique aspect of SIA is its ability to combine multiple ECM fibers into the same scaffold, such as laminin and fibronectin (Figure 12.9C), which should enable the engineering of scaffolds that more closely mimic the structure and composition of the native cardiac ECM. This approach has been used to engineer anisotropic cardiac constructs such as CM threads and sheets; however, the current limitation is how to extend this technology to 3-D engineered cardiac tissues.

12.4.3 Synthetic and Naturally Derived Hydrogels

Naturally derived hydrogels are widely used in cardiac tissue engineering because they are relatively simple to fabricate and possess many of the properties of the native cardiac ECM, including a fibrillar network morphology, integral cell-adhesive binding sites, high water content, and high porosity [79]. For example, collagen type I can be polymerized into a hydrogel at physiologic temperatures and has been used to engineer cardiac tissue with a high density of CMs and good electrical coupling [80]. Matrigel is another example, consisting primarily of a mixture of the basement membrane proteins laminin, collagen type IV, and entactin. It can be polymerized as a hydrogel with embedded CMs to engineer 3-D cardiac tissues with high cell density and contractile properties [81–83]. Multicomponent ECM gels have also been derived from several tissues such as porcine bladder and more recently from porcine myocardium (Figure 12.10A), which have been decellularized, lyophilized, and then digested enzymatically to extract the ECM components into the solution [84,85]. These ECM-based hydrogels can be polymerized under physiologic conditions due to the high collagen type I content and closely match the ECM protein composition of the native myocardium, though GAGs, fibronectin, and elastin may be lost [20,86–88]. Culturing CMs in these myocardium-derived ECM gels has shown enhanced cell migration and differentiation compared with regular collagen type I hydrogels [89,90]. These gels have also been injected *in vivo* to improve postinfarct recovery and have been shown to promote angiogenesis by binding growth factors more effectively than pure collagen type I hydrogels [91].

Natural hydrogels also present the unique advantage of being easily degraded and remodeled by the cells, which facilitates cell self-organization into 3-D constructs. For example, Zimmermann *et al.* have seeded CMs in ring-shaped

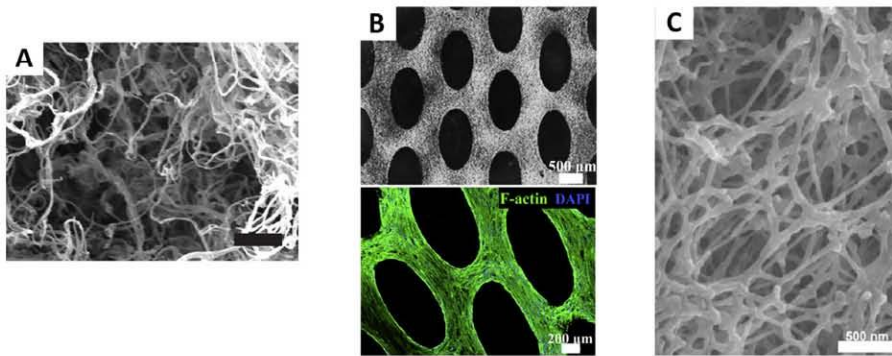


FIGURE 12.10 Examples of hydrogels for cardiac tissue engineering. Myocardial ECM gels can be obtained by decellularization, lyophilization, and enzymatic digestion. (A) The solubilized ECM components gel under physiological conditions into fibrous multicomponent hydrogels with ECM-like structure revealed by SEM. Scale bar is 1 μm . (B) Fibrin–matrigel hydrogels cast around an array of micropillars are remodeled by myocytes to form a contractile cardiac construct with local anisotropy. Scale bars are 500 μm (top) and 200 μm (bottom). (C) Synthetic polypeptides are designed to self-assemble into nanofibrous hydrogels and to mimic VEGF to induce angiogenesis. (Adapted with permission from References 89, 94, and 100.) (See insert for color representation of the figure.)

collagen–matrigel hydrogels cast around Teflon cylinders. Over time, the embedded cells pull and compact the surrounding ECM gel, causing the construct to contract around the inner cylinder and increase circumferential tension. This mechanical strain induced CM alignment and the formation of 3-D contractile, anisotropic cardiac tissue, termed engineered heart tissue [92]. Related work has demonstrated the formation of functional engineered heart tissue using additional ECM protein gels such as fibrin [93]. Furthermore, CMs and cardiac fibroblasts have been combined to create anisotropic cardiac tissue using sutures as anchor points to form self-organized cardiac fibers and using fibrin–matrigel cast around microfabricated post arrays to produce anisotropic cardiac sheets (Figure 12.10B) [94,95].

There are many advantages to natural hydrogels, but there are also limitations that need to be considered. First, the ECM proteins must be obtained from an animal or cell source, which introduces batch-to-batch variability in properties and an increase in cost. Furthermore, the animal source of these ECM proteins has the potential to induce an unwanted inflammatory immune response when implanted *in vivo*. Second, these hydrogels are typically isotropic in microstructure, which limits their ability to engineer anisotropic cardiac tissue. As mentioned, cell-generated compaction of these gels can be used to induce alignment, but engineering anisotropy into the scaffold at the time of fabrication may be advantageous. Third, the ability of cells to degrade and remodel the ECM hydrogels can be a problem if it is degraded too rapidly and the mechanical properties deteriorate before adequate muscle tissue has formed. Thus, the cell and ECM density, cross-link density, and susceptibility to MMP degradation must be carefully tuned to optimized cardiac muscle formation.

Synthetic hydrogels offer a number of advantages over natural hydrogels because the chemical structure, molecular weight, cross-link density, water content, hydrolytic stability, and cross-linking chemistry can be readily tuned. Furthermore, recent advances have enabled the integration of custom polypeptides that functionalize synthetic hydrogels with biologically active cell binding and enzymatic degradation sites. For example, the fibronectin-derived adhesion ligand amino acid sequence arginine–glycine–aspartic acid–serine–proline (RGDSP) integrated into PEG hydrogels improved viability of the HL-1 CM cell line [96]. In another example, Kraehenbuehl *et al.* synthesized a bioactive PEG hydrogel featuring adhesion ligands for the integrins $\alpha_v\beta_3$ and $\alpha_5\beta_1$, as well as an MMP substrate site, which promoted CM survival and angiogenesis when injected together with endothelial cells into an infarct [97]. A similar study showed that PEG hydrogels with MMP degradability and integrin-binding RGDSP polypeptides could improve cardiac progenitor cell differentiation [98]. A different approach is the design of synthetic polypeptides that self-assemble into nanofibrous hydrogels under specific stimuli, similar to the way ECM proteins assemble into fibers. For example, polypeptides can be delivered as an injectable solution that polymerizes *in situ* and they can be modified to deliver growth factors such as pro-angiogenic vascular endothelial growth factor (VEGF) [97]. Guo *et al.* successfully added a heparin-binding domain sequence to the peptide RADA16 (its amino acid sequence is arginine–alanine–aspartic acid–alanine, repeated four times) to trigger a sustained and continuous release of VEGF, mimicking a natural release profile [99]. In another example, Webber *et al.* designed a polypeptide with a sequence mimicking VEGF that fostered angiogenesis *in vivo* (Figure 12.10C) [100]. Self-assembling polypeptides have also been modified to bind other growth factors such as the platelet-derived growth factor (PDGF), which is essential during cardiovascular development. When injected *in vivo*, such self-assembling polypeptides demonstrated a protective effect on CMs near the infarct site and induced angiogenesis [101].

These synthetic hydrogels are an area of active research and are continually improving, however, there are limitations that need to be considered. First, there is generally poor microstructural control of anisotropy, similar to natural hydrogels, and thus most of these hydrogels are polymerized as isotropic systems. Although the cost of synthesizing synthetic hydrogels is usually relatively inexpensive, certain monomers can be expensive and the integrated polypeptides used to create biofunctionality add significant cost to the system. Furthermore, even though biological motifs such as integrin ligands and MMP degradation sites are added, this represents only a tiny fraction of functional binding sites within intact ECM proteins. For example, growth factor binding sites and mechanosensitive changes in protein conformation are typically absent.

12.4.4 Nano- and Microfabricated Scaffolds

Nano- and microfabrication techniques for cardiac tissue engineering enable the formation of scaffolds with anisotropic structure on the same scale as fibers in the native cardiac ECM. In 2-D, sheets of cardiac muscle have been engineered using photolithographic techniques to generate microscale surface topography, nanoscale

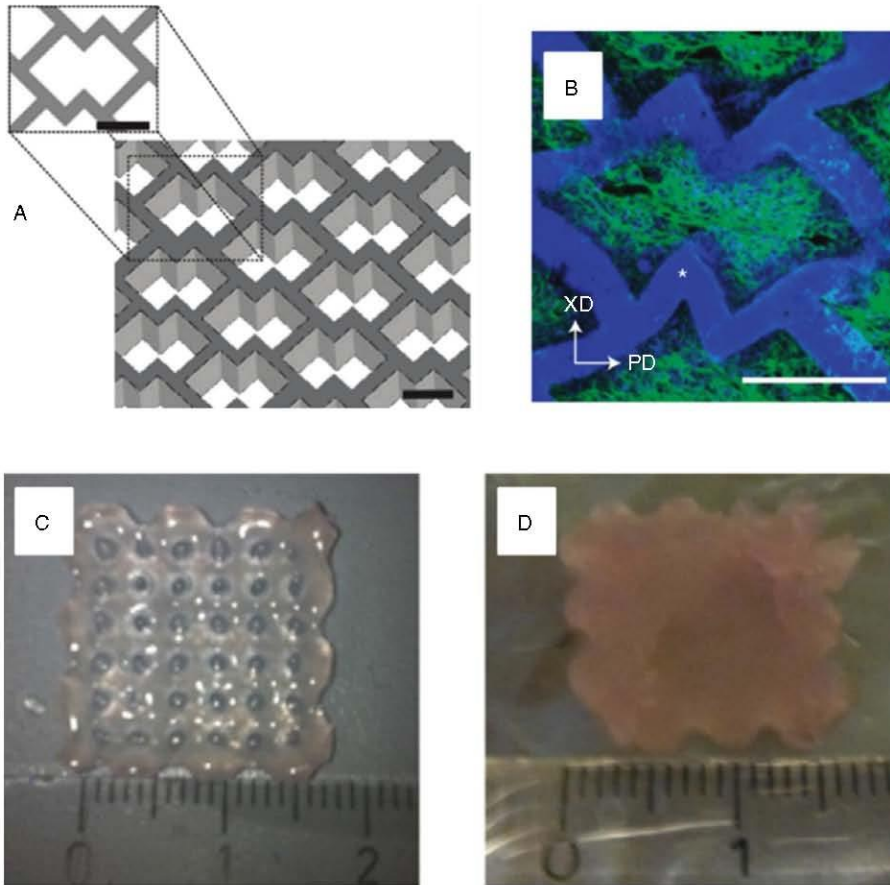


FIGURE 12.11 Microfabricated scaffolds for cardiac tissue engineering. (A) Design of PGS scaffolds laser-cut to create an accordion-like honeycomb structure. (B) The structural anisotropy of the scaffolds guided myocyte alignment, observed by immunostaining for F-actin (green) and nuclei (blue). 3-D printing can fabricate scaffolds layer by layer, with control over the microarchitecture. 2×2 cm 3-D-printed scaffolds with (C) or without (D) ~ 1 mm pores can be seeded with cardiac progenitors. Scale bars are $200 \mu\text{m}$ in A and B, and the ruler is in centimeters in C and D. (Adapted with permission from References 18 and 107.)

surface topography, and micropatterned fibronectin lines on the cell culture substrates [102–105]. These approaches are effective at cardiac tissue engineering in 2-D, but are planar fabrication techniques and thus difficult to translate to 3-D. To address these limitations, two techniques traditionally applied with industrial plastics and metals, laser cutting, and 3-D printing, are now being used to fabricate tissue engineering scaffolds. Laser cutting is a subtractive method that uses a focused, high-powered laser to cut and ablate material. For example, accordion-like honeycombs were cut into PGS scaffolds to create an anisotropic structure that guided uniaxial CM alignment *in vitro* (Figure 12.11A,B) [18]. Furthermore, the constructs

had anisotropic mechanical properties with a tensile modulus of 32 kPa parallel and 19 kPa perpendicular to the myofiber direction, comparable with the native rat myocardium (54 kPa and 20 kPa, respectively). Researchers have also used laser cutting to create blood vessel-like parallel channels in PGS sponges to increase medium perfusion and improve CM viability [106]. However, laser cutting works best for making vertical cuts on planar materials, limiting the complexity of 3-D scaffold architectures that can be engineered, and resolution is typically greater than the diameter of most ECM fibers, for example, 100 μm . Another approach that is advancing rapidly is 3-D printing, that is, solid-free form fabrication, which is an additive technique that deposits material layer by layer to create scaffolds with control of the 3-D architecture. In one of the first cardiac tissue engineering applications, alginate gels were printed as 2×2 cm meshes in simple square lattice pattern and seeded with CM progenitor cells that attached and maintained viability (Figure 12.11C,D) [107]. Miller *et al.* also demonstrated that 3-D printing can be used to create microvascular networks, which though achieved in the context of engineered liver tissue, could be readily adapted to create a perfusable engineered cardiac construct [108]. However, currently the resolution of 3-D printing technology using hydrogels is limited to hundreds of micrometers and improves to ~ 50 μm using thermoplastics such as PLA. Given the demonstrated effectiveness of nano- and microscale features in cardiac tissue engineering, improvements in 3-D printing will be required for it to become a viable scaffold fabrication technique. Fortunately, this is a rapidly developing area of research and there are already 3-D printers that can achieve micrometer scale resolution and will likely be adapted to use biomaterials suitable for cardiac tissue engineering in the near future.

12.4.5 Cell-Generated ECM Scaffolds

The scaffold fabrication techniques described so far can mimic various aspects of the cardiac ECM, but they do not replicate the actual composition and structure. To address this, researchers have tried to minimize the number of artificial cues and instead, induce cardiac cells *in vitro* to synthesize and assemble their own ECM and self-organize into a tissue. These cell-generated ECM scaffolds, a process also termed scaffold-free tissue engineering, can produce CM-dense tissues with tightly integrated ECM composed of the major protein components including collagens, fibronectin, and laminin. For example, Okano and coworkers pioneered cell sheet engineering by developing a thermoresponsive cell culture dish based on a poly(N-isopropylacrylamide) (PIPAAm) grafted surface [109]. CMs cultured on these substrates formed dense, 2-D confluent monolayers that, when released, maintained structural integrity with robust cell–cell junctions and an interconnected ECM. Anisotropic CM sheets have been engineered by modification of the grafted PIPAAm surface (Figure 12.12) and microcontact printing of fibronectin lines on the PIPAAm surface [110,111]. The transition from 2-D sheets to 3-D is achieved by stacking cell sheets to form multilayered constructs. Up to four layers have been demonstrated to couple together and beat synchronously, and when engrafted on an infarct *in vivo*, improved heart function and cell survival compared with cell injection [112,113]. However, these cell sheet scaffolds are limited to ~ 100 μm in thickness due to the

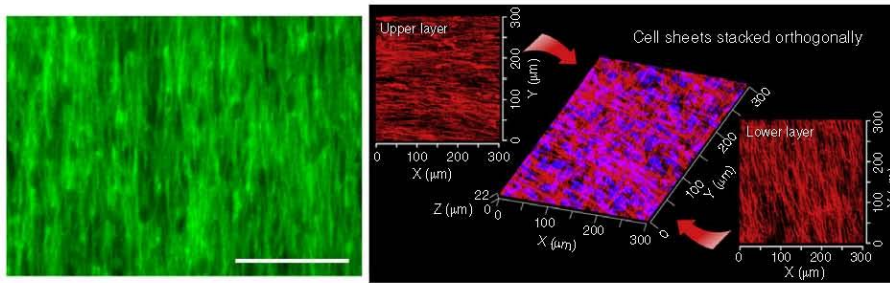


FIGURE 12.12 Cell sheet engineering is a scaffold-free approach to cardiac tissue engineering. Human fibroblasts were seeded on an anisotropic PIPAAm layer. After release, the cell sheets produced their own anisotropic ECM, revealed by observation of highly aligned collagen type I fibers (green, left). Aligned cell sheets can be stacked at different angles to create multilayer constructs (right) with F-actin (red) and nuclei (blue). Scale bar is 100 μm . (Adapted with permission from Reference 110.) (See insert for color representation of the figure.)

lack of microvasculature and, thus, thick 3-D scaffolds suitable for grafting in the human heart are still in development. Another cell-generated ECM scaffold approach, in this case designed to create larger 3-D scaffolds, uses suspension culture on rotating orbital shakers to generate a cell mass that assembles a 3-D ECM and dense CM tissue. Stevens *et al.* demonstrated the ability to combine CMs, endothelial cells, and fibroblasts to create a 3-D vascularized, engineered cardiac tissue that functionally integrated in the rat heart when implanted [114]. While this approach did not produce anisotropic muscle tissue, it does demonstrate the potential to use cell-generated ECM to engineer larger 3-D vascularized constructs. In total, these examples of cell-generated ECM constructs demonstrate that many aspects of the native cardiac ECM can be replicated by inducing cardiac cells to make their own ECM. As these techniques develop further, it is likely that the structural and functional properties of these constructs will be improved.

12.4.6 Decellularized ECM Scaffolds

Rather than mimicking the native cardiac ECM, recent work has focused on using the cardiac ECM itself as a tissue engineering scaffold. In 2008, Ott *et al.* demonstrated that the rat heart can be decellularized to produce an ECM scaffold that retains the structure and most of the protein composition of the native cardiac ECM and will support CM integration and muscle formation [133]. To do this, whole rat hearts were perfusion decellularized through the coronary vasculature using the detergent SDS to produce a collagen type I scaffold with lesser amounts of laminin, collagen type IV, and other components (Figure 12.13). Endothelial cells seeded into the vasculature could repopulate the capillary network, while CMs injected into the myocardium could repopulate sections of the ventricle and spontaneously contract. This has served as an important proof of concept that mimicking the cardiac ECM in detail, in this case by using the cardiac ECM itself, can enable the engineering of

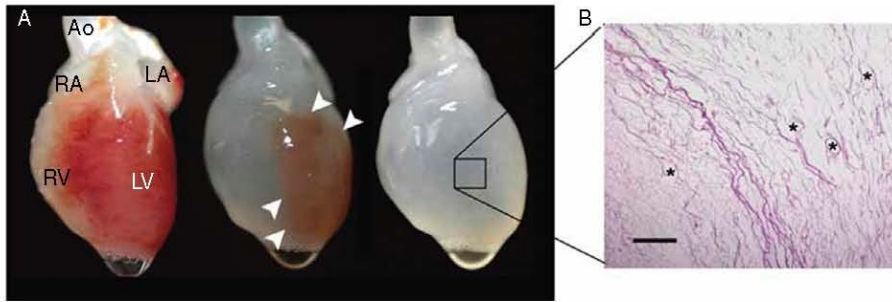


FIGURE 12.13 Decellularization of whole rat hearts. (A) Photographs of cadaveric rat hearts before, during and after perfusion of SDS detergent over 12 hours (1% SDS in deionized water, 77.4 mmHg, 20°C); Ao, aorta; LA, left atrium; LV, left ventricle; RA, right atrium; RV, right ventricle. The RV, then the atria and the LV are cleared of cellular material, rendering the heart translucent. (B) H&E staining of decellularized heart showing leftover matrix and the complete absence of cells. Scale bar is 200 μm . The technique maintains large vasculature conduits (black asterisks). H&E, hematoxylin and eosin. (Adapted with permission from Reference 133.)

functional, vascularized cardiac tissues. However, there are limitations, as the recellularized hearts generated only 2% of the contractile force of normal adult rat hearts, highlighting the challenge of repopulating whole decellularized hearts with the constituent cells. For example, the extreme density and small pore size of the ECM in the myocardium ($\sim 20 \mu\text{m}$) inhibits cell infiltration and homogenous cell seeding throughout the construct, leading to inadequate CM density [20]. Of course, many research groups are actively working to address these challenges (see Reference 116 for an in-depth review). In an alternative approach, Godier-Furnémont *et al.* fabricated a composite graft made of decellularized human cardiac ECM sheets held together into a 3-D construct using fibrin glue seeded with human mesenchymal progenitor cells [87]. When implanted *in vivo* in a mouse MI model, this composite graft improved cardiac output, demonstrating the potential regenerative cardiac therapy. Current research is focused (a) on improving scaffolds for cardiac tissue engineering through characterization and optimization of the decellularization process to better preserve ECM structure and (b) on expanding the techniques beyond the rat heart to clinically translatable porcine and cadaveric human hearts [20,115–118].

12.5 PERSISTENT CHALLENGES

12.5.1 Cell Sources for Cardiomyocytes

Cardiac tissue engineering requires cardiac cells, and CMs are the most difficult cell type to obtain in sufficient numbers. Human CMs are terminally differentiated and cannot be expanded in culture to generate more CMs. Furthermore, human adult CMs lack the necessary plasticity to attach and integrate into a tissue engineering

scaffold, and instead, will rapidly die. Thus, human CMs with developmental plasticity must be derived from some type of stem cell population. Adult cardiac stem cells and cardiac progenitor cells have been identified by the expression of the transcription factors c-KIT and Sca-1, are self-renewing, and can differentiate into CMs, smooth muscle cells, and endothelial cells [119,120]. In the infarcted area, they produce new muscles as well as new capillaries that link to the existing coronary vasculature. Furthermore, they can be consistently isolated for culture *in vitro* using the cardiosphere technique [121]. However, their role *in vivo* and their ability to reliably deliver large number of CMs for cardiac tissue engineering is still controversial, and to date has not been proven as a viable source for large numbers of new CMs [3]. Human embryonic stem cells (hESCs) can be differentiated into mature cardiac cells including CMs, cardiac fibroblasts, and endothelial cells [122,123]. However, while useful for proof of concept, hESCs are allogeneic and, thus, an engineered cardiac construct used *in vivo* would require immunosuppression, similar to a heart transplant. Furthermore, ethical concerns and the cost associated with harvesting cells from human embryos have led to the development of alternative approaches. Human induced pluripotent stem cells (hiPSCs) developed by Yamanaka and coworkers enable patient-specific adult cells to be reverted to a pluripotent state and then differentiated to nearly any cell type, including CMs [124–127]. This is a potentially unlimited source of CMs and other cardiac cells without the ethical concerns and immune rejection issues of hESCs. However, CMs derived from ESCs or hiPSCs are embryonic in phenotype (i.e., immature) and have the potential to form teratomas. Recent efforts have sought to circumvent the pluripotent stem cell state by the direct reprogramming, or transdifferentiation, of fibroblasts into CMs, but have not yet been tested for cardiac tissue engineering [128–130]. What this means is that human CMs can be differentiated from hESCs and hiPSCs in large numbers suitable for cardiac tissue engineering, however, significant work remains in optimizing the differentiation process to obtain specific CM types, standardizing the process to obtain consistent results, and ensuring cells are terminally differentiated, all of which are necessary for these cells to be clinically translatable in an engineered tissue.

12.5.2 Vascularization

Vascularization and nutrient mass transport is a persistent challenge in the field of tissue engineering as a whole and particularly important in cardiac tissue engineering due to the high metabolic activity of muscle tissue. To address this issue, researchers have developed multiple approaches, such as bio-inspired materials and scaffolds that deliver VEGF to increase vasculogenesis when implanted *in vivo* [99,100,131,132]. Additionally, CMs and endothelial cells can be cocultured in cell sheets, synthetic scaffolds, hydrogels, and acellular ECM scaffolds to promote neovessel formation [21,81,133–137]. Scaffolds can also be engineered with channels to promote capillary network formation or pores for vascular invasion from the host when implanted [61,138]. 3-D printing and soft lithography have also been used to engineer 3-D vascular networks [108,139,140]. All of these methods are useful tools to investigate the mechanisms behind the formation and function of microvascular

networks. However, these approaches have limitations, and specifically for cardiac tissue engineering, cannot generate the high-density, parallel capillary networks found in the myocardium. New advances in the engineering of microvascular networks are needed to engineer dense, anisotropic cardiac tissues with embedded microvascular networks that can provide sufficient nutrient supply.

12.6 THE FUTURE OF CARDIAC TISSUE ENGINEERING

In this chapter, we have described the structure and function of the heart and a range of techniques to mimic the native cardiac ECM for the design and fabrication of cardiac tissue engineering scaffolds. Mimicking the cardiac ECM, whether composition, structure, or mechanical properties, provides clear benefits and results in engineered cardiac tissue, with improved electromechanical function. While we have organized these various fabrication approaches into distinct sections, it should be realized that many researchers are combining multiple techniques in order to engineer next-generation scaffolds with better performance. As the field evolves, we anticipate that new techniques will enable improved engineering of the cellular environment from the nanometer to macroscales in order to instruct cardiac cells to form cardiac tissue. For example, design inspiration may be drawn from cardiac morphogenesis during embryonic development, which in humans is the only period when there is significant CM proliferation and muscle formation. Particularly, the ECM cues that guide this process could be integrated into cardiac tissue engineering scaffolds to promote regeneration in adults. Ultimately, as cardiac tissue engineering research evolves and matures, recovering from heart failure should no longer require a transplant. Instead, treating an MI or heart failure should be possible by implanting an engineered cardiac graft to replace damaged tissue or to serve as a scaffold to enhance endogenous cardiac repair.

REFERENCES

- [1] Go, A.S., Mozaffarian, D., Roger, V.L., Benjamin, E.J., Berry, J.D., Borden, W.B., Bravata, D.M., Dai, S., Ford, E.S., Fox, C.S., Franco, S., Fullerton, H.J., Gillespie, C., Hailpern, S.M., Heit, J.A., Howard, V.J., Huffman, M.D., Kissela, B.M., Kittner, S.J., Lackland, D.T., Lichtman, J.H., Lisabeth, L.D., Magid, D., Marcus, G.M., Marelli, A., Matchar, D.B., McGuire, D.K., Mohler, E.R., Moy, C.S., Mussolino, M.E., Nichol, G., Paynter, N.P., Schreiner, P.J., Sorlie, P.D., Stein, J., Turan, T.N., Virani, S.S., Wong, N.D., Woo, D., Turner, M.B. *Circulation* **2013**, *127*, e6–e245.
- [2] Sedmera, D., Thompson, R.P. *Dev. Dyn.* **2011**, *240*, 1322–1334.
- [3] Laflamme, M.A., Murry, C.E. *Nature* **2011**, *473*, 326–335.
- [4] Bergmann, O., Bhardwaj, R.D., Bernard, S., Zdunek, S., Barnabé-Heider, F., Walsh, S., Zupicich, J., Alkass, K., Buchholz, B.A., Druid, H., Jovinge, S., Frisén, J. *Science* **2009**, *324*, 98–102.
- [5] Senyo, S.E., Steinhauser, M.L., Pizzimenti, C.L., Yang, V.K., Cai, L., Wang, M., Wu, T.-D., Guerin-Kern, J.-L., Lechene, C.P., Lee, R.T. *Nature* **2013**, *493*, 433–436.

- [6] Jahanmir, S., Hunsberger, A.Z., Heshmat, H., Tomaszewski, M.J., Walton, J.F., Weiss, W.J., Lukic, B., Pae, W.E., Zapanta, C.M., Khalapyan, T.Z. *Artif. Organs* **2008**, *32*, 366–375.
- [7] Joyce, L.D., DeVries, W.C., Hastings, W.L., Olsen, D.B., Jarvik, R.K., Kolff, W.J. *Trans. Am. Soc. Artif. Intern. Organs* **1983**, *29*, 81–87.
- [8] Gray, N.A., Selzman, C.H. *Am. Heart J.* **2006**, *152*, 4–10.
- [9] Davani, S., Deschaseaux, F., Chalmers, D., Tiberghien, P., Kantelip, J.-P. *Cardiovasc. Res.* **2005**, *65*, 305–316.
- [10] Passier, R., Van Laake, L.W., Mummery, C.L. *Nature* **2008**, *453*, 322–329.
- [11] Segers, V.F.M., Lee, R.T. *Nature* **2008**, *451*, 937–942.
- [12] Forrester, J.S., Price, M.J., Makkar, R.R. *Circulation* **2003**, *108*, 1139–1145.
- [13] Clifford, D.M., Fisher, S.A., Brunskill, S.J., Doree, C., Mathur, A., Watt, S., Martin-Rendon, E. *Cochrane Database Syst. Rev.* **2012**, (2), CD006536.
- [14] Menasché, P. *Circulation* **2009**, *119*, 2735–2740.
- [15] Gerdes, A.M., Capasso, J.M. *J. Mol. Cell. Cardiol.* **1995**, *27*, 849–856.
- [16] Bershtitsky, S.Y., Tsaturyan, A.K. *Biophys. J.* **1995**, *69*, 1011–1021.
- [17] Janssen, P.M., Lehnart, S.E., Prestle, J., Hasenfuss, G. *J. Mol. Cell. Cardiol.* **1999**, *31*, 1419–1427.
- [18] Engelmayr, G.C., Cheng, M., Bettinger, C.J., Borenstein, J.T., Langer, R., Freed, L.E. *Nat. Mater.* **2008**, *7*, 1003–1010.
- [19] Chen, Q.-Z., Harding, S.E., Ali, N.N., Lyon, A.R., Boccaccini, A.R. *Mater. Sci. Eng. R Rep.* **2008**, *59*, 1–37.
- [20] Wang, B., Tedder, M.E., Perez, C.E., Wang, G., de Jongh Curry, A.L., To, F., Elder, S.H., Williams, L.N., Simionescu, D.T., Liao, J. *J. Mater. Sci. Mater. Med.* **2012**, *23*, 1835–1847.
- [21] Wang, B., Borazjani, A., Tahai, M., Curry, A.L.D.J., Simionescu, D.T., Guan, J., To, F., Elder, S.H., Liao, J. *J. Biomed. Mater. Res. A* **2010**, *94*, 1100–1110.
- [22] Sarig, U., Au-yeung, G.C.T., Wang, Y., Bronshtein, T., Dahan, N., Boey, F.Y.C., Venkatraman, S.S., Machluf, M. *Tissue Eng. A* **2012**, *18*, 2125–2137.
- [23] Fomovsky, G.M., Holmes, J.W. *Am. J. Physiol. Heart Circ. Physiol.* **2010**, *298*, H221–H228.
- [24] Engler, A.J., Carag-Krieger, C., Johnson, C.P., Raab, M., Tang, H.-Y., Speicher, D.W., Sanger, J.W., Sanger, J.M., Discher, D.E. *J. Cell Sci.* **2008**, *121*, 3794–3802.
- [25] Armour, J.A. *Am. J. Physiol. Regul. Integr. Comp. Physiol.* **2004**, *287*, R262–R271.
- [26] Pennisi, D.J., Rentschler, S., Gourdie, R.G., Fishman, G.I., Mikawa, T. *Int. J. Dev. Biol.* **2002**, *46*, 765–775.
- [27] Moorman, A.F.M., de Jong, F., Denyn, M.M.F.J., Lamers, W.H. *Circ. Res.* **1998**, *82*, 629–644.
- [28] Young, R.J., Panfilov, A.V. *Proc. Natl. Acad. Sci. U.S.A.* **2010**, *107*, 15063–15068.
- [29] Nogami, A. *Pacing Clin. Electrophysiol.* **2011**, *34*, 624–650.
- [30] Kimura, K., Ieda, M., Fukuda, K. *Circ. Res.* **2012**, *110*, 325–336.
- [31] Stoker, M.E., Gerdes, A.M., May, J.F. *Anat. Rec.* **1982**, *202*, 187–191.
- [32] Kaneko, N., Matsuda, R., Toda, M., Shimamoto, K. *Am. J. Physiol. Heart Circ. Physiol.* **2011**, *300*, H754–H761.
- [33] Banerjee, I., Fuseler, J.W., Price, R.L., Borg, T.K., Baudino, T.A. *Am. J. Physiol. Heart Circ. Physiol.* **2007**, *293*, H1883–H1891.
- [34] Mandarim-De-Lacerda, C.A., Meirelles Pereira, L.M. *Pathobiology* **2008**, *68*, 36–42.
- [35] Brutsaert, D.L. *Physiol. Rev.* **2003**, *83*, 59–115.
- [36] Ramaciotti, C., Sharkey, A., McClellan, G., Winegrad, S. *Proc. Natl. Acad. Sci. U.S.A.* **1992**, *89*, 4033–4036.

- [37] Narmoneva, D.A., Vukmirovic, R., Davis, M.E., Kamm, R.D., Lee, R.T. *Circulation* **2004**, *110*, 962–968.
- [38] Vliegen, H.W., Van der Laarse, A., Cornelisse, C.J., Eulderink, F. *Eur. Heart J.* **1991**, *12*, 488–494.
- [39] Spinale, F.G. *Physiol. Rev.* **2007**, *87*, 1285–1342.
- [40] Farhadian, F., Contard, F., Sabri, A., Samuel, J.L., Rappaport, L. *Cardiovasc. Res.* **1996**, *32*, 433–442.
- [41] Lipke, D.W., McCarthy, K.J., Elton, T.S., Arcot, S.S., Oparil, S., Couchman, J.R. *Hypertension* **1993**, *22*, 743–753.
- [42] Gazoti Debessa, C.R., Mesiano Maifrino, L.B., Rodrigues de Souza, R. *Mech. Ageing Dev.* **2001**, *122*, 1049–1058.
- [43] Eghbali, M., Weber, K.T. *Mol. Cell. Biochem.* **1990**, *96*, 1–14.
- [44] Weber, K.T. *J. Am. Coll. Cardiol.* **1989**, *13*, 1637–1652.
- [45] Pope, A.J., Sands, G.B., Smail, B.H., LeGrice, I.J. *Am. J. Physiol. Heart Circ. Physiol.* **2008**, *295*, H1243–H1252.
- [46] Samarel, A.M. *Am. J. Physiol. Heart Circ. Physiol.* **2005**, *289*, H2291–H2301.
- [47] Gerson, C.J., Elkins, R.C., Goldstein, S., Heacox, A.E. *Cryobiology* **2012**, *64*, 33–42.
- [48] Mao, Y., Schwarzbauer, J.E. *Matrix Biol.* **2005**, *24*, 389–399.
- [49] Singh, P., Carraher, C., Schwarzbauer, J.E. *Annu. Rev. Cell Dev. Biol.* **2010**, *26*, 397–419.
- [50] Ertl, G., Frantz, S. *Cardiovasc. Res.* **2005**, *66*, 22–32.
- [51] Liehn, E.A., Postea, O., Curaj, A., Marx, N. *J. Am. Coll. Cardiol.* **2011**, *58*, 2357–2362.
- [52] Yang, J.T., Rayburn, H., Hynes, R.O. *Development* **1993**, *119*, 1093–1105.
- [53] Schenke-Layland, K., Nsair, A., Van Handel, B., Angelis, E., Gluck, J.M., Votteler, M., Goldhaber, J.I., Mikkola, H.K., Kahn, M., MacLellan, W.R. *Biomaterials* **2011**, *32*, 2748–2756.
- [54] Jugdutt, B.I. *Circulation* **2003**, *108*, 1395–1403.
- [55] Spotnitz, H.M. *J. Thorac. Cardiovasc. Surg.* **2000**, *119*, 1053–1077.
- [56] Buckberg, G., Hoffman, J.I.E., Mahajan, A., Saleh, S., Coghlán, C. *Circulation* **2008**, *118*, 2571–2587.
- [57] Schwartzman, D., Chang, I., Michele, J.J., Mirotznic, M.S., Foster, K.R. *J. Interv. Card. Electrophysiol.* **1999**, *3*, 213–224.
- [58] Stella, J.A., Amore, A.D., Wagner, W.R., Sacks, M.S. *Acta Biomater.* **2010**, *6*, 2365–2381.
- [59] Radisic, M., Park, H., Martens, T.P., Salazar-Lazaro, J.E., Geng, W., Wang, Y., Langer, R., Freed, L.E., Vunjak-Novakovic, G. *J. Biomed. Mater. Res. A* **2008**, *86*, 713–724.
- [60] Radisic, M., Park, H., Chen, F., Salazar-Lazzaro, J.E., Wang, Y., Dennis, R., Langer, R., Freed, L.E., Vunjak-Novakovic, G. *Tissue Eng.* **2006**, *12*, 2077–2091.
- [61] Madden, L.R., Mortisen, D.J., Sussman, E.M., Dupras, S.K., Fugate, J.A., Cuy, J.L., Hauch, K.D., Laflamme, M.A., Murry, C.E., Ratner, B.D. *Proc. Natl. Acad. Sci. U.S.A.* **2010**, *107*, 15211–15216.
- [62] Shapiro, L., Cohen, S. *Biomaterials* **1997**, *18*, 583–590.
- [63] Sapir, Y., Kryukov, O., Cohen, S. *Biomaterials* **2011**, *32*, 1838–1847.
- [64] Gonnerman, E.A., Kelkhoff, D.O., McGregor, L.M., Harley, B.A.C. *Biomaterials* **2012**, *33*, 8812–8821.
- [65] Kumber, S.G., James, R., Nukavarapu, S.P., Laurencin, C.T. *Biomed. Mater.* **2008**, *3*, 034002.
- [66] Teo, W.E., Ramakrishna, S. *Nanotechnology* **2006**, *17*, R89–R106.

- [67] Kai, D., Prabhakaran, M.P., Jin, G., Ramakrishna, S. *J. Biomed. Mater. Res. B Appl. Biomater.* **2011**, *98B*, 379–386.
- [68] Ricotti, L., Polini, A., Genchi, G.G., Ciofani, G., Iandolo, D., Mattoli, V., Menciassi, A., Dario, P., Pisignano, D. *Conf. Proc. IEEE Eng. Med. Biol. Soc.* **2011**, *2011*, 3597–3600.
- [69] Amoroso, N.J., D'Amore, A., Hong, Y., Rivera, C.P., Sacks, M.S., Wagner, W.R. *Acta Biomater.* **2012**, *8*, 4268–4277.
- [70] Shin, M., Ishii, O., Sueda, T., Vacanti, J.P. *Biomaterials* **2004**, *25*, 3717–3723.
- [71] Zong, X., Bien, H., Chung, C.-Y., Yin, L., Fang, D., Hsiao, B.S., Chu, B., Entcheva, E. *Biomaterials* **2005**, *26*, 5330–5338.
- [72] Li, M., Guo, Y., Wei, Y., MacDiarmid, A.G., Lelkes, P.I. *Biomaterials* **2006**, *27*, 2705–2715.
- [73] Fernandes, E., Zucolotto, V., De Queiroz, A. *J. Macromol. Sci. Pure Appl. Chem.* **2010**, *47*, 1203–1207.
- [74] Sreerekha, P.R., Menon, D., Nair, S.V., Chennazhi, K.P. *Tissue Eng. A* **2013**, *19*, 849–859.
- [75] Hosseinkhani, H., Hosseinkhani, M., Hattori, S., Matsuoka, R., Kawaguchi, N. *J. Biomed. Mater. Res. A* **2010**, *94*, 1–8.
- [76] Mellado, P., McIlwee, H.A., Badrossamay, M.R., Goss, J.A., Mahadevan, L., Kit Parker, K. *Appl. Phys. Lett.* **2011**, *99*, 203107.
- [77] Badrossamay, M.R., McIlwee, H.A., Goss, J.A., Parker, K.K. *Nano Lett.* **2010**, *10*, 2257–2261.
- [78] Feinberg, A.W., Parker, K.K. *Nano Lett.* **2010**, *10*, 2184–2191.
- [79] Li, Z., Guan, J. *Polymers* **2011**, *3*, 740–761.
- [80] Yost, M.J., Baicu, C.F., Stonerock, C.E., Goodwin, R.L., Price, R.L., Davis, J.M., Evans, H., Watson, P.D., Gore, C.M., Sweet, J., Creech, L., Zile, M.R., Terracio, L. *Tissue Eng.* **2004**, *10*, 273–284.
- [81] Leung, B.M., Sefton, M.V. *Tissue Eng. A* **2010**, *16*, 3207–3218.
- [82] Sondergaard, C.S., Mathews, G., Wang, L., Jeffreys, A., Sahota, A., Wood, M., Ripplinger, C.M., Si, M.-S. *Ann. Thorac. Surg.* **2012**, *94*, 1241–1249.
- [83] Dengler, J., Song, H., Thavandiran, N., Massé, S., Wood, G.A., Nanthakumar, K., Zandstra, P.W., Radisic, M. *Biotechnol. Bioeng.* **2011**, *108*, 704–719.
- [84] Freytes, D.O., Martin, J., Velankar, S.S., Lee, A.S., Badylak, S.F. *Biomaterials* **2008**, *29*, 1630–1637.
- [85] Duan, Y., Liu, Z., O'Neill, J., Wan, L.Q., Freytes, D.O., Vunjak-Novakovic, G. *J. Cardiovasc. Transl. Res.* **2011**, *4*, 605–615.
- [86] Cigliano, A., Gandaglia, A., Lepedda, A.J., Zinellu, E., Naso, F., Gastaldello, A., Aguiari, P., De Muro, P., Gerosa, G., Spina, M., Formato, M. *Biochem. Res. Int.* **2012**, *2012*, 979351.
- [87] Godier-Furnémont, A.F.G., Martens, T.P., Koeckert, M.S., Wan, L., Parks, J., Arai, K., Zhang, G., Hudson, B., Homma, S., Vunjak-Novakovic, G. *Proc. Natl. Acad. Sci. U.S.A.* **2011**, *108*, 7974–7979.
- [88] Johnson, T.D., Lin, S.Y., Christman, K.L. *Nanotechnology* **2011**, *22*, 494015.
- [89] Singelyn, J.M., DeQuach, J.A., Seif-Naraghi, S.B., Littlefield, R.B., Schup-Magoffin, P.J., Christman, K.L. *Biomaterials* **2009**, *30*, 5409–5416.
- [90] French, K.M., Boopathy, A.V., Dequach, J.A., Chingozha, L., Lu, H., Christman, K.L., Davis, M.E. *Acta Biomater.* **2012**, *8*, 4357–4364.
- [91] Seif-Naraghi, S.B., Horn, D., Schup-Magoffin, P.J., Christman, K.L. *Acta Biomater.* **2012**, *8*, 3695–3703.
- [92] Zimmermann, W.-H. *Circ. Res.* **2001**, *90*, 223–230.

- [93] Schaaf, S., Shibamiya, A., Mewe, M., Eder, A., Stöhr, A., Hirt, M.N., Rau, T., Zimmermann, W.-H., Conradi, L., Eschenhagen, T., Hansen, A. *PLoS ONE* **2011**, *6*, e26397.
- [94] Zhang, D., Shadrin, I.Y., Lam, J., Xian, H.-Q., Snodgrass, H.R., Bursac, N. *Biomaterials* **2013**, *34*, 5813–5820.
- [95] Baar, K., Birla, R., Boluyt, M.O., Borschel, G.H., Arruda, E.M., Dennis, R.G. *FASEB J.* **2005**, *19*, 275–277.
- [96] Jongpaiboonkit, L., King, W.J., Lyons, G.E., Paguirigan, A.L., Warrick, J.W., Beebe, D.J., Murphy, W.L. *Biomaterials* **2008**, *29*, 3346–3356.
- [97] Kraehenbuehl, T.P., Ferreira, L.S., Hayward, A.M., Nahrendorf, M., van der Vlies, A.J., Vasile, E., Weissleder, R., Langer, R., Hubbell, J.A. *Biomaterials* **2011**, *32*, 1102–1109.
- [98] Kraehenbuehl, T.P., Zammaretti, P., Van der Vlies, A.J., Schoenmakers, R.G., Lutolf, M.P., Jaconi, M.E., Hubbell, J.A. *Biomaterials* **2008**, *29*, 2757–2766.
- [99] Guo, H., Cui, G., Yang, J., Wang, C., Zhu, J., Zhang, L., Jiang, J., Shao, S. *Biochem. Biophys. Res. Commun.* **2012**, *424*, 105–111.
- [100] Webber, M.J., Tongers, J., Newcomb, C.J., Marquardt, K.-T., Bauersachs, J., Losordo, D.W., Stupp, S.I. *Proc. Natl. Acad. Sci. U.S.A.* **2011**, *108*, 13438–13443.
- [101] Hsieh, P.C.H., Davis, M.E., Gannon, J., MacGillivray, C., Lee, R.T. *J. Clin. Invest.* **2006**, *116*, 237.
- [102] Chung, C., Bien, H., Sobie, E.A., Dasari, V., McKinnon, D., Rosati, B., Entcheva, E. *FASEB J.* **2011**, *25*, 851–862.
- [103] Kim, D.-H., Lipke, E.A., Kim, P., Cheong, R., Thompson, S., Delannoy, M., Suh, K.-Y., Tung, L., Levchenko, A. *Proc. Natl. Acad. Sci. U.S.A.* **2010**, *107*, 565–570.
- [104] Feinberg, A.W., Feigel, A., Shevkopyas, S.S., Sheehy, S., Whitesides, G.M., Parker, K.K. *Science* **2007**, *317*, 1366–1370.
- [105] Feinberg, A.W., Alford, P.W., Jin, H., Ripplinger, C.M., Werdich, A.A., Sheehy, S.P., Grosberg, A., Parker, K.K. *Biomaterials* **2012**, *33*, 5732–5741.
- [106] Radisic, M., Deen, W., Langer, R., Vunjak-Novakovic, G. *Am. J. Physiol. Heart Circ. Physiol.* **2005**, *288*, H1278–H1289.
- [107] Gaetani, R., Doevendans, P.A., Metz, C.H.G., Alblas, J., Messina, E., Giacomello, A., Sluijter, J.P.G. *Biomaterials* **2012**, *33*, 1782–1790.
- [108] Miller, J.S., Stevens, K.R., Yang, M.T., Baker, B.M., Nguyen, D.-H.T., Cohen, D.M., Toro, E., Chen, A.A., Galie, P.A., Yu, X., Chaturvedi, R., Bhatia, S.N., Chen, C.S. *Nat. Mater.* **2012**, *11*, 768–774.
- [109] Shimizu, T., Yamato, M., Kikuchi, A., Okano, T. *Tissue Eng.* **2001**, *7*, 141–151.
- [110] Takahashi, H., Nakayama, M., Shimizu, T., Yamato, M., Okano, T. *Biomaterials* **2011**, *32*, 8830–8838.
- [111] Williams, C., Xie, A.W., Yamato, M., Okano, T., Wong, J.Y. *Biomaterials* **2011**, *32*, 5625–5632.
- [112] Sekine, H., Shimizu, T., Dobashi, I., Matsuura, K., Hagiwara, N., Takahashi, M., Kobayashi, E., Yamato, M., Okano, T. *Tissue Eng. A.* **2011**, *17*, 2973–2980.
- [113] Shimizu, T., Okano, T. *Biomaterials* **2003**, *24*, 2309–2316.
- [114] Stevens, K.R., Kreutziger, K.L., Dupras, S.K., Korte, F.S., Regnier, M., Muskheli, V., Nourse, M.B., Bendixen, K., Reinecke, H., Murry, C.E. *Proc. Natl. Acad. Sci. U.S.A.* **2009**, *106*, 16568–16573.
- [115] Weymann, A., Loganathan, S., Takahashi, H., Schies, C., Claus, B., Hirschberg, K., Soós, P., Korkmaz, S., Schmack, B., Karck, M., Szabó, G. *Circ. J.* **2011**, *75*, 852–860.
- [116] Badylak, S.F., Taylor, D., Uygun, K. *Annu. Rev. Biomed. Eng.* **2011**, *13*, 27–53.
- [117] Akhyari, P., Aubin, H., Gwanmesia, P., Barth, M., Hoffmann, S., Huelsmann, J., Preuss, K., Lichtenberg, A. *Tissue Eng. C Methods* **2011**, *17*, 915–926.

- [118] Crapo, P.M., Gilbert, T.W., Badylak, S.F. *Biomaterials* **2011**, *32*, 3233–3243.
- [119] Beltrami, A.P., Barlucchi, L., Torella, D., Baker, M., Limana, F., Chimenti, S., Kasahara, H., Rota, M., Musso, E., Urbanek, K., Leri, A., Kajstura, J., Nadal-Ginard, B., Anversa, P. *Cell* **2003**, *114*, 763–776.
- [120] Oh, H., Bradfute, S.B., Gallardo, T.D., Nakamura, T., Gaussen, V., Mishina, Y., Pocius, J., Michael, L.H., Behringer, R.R., Garry, D.J., Entman, M.L., Schneider, M.D. *Proc. Natl. Acad. Sci. U.S.A.* **2003**, *100*, 12313–12318.
- [121] Davis, D.R., Zhang, Y., Smith, R.R., Cheng, K., Terrovitis, J., Malliaras, K., Li, T.-S., White, A., Makkar, R., Marbán, E. *PLoS ONE* **2009**, *4*, e7195.
- [122] Chien, K.R., Domian, I.J., Parker, K.K. *Science* **2008**, *322*, 1494–1497.
- [123] Caspi, O., Lesman, A., Basevitch, Y., Gepstein, A., Arbel, G., Habib, I.H.M., Gepstein, L., Levenberg, S. *Circ. Res.* **2007**, *100*, 263–272.
- [124] Takahashi, K., Yamanaka, S. *Cell* **2006**, *126*, 663–676.
- [125] Takahashi, K., Tanabe, K., Ohnuki, M., Narita, M., Ichisaka, T., Tomoda, K., Yamanaka, S. *Cell* **2007**, *131*, 861–872.
- [126] Gai, H., Leung, E.L.-H., Costantino, P.D., Aguila, J.R., Nguyen, D.M., Fink, L.M., Ward, D.C., Ma, Y. *Cell Biol. Int.* **2009**, *33*, 1184–1193.
- [127] Zhang, J., Wilson, G.F., Soerens, A.G., Koonce, C.H., Yu, J., Palecek, S.P., Thomson, J.A., Kamp, T.J. *Circ. Res.* **2009**, *104*, e30–e41.
- [128] Qian, L., Huang, Y., Spencer, C.I., Foley, A., Vedantham, V., Liu, L., Conway, S.J., Fu, J., Srivastava, D. *Nature* **2012**, *485*, 593–598.
- [129] Song, K., Nam, Y.-J., Luo, X., Qi, X., Tan, W., Huang, G.N., Acharya, A., Smith, C.L., Tallquist, M.D., Neilson, E.G., Hill, J.A., Bassel-Duby, R., Olson, E.N. *Nature* **2012**, *485*, 599–604.
- [130] Teunissen, B.E.J., Smeets, P.J.H., Willemsen, P.H.M., De Windt, L.J., Van der Vusse, G.J., Van Bilsen, M. *Cardiovasc. Res.* **2007**, *75*, 519–529.
- [131] Lin, Y.-D., Luo, C.-Y., Hu, Y.-N., Yeh, M.-L., Hsueh, Y.-C., Chang, M.-Y., Tsai, D.-C., Wang, J.-N., Tang, M.-J., Wei, E.I.H., Springer, M.L., Hsieh, P.C.H. *Sci. Transl. Med.* **2012**, *4*, 146ra109.
- [132] Ruhrberg, C., Gerhardt, H., Golding, M., Watson, R., Ioannidou, S., Fujisawa, H., Betscholtz, C., Shima, D.T. *Genes Dev.* **2002**, *16*, 2684–2698.
- [133] Ott, H.C., Matthiesen, T.S., Goh, S.-K., Black, L.D., Kren, S.M., Netoff, T.I., Taylor, D.A. *Nat. Med.* **2008**, *14*, 213–221.
- [134] Bel, A., Planat-Bernard, V., Saito, A., Bonnevie, L., Bellamy, V., Sabbah, L., Bellabas, L., Brinon, B., Vanneaux, V., Pradeau, P., Peyrard, S., Larghero, J., Pouly, J., Binder, P., Garcia, S., Shimizu, T., Sawa, Y., Okano, T., Bruneval, P., Desnos, M., Haggège, A.A., Casteilla, L., Pucéat, M., Menasché, P. *Circulation* **2010**, *122*, S118–S123.
- [135] Sekine, H., Shimizu, T., Hobo, K., Sekiya, S., Yang, J., Yamato, M., Kurosawa, H., Kobayashi, E., Okano, T. *Circulation* **2008**, *118*, S145–S152.
- [136] Masumoto, H., Matsuo, T., Yamamizu, K., Uosaki, H., Narazaki, G., Katayama, S., Marui, A., Shimizu, T., Ikeda, T., Okano, T., Sakata, R., Yamashita, J.K. *Stem Cells* **2012**, *30*, 1196–1205.
- [137] Mo, X., Xu, C., Kotaki, M., Ramakrishna, S. *Biomaterials* **2004**, *25*, 1883–1890.
- [138] Maidhof, R., Marsano, A., Lee, E.J., Vunjak-Novakovic, G. *Biotechnol. Prog.* **2010**, *26*, 565–572.
- [139] Wu, W., DeConinck, A., Lewis, J.A. *Adv. Mater.* **2011**, *23*, H178–H183.
- [140] Zheng, Y., Chen, J., Craven, M., Choi, N.W., Totorica, S., Diaz-Santana, A., Kermani, P., Hempstead, B., Fischbach-Teschl, C., López, J.A., Stroock, A.D. *Proc. Natl. Acad. Sci. U.S.A.* **2012**, *109*, 9342–9347.
- [141] Savadjiev, P., Strijkers, G.J., Bakermans, A.J., Piuze, E., Zucker, S.W., Siddiqi, K. *Proc. Natl. Acad. Sci. U.S.A.* **2012**, *109*, 9248–9253.

- [142] Lee, J., Beighley, P., Ritman, E., Smith, N. *Med. Image Anal.* **2007**, *11*, 630–647.
- [143] O'Brien, F., Harley, B., Yannas, I., Gibson, L. *Biomaterials* **2004**, *25*, 1077e86.
- [144] Soliman, S., Pagliari, S., Rinaldi, A., Forte, G., Fiaccavento, R., Pagliari, F., Franzese, O., Minieri, M., Di Nardo, P., Licoccia, S., Traversa, E. *Acta Biomater.* **2010**, *6*, 1227–1237.